

# POLITECNICO DI MILANO

School of Industrial and Information Engineering, Department of  
Chemistry, Materials and Chemical Engineering "G. Natta"

**Master of Science in Chemical Engineering**



## **Discontinuous Anodizing Treatment to Increase Commercially Pure Titanium Corrosion Resistance**

Supervisor: professor Marco ORMELLESE

Co-Supervisor: Davide PRANDO

Master Thesis by:

Martina BRUNO– ID 883964

Academic Year 2017/2018

# Ringraziamenti

*Desidero ringraziare prima di tutto il professor Ormellese senza il quale non avrei potuto prendere parte a questo progetto e a tutta la famiglia del PolillaPP che mi ha accolto con gentilezza e amicizia. In particolare, la mia gratitudine va' alla professoressa Pedefferri, all'ingegner Beretta e ai neo-dottorandi Luca Casanova e Umberto Bellè senza i quali non sarei riuscita a completare questo piccolo tassello nella ricerca sul Titanio.*

*Ringrazio profondamente Davide, il dottorando che mi ha seguita costantemente e con infinita pazienza nel mio lavoro in laboratorio, non perdendo mai la speranza anche nelle situazioni più difficili e lottando con tenacia per comprendere, seppur in modo parziale fenomeni incomprensibili. Il suo amore per la conoscenza dovrebbe essere esempio per molti ricercatori di generazioni future.*

*Queste poche righe non basteranno mai a ringraziare dovutamente Gabriele, mio compagno di scuola e di vita, che ha da sempre creduto in me anche quando io avevo smesso di farlo. Sarebbe banale forse dire che senza di lui non sarei quella che sono, ma è così. Lui mi ha insegnato la pazienza, il silenzio e la lungimiranza di vedere oltre il fatto o l'azione istantanea di una persona per coglierne motivazioni profonde. Incoraggiandomi, ascoltandomi e proteggendomi è sempre stato calma per la mia tempesta.*

*Ringrazio mia sorella Costanza per avermi sempre portato un raggio di sole in camera mentre studiavo le materie più nere. Col suo sorriso e la sua allegria questi cinque anni sono passati in modo molto più leggero di quanto potessi immaginare. Spero presto di poter leggere i suoi di ringraziamenti e di vederla realizzare quello che già si porta dentro.*

*Vorrei ringraziare i miei genitori per tutti i sacrifici che hanno fatto per me, per avermi ascoltata e incoraggiata lasciandomi piena libertà e fiducia in questo cammino. Li ringrazio soprattutto per aver capito che i figli sono frecce lanciate verso un futuro che ai genitori non è dato conoscere e, una volta lanciata la freccia, l'arciere ne perde il controllo.*

*Vorrei ringraziare tutti gli amici che mi hanno accompagnato in questi cinque anni di università in particolare, Elena, Manuel, Michael, Nicolò, Matteo Perego ed Enrico, i migliori compagni di pranzi sul prato mai visti.*

*Vorrei dedicare poche righe ad amici speciali, come Federico amico fedele, sensibile e forte nelle sue fragilità sempre capace di rialzarsi. Poi viene Nicole così timida e insicura,*

*ma forte nel difendere chi ama e Matteo Brugnoli, il gigante buono, semplice e schietto come pochi altri.*

*Da ultimo ma non per importanza, vorrei ringraziare Giada, mia cara amica da anni che mi ha sempre ascoltata e spronata a diventare ciò che desideravo con fatica e sudore. So che sarà la migliore insegnante del mondo e questo sarà solo il primo di molti ringraziamenti che riceverà.*

# ***Abstract***

Titanium is one of the metal with exceptional mechanical characteristics and almost the only one with outstanding corrosion resistance. For these reasons, it is one of the most studied metals in industries like automotive, food, medical, aerospace and petrochemical.

However, even in few environments also titanium suffers many problems of corrosion. For this reason, in the first chapter, a detailed overview of the chemicals and the corrosion forms that could attack titanium is discussed. Among all the possible forms of corrosion, titanium mainly suffers of pitting corrosion which is one of the most aggressive. This type of corrosion is deeper developed in the first chapter.

In the second chapter the main treatments that can be applied to further enhance its corrosion resistance are described: chemical and thermal oxidation, ion implantation and grain refinement, along with the various elements with which titanium can be alloyed to improve its mechanical characteristics.

Then, a review on the surface treatments that can be applied to titanium in order to control the formation of the protective oxide layer in surface is reported. These surface treatments are traditional anodizing and anodic spark deposition anodizing (ASD), which are the most used ones as they are cheap, easy to perform and the oxide that will grow is easily tunable. Later in the chapter, the focus goes on discontinuous anodizing, that is the key point of this work, as it allows to obtain the same results in improving the pitting resistance but with a lower energy consumption. In the literature, discontinuous anodizing has been applied mainly on magnesium and aluminium, but considering the appealing results reported and the energy savings linked with this treatment, it has been decided to apply it on titanium grade 2 samples for this thesis work.

A detailed surface characterization, in terms of morphology and roughness was conducted on titanium before any corrosion enhancing treatment. This allowed to define a proper pre-treatment to remove surface contamination while maintaining surface conditions similar to the as-received metal, thus, to not require any pre-treatment during industrial treatment application while keeping the necessary laboratory control over sample surface characteristics.

Discontinuous anodizing is performed in the form of duty cycle, in particular have been investigated the 25% and 75% to be compared to a DC anodizing, with a frequency of 20

Hz and 1000 Hz for each case and three different final potentials: 120 V, 160 V and 220 V. Each of the fifteen anodizing condition was repeated twice to ensure measurements repeatability, while recording the initial and final temperature of the solution and the peaks and plateau of anodizing current.

Then, each specimen has been observed with XRD, to analyse its surface composition, and with SEM, to obtain a detailed image of the surface porosity that, then, has been examined with IMAGEJ, an image processing software, and statistically investigated to have a clearer idea of pore dimensions and distributions.

As final analysis, an electrochemical potentiodynamic test has been performed on each sample, all in the same electrolyte, sodium bromide, and all with the same analysis parameters, to test the pitting corrosion resistance.

The duty cycle used to anodize the specimens significantly affected the morphology, composition and corrosion resistance of titanium, allowing to determine the most effective parameters and conditions for the treatment. The results of the tests, for this reason, have been crossed to find correlations between porosity and corrosion resistance to find the best anti-corrosive treatment for a possible industrial application.

# Sommario

Il titanio, grazie alle sue eccezionali caratteristiche meccaniche e la sua straordinaria resistenza a corrosione, è uno dei metalli più studiati al giorno d'oggi. Queste caratteristiche lo rendono il materiale adatto per applicazioni in ambienti aggressivi in innumerevoli campi industriali, come automobilistico, aerospaziale, sanitario, alimentare e petrolchimico.

Una breve storia della sua scoperta e le sue principali caratteristiche sono riportate nel capitolo 1, in cui vengono descritte anche le forme di corrosione che possono interessare il titanio, ponendo particolare attenzione alle forme di corrosione localizzata, il caso di maggiore interesse.

All'inizio del secondo capitolo, viene riportata una breve panoramica sui trattamenti superficiali che possono essere applicati al titanio per migliorare ulteriormente le sue proprietà, tra cui l'ossidazione chimica e termica, l'impiantazione ionica e l'affinamento del grano. Successivamente vengono descritti anche i principali elementi alliganti che favoriscono l'incremento della resistenza a corrosione del titanio.

Successivamente, l'attenzione viene riposta sui trattamenti superficiali che maggiormente permettono di controllare e modificare l'ossido superficiale del titanio, responsabile della sua straordinaria resistenza a corrosione. Questi trattamenti sono l'anodizzazione tradizionale e la *anodic spark deposition (ASD)*, che, oltre che i più semplici da attuare, sono anche i più economici e dunque i più utilizzati. Un caso particolare di ASD, l'anodizzazione discontinua o pulsata, è il punto focale di questa tesi. Questo trattamento, infatti, nella letteratura viene riportato come una valida alternativa all'anodizzazione tradizionale, poiché a parità di potenziale di anodizzazione permette un minor dispendio energetico ed un ossido più prestante. Per questo motivo, in questo lavoro di tesi, l'anodizzazione discontinua, finora applicata principalmente su magnesio e alluminio, viene applicata sul titanio grado 2.

Prima dell'anodizzazione, alcuni dei provini, sono stati osservati al microscopio ottico, subito dopo la preparazione superficiale, lappatura e pulizia ad ultrasuoni, per studiarne la rugosità e la morfologia, e i risultati sono riportati nel paragrafo 4.1.

L'anodizzazione discontinua viene applicata ai provini di titanio nella forma di *duty cycle*, in particolare sono stati studiati i *duty cycles* 25% e 75% da confrontare con l'anodizzazione in corrente continua per ogni valore di potenziale. I potenziali utilizzati sono 120 V, 160 V e

220 V. Ogni anodizzazione pulsata viene effettuata con due valori differenti di frequenza, 20 Hz e 1000 Hz.

Ciascuna delle quindici possibilità viene poi ripetuta due volte, per assicurare la ripetibilità della misura, e ogni anodizzazione viene eseguita nello stesso elettrolita, acido solforico, con una particolare attenzione all'incremento di temperatura per ogni prova e a picchi e *plateau* di corrente rilevati.

Successivamente, ogni campione viene analizzato ai raggi X (XRD), per studiarne la composizione superficiale, e al microscopio elettronico (SEM), per ottenere una dettagliata immagine della porosità superficiale. Quest'ultima immagine viene poi analizzata con un programma informatico per l'elaborazione digitale delle immagini, ImageJ, che restituisce una chiara immagine della porosità e una tabella con i pori rilevati e la loro dimensione. Questa tabella viene poi utilizzata per effettuare una analisi statistica ed ottenere la loro distribuzione.

Infine, un test elettrochimico potenziodinamico viene effettuato su ciascun provino, per verificare l'effettiva resistenza a corrosione dell'ossido formatosi con i vari parametri di anodizzazione, tutti nello stesso elettrolita, bromuro di sodio nelle stesse condizioni di concentrazione, temperatura e pH, e tutti con gli stessi parametri di analisi.

Il *duty cycle* utilizzato per l'anodizzazione modifica in modo significativo la morfologia, composizione e resistenza a corrosione del titanio permettendo di determinare i parametri e le condizioni più efficaci per il trattamento. I risultati degli esperimenti, per questo motivo, sono stati incrociati per trovare una correlazione tra la porosità e la resistenza a corrosione per determinare il migliore trattamento anticorrosivo per una possibile applicazione industriale.

Infine, dai risultati ottenuti non è stato solo possibile ricavare il trattamento meno dispendioso e più performante, ma anche parametri in grado di modificare le proprietà superficiali del titanio, come la sua porosità, lo spessore dell'ossido e la sua cristallinità. Questa possibilità rende questo lavoro una prima base per successivi studi, volti ad una comprensione più profonda dell'effetto di ogni parametro elettrochimico sull'ossido e ad applicazioni con esigenze di caratteristiche superficiali specifiche di porosità, grandezza del poro e cristallinità.

# Table of contents

Ringraziamenti .....	II
Abstract .....	IV
Sommario .....	VI
Table of contents.....	VIII
List of figures .....	XI
List of tables .....	XIX
Work purposes .....	XXIV
Chapter 1 – Titanium.....	1
1.1 Titanium .....	1
1.1.1 Physical and Chemical Characteristics .....	1
1.2 Corrosion Assessment.....	3
1.2.1 Forms of corrosion .....	4
1.2.1.1 Generalized Corrosion.....	5
1.2.1.2 Pitting Corrosion.....	11
1.2.1.3 Crevice Corrosion .....	14
1.2.1.4 Fretting Fatigue Cracking .....	15
1.2.1.5 Stress Corrosion Cracking.....	15
1.2.1.6 Hydrogen Embrittlement .....	16
Chapter 2 – Surface Treatments .....	18
2.1 Alloying with noble elements .....	18
2.2 Thermal Oxidation .....	19
2.3 Chemical Oxidation .....	20
2.4 Ion Implantation .....	20
2.5 Grain Refinement .....	21

2.6 Anodization .....	22
2.2.1 Standard Anodization.....	28
2.6.2 Anodic Spark Deposition .....	29
2.6.3 Nanotubes production through anodization technique .....	32
2.6.4 Brief description of anodic oxide of other valve metals .....	34
2.7 Discontinuous anodizing .....	38
2.7.1 Discontinuous anodizing on other metals.....	40
2.7.2 Discontinuous anodizing on titanium.....	44
Chapter 3 - Materials and methods .....	48
3.1 Original samples.....	48
3.2 Surface analysis.....	49
3.2.1 SEM.....	49
3.2.2 XRD .....	49
3.2.3 Optical microscope.....	49
3.3 Analysis of porosity .....	49
3.4 Potentiodynamic testing .....	52
3.4.1 Electrolyte .....	52
3.4.2 Setup.....	53
3.4.3 Finalizing anodising setup .....	54
3.4.3.1 Equipment .....	54
3.4.3.2 Testing, problems and solution.....	56
Chapter 4 – Results .....	59
4.1 Material characterization results .....	59
4.1.1 Superficial roughness .....	59
4.1.2 Metallurgy test results .....	60
4.2 Test electrolyte.....	64
4.3 Anodizing.....	69
4.3.1 Test details .....	69
4.3.2 Surface morphology .....	70
4.3.3 Samples crystallinity.....	72
4.3.4 Potentiodynamic tests results.....	82
Chapter 5 – Discussion .....	91
5.1 Morphology.....	91
5.2 Crystallinity.....	102
5.3 Corrosion resistance .....	119
5.3.1 Correlation among crystallinity, porosity and corrosion resistance .....	152

Chapter 6 – Conclusions.....	158
Bibliography .....	160

## ***List of figures***

Figure 1.1 Crystal structures of a) rutile, b) anatase and c) brookite. ....	3
Figure 1.2 Typical polarization curve showing $E_r$ : repassivation potential; $E_p$ pitting potential for a metal, like stainless steel, in a chloride solution. ....	5
Figure 1.3 An ideal schematic mechanism of the corrosion process of titanium in 0.05 M $H_2SO_4$ solutions with various fluoride concentrations. ....	6
Figure 1.4 Limit values of $F^-$ concentration and pH obtained by anodic polarization (circles) and immersion (squares) tests, at which corrosion behaviour of titanium changes. ....	7
Figure 1.5 Composition limits for avoiding rapid, pyrophoric reactions of titanium in red-fuming nitric acid. ....	10
Figure 2.1 Titanium oxide structures with different surface treatments. ....	14
Figure 2.2 Schematic representation of an anodizing cell. ....	15
Figure 2.3 Characteristics and morphology of anodic oxide layers. ....	18
Figure 2.4 Schematic representation of oxide layer grown in absence of fluorides (a) and the mechanism of nanotubes formation in presence of fluorides (b). ....	25
Figure 2.5 SEM image showing $TiO_2$ nanotube layers grown with different electrolytes. ....	26
Figure 2.6 Anodic oxides with nanotubular morphology obtained on a) titanium, b) zirconium, c) niobium and d) tantalum. ....	29
Figure 2.7 Sketch diagram of the unipolar current mode. ....	30
Figure 2.8 Sketch diagram of the bipolar current mode. ....	31
Figure 2.9 PEO current applications a) and control modes b). ....	31
Figure 2.10 Pictures of anodized AZ91HP, a magnesium alloy, at three duty cycles: a) 15%, b) 25%, c) 35%. All three at a final voltage of 480 V, current density 20 mA/cm <sup>2</sup> and frequency 600 Hz. ....	33

Figure 2.11 Surface morphologies of AZ91HP at three duty cycles: a) 15%, b) 25%, c) 35%. All three at a final voltage of 480 V, current density 20 mA/cm <sup>2</sup> and frequency 600 Hz. ...	34
Figure 2.12 Diagram showing the effects of different duty cycles on the distribution of microdischarges. Figure a) represents the high duty cycles effect, while figure b) the low duty cycle effect. ....	36
Figure 2.13 Representative SEM images at different duty cycles: A) 2%, B) 100%. ....	36
Figure 3.1 SEM picture of an anodized sample with applied a threshold of 90. ....	42
Figure 3.2 Binary mask of a sample with applied a threshold of 90. ....	42
Figure 3.3 Final negative and binary image of a sample superimposed to the initial one and original image. ....	43
Figure 3.4 Transcription of the macro used to automatize the ImageJ process. ....	43
Figure 3.5 Potentiodynamic test setup. a) glass cell, b) reference electrode, c) counter electrode, d) copper contact for working electrode, e) schematics of a cell ready to work....	46
Figure 3.6 Asterion AST 751. ....	46
Figure 3.7 Steady state panel. ....	47
Figure 3.8 Schematics of an electrochemical cell for anodization. ....	48
Figure 3.9 Design of the polymeric cell with the sample mounted in. ....	49
Figure 3.10 PLA cell. ....	49
Figure 3.11 a) Abrupt duty cycle and b) duty cycle with ramp. ....	50
Figure 4.1 CP titanium sample exposed to Kroll's solution at room temperature for 45 seconds.....	53
Figure 4.2 CP titanium sample exposed to Kroll's solution at room temperature for 60 seconds.....	53
Figure 4.3 CP titanium sample exposed to Kroll's solution at room temperature for 75 seconds.....	54
Figure 4.4 CP titanium sample exposed to Kroll's solution at room temperature for 45 seconds.....	54
Figure 4.5 CP titanium sample exposed to Kroll's solution at room temperature for 60 seconds.....	55

Figure 4.6 CP titanium sample exposed to Kroll's solution at room temperature for 75 seconds.....	55
Figure 4.7 Potentiodynamic curves of samples anodized at 20 V and 150 V and tested in NaF at different molarities, temperatures and pH.....	57
Figure 4.8 Potentiodynamic curves of samples anodized at 150 V and tested in $K_3[Fe(CN)_6]$ .....	58
Figure 4.9 Potentiodynamic curves of samples anodized at 150 V and tested in $FeCl_3$ .....	59
Figure 4.10 Potentiodynamic curves of samples anodized at 150 V and tested in NaBr.....	60
Figure 4.11 SEM pictures of the samples anodized at a final voltage of 220 V and a) Duty cycle 25% 20 Hz, b) Duty cycle 25% 1000 Hz, c) Duty cycle 75% 20 Hz, d) Duty cycle 75% 1000 Hz and e) DC.....	62
Figure 4.12 SEM pictures of the samples anodized at a final voltage of 160 V and a) Duty cycle 25% 20 Hz, b) Duty cycle 25% 1000 Hz, c) Duty cycle 75% 20 Hz, d) Duty cycle 75% 1000 Hz and e) DC.....	63
Figure 4.13 SEM pictures of the samples anodized at a final voltage of 120 V and a) Duty cycle 25% 20 Hz, b) Duty cycle 25% 1000 Hz, c) Duty cycle 75% 20 Hz, d) Duty cycle 75% 1000 Hz and e) DC.....	63
Figure 4.14 XRD analysis of anodized titanium at 120 V, 160 V and 220 V in DC.....	64
Figure 4.15 XRD analysis of titanium anodized with a duty cycle 25% and a frequency of 20 Hz at 120 V, 160 V and 220 V.....	65
Figure 4.16 XRD analysis of titanium anodized with a duty cycle 25% and a frequency 1000 Hz at 120 V, 160 V and 220 V.....	66
Figure 4.17 XRD analysis of titanium anodized with a duty cycle 75% and a frequency 20 Hz at 120 V, 160 V and 220 V.....	67
Figure 4.18 XRD analysis of titanium anodized with a duty cycle 75% and a frequency 1000 Hz at 120 V, 160 V and 220 V.....	67
Figure 4.19 XRD analysis of titanium anodized with a duty cycle 25% and at 120 V with 1000 Hz and 20 Hz.....	68

Figure 4.20 XRD analysis of titanium anodized with a duty cycle 25% and at 160 V with 1000 Hz and 20 Hz.....	69
Figure 4.21 XRD analysis of titanium anodized with a duty cycle 25% and at 220 V with 1000 Hz and 20 Hz.....	70
Figure 4.22 XRD analysis of titanium anodized with a duty cycle 75% and at 120 V with 1000 Hz and 20 Hz.....	71
Figure 4.23 XRD analysis of titanium anodized with a duty cycle 75% and at 160 V with 1000 Hz and 20 Hz.....	72
Figure 4.24 XRD analysis of titanium anodized with a duty cycle 75% and at 220 V with 1000 Hz and 20 Hz.....	73
Figure 4.25 XRD analysis of titanium anodized with 20 Hz of frequency at 120 V with 25% and 75% of duty cycle.....	74
Figure 4.26 XRD analysis of titanium anodized with 20 Hz of frequency at 160 V with 25% and 75% of duty cycle.....	75
Figure 4.27 XRD analysis of titanium anodized with 20 Hz of frequency at 220 V with 25% and 75% of duty cycle.....	76
Figure 4.28 XRD analysis of titanium anodized with 1000 Hz of frequency at 120 V with 25% and 75% of duty cycle.....	77
Figure 4.29 XRD analysis of titanium anodized with 1000 Hz of frequency at 160 V with 25% and 75% of duty cycle.....	78
Figure 4.30 XRD analysis of titanium anodized with 1000 Hz of frequency at 220 V with 25% and 75% of duty cycle.....	78
Figure 4.31 Potentiodynamic test results of DC anodization .....	80
Figure 4.32 Potentiodynamic tests results of anodization with duty cycle 25% and frequency 1000 Hz.....	81
Figure 4.33 Potentiodynamic tests results of anodization with duty cycle 25% and frequency 20 Hz.....	81
Figure 4.34 Potentiodynamic tests results of anodization with duty cycle 75% and frequency 1000 Hz.....	82

Figure 4.35 Potentiodynamic tests results of anodization with duty cycle 75% and frequency 20 Hz.....	82
Figure 4.36 Potentiodynamic tests results of anodization with voltage 220 V and frequency 1000 Hz.....	83
Figure 4.37 Potentiodynamic tests results of anodization with voltage 160 V and frequency 1000 Hz.....	83
Figure 4.38 Potentiodynamic tests results of anodization with voltage 120 V and frequency 1000 Hz.....	84
Figure 4.39 Potentiodynamic tests results of anodization with voltage 220 V and frequency 20 Hz.....	84
Figure 4.40 Potentiodynamic tests results of anodization with voltage 160 V and frequency 20 Hz.....	85
Figure 4.41 Potentiodynamic tests results of anodization with voltage 120 V and frequency 20 Hz.....	85
Figure 4.42 Potentiodynamic tests results of anodization with voltage 120 V and duty cycle 25%.....	86
Figure 4.43 Potentiodynamic tests results of anodization with voltage 160 V and duty cycle 25%.....	86
Figure 4.44 Potentiodynamic tests results of anodization with voltage 220 V and duty cycle 25%.....	87
Figure 4.45 Potentiodynamic tests results of anodization with voltage 120 V and duty cycle 75%.....	87
Figure 4.46 Potentiodynamic tests results of anodization with voltage 160 V and duty cycle 75%.....	88
Figure 4.47 Potentiodynamic tests results of anodization with voltage 220 V and duty cycle 75%.....	88
Figure 5.1 Density curves of samples anodized with DC.....	89
Figure 5.2 Density curves of samples anodized with duty 25% and frequency 20 Hz.....	90

Figure 5.3 Density curves of samples anodized with duty 25% and frequency 1000 Hz.....	91
Figure 5.4 Density curves of samples anodized with duty 75% and frequency 20 Hz.....	92
Figure 5.5 Density curves of samples anodized with duty 75% at frequency 1000 Hz.....	93
Figure 5.6 Density curve of samples anodized with DC at voltage 120 V.....	94
Figure 5.7 Density curves of samples anodized with both duties at frequency 1000 Hz and voltage 120 V.....	95
Figure 5.8 Density curves of samples anodized with both duties at frequency 20 Hz and voltage 120 V.....	96
Figure 5.9 Density curve of samples anodized with DC at voltage 160 V.....	97
Figure 5.10 Density curves of samples anodized with both duties at frequency 20 Hz and voltage 160 V.....	98
Figure 5.11 Density curve of samples anodized with DC and voltage 220 V.....	99
Figure 5.12 Density curves of samples anodized with both duties at frequency 20 Hz and voltage 220 V.....	100
Figure 5.13 Density curves of samples anodized with both duties at frequency 1000 Hz and voltage 120 V.....	101
Figure 5.14 Density curves of samples anodized with both duties at frequency 1000 Hz and voltage 160 V.....	102
Figure 5.15 Density curves of samples anodized with both duties at frequency 1000 Hz and voltage 220 V.....	103
Figure 5.16 Areas of the anatase and rutile curves of anodized titanium at 120 V, 160 V and 220 V in DC.....	106
Figure 5.17 Areas of anatase and rutile curves of titanium anodized with a duty cycle of 25% and a frequency of 20 Hz at 120 V, 160 V and 220 V.....	107

Figure 5.18 Areas of anatase and rutile curves of titanium anodized with a duty cycle of 25% and a frequency of 1000 Hz at 120 V, 160 V and 220 V.....	108
Figure 5.19 Areas of anatase and rutile curves of titanium anodized with a duty cycle of 75% and a frequency of 20 Hz at 120 V, 160 V and 220 V.....	109
Figure 5.20 Areas of anatase and rutile curves of titanium anodized with a duty cycle of 75% and a frequency of 1000 Hz at 120 V, 160 V and 220 V.....	110
Figure 5.21 Areas of anatase and rutile curves of titanium anodized with a duty cycle of 25% and a voltage of 120 V at 20 Hz and 1000 Hz.....	111
Figure 5.22 Areas of anatase and rutile curves of titanium anodized with a duty cycle of 25% and a voltage of 160 V at 20 Hz and 1000 Hz.....	112
Figure 5.23 Areas of anatase and rutile curves of titanium anodized with a duty cycle of 25% and a voltage of 220 V at 20 Hz and 1000 Hz.....	113
Figure 5.24 Areas of anatase and rutile curves of titanium anodized with a duty cycle of 75% and a voltage of 120 V at 20 Hz and 1000 Hz.....	114
Figure 5.25 Areas of anatase and rutile curves of titanium anodized with a duty cycle of 75% and a voltage of 160 V at 20 Hz and 1000 Hz.....	115
Figure 5.26 Areas of anatase and rutile curves of titanium anodized with a duty cycle of 75% and a voltage of 220 V at 20 Hz and 1000 Hz.....	116
Figure 5.27 Areas of anatase and rutile curves of titanium anodized with 20 Hz of frequency at 120 V with 25% and 75% duty cycle.....	117
Figure 5.28 Areas of anatase and rutile curves of titanium anodized with 20 Hz of frequency at 160 V with 25% and 75% duty cycle.....	118
Figure 5.29 Areas of anatase and rutile curves of titanium anodized with 20 Hz of frequency at 220 V with 25% and 75% duty cycle.....	119
Figure 5.30 Areas of anatase and rutile curves of titanium anodized with 1000 Hz of frequency at 120 V with 25% and 75% duty cycle.....	120
Figure 5.31 Areas of anatase and rutile curves of titanium anodized with 1000 Hz of frequency at 160 V with 25% and 75% duty cycle.....	121
Figure 5.32 Average of the current densities at 1 V, 2 V and at pitting potential with standard deviations.....	118

Figure 5.33 Average of the current densities at 1 V, 2 V and at pitting potential with corresponding standard deviations of samples anodized at 120 V,160 V and 220 V with 20 Hz and 25% duty cycle. ....	120
Figure 5.34 Average of the current densities at 1 V, 2 V and at pitting potential with corresponding standard deviations of samples anodized at 120 V,160 V and 220 V with 1000 Hz and 25% duty cycle.....	122
Figure 5.35 Average of the current densities at 1 V, 2 V and at pitting potential with corresponding standard deviations of samples anodized at 120 V,160 V and 220 V with 20 Hz and 75% duty cycle.....	124
Figure 5.36 Average of the current densities at 1 V, 2 V and at pitting potential with corresponding standard deviations of samples anodized at 120 V,160 V and 220 V with 1000 Hz and 75% duty cycle.....	126
Figure 5.37 Average of the current densities at 1 V, 2 V and at pitting potential with corresponding standard deviations of samples anodized at 120 V with 25% duty cycle.....	128
Figure 5.38 Average values of current densities with standard deviation at pitting potential, at 1 V and at 2 V for duty 25% at 120 V, at different frequencies.....	129
Figure 5.39 Average of the current densities at 1 V, 2 V and at pitting potential with corresponding standard deviations of samples anodized at 220 V with 25% duty cycle. ....	131
Figure 5.40 Average of the current densities at 1 V, 2 V and at pitting potential with corresponding standard deviations of samples anodized at 220 V with 25% duty cycle. ....	133
Figure 5.41 Average of the current densities at 1 V, 2 V and at pitting potential with corresponding standard deviations of samples anodized at 160 V with 75% duty cycle. ....	135
Figure 5.42 Average of the current densities at 1 V, 2 V and at pitting potential with corresponding standard deviations of samples anodized at 220 V with 75% duty cycle..	136
Figure 5.43 Average of the current densities at 1 V, 2 V and at pitting potential with corresponding standard deviations of samples anodized at 120 V with 20 Hz. ....	138
Figure 5.44 Average of the current densities at 1 V, 2 V and at pitting potential with corresponding standard deviations of samples anodized at 160 V with 20 Hz.....	139

Figure 5.45 Average of the current densities at 1 V, 2 V and at pitting potential with corresponding standard deviations of samples anodized at 220 V with 20 Hz. ....	141
Figure 5.46 Average of the current densities at 1 V, 2 V and at pitting potential with corresponding standard deviations of samples anodized at 120 V with 1000 Hz. ....	143
Figure 5.47 Average of the current densities at 1 V, 2 V and at pitting potential with corresponding standard deviations of samples anodized at 160 V with 1000 Hz. ....	145
Figure 5.48 Average of the current densities at 1 V, 2 V and at pitting potential with corresponding standard deviations of samples anodized at 220 V with 1000 Hz.....	146
Figure 5.49 Comparison of pitting potentials with different treatments.....	147
Figure 5.50 Area covered by pores of samples anodized at 120 V, 160 V and 220 V with different treatments.....	148
Figure 5.51 Number of pores with different treatments.....	156

## ***List of tables***

Table 1.1 Chemical specifications of titanium grade 2. ....	2
Table 1.2 Mechanical properties of titanium grade 2. ....	2
Table 1.3 Titanium corrosion rates varying the temperature and the concentration of nitric acid. ....	8
Table 1.4 Corrosion rates of titanium in hydrochloric acids. ....	9
Table 2.1 Free corrosion potential ( $E_{corr}$ ) and polarization resistance ( $R_p$ ) on titanium samples implanted with different amounts of carbon. ....	12
Table 2.2 Free corrosion potential (OCP, V SCE) and mass loss rate ( $g/m^2h$ ) for coarse grain (CG) and ultrafine grain (UFG) titanium, measured in HCl and $H_2SO_4$ acids. ....	13
Table 3.1 Chemical composition and mechanical characteristics of titanium grade 2. ....	40
Table 4.1 Superficial roughness results in $\mu m$ of the sample polished with a 320 grit SiC paper.....	51
Table 4.2 Superficial roughness results in $\mu m$ of the sample polished with a 600 grit SiC paper.....	51
Table 4.3 Superficial roughness results in $\mu m$ of the sample polished with a 1200 grit SiC paper.....	52

Table 4.4 Analysis of grain dimensions, areas in $\mu\text{m}^2$ .....	56
Table 4.5 Experiments performed.....	61
Table 5.1 Areas under the XRD curves for crystallinity phase of the oxide layer.....	102
Table 5.2 Areas under the XRD curves for crystallinity phase of the oxide layer of the anodized titanium with 25% duty cycle and a frequency of 20 Hz at 120 V, 160 V and 220 V.....	103
Table 5.3 Areas under the XRD curves for crystallinity phase of the oxide layer of the anodized titanium with 25% duty cycle and a frequency of 1000 Hz at 120 V, 160 V and 220 V.....	104
Table 5.4 Areas under the XRD curves for crystallinity phase of the oxide layer of the anodized titanium with 75% duty cycle and a frequency of 20 Hz at 120 V, 160 V and 220 V.....	105
Table 5.5 Areas under the XRD curves for crystallinity phase of the oxide layer of the anodized titanium with 75% duty cycle and a frequency of 1000 Hz at 120 V, 160 V and 220 V.....	106
Table 5.6 Pitting potentials, current densities and number of the sample anodized in DC at 120 V, 160 V and 220 V. ....	119
Table 5.7 Current densities and number of the sample anodized in DC at 120 V, 160 V and 220 V and a potential equal to 1 V.....	119
Table 5.8 Current densities and number of the sample anodized in DC at 120 V, 160 V and 220 V and a potential equal to 2 V. ....	119
Table 5.9 Pitting potentials, current densities and number of the sample anodized with duty cycle of 25% and a frequency of 20 Hz at 120 V, 160 V and 220 V.....	121
Table 5.10 Current densities and number of the sample anodized with duty cycle of 25% and a frequency of 20 Hz at 120 V, 160 V and 220 V at 1 V.....	121
Table 5.11 Current densities and number of the sample anodized with duty cycle of 25% and a frequency of 20 Hz at 120 V, 160 V and 220 V at 2 V.....	121
Table 5.12 Pitting potentials, current densities and number of the sample anodized with duty cycle of 25% and a frequency of 1000 Hz at 120 V, 160 V and 220 V.....	123
Table 5.13 Current densities and number of the sample anodized with duty cycle of 25% and a frequency of 1000 Hz at 120 V, 160 V and 220 V at 1 V.....	123

Table 5.14 Current densities and number of the sample anodized with duty cycle of 25% and a frequency of 1000 Hz at 120 V, 160 V and 220 V at 2 V.....	124
Table 5.15 Pitting potentials, current densities and number of the sample anodized with duty cycle of 75% and a frequency of 20 Hz at 120 V, 160 V and 220 V.....	125
Table 5.16 Current densities and number of the sample anodized with duty cycle of 75% and a frequency of 20 Hz at 120 V, 160 V and 220 V at 1 V.....	126
Table 5.17 Current densities and number of the sample anodized with duty cycle of 75% and a frequency of 20 Hz at 120 V, 160 V and 220 V at 2 V.....	126
Table 5.18 Pitting potentials, current densities and number of the sample anodized with duty cycle of 75% and a frequency of 1000 Hz at 120 V, 160 V and 220 V.....	127
Table 5.19 Current densities and number of the sample anodized with duty cycle of 75% and a frequency of 1000 Hz at 120 V, 160 V and 220 V at 1 V.....	128
Table 5.20 Current densities and number of the sample anodized with duty cycle of 75% and a frequency of 1000 Hz at 120 V, 160 V and 220 V at 2 V.....	128
Table 5.21 Pitting potentials, current densities and number of the sample anodized with duty cycle of 75% and a frequency of 1000 Hz at 120 V, 160 V and 220 V.....	130
Table 5.22 Current densities and number of the sample anodized with duty cycle of 75% and a frequency of 1000 Hz at 120 V, 160 V and 220 V at 1 V.....	130
Table 5.23 Current densities and number of the sample anodized with duty cycle of 75% and a frequency of 1000 Hz at 120 V, 160 V and 220 V at 2 V.....	130
Table 5.24 Pitting potentials, current densities and number of the sample anodized with duty cycle of 75% and a frequency of 1000 Hz at 120 V, 160 V and 220 V.....	132
Table 5.25 Current densities and number of the sample anodized with duty cycle of 75% and a frequency of 1000 Hz at 120 V, 160 V and 220 V at 1 V.....	132
Table 5.26 Current densities and number of the sample anodized with duty cycle of 75% and a frequency of 1000 Hz at 120 V, 160 V and 220 V at 2 V.....	132
Table 5.27 Pitting potentials, current densities and number of the sample anodized with duty cycle of 75% and a frequency of 1000 Hz at 120 V, 160 V and 220 V.....	133
Table 5.28 Current densities and number of the sample anodized with duty cycle of 75% and a frequency of 1000 Hz at 120 V, 160 V and 220 V at 1 V.....	134
Table 5.29 Current densities and number of the sample anodized with duty cycle of 75% and a frequency of 1000 Hz at 120 V, 160 V and 220 V at 2 V.....	134

Table 5.30 Pitting potentials, current densities and number of the sample anodized with duty cycle of 75% and a frequency of 1000 Hz at 120 V, 160 V and 220 V.....	135
Table 5.31 Current densities and number of the sample anodized with duty cycle of 75% and a frequency of 1000 Hz at 120 V, 160 V and 220 V at 1 V.....	136
Table 5.32 Current densities and number of the sample anodized with duty cycle of 75% and a frequency of 1000 Hz at 120 V, 160 V and 220 V at 2 V.....	136
Table 5.33 Pitting potentials, current densities and number of the sample anodized with duty cycle of 75% and a frequency of 1000 Hz at 120 V, 160 V and 220 V.....	137
Table 5.34 Current densities and number of the sample anodized with duty cycle of 75% and a frequency of 1000 Hz at 120 V, 160 V and 220 V at 1 V.....	138
Table 5.35 Current densities and number of the sample anodized with duty cycle of 75% and a frequency of 1000 Hz at 120 V, 160 V and 220 V at 2 V.....	138
Table 5.36 Pitting potentials, current densities and number of the sample anodized with duty cycle of 75% and a frequency of 1000 Hz at 120 V, 160 V and 220 V.....	139
Table 5.37 Current densities and number of the sample anodized with duty cycle of 75% and a frequency of 1000 Hz at 120 V, 160 V and 220 V at 1 V.....	140
Table 5.38 Current densities and number of the sample anodized with duty cycle of 75% and a frequency of 1000 Hz at 120 V, 160 V and 220 V at 2 V.....	141
Table 5.39 Pitting potentials, current densities and number of the sample anodized with frequency of 20 Hz and different duty cycles at 120 V.....	141
Table 5.40 Current densities and number of the sample anodized with different duty cycles and a frequency of 20 Hz at 120 V at 1 V.....	142
Table 5.41 Current densities and number of the sample anodized with different duty cycles and a frequency of 20 Hz at 120 V at 2 V.....	142
Table 5.42 Pitting potentials, current densities and number of the sample anodized with frequency of 20 Hz and different duty cycles at 160 V.....	143
Table 5.43 Current densities and number of the sample anodized with different duty cycles and a frequency of 20 Hz at 160 V at 1 V.....	143
Table 5.44 Current densities and number of the sample anodized with different duty cycles and a frequency of 20 Hz at 160 V at 2 V.....	144
Table 5.45 Pitting potentials, current densities and number of the sample anodized with frequency of 20 Hz and different duty cycles at 220 V.....	145
Table 5.46 Current densities and number of the sample anodized with different duty cycles and a frequency of 20 Hz at 220 V at 1 V.....	145
Table 5.47 Current densities and number of the sample anodized with different duty cycles and a frequency of 20 Hz at 220 V at 2 V.....	145
Table 5.48 Pitting potentials, current densities and number of the sample anodized with frequency of 1000 Hz and different duty cycles at 120 V.....	146
Table 5.49 Current densities and number of the sample anodized with different duty cycles and a frequency of 1000 Hz at 120 V at 1 V.....	147

Table 5.50 Current densities and number of the sample anodized with different duty cycles and a frequency of 1000 Hz at 120 V at 2 V.....	147
Table 5.51 Pitting potentials, current densities and number of the sample anodized with frequency of 1000 Hz and different duty cycles at 160 V.....	148
Table 5.52 Current densities and number of the sample anodized with different duty cycles and a frequency of 1000 Hz at 160 V at 1 V.....	149
Table 5.53 Current densities and number of the sample anodized with different duty cycles and a frequency of 1000 Hz at 160 V at 2 V.....	149
Table 5.54 Pitting potentials, current densities and number of the sample anodized with frequency of 1000 Hz and different duty cycles at 220 V.....	150
Table 5.55 Current densities and number of the sample anodized with different duty cycles and a frequency of 1000 Hz at 220 V at 1 V.....	150
Table 5.56 Current densities and number of the sample anodized with different duty cycles and a frequency of 1000 Hz at 220 V at 2 V.....	151
Table 5.57 Calculated average current with different treatments.....	156

## ***Work purposes***

The aim of this work is to push further the limits of actual anodizing treatments applied on titanium to increase its corrosion resistance. This is done introducing anodizing regimes that produce good results on other light metals, adapting them to titanium case to produce the most corrosion resistant, less porous and economically affordable oxide layer.

The reason behind the application of discontinuous or pulsed anodizing is the different morphology of the oxide obtained with this method. When the current is zero or in the range of a negative pulse, the melted areas, caused by the sparks, have time to solidify obtaining, in the end, a considerably different morphology of the surface layer. The oxide obtained in this way shows a higher corrosion resistance, respect to a sample anodized in direct current with the same value of final voltage.

A further advantage of this technique is the reduction of the energy consumption, particularly high in case of traditional anodizing, especially during Anodic Spark Deposition (ASD) regime. In fact, in discontinuous or pulsed anodizing, thanks to the periodic interruption in the flowing of current to the sample, the whole current needed is considerably lower. In this thesis work, for the aim mentioned above, the current needed for each test has been registered and reported in order to precisely quantify the advantage of the method.

For these reasons, the purpose of this thesis work was to successfully produce protective oxide layers on titanium surface, identifying the anodization waveform and variables that affect the achievement of improved corrosion resistance and connecting them to the morphology of the oxide itself. In addition, a comparison among the different methods in terms of energy savings has been done, in order to find a compromise between the morphology and corrosion resistance of the oxide and the costs needed for the test.

The electrolyte, in which the discontinuous anodizing has been performed, has been chosen testing a large number of solutions, mainly acids and salts, to find the right concentration and composition for the aim.

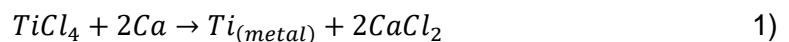
Corrosion resistance, in particular to pitting, has been potentiodynamically tested so that the improvements could be immediately detected. For this reason, a large variety of electrolytes has been experimented in order to find the adequate aggressiveness of solution. Along with the composition, also concentration, pH and temperature have been tested to find the right values for the aim.

# Chapter 1 – Titanium

## 1.1 Titanium

Even if Titanium is the fourth most abundant metal on the Earth's surface, its discovery dates back only to 1791, when Reverend William Gregor recognized it as a new element during his studies on ilmenite minerals. At first, when it was found in the Manaccan valley (Cornwall), it was named "manaccanite". A few years later, the German chemist Heinrich Klaproth rediscovered it in form of its rutile oxide, renaming it "Titanium" after the Titans, mythological first sons of the goddess Gaia (Earth in Greek mythology). [1]

However, its first use as metal dates to the 30's of the Nineteenth century, when William Justin Kroll proved it could be produced by reduction of titanium tetrachloride ( $TiCl_4$ ) with calcium[2] :



### 1.1.1 Physical and Chemical Characteristics

The characteristics of the metal appear immediately outstanding: in its metallic form, Titanium has a low density ( $4.51 \text{ g/cm}^3$ ) and boasts the highest strength to weight ratio of all pure metals ( $76 \text{ kN}\cdot\text{m/kg}$ ), reaching even higher values when properly alloyed. [3] This key property allowed titanium to become a backbone material in the aerospace industry. Besides its mechanical properties, titanium shows excellent corrosion resistance, leading to its more recent applications in other sectors, such as prosthetics, food industry, petrochemical plants and refinery, power plants, heat exchangers and marine structures.[4, 5]

It shows a silvery grey-white appearance, is a transition metal of the d-block, characterized by a density of  $4.51 \text{ g/cm}^3$ , high strength, ductility and very high corrosion resistance, superior to stainless steel.

Its high melting point,  $1650^\circ\text{C}$  makes it a good refractory metal, but when the temperature is higher than  $430^\circ\text{C}$  it loses tensile strength. [6]

While the first titanium alloy was created in the United States in 1940s, nowadays titanium is commercially available in many forms and composition. The quantities of each component are classified and organized in Grades by ASTM. Grades from 1 to 4 are considered “commercially pure”, as they are unalloyed but present a certain amount of impurities, especially oxygen: grade 1 contains maximum 0.18%, while grade 4 contains maximum 0.4%. These four grades differ slightly by mechanical properties (increasing from 1 to 4) and corrosion resistance (decreasing from 1 to 4). Corrosion resistance is significantly improved in grades 7 (Ti grade 2 + 0.12÷0.25% Pd), 12 (Ti grade 2 + 0.2÷0.4%Mo, 0.6÷0.9%Ni) and 16 (Ti grade 2 + 0.04÷0.08%Pd). However, the most common titanium alloy is Grade 5: it is an alpha-beta alloy and it consists of 6% aluminum, 4% vanadium, and trace amounts of iron. This Titanium alloy is also often referred to as Ti 6Al-4V, Ti-6Al-4V or Ti 6-4. [7]

*Table 1.1 Chemical specifications of titanium grade 2.*

Elements	Content
<b>Carbon, C</b>	<0.08%
<b>Iron, Fe</b>	<0.3%
<b>Oxygen, O</b>	<0.25%
<b>Hydrogen, H</b>	<0.015%
<b>Nitrogen, N</b>	<0.03%
<b>Titanium, Ti</b>	Balance

*Table 1.2 Mechanical properties of titanium grade 2.*

Mechanical property	Value
<b>Yield strenght</b>	275 MPa
<b>Ultimate tensile strength</b>	345 MPa
<b>Elongation</b>	>20%
<b>Reduction of area</b>	>30%

Its main employment, after the Second World War, was in the aerospace industry, due to the excellent strength/weight ratio, which is the highest among all metals and can be alloyed with a lot of other elements, such as: aluminium, iron, molybdenum and vanadium; but nowadays it is spread in an increasing number of applications: chemical and petrochemical plants, refineries, food industries, power plants and automotive. [7]

Thanks to its outstanding corrosion resistance, its biocompatibility and its low toxicity it is one of the most used metals in the medical field, for the production of orthodontic, prosthetic and cardiovascular implants. Biocompatibility is related to corrosion resistance, as lower

corrosion means lower amounts of ions released in the human body, which can lead to rejection; in addition, a properly tuned oxide, grown by anodic oxidation, can stimulate the growth of hydroxyapatite, one of the main components of bones. It is important to consider, however, that bacterial colonies, as those of *Streptococcus Mutans* in the oral environment, and fluoride ions present in toothpaste may be very dangerous for titanium. [7]

Titanium and its alloys are chemically active metals, which nonetheless have high corrosion resistance. Such property is due to the spontaneous formation, in presence of bondable oxygen, of a passive coating of titanium dioxide. In aerated environments, the film reaches 1.5-10 nm in thickness, it is compact, and it shows good adhesion with the metal substrate beneath. The oxide is responsible for the corrosion resistance, as it is chemically stable in a wide range of chemical environments.[8, 9]

Despite this, titanium and its alloys can be susceptible to localized and generalized corrosion in strongly reducing acid media, crevice attack in halides-containing solutions, stress corrosion cracking in certain higher-strength alloys, hydrogen embrittlement, fretting corrosion and erosion. These limitations can be overcome to a great extent by the addition of small percentages (<0.25% wt) of platinum group metals (PGMs), to promote cathodic reaction and bring titanium to its passive region where it forms the stable oxide; however, the inclusion of such elements is expensive.[10]

## ***1.2 Corrosion Assessment***

The excellent corrosion resistance of titanium is due to a very thin film of titanium oxide, TiO<sub>2</sub>, 1.5-10 nm thick, that forms immediately in contact with air as pure titanium is very reactive in presence of oxygen and this is the main characteristic of the so-called **valve metals**.

An oxide layer is not itself enough to provide protection; it must be chemically stable, amorphous, extremely adherent and in addition, when mechanically damaged, it must reform so quickly that the material under remains protected, as TiO<sub>2</sub> does. In very aggressive environments, however, this oxide is not enough for protection and so titanium is alloyed with other metals, which promote cathodic reactions to help the system reaching a passive condition, or a surface treatment, for instance anodic oxidation, is performed.

Even if the oxide layer of titanium is responsible for its high corrosion resistance, it is not a homogeneous and invariant layer, but its nature and composition of the film depends on the environmental conditions (chemicals availability, temperature, and pressure) in which is

formed. In aqueous solutions and in aerated environments at room temperature, such diffusion barrier is composed of three layers: the least superficial, in contact with the metallic titanium, is  $\text{TiO}$ ; an intermediate layer of  $\text{Ti}_2\text{O}_3$  follows; the third layer is the one facing the environment, consisting in  $\text{TiO}_2$ . In general, the oxide layer does not have a uniform structure, for example titanium dioxide with an anatase structure has been found in an amorphous matrix. If the temperature is around  $1600^\circ\text{C}$ , instead, the oxide formed is mainly  $\text{Ti}_2\text{O}_3$ , a rare form.

When formed at temperatures higher than  $150^\circ\text{C}$ , the  $\text{TiO}_2$  layer, in the form of rutile, is crystalline and more chemically resistant while at intermediate temperatures the oxide is less protective and in the form of anatase. [7] Anatase and rutile, along with brookite, are the most common structures of titanium dioxide found in nature.

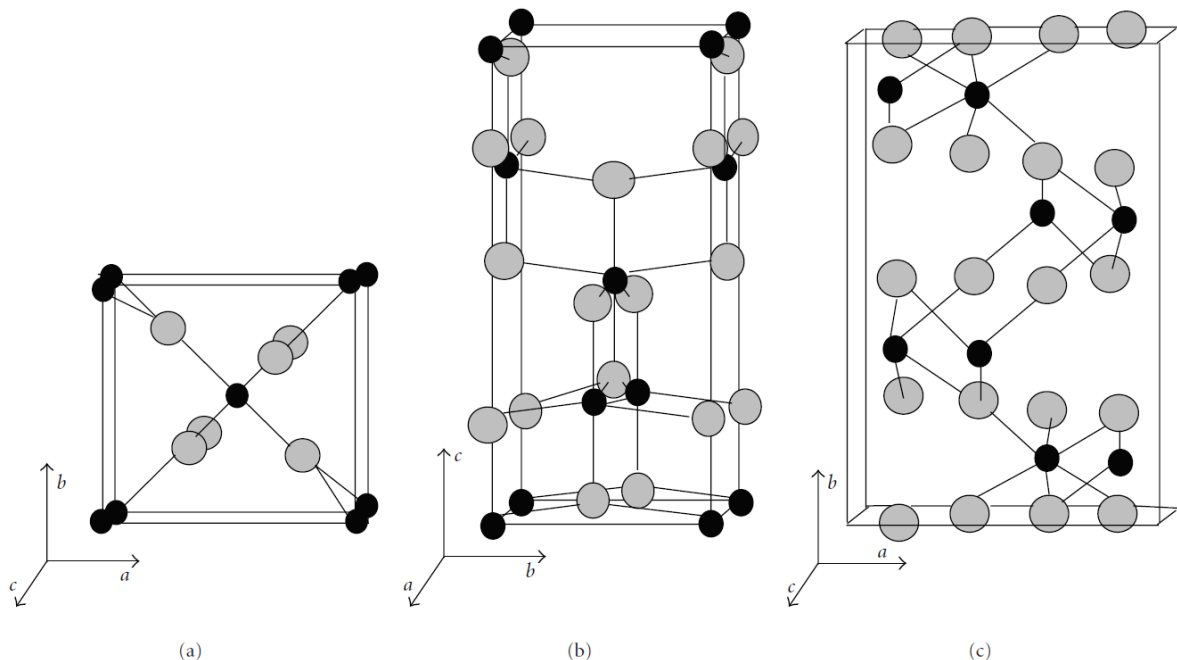


Figure 1.1 Crystal structures of a) rutile, b) anatase and c) brookite. [11]

When titanium is in passive condition, due to the thin oxide layer, the typical values of corrosion rate are lower than  $0.2 \text{ mm/year}$ , a negligible value.

### 1.2.1 Forms of corrosion

In very aggressive environments titanium can suffer both generalized and localized corrosion, mainly pitting and crevice, but also hydrogen embrittlement, stress corrosion cracking, fretting corrosion and erosion. The most critical and highly localized form is pitting corrosion, as, once initiated, the propagation is extremely fast and difficult to stop, due to localized breaking of the protective layer promoted by the presence of concentrated halides, such as salty water above  $200^\circ\text{C}$  or bromide-containing species. [4, 5]

### **1.2.1.1 Generalized Corrosion**

Generalized corrosion is the most common type of corrosion and it is also known as "general attack corrosion " or "uniform corrosion". In this case the dissolution of the metal substrate proceeds uniformly creating a roughing of the surface due to the corrosion products. This phenomenon leads to relatively uniform diminishing of attacked materials' thickness. The mechanism of the attack typically is an electrochemical process that takes place at the surface of the material. Differences in composition or orientation between small areas on the metal surface create anodes and cathodes that facilitate the corrosion process. [14] The main cause of general corrosion problem in real plants are linked with the wrong choice of the material during the design phase. In facts, general corrosion often can be tolerated because the effect of metal loss is relatively easy to assess, and allowances can be made in the initial design. [14] In the case of titanium, when it reaches its stable passive condition, corrosion rates do typically not exceed 0.02 mm/year, well below the 0.13 mm/year accepted in design. [15] Such a small acceptable corrosion is attributable to the finite oxidation (as previously stated) of titanium alloy surfaces. After a brief time of oxidation, natural oxide stops growing; however, any further oxide film growth (i.e. caused by anodization) would be easily detectable by naked-eye exam once it exceeds 30 nm, [16] as titanium oxide changes color as its thickness grows: the color acquired is strongly dependent on the thickness, as it is due to an interference phenomenon between the light reflected by the oxide and the light reflected by the metal underneath. [17]

Because of the ease of development of the protective oxide, corrosion resistance of titanium can be studied analyzing the thermodynamic window in which the oxide itself is stable. The Pourbaix diagram (pH vs potential) of Ti and its oxides in water system is reported in Figure1.2. The diagram shows how titanium passivity covers a wide range of pH and potential. Corrosion is limited to low values of pH at low potentials where strongly anodic oxidizing conditions cause the oxide to dissolve, and at high potentials where the strongly cathodic reducing conditions promote the formation of hydrides.

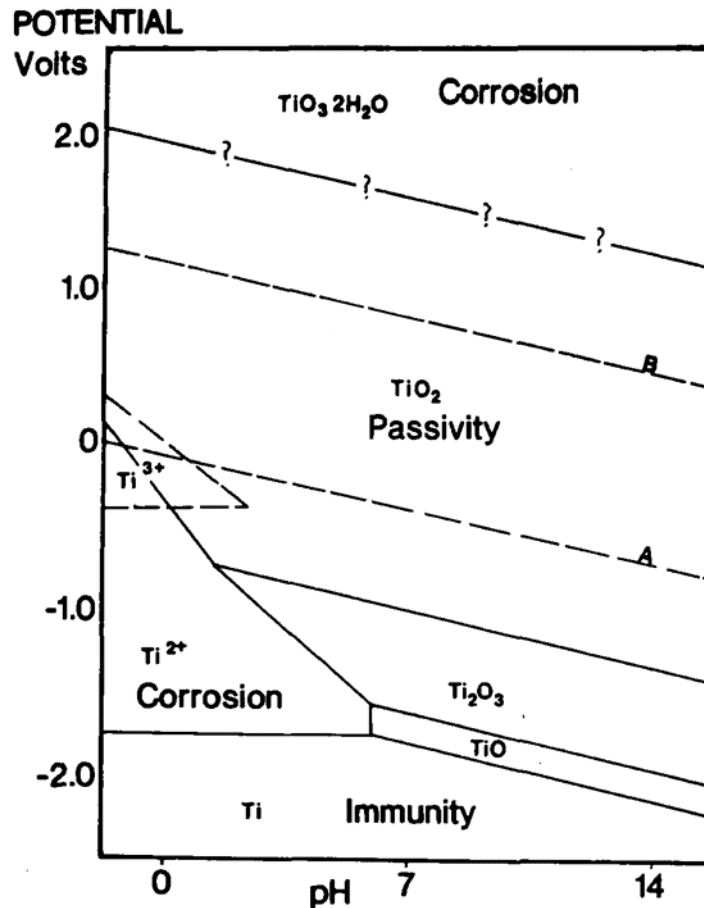
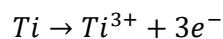


Figure 1.2 Pourbaix diagram of Titanium [18]

Titanium is susceptible to corrosion in pure reducing inorganic acids (those that generate H<sub>2</sub> during the reaction with the metal), especially at high temperatures. This category counts acids such as sulfuric, hydrochloric and phosphoric.[19] Hydrofluoric acid has an even stronger effect, rapidly dissolving the oxide.[20] In case of attack of these reducing acids, after the oxide is removed the unprotected metal is dissolved to its trivalent ion:



If dissolved oxygen or other oxidizing species are present, the Ti<sup>3+</sup> ion is readily oxidized to a less soluble form, Ti<sup>4+</sup>, which hydrolyzed to form TiO<sub>2</sub>. In fact, the general corrosion behavior of titanium can be affected beneficially by small amounts of oxidant contaminations in a given environment. For example, the corrosion rate of unalloyed titanium in 5 wt.% HCl at 190°C is approximately 28,45 mm/year; introducing a small amount of oxidizing chlorine into the aqueous solution allow it to drop to 0.025 mm/year. The metal's corrosion rate in aqueous 40 wt.% H<sub>2</sub>SO<sub>4</sub> at 35°C can be reduced from 8 to 0.008 mm/year just by adding 0.01 wt.% of ferric ions (i.e. an oxidizing agent). [20]

To just give an idea of titanium corrosion resistance, the main industrial environments are discussed.

**Seawater** is a very corrosive environment due to the presence of pollutant and water, which are the essential elements to make corrosion start. However, the presence of the oxide protective layer makes titanium almost resistant to any condition in marine environment. Titanium is a prominent material in seawater applications, as it perfectly resistant to almost any condition in this environment.[21] It is not affected by wet-dry cycling, nor by microbial induced corrosion (MIC). This behavior leads to the satisfactory experience of the application of titanium in coastal power-plant condensers and in both low-temperature and high-temperature regions of desalination plants [22]: in heat exchangers the temperature reaches 130°C, while titanium is unaffected by generalized corrosion up to 260°C. Exposure of titanium for many years to depths of over a mile below the ocean surface has not produced any measurable corrosion. Pitting and crevice corrosion are completely absent, even if marine deposits form. The presence of sulfides in seawater does not affect the resistance of titanium to corrosion.[23] Exposure of titanium to marine atmospheres or splash or tide zone does not cause corrosion. Other than heat exchangers, titanium is suitable for other applications including seawater, such as sub-marine hulls, ships, oil and gas platforms, desalinization and salt production evaporators, and water jet propulsion systems.[24]

Titanium is also well-known for its application in the **human body**. In facts, it is the only metal used in prosthetic, cardiovascular, and orthodontic implants due to its mechanical characteristics but also for its very low corrosion velocity.[25] As already said, lower is the corrosion, lower is the value of ions dispersed in the human body, fact that gives to titanium its outstanding biocompatibility. The in vitro and in vivo tests [26] result in a high stability of titanium for very long time which is fundamental for applications, like human body, without the possibility of inspections.[27] The well-behavior of titanium in human body can be further improved with the implantation of ions like P or Ca and the increasing of the surface area. These treatments lead to a boost bone growth on the titanium surface which brings to a higher corrosion and mechanical resistance.[28]

Concerning the chemicals, the most dangerous halides seem to be **fluoride ions**, in aqueous solutions, dissolving titanium as  $TiF_6^{2-}$  and  $TiF_6^{3-}$ , the passivity is lost and an increase in corrosion rate or a decrease in open circuit potential is observed. The pH threshold for titanium corrosion varies with  $F^-$  concentration, in particular there is a linear correlation (Figure 1.4) between pH threshold and the logarithm of the fluoride concentration, in addition, the presence of oxygen influences the critical pH that shifts from 3.8 to 5.1 with 0.05% in weight of NaF and from 5.5 to 6.0 with 1.0% NaF, passing from aerated to deaerated conditions. In particular, small quantities of fluoride ions, even 0.002M, react with titanium forming  $TiF_4$  and the passive film is dissolved, the bare metal is then

oxidized to soluble trivalent ions that, in presence of oxygen, are oxidized to  $Ti^{4+}$  and forms insoluble titanium dioxide. [29]

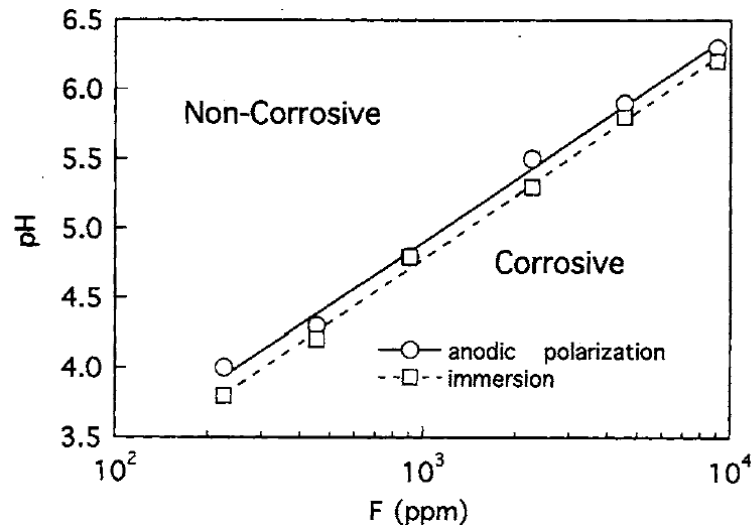


Figure 1.4 Limit values of  $F$  concentration and  $pH$  obtained by anodic polarization (circles) and immersion (squares) tests, at which corrosion behaviour of titanium changes. [29]

Increasing the concentration of fluoride ions and reaching the critical value, the system results less stable showing an unstable passivity and the existence of 3 different corrosion potentials. This behaviour can be explained by Figure 1.3, representing potentiodynamic curves for fluoride content up to 0.0005 M in  $H_2SO_4$  0.005 M.

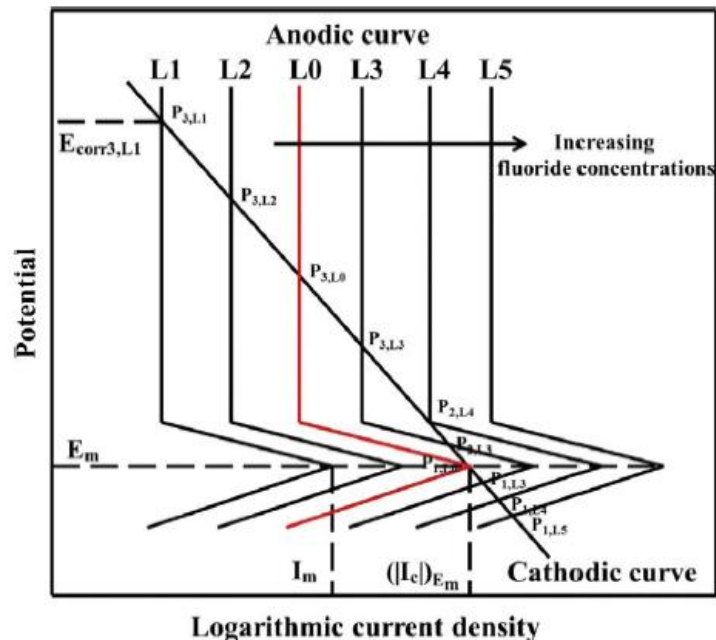


Figure 1.5 An ideal schematic mechanism of the corrosion process of titanium in 0.05 M  $H_2SO_4$  solutions with various fluoride concentrations. L0, L1, L2, L3, L4, L5 stand for the ideal anodic polarization curves with fluoride concentration of the critical value, 0 M, 0.0005 M, 0.002 M, 0.003

$M$ ,  $0.005 M$ , respectively.  $P_{i,L_j}$  stands for the intersection of the cathodic polarization curve and the single  $L_j$  anodic curve, with  $i = 1$  for the intersection in active region,  $i = 2$  for that in active-passive region,  $i = 3$  for that in passive region and  $j$  from 0 to 5.  $E_{corr3}$ ,  $L1$  stands for free corrosion potential in passive region (3) of anodic curve  $L1$ .  $E_m$  is the critical potential to have passivation. [30]

In the case of curve  $L3$ , corresponding to  $0.002 M$  fluoride concentration, there are 3 intersections of cathodic and anodic curves, in the active, active-passive and passive regions, which reflects the possibility of measuring 3 corrosion potentials in potentiodynamic tests. The condition in which the maximum anodic current ( $I_m$ ) is equal to the cathodic current ( $|I_c|$ ) $_{E_m}$  can be defined as the critical value that discriminates between spontaneous passivity of titanium and active state.

An ideal representation of titanium oxide behavior shows the effect of fluorides on the barrier layer (Figure 1.5). Even before reaching the critical amount of fluorides, the surface is affected by its presence: fluorides can modify the barrier, transforming the compact oxide into a porous one, without reaching the underlying metal. Once the critical value is exceeded, all the barrier layer is transformed into a porous and non-protective oxide.

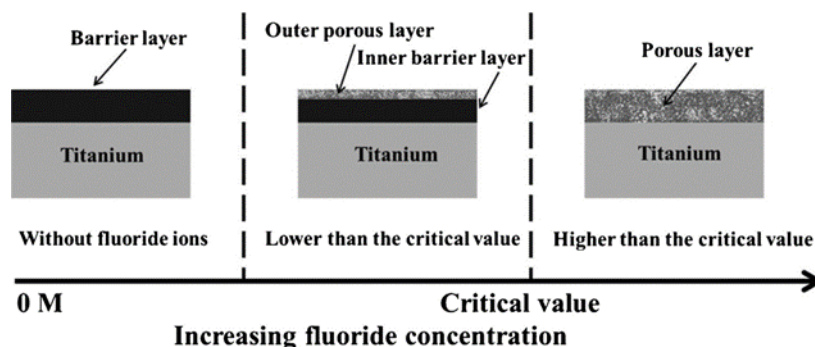


Figure 1.6 Schematic diagram of the influence of fluorides on the nature of the oxide layer.[30]

**Sulphuric acid**, at room temperature or below, at a concentration up to 10 wt.% does not attack titanium, but increasing the temperature the bearable concentration decreases rapidly, with 1 wt.% at boiling temperature the corrosion rate results of 9 mm/y. [31] Sulfuric acid is a widely used chemical in chemical plants, and in desalinization plants in descaling due to carbonates' excellent dissolution in the acid. Titanium is commonly used for  $H_2SO_4$  containing environments. However, at high temperatures, the corrosion rate increases catastrophically in deaerated solutions. Injecting even small amounts of oxidizing agents or heavy metal ions significantly increases corrosion resistance.[32]

In **phosphoric acid** the behaviour of titanium is uniform with increase in temperature and acid concentration. Unalloyed titanium is resistant to naturally aerated pure solutions of

phosphoric acid up to 30% at room temperature. This resistance decreases to about 10% pure acid at 60°C and 2% 100°C. At higher temperatures (250°C), titanium is reported to undergo mild corrosion in 1% phosphoric acid, with the formation of a thin layer of white corrosion products, made of well-crystallized fine fibers. In more concentrated solution (10%) titanium suffers more severe corrosion. A thick layer (25 μm) of corrosion products consisting of titanium oxide phosphate hydrate forms in the first 24 h of exposure; however, this doesn't completely inhibit corrosion, whose rate in this condition is around 1.9 mm/year.[33]

Titanium generally shows good corrosion resistance to **organic media** and is steadily finding increasing application in equipment for handling organic compounds. Titanium is a standard construction material in the production of acetaldehyde by oxidation of ethylene in an aqueous solution of metal chlorides.[23]

Titanium is highly resistant to oxidizing acids, as **nitric acid**, over a wide range of concentrations and temperatures. However, in hot and pure nitric acid as well as in condensed vapour environments, it suffers accelerated dissolution. [34] In fact, while titanium works well in white fuming nitric acid, red fuming nitric acid may be an issue at high temperatures and concentrations. Stress corrosion cracking causes the formation of a surface deposit of finely divided titanium grains, which are very reactive: the slightest mechanical perturbation can ignite pyrophoricity.

Table 1.3 Titanium corrosion rates varying the temperature and the concentration of nitric acid. [7]

HNO <sub>3</sub> concentration (%)	35°C	60°C	100°C	190°C	200°C	290°C
5	0.002	-	0.015	-	-	-
10	0.004	0.012	0.023	-	-	-
20	0.0045	0.017	0.0038	-	-	0.36
30	0.0069	0.022	0.10	1.5	3.5	-
40	0.0058	0.0175	0.05	2.8	5.0	-
50	0.0058	0.010	0.18	2.8	-	-
60	0.0071	0.008	0.05	1.5	-	-
69.5	0.011	0.0079	0.019	-	-	-
70	-	-	-	0.38	-	1.1
98	0.002	-	-	-	-	-

At room temperature, titanium resists up to 5% concentrated **hydrochloric acid** [7], and just up to 0.5% at 100°C. Deaerated solutions increase corrosion at lower acid concentrations, but reduce corrosion in concentrations above 10%.

Table 1.4 Corrosion rates of titanium in hydrochloric acids. [1]

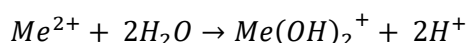
Reagent	Concentration (%)	Temperature (°C)	Corrosion rate (mm/year)
<b>Hydrochloric acid (aerated)</b>	1	35	0.003
	-	50	0.006
	-	60	0.004
	-	100	0.46-2.48
	-	Boiling	1.83
	2	50	0.028
	-	60	0.016
	-	66	0.61
	-	100	7.00
	6	25	0.07
	-	50	2.10
	-	52	0.68
	-	100	44.45
	37	35	15.00
<b>Hydrochloric acid (de-aerated)</b>	1	35	0.003
	-	Boiling	0.0025-2.00
	3	35	0.13
	-	Boiling	6.10
	5	35	0.28
	20	35	3.18

### 1.2.1.2 Pitting Corrosion

Leaving behind the effects of the generalized corrosion in many environments, it is now analysed the forms of localised corrosion with an excursus on the nature and the effects of each of them. The first form of localized corrosion is pitting. As the name itself reveals, this kind of corrosion creates on the metal surface pits, due to the localized dissolution of the metal and the breakdown of its passive layer.[56] Passive metals find their corrosion resistance strength in their passive oxide film, which could be susceptible to localized breakdown resulting in accelerated dissolution of the underlying metal. Commercial titanium alloys generally present surface heterogeneities, such as inclusions, second-phase particles, dislocations, or mechanical damage, and such heterogeneities can act as sites for pit initiation. [35] The majority of defects in the oxide layer for titanium, but also for other

metals such as nickel and iron, are point defects in a very high concentration ( $10^{19}$  -  $10^{21}$   $\text{cm}^{-3}$ ) [36] so that ion migration is dominated by lattice diffusion through those.

If the attack initiates on an open surface, it is called pitting corrosion; at an occluded site it is called crevice corrosion. These closely related forms of localized corrosion can lead to accelerated failure of structural components by perforation, or by acting as an initiation site for cracking. [37] Pitting corrosion only occurs in presence of aggressive anionic species, such as halide ions. The severity of pitting tends to vary with the logarithm of bulk anion concentration. [38] The more conventional explanation for pitting corrosion is that it is an autocatalytic process, as once a pit starts to grow, the conditions developed are such that further pit growth is promoted. The oxidation of metal to its soluble ions results in localized acidity that is maintained by the spatial separation of the cathodic and anodic half-reactions, which creates a potential gradient and electromigration of aggressive anions into the pit. The local pit environment becomes depleted in cathodic reactant (e.g. oxygen), which shifts the cathodic reaction to the exposed surface that surrounds the pit, where this reactant is more abundant. The pit environment becomes enriched in metal cations and anionic species, which electromigrate into the pit to maintain charge neutrality by balancing the charge associated with cation concentration. The pH in the pit decreases owing to cation hydrolysis, following the reaction [37]



The acid environment so generated creates more aggressive conditions and helps to propagate the pit.

It is experimentally observed [39] that, when a pit nucleates, no other pits form in the surrounding area and the reason is that the spot of the pit behaves as the anodic site, where the corrosion process occurs, while the region around is the cathodic site, where oxygen reduction takes place changing the value of the pH and inhibiting the formation of new ones. On the other hand, when the cause of the formation of pits is the application of an external current, once one is nucleated in a certain spot, they can spread all over the interested surface with a rate of corrosion governed by the solubility of the passive layer in the solution formed inside the pit.

The most important parameter, to study this type of corrosion, is the *Pitting Potential* ( $E_p$ ). In facts, it was found that electrochemical depassivation, or pitting, appears only above a certain potential, function of the scan rate of the experiment, and the process initiates almost immediately, while, below this value, the material is safe, no matter the duration of the

exposure. This potential depends on the environment in which the material is immersed, the temperature, the pH and the type of material itself. [39]

The second parameter to consider is the *Repassivation or Protection Potential ( $E_r$ )*. Pourbaix reported that pits keep growing even when the potential is lowered below  $E_p$ ; they will stop only when the potential becomes lower than  $E_r$ , whose value is related to the occlusion of the pit. [40]

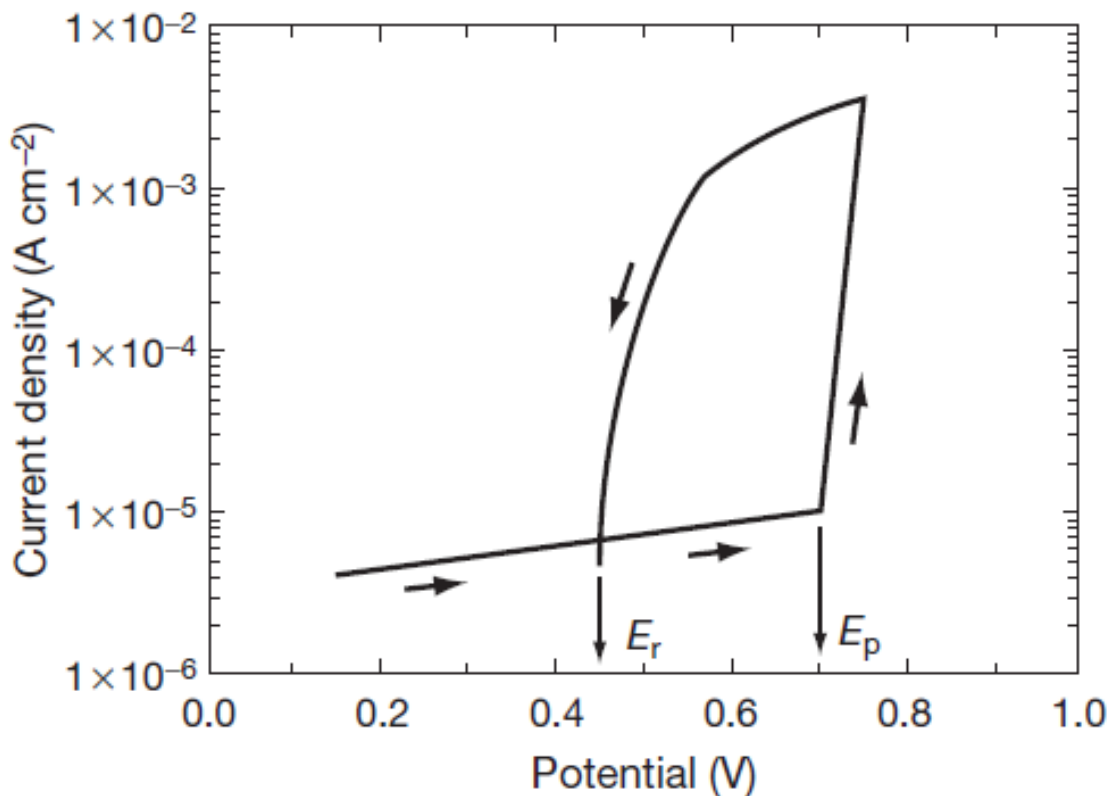


Figure 1.3 Typical polarization curve showing  $E_r$ : repassivation potential;  $E_p$  pitting potential for a metal, like stainless steel, in a chloride solution. [39]

Differently from fluoride ions, which causes mostly generalized corrosion, bromine produces pitting corrosion, when in liquid form at room temperature, while in vapour form is inert.

Generally, titanium exhibits excellent pitting corrosion resistance due to its passive film, which is mechanically strong and chemically unreactive in most environments. However, there are some environments in which titanium is not immune, and can be susceptible to various forms of corrosion, including pitting. The susceptibility to pitting corrosion is strongly dependent on temperature and on concentration of halide ions, whose severity in general follows the order  $F^- < Cl^- < I^- < Br^-$ . [41]

As done for the different environments in general corrosion, some halides ions are analysed in order to understand their ability to promote pitting on the surface metal.

In presence of **chlorides**, pitting requires values of potential much higher than the spontaneous corrosion potential [42] and the accumulation of metal chloride (or oxychloride) at the metal/film interface causes oxide film rupture as nucleation event. [43] The presence of oxidizing metal ions can cause severe pitting, as  $E_p$  value follows the sequence: no addition >  $\text{FeCl}_2$  >  $\text{FeCl}_3$  >  $\text{CuCl}_2$ . Conversely, the addition of oxygen containing anions, namely  $\text{SO}_4^{2-}$ ,  $\text{SeO}_4^{2-}$ ,  $\text{CrO}_4^{2-}$  and  $\text{HPO}_4^{2-}$  retards pitting corrosion of Ti in chloride-containing solutions.

**Bromides** are the halides ions that result in the strongest pitting corrosion on Ti. Experimental data show how pitting conditions in bromides require much lower potential values than in chlorides, suggesting a strong chemical interaction between the titanium oxide film surface and bromine ions. [44] The chemical specificity of breakdown to solutions containing Br<sup>-</sup> clearly eliminates any mechanism involving simple electrical or thermal breakdown, as occurs in metal/dielectric/metal structures. Huo et al. [45] investigated pit initiation on titanium in presence of bromides. Prior to the pit initiation, Br<sup>-</sup> ions were absorbed and accumulated on localized spots of the  $\text{TiO}_2$  film, forming bromide nuclei containing mostly TiBr. Increasing the potential, when the specimen was polarized just below the pitting condition, such nuclei tend to grow into "critical nuclei". It might be the requisite condition for pit initiation that concentration of Br<sup>-</sup> in bromide nuclei reached the critical concentration. Casillas et al. [44] suggest the mechanism behind pitting corrosion in bromides, which respects two fundamental experimental observations: the microscopic sites at which breakdown occurs are electrochemically active (higher electrical conductivity of the oxide on the spots), and oxide breakdown occurs at more positive potentials with increasing average oxide film thickness.

### 1.2.1.3 Crevice Corrosion

Crevice corrosion is a localized form of corrosion usually associated with a stagnant solution on the micro-environmental level. Such stagnant microenvironments tend to occur in crevices such as those formed under gaskets, washers, insulation material, fastener heads, surface deposits, disbonded coating, threads, lap joints and clamps. [46]

Crevice corrosion affects titanium only in hot chloride solutions with a very strong dependence on the temperature, generally above 70°C, regardless the pH, while if the latter is above 10, crevice starts regardless the temperature, although a crevice gap of 50 µm is required to initiate crevice phenomena. [7]

As many other forms of localized corrosion, it is divided into 3 stages: initiation, propagation and repassivation; when passivity is locally broken and, due to occluded geometry, oxygen cannot permeate to promote repassivation, dissolution takes place within the crevice. In

situ, pH remains neutral because of the diffusion and concentration of halides and sulphates, meanwhile titanium ions hydrolyse, and corrosion products are deposited. During propagation stage, oxygen penetrates the crevice site where it reduces and gets consumed until hydrogen evolution starts; corrosion penetration is controlled by the ohmic drop between anodic and cathodic regions, the cathodic reaction causes a local pH increase that leads to a possible repassivation.

#### ***1.2.1.4 Fretting Fatigue Cracking***

Fretting-fatigue failure initially begins as surface and near-surface damage as a result of the fretting action. This damage takes the form of significant plastic strain at the surface, disruption of the surface films or oxides and material transfer. The disruption of the surface films or oxides through fretting may accelerate fatigue failure because (i) it enhances direct metal to metal contact, resulting in micro-welding of the faces, and consequently higher local shear forces, and (ii) the continuous production-destruction cycle of the oxide may produce particles that act as an abrasive third body to produce fretting wear and initiate cracks. [47]

Titanium and its alloys are known to be particularly susceptible to fretting-initiated fatigue and, in highly stressed locations, the use of these alloys requires particular surface treatments, e.g. shot-peening, hard and soft coatings or solid-state lubricants, that inhibit the initiation of cracks during fretting. [47]

Concerning **erosion and cavitation**, titanium is safe up to a velocity of the media of 36 m/s [7].

#### ***1.2.1.5 Stress Corrosion Cracking***

Stress corrosion cracking, known also as SCC, is that kind of corrosion caused by the effects of both tensile stresses and an aggressive environment. Occurrence of SCC depends on the simultaneous achievement of three requirements: a susceptible material, an aggressive enough environment, and sufficient tensile stress. Precorrosion followed by loading in an inert environment will not result in any significant crack propagation, while simultaneous environmental exposure and application of stress will cause time-dependent subcritical crack propagation: this is important because it is often possible to eliminate or reduce SCC susceptibility by modifying either the metallurgical characteristics of the metal or the environment composition. [48] Another important aspect of SCC is the requirement for tensile stress, such as those coming out from cold work, residual stresses from fabrication, and/or externally applied loads. Titanium, differently from steel, is almost

immune to Stress Corrosion Cracking in a quite wide variety of media and conditions. In presence of nitric acid, for example, at room temperature and in high concentrations the corrosion rate is less than 0.005 in/y (0.1255 mm/y) [49]. Even when boiling this acid does not attack titanium, with the exception of the red fuming nitric acid, in which a violent pyrophoric effect can occur if the nitrogen peroxide content is higher than 1%.[50, 51] anhydrous methanol, nitrogen tetroxide (N<sub>2</sub>O<sub>4</sub>), liquid or solid cadmium, liquid mercury.

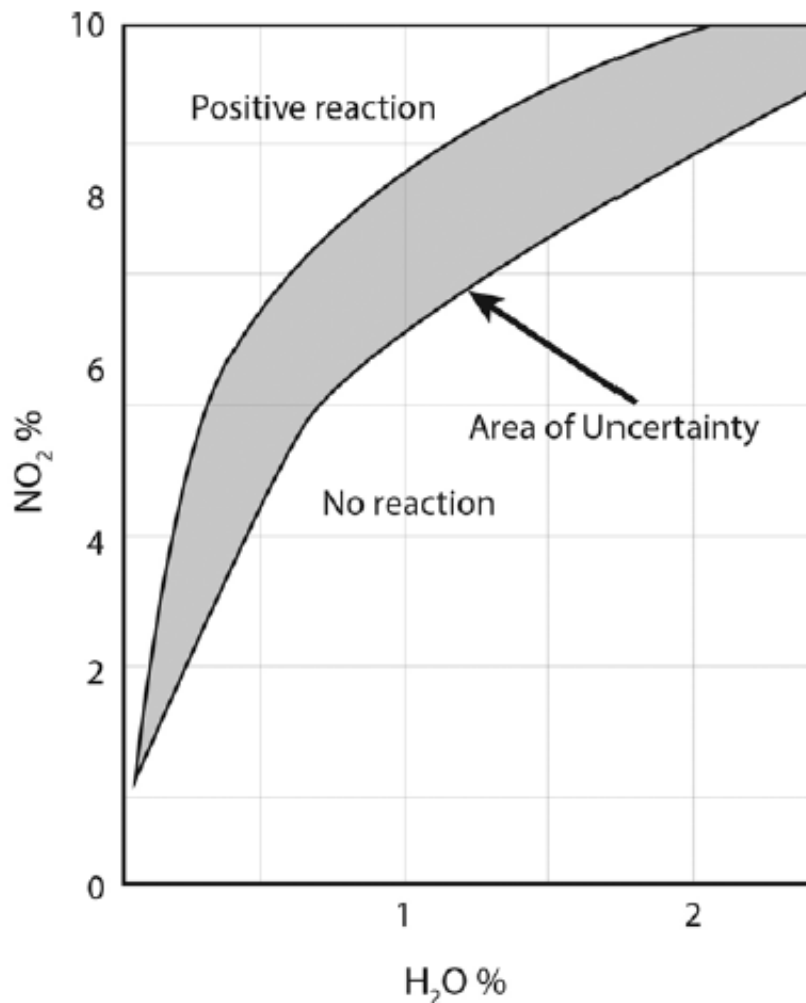


Figure 1.5 Composition limits for avoiding rapid, pyrophoric reactions of titanium in red-fuming nitric acid.[7]

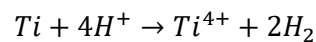
### 1.2.1.6 Hydrogen Embrittlement

Hydrogen embrittlement is the process by which metals become brittle and tend to develop cracks due to the introduction and diffusion through the bulk of hydrogen.

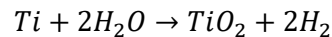
Although SCC considers hydrogen adsorption to promote cracking, hydrogen-induced cracking (HIC) requires much more hydrogen to be absorbed by the metal. When hydrogen is absorbed in the metal, it causes embrittlement depending on the metal nature. There are

three forms of hydrogen embrittlement: internal hydrogen embrittlement (resulting from hydrogen entrapped during processing), external hydrogen embrittlement (diffusion of hydrogen in the metal matrix without the formation of new phases) and hydrogen reaction embrittlement. The latter is the form found in titanium and consists in the chemical reaction of hydrogen with the metal, forming new phases (hydrides and gas bubbles) that generate voids that eventually may cause failure. In fact, hydrogen embrittlement affects titanium only in  $\alpha$  and  $\beta$  phase because of the low hydrogen solubility in this kind of structure. When hydrogen is absorbed it can have two possible consequences: precipitation of a new microstructural titanium hydride phase and generation of methane gas bubbles due to chemical reaction with carbon at grains' boundaries, causing failure because of the growth of voids. [7]

Hydrogen in titanium comes from different sources. Crevice corrosion, once initiated, is supported by reduction of protons inside the crevice, leading to the absorption of atomic hydrogen in sufficient quantities to produce extensive hydride formation: [52]



In case of passive non-creviced or inert crevice conditions, corrosion could be sustained by reaction with water under neutral conditions, following the slow-rate reaction:



In the first step to possible failure by hydrogen-induced cracking (HIC), hydrogen generated must pass through the  $TiO_2$  film before absorption into the underlying titanium alloy. For absorption to proceed, redox transformation ( $Ti^{4+} \rightarrow Ti^{3+}$ ) in the oxide film is necessary. This requires significant cathodic polarization of the metal, generally achievable in field only by galvanic coupling to other active materials (i.e. carbon steel) or the application of a cathodic protection potential. [53] When titanium with low hydrogen concentrations is stressed at slow rates, plastic collapse is observed without the occurrence of fast unstable fracture. The ductile collapse pre-empts the brittle fracture under these circumstances, presumably because plastic deformation prevents the attainment of a sufficiently high stress. For hydrogen concentrations above a critical value, fast fracture takes place at a relatively low stress intensity factor and plastic collapse is no longer observed.

## ***Chapter 2 – Surface Treatments***

To solve many of the problems that Titanium shows in aggressive environments, several techniques are used. In fact, as already seen in the corrosion assessment of titanium, also this high corrosion resistant metal exhibits problems in very aggressive environments and only gold remains as the real corrosion resistant metal. However, the rate of corrosion varies greatly varying the metal and environment, spanning from millimeters per day (typically in extraordinary cases of severe galvanic coupling or impressed currents) to millimeters per millennia (negligible). Corrosion is a surface phenomenon, so the development of a protective passive layer is required to reach passive state, in which corrosion proceeds at very low rates. For this reason, barrier layer modification treatments are crucial to increase corrosion resistance of metals.

### ***2.1 Alloying with noble elements***

Titanium grades 7, 12 and 16 are those developed specifically to enhance corrosion resistance by alloying with more noble metals, such as PGMs (Platinum group metals), Mo, Zr, Cr. [54, 55] PGMs have the effect to facilitate cathodic depolarization in acids, accelerating cathodic hydrogen evolution reaction (HER) on titanium; the addition of even minute quantities in the alloy allows for drastic reductions in corrosion rates. Mo, Zr and Cr are more thermodynamically stable, acid-resistant elements (compared with Ti), and are used to enhance the stability of the oxide. [56] The addition of palladium [57], for instance, improves the resistance to reducing acids, such as sulphuric, hydrochloric and phosphoric, but also raises the critical temperature at which crevice corrosion in sea water might occur. Nakagawa et al. [58] prove that alloying with Pd alters cathodic process and results in lower over-voltage for HER: this may shift the working potential in the passive region of the alloy. They also found that Pd adsorbs hydrogen to form a protective layer of titanium hydride. Figure 16 illustrates how cathode modification (PGMs) facilitates titanium passivation via avoiding the critical anodic (active) loop.

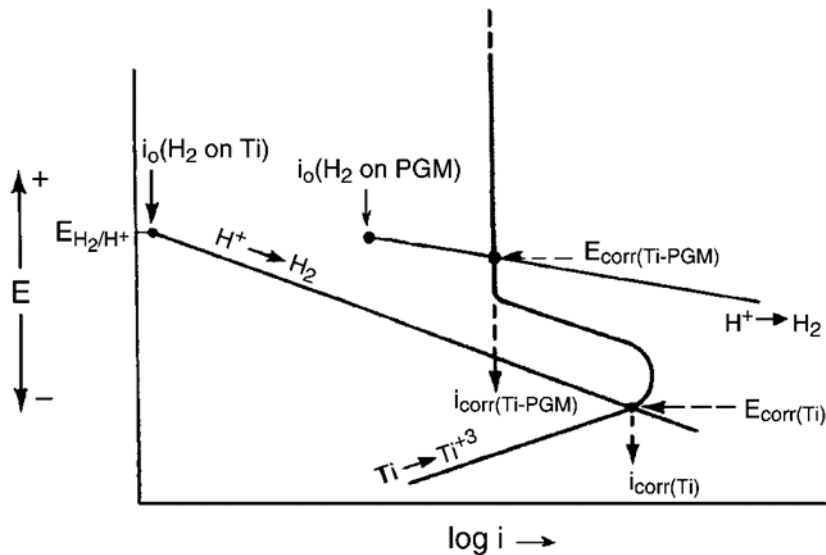


Figure 2.1 Evans Diagram showing how alloying titanium with PGMs achieves passivation in reducing acids via cathodic depolarization. [56]

Among the PGMs, palladium is the one that gives the highest corrosion resistance to titanium, to the point that Ti-Pd alloy was proposed for the manufacture of high-level nuclear waste containers; [59] however, the use of higher quantities of cheaper PGMs such as Ru is gaining weight in the industry. [56] Brossia and Cragolino [60] report a comparison between Ti grade 2 and 7 on the pitting resistance point of view, in 1 M solution of Cl<sup>-</sup> at 95°C. The pitting potential increases from 1.08 V vs SCE to 7.69 V vs SCE by passing from Ti grade 2 to Ti grade 7 (with 0.2% of Pd).<sup>8</sup>

One of the most used treatment for alloying is nitration, the introduction of nitrogen in the first microns of the sample, by physical (PVD) or chemical vapour deposition (CVD), to promote the formation of titanium nitride that causes an increase in the corrosion resistance. Unfortunately, this method is often expensive and complicated to perform, so it is preferred to modify the natural surface oxide, increasing its thickness and alter its morphology. There are several treatments to exploit this, such as thermal oxidation, chemical oxidation, ion implantation, grain refinement and anodic oxidation.

## 2.2 Thermal Oxidation

Thermal oxidation is one of the less used methods even if it is the simplest and the least expensive one. [61] The oxide formed is amorphous or poorly crystallized, anatase or rutile depending on the treatment temperature and highly stable but can be disrupted by very low shear stresses. The thickness varies from tens of nm at 500-600°C to hundreds of nm at around 700°C. [57] The chemical resistance of this oxide is so high that its removal requires

sand-blasting or a caustic descaling bath. At a temperature of 500°C the layer is thin and adherent, a small grain structure appears at a temperature of 650°C and increasing again up to 800°C the grains cover completely the surface and are oriented perpendicular to the substrate.[57] The thickness of the oxide increases with the treatment temperature and, as a consequence also the corrosion resistance. It is not recommended to increase the temperature above 800°C as it would cause spallation of the layer and a consequent reduction in the mechanical properties.

## ***2.3 Chemical Oxidation***

Chemical oxidation consists in the exposure of the sample to a heated environment, 60-90°C, of H<sub>2</sub>O<sub>2</sub> or NaOH and, to remove surface contaminants, acids like H<sub>2</sub>SO<sub>4</sub> or HCl can be added. The thickness of the oxide increases almost linearly with the duration of the treatment and the oxide grown with this method is comparable to the one obtained by anodization or thermal oxidation. The layer obtained in solutions containing HCl is the thickest and the addition of SO<sub>4</sub><sup>-</sup> ions promoted the formation of anatase while the addition of Cl<sup>-</sup> ions favoured the formation of rutile. [57]

## ***2.4 Ion Implantation***

This method is particularly used to obtain the most biocompatibility surfaces because of the selectivity of implanted ions. According to EIS analyses, implantation of calcium at a dose of 10<sup>17</sup> Ca<sup>+</sup>/cm<sup>2</sup> with ion energy 25 keV produces an increment in uniform corrosion resistance of titanium in SBF environment. However, the formation of pits is reported in corrosion tests after this treatment. The mechanism of initiation of the pits on the surface of implanted titanium is not explained yet, it is suggested that the alteration of chemical composition of the oxide layer results in a weakening of the oxide towards localized corrosion. The same test performed on samples implanted with 10<sup>17</sup> - 3·10<sup>17</sup> P<sup>+</sup>/cm<sup>2</sup> shows that for dose higher than 10<sup>6</sup>, a new TiP phase appears in the oxide. Phosphorous implantation causes an increase in corrosion resistance performances [57] as it stabilizes amorphous structure. The implantation of both calcium and phosphorous is performed to avoid pitting. A high corrosion resistance effect is obtained by carbon implantation, the best improvement is obtained with a dose of 2·10<sup>17</sup> ions/cm<sup>2</sup>, the resulting effect is the formation of a continuous, solid and nanocrystalline TiC layer.

Table 2.1 Free corrosion potential ( $E_{corr}$ ) and polarization resistance ( $R_p$ ) on titanium samples implanted with different amounts of carbon. [57]

C implanted dose	$E_{corr}$ (mV)	$R_p$ ( $M\Omega\text{ cm}^2$ )
Not implanted	-95	2.5
$55 \times 10^{15}$ ions/cm <sup>2</sup>	34	6
$1 \times 10^{16}$ ions/cm <sup>2</sup>	65	12
$1 \times 10^{17}$ ions/cm <sup>2</sup>	220	50
$2 \times 10^{17}$ ions/cm <sup>2</sup>	330	54

## 2.5 Grain Refinement

Ultra-fine grains are obtained with equal channel angular pressing (ECAP) technique, reaching an average grain size of 300 nm. A lower corrosion rate is experimented along with a more positive free corrosion potential. This effect was due to the higher energy of grain boundaries. Corrosion tends to take place in grain-boundaries regions and a large extent of grain boundaries in nanocrystalline materials enhances passivation kinetics, leading to rapid formation of a stable passive layer.

Table 2.2 Free corrosion potential (OCP, V SCE) and mass loss rate ( $\text{g/m}^2\text{h}$ ) for coarse grain (CG) and ultrafine grain (UFG) titanium, measured in HCl and  $\text{H}_2\text{SO}_4$  acids. [57]

	Solution					
	1 M HCl	3 M HCl	5 M HCl	1 M $\text{H}_2\text{SO}_4$	3 M $\text{H}_2\text{SO}_4$	5 M $\text{H}_2\text{SO}_4$
CG Ti OCP, V	0.193	-0.252	-0.362	0.237	-0.235	-0.352
UFG Ti OCP, V	0.210	-0.242	-0.358	0.256	-0.223	-0.345
OCP difference, %	8.8	4.7	1.1	8.0	5.1	2.0
CG Ti corr. rate ( $\text{g/m}^2\text{h}$ )	0.62	1.37	1.98	0.76	1.46	1.87
UFG Ti corr. rate ( $\text{g/m}^2\text{h}$ )	0.42	0.90	1.38	0.58	0.78	1.09
Corr. rate difference, %	32	34	30	24	47	43

The easiest, cheapest and so the most used one is **anodic oxidation**. The thickness of the oxide artificially grown can vary from 40 nm, with an anodizing potential of 10 V, to 250 nm,

with 100 V. When the potential applied rises above 100 V, pores begin to nucleate on the surface of the oxide layer and a dielectric breakdown occurs when the film reaches a critical thickness. This phenomenon is associated with the appearance of visible micro-arcs rapidly moving on the surface and irregular current peaks in potentiostat mode. This particular case of anodizing is called **anodic spark deposition (ASD)**, **plasma electrolytic oxidation (PEO)** or **micro-arc oxidation (MAO)**. [62]

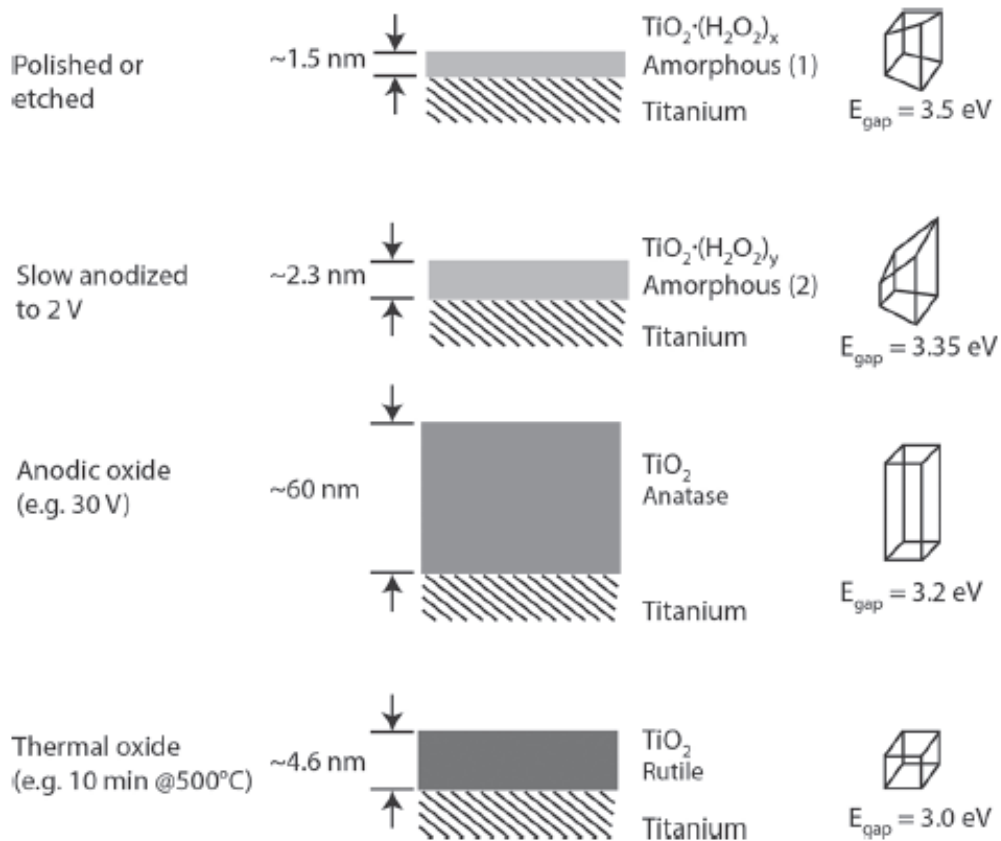


Figure 2.1 Titanium oxide structures with different surface treatments. [57]

## 2.6 Anodization

Titanium, as all the metals that belong to the IV and IVB groups, is a valve metal. Valve metals are such metals that allow the formation of ionically conductive oxides. In presence of an electrolyte, due to their great affinity to oxygen, valve metals form spontaneously an oxide protective layer, which makes them incredibly corrosion resistant materials. [63] To all these materials and their alloys, it is applied the so-called anodic oxidation process in

order to tune some surface-related properties such as porosity, conductance, surface area per unit of volume, etc. The chemical nature of the film strongly influences its features, i.e. its conductance (semiconductive or insulating), corrosion resistance or biochemical properties. By controlling the artificial formation of the oxide layer on the valve metal, it is possible to engineer surface solutions. In this complex scenario, anodic oxidation is an effective solution to control the oxide parameters. [64]

This methodology is based on the construction of an electrical closed circuit in which the valve metal is the anodic electrode connected to a power supply, itself connected to a counter-electrode in an electrolytic solution. In this way, when applied to Ti, it is possible to polarize titanium by imposing a current flow between the two electrodes. Then, the Ti atoms are oxidized to  $Ti^{4+}$  ions, which reacting with oxygen atoms from the electrolyte form the protective layer. The growth mechanism is based on the inward and outward migration in which  $O^{2-}$  charge carriers reach the metal surface where the  $Ti^{2+}$  cations are produced and then oxidized to  $Ti^{4+}$  ions which diffuse in the opposite way through the oxide layer. In Fig. 2.2 the representation of a classical anodizing cell is shown.

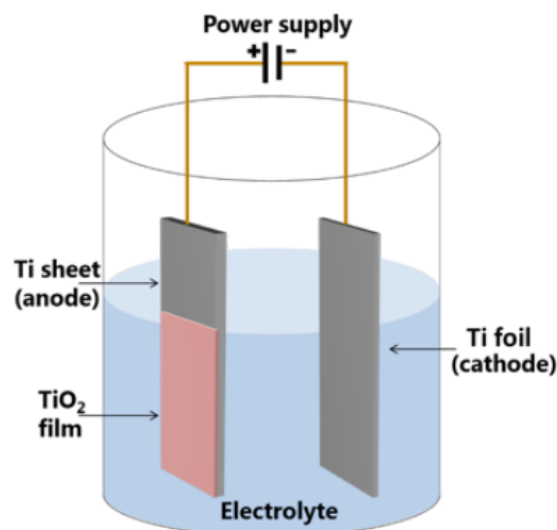


*Figure 2.2 Schematic representation of an anodizing cell.[65]*

The assembly of the electrochemical cell and the treatment procedure is easier than PVD (Physical Vapour Deposition) or other corrosion improvement technique, e.g. Ion implantation. The electrolytes can be acids (e.g. sulphuric acid or phosphoric acid) or salts (e.g. ammonium sulphate or sodium sulphate). However, for each solution is very important to evaluate the aggressiveness of the electrolytes in order to avoid high dissolution rates which compromise the growth of a compact oxide layer.[66] For instance, among acid, basic and salts electrolytes, the acid ones give the best results in terms of

thickness and adherence of the oxide film, but very strong acids like HF or HClO<sub>4</sub> have a strong tendency to dissolve the oxide.[67] Moreover, the addition of halogen acids to the electrolyte solution is proven to roughen the surface (i.e. HCl or HBr) [68] while anodization is an useful technique which can modify the characteristics of the metals oxide layer in term of thickness, surface pore configuration, composition due to anionic incorporation as well as crystal structures[69]. Both titanium itself and its oxide, TiO<sub>2</sub> have important properties that make titanium anodizing particularly relevant for scientific and technological applications, such as memristors, sensors devices like lambda probes and VOC's detectors. For instance, its lightweight and mechanical resistance make the metal particularly suitable for applications in bioengineering, where a large part of osteosynthesis devices and prostheses consist of titanium anodized in suitable conditions in order to improve its biocompatibility and reduce possible wear and metal ion release. Moreover, the semiconductive nature of crystalline titanium oxides makes it suitable for photoactive applications, as anode in dye-sensitized solar cells, as photocatalyst in environmental clean-up technologies, and as sensor in environmental applications. [70]

Actually, depending on the oxide layer characteristics that are needed, it is possible to perform the anodization with different parameters. It is fundamental to fully understand the anodic oxidation mechanism to predict how the anodizing parameters influence the result.

First of all, the *current density* and the *feeding voltage* are the main parameters to tune and control layer thickness and its crystalline phase While low voltages (below 130 V) allow to obtain an amorphous, smooth thin layer (up to 300 nm), high voltages (100 V to 500 V) are typical of the Anodic Spark Deposition process which leads to a partially crystalline oxide, with crystallites size from few micrometres to a hundred of micrometres. This surface looks glossy with pores. The pores are due to the formation of arcs in the weak sites of the oxide and these arcs move then over the whole surface. The high energy density they bring causes the local melting of the oxide which, on one hand modifies oxide crystallinity on the other allows the ions in the electrolyte to enter in the solid matrix modifying the oxide composition. [71] It is possible to calculate the thickness of the oxide layer through the Faraday's Law. This law is associated with the theory of the high field-assisted ionic transport which can explain the relationship between the anodic current and the electric field strength across the anodic film:

$$i = A \exp(BE) \quad 2)$$

Where  $i$  is the ionic current,  $A$  and  $B$  are electronic constants and  $E$  is the electric field strength which can be replaced by  $V/d$ , with  $V$  as forming voltage and  $d$  as oxide layer thickness. These laws explain why during a galvanostatic anodizing, due to the necessity

to maintain constant the current density, a constant electric field strength is established.[72] Being the electric field strength constant, while the thickness increases also the voltage has to increase. So, during the first part of the oxide growth, the oxide layer grows linearly with the voltage applied, with a constant velocity that depends on the electrolyte and its concentration. After the first range of voltage, until 120 V, other phenomena take place and the linearity is lost.[69] However, the exact value of breakdown of the oxide layer, i.e. the value of the voltage which fixes the passage from a linear dependence of the oxide growth with the voltage to a non-linear trend, is not univocally defined. In facts, the oxide layer starts to present pores with the evolution of gases and with the onset of the crystallization of the oxide itself, even after the 70 V. [22, 26] The range shown in the dielectric breakdown potentials of  $\text{TiO}_2$  is related to differences in the anodization electrolyte, temperature, current density, and uniformity (thickness and crystallinity) of the formed oxide.

In the dielectric breakdown conditions the oxide is crystallized causing the loss of linearity and the parameter that affects thickness is now the time interval of maintenance of the voltage output, i.e. the time the voltage is maintained constant. [74] The last methodology is the anodization of Ti in presence of fluoride electrolytes, which leads to the creation of a nanotubular surface structure. The fluoride ions locally perforate the oxide layer while, around the hole just formed, the oxide continues to grow. The final configuration is a nanotubular surface. This is an interesting application of anodization because of its specific surface area. In facts, the remarkable increase of the surface area makes the nanotubular surface of anodized Ti a suitable solid matrix for the dispersion of active sites, being the rates of heterogeneous reactions dependent on the surface area. As for the dielectric breakdown condition, the nanotubular anodization thickness is strongly influenced by the

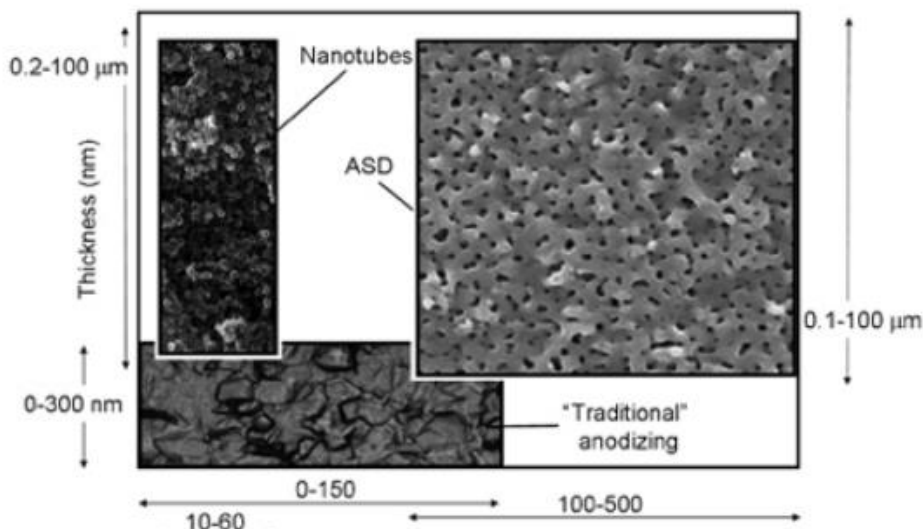


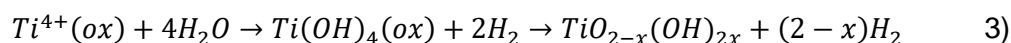
Figure 2.3 Characteristics and morphology of anodic oxide layers. [74]

maintenance time (i.e. the time the voltage is maintained constant after an initial growth), but in this case, there is also an asymptotic trend which limits the growth. The longer is the maintenance time, the thicker is the nanotubular oxide. The second important dimension of the nanotubes is the diameter of the tubes which is mainly influenced by the voltage. The pore diameter increases increasing the voltage which is generally a value between 10 V and 60 V. [75] The current density effect is as important as the voltage feeding one. A low current density leads to a slow oxidation rate and lower potentials achieved. On the opposite side, high current density allows to reach higher potential with higher potential growth rate. At higher and higher current densities there is the presence of the crystallized form of Ti, i.e. anatase and rutile. The anatase form is the first to be detected, then at higher current densities also rutile, more thermodynamically stable, is present.

Anyway, also the *nature* and the *concentration of the electrolyte* constitute important parameters in the evaluation of the oxide growth, even if not fully understood. The anodic oxidation is the dynamic equilibrium result between the tendency of the electrolyte to dissolve the oxide film and its formation.[72] Generally, acid electrolytes given by far the best results. However, a very strong acid such as HF or HClO<sub>4</sub> have strong tendencies toward dissolving the films produced. Thus, the anodic films in these cases were essentially nonadherent. The very weak acids, such as the usual organic acids, produced very adherent but limited thickness translucent films. Acids, such as sulfuric, tended to yield heavy, opaque, amorphous, films. Strongly basic electrolytes either result in precipitates of titanium oxide or reacted so rapidly with the titanium surface that the entire substrate is quickly converted to oxide. Thus, it is difficult to control the anodic process utilizing these electrolytes. Most neutral or near neutral salt-type electrolytes yield only very thin translucent films. [67] From literature, it is possible to see that alkaline electrolytes, such as sodium and calcium hydroxides present a very low ability to form the oxide layer, being the anodic formation voltage, i.e. the dynamic equilibrium voltage between dissolution and growth of the oxide, very low. On the contrary, acid compounds like sulfuric and phosphoric acids present a high growth velocity which exceeds the dissolution one.[69] So, the electrolyte features that exert an influence on the growing oxide are the amount of oxygen containing species available to oxide formation, the incorporation of electrolyte ions in the film and the tendency to dissolve the oxide itself. Based on these observations, it is possible to identify the peculiarities of common electrolyte anions: phosphate ions tend to be incorporated in the oxide and delay its crystallization, while sulphur accelerates oxide breakdown and crystallization; halides (e.g., chloride and fluoride ions) induce a localized oxide dissolution, creating peculiar nanostructures.[64] In general, looking at the electrolyte

concentration, the anodic forming voltage decreases with the increase of the concentration. Therefore, the total amount of anodic charge and anodizing time increases. [20, 23]

The effect of the *electrolyte temperature* is also quite relevant in the final thickness of the oxide layer. To fully explain the behaviour of the system subjected to a variation of temperature, it is necessary to look at the thermodynamics of the reaction at the interface.



This is an exothermic reaction, and, by definition, it is favoured at low temperature. However, during the anodization the temperature increases directly proportional to the electric power in the pre-breakdown stage. [69] So, the growth of the oxide layer is inhibited due to the increasing of the temperature during the anodization. Moreover, the increasing of temperature makes the electrolyte more conductive and less resistive, so the forming voltage is again decreased. [19, 26]

Another parameter is the *agitation of the electrolytic solution*. The effect of the agitation is mainly linked with the gas evolution, i.e. production of H<sub>2</sub> and O<sub>2</sub>, at the anode interphase. The gases present at the interface act as obstacle to the ionic current which increases the anodic forming voltage and they reduce the available area to the electrochemical reaction by the presence of the gas bubbles. So, if the agitation is enough to spread the gas bubbles far from the metal surface, the total forming voltage is decreased. [69]

The *ratio of the area of cathode and anode* is another parameter used to control the anodizing process. Under a constant density current conditions, a reduced area of the cathode leads to a shorter anodizing time to reach the pre-set voltage due to the increase of the resistance between the cathode and the electrolytic solution. [69]

As beforementioned, the titanium anodization, depending on the parameters set, can lead to three different surface layouts:

1. Amorphous and compact oxide layer up to hundred nanometres thick, which is the result of the standard anodization and leads to a coloured surface
2. Crystalline and porous layer from few micrometres to a hundred of micrometres. It comes from the anodization beyond the breakdown voltage (i.e. 100 V) with the so called, Anodic Spark Deposition (ASD) or Plasma Electronic Oxidation (PEO) or MicroArc Oxidation (MAO).
3. Titanium dioxide nanotubes derived from the anodization in presence of fluoride-containing electrolytes.

## 2.2.1 Standard Anodization

This technique has been the first to be discovered and studied since 1950s. [77] The starting point was the presence of colours due to the corrosion of metals and the formation of an oxide layer. From these studies, it was highlighted the presence of the interference phenomenon which is the cause of the formation of coloured surface. Generally speaking, interference colours are generated by thin transparent films, like in this case the anodizing amorphous oxide layer.[27, 28] The light is reflected only in part by the film, while the leftover is refracted inside the film. Depending on the refractive indices of the titanium dioxides and on the light components strengthened by exiting the oxide phase, the hue changes.

$$n_{TiO_2}\lambda = 2d \sin\theta \quad 4)$$

where  $n_{TiO_2}$  is the refractive index of titanium dioxide,  $\lambda$  is the radiation wavelength giving constructive or destructive interference and  $\theta$  the angle of incidence of light. The relation between the colours present on titanium surface and the oxide thickness can be used mainly to understand the thickness of the oxide without complex surface analysis [64, 78]. Oxide thickness is directly proportional to the feeding voltage; with growing voltage, the chromatic scale that can be achieved consists of the following order of colours: yellow – purple – blue – light blue – silver – yellow – pink – violet – cobalt blue – green – yellow/green – pink – green. [29, 30] The oxide growth rate in the typical electrolytes used to produce interference colours (i.e., diluted acids such as phosphoric acid and sulfuric acid) is close to 2 nm/V, and colours are lost either when the oxide thickness is not comparable to the visible light wavelengths, which means that it cannot give interference phenomena anymore, or when the oxide structure changes, with the incorporation of different chemical species into the film or with the formation of crystal structures, which both lead to the change of the optical properties of the film. In fact, coloured oxides exhibit in most cases amorphous structure; anodizing in sulfuric acid with suitable current densities and cell voltages causes a partial conversion of the oxide to anatase or rutile, as nanocrystals embedded in the amorphous matrix, due to the establishment of anodic spark deposition conditions. For a feeding voltage ranging from 70 V to 120 V, depending on the substrate, electrolyte and current density, oxides showing both interference colours and semicrystalline structure can be obtained, while for higher voltages anodic spark deposition deeply affects the whole surface, causing a sharp increase of the oxide thickness and modification of the surface morphology, and the consequent loss of interference conditions.[74]

The most important anodizing parameter is the applied voltage, which is linearly correlated to the thickness of the oxide layer. The film generated is amorphous and compact, until the voltage is sufficiently increased to generate crystalline nucleus in the amorphous matrix. This threshold is called dielectric breakdown voltage and it is dependent on the electrolyte activity and the electric field inside the oxide. The formation of the crystallized form is linked with the start of the oxygen evolution phenomenon, mainly due to the electric conductivity properties of the anatase phase. The gas evolution is not a limiting step for the anodizing process, but it is a current consuming phenomenon which slows down the anodizing rate. Increasing step by step the voltage applied, the anatase peak becomes more and more pronounced, until also the rutile phase starts to be formed. In this case, the process is called ASD. However, the two different types of layers formed, i.e. amorphous and crystalline, exhibit different properties: while the amorphous shows better corrosion resistance properties, being not porous, the crystalline one exhibits better charge transfer properties. The semiconductive behaviour of the anatase phase is the most important advantages exploited by the recent applications of ASD. [30, 31]

The choice of the electrolyte solution is fundamental for the complete understanding of the oxide growth and thickness. Looking at the acidic components, sulphuric acid exhibits the best performances, in terms of oxide growth rate, at 0.5 M of concentration. [19, 23]

Concerning oxide composition, a perfect oxide should present a  $\text{TiO}_2$  stoichiometry; this condition, which is typical of oxides produced by chemical synthesis or physical deposition, is usually not complied with by anodic oxides, which present several possible deviations from  $\text{TiO}_2$ . Low voltage anodizing – traditional anodizing – often produces sub-stoichiometric  $\text{TiO}_{2-x}$  due to the oxidation mechanism, which involves the migration of  $\text{Ti}^{4+}$  from the metal surface across the oxide and towards the outer surface in contact with the electrolyte, and of  $\text{O}^{2-}$  ions along the opposite path. The oxide generally builds up in between the two interfaces, thanks to the mobility of both ions. The inner surface in contact with the metal accounts for the most pronounced sub-stoichiometry.[70]

### ***2.6.2 Anodic Spark Deposition***

When the process of anodization starts, the oxide layer grows linearly with the increasing of the feeding voltage forming a compact dielectric barrier which prevents the flowing of the ionic current through the oxide itself. So, the process slows down, but if the cell exceeds a certain threshold limit, the barrier can be overcome. This value is called dielectric breakdown and corresponds approximately to 100 V depending on the electrolyte, anode composition and current density. In these particular conditions, the current concentrates in the weak points of the oxide layer, where the insulation is less

effective, causing so high values of electric field to start the atoms ionization and a localized microplasma state. In that points a localized electric field of  $10^6$  A/m<sup>2</sup> causes the instantaneous melting and solidification of the oxide layer heated up to 5000-6000 K. [70] This breakdown value is clearly recognizable due to the formation of sparks that move from the starting weak point along the whole surface creating electric arcs. The effects of this anodizing phenomenon are visible also in the morphology of the surface. In facts, the surface presents a glassy plane surrounded by the craters leaved by the sparks. The dimension of craters varies from 200 nm to 2-3  $\mu\text{m}$  and depends on processing parameters; generally, the longer the sparking process the bigger the mean pore size.[83] For thick layers (time of electrolysis 12 and 15 min), the pore size is irregular, it varies between some square nanometres up to 9  $\mu\text{m}^2$  with no predominant occurrence of a certain pore size. To the contrary, thinner layers (time of electrolysis 3 and 6 min) show predominately small pores of about 1  $\mu\text{m}^2$  in size. This behaviour is typical for the layers obtained by anodic spark deposition. [84] Pores can be roundly shaped, ellipsoidal or irregular, with elongated shapes. The deposited coating doesn't follow a linear growth rate with applied voltage any more: as anticipated, the process is not just an electrochemical oxidation of the surface, but involves sparks followed by the oxide melting and quenching, which change drastically the reaction mechanism and kinetics. The oxide microstructure deeply differs from that obtained by traditional anodizing, since sparking produces conditions suitable for oxide crystals nucleation. [74] Crystallization is never complete, since solidification rate is too high, almost instantaneous. While at the beginning of ASD conditions crystallites have anatase structure, the more the process is complete, the more crystals tend to undergo an allotropic transformation to rutile, probably induced both by the increase of crystals dimension with time during the process and by annealing effects. [70] Nevertheless, the longer the treatment and the higher the cell voltage, the more uniform the oxide layer surface morphology and structure. So, ASD anodizing process can be organized in different steps: first of all, the primary formation of an oxide insulating layer compact and amorphous, second step by increasing the voltage, the voltage breakdown value is reached and the microarc phenomenon starts. Then, in the arc starting point the substrate reacts with the electrolyte creating a thicker oxide layer even more insulating than the previous one.[83] This is the reason why the longer the ASD process and the greater the number of microarcs in different points of the surface, the more uniform and homogeneous will be the ceramic oxide layer. As already said, the high temperature near the microarc hot spot provokes the nucleation of crystalline phase within the amorphous one. This change of the main oxide phase, rather than being detrimental, generates unexpected properties of ionic conductivity that find application mainly in gas sensing devices, especially for the detection of oxygen – such as in lambda probes – and

volatile organic compounds (VOCs). Moreover, oxygen vacancies at the metal/oxide interface can introduce a memristive behaviour, i.e., resistivity becomes a function of current previously travelled through the oxide in the past (integral of the current), showing a bias-dependent switching response to current. [22, 34] Memristive devices are seen as the future generation of non-volatile memories with fast access and improved data density and they are expanding their applications in the development of artificial neural networks. Besides time of electrolysis, also the concentration and the nature of the electrolyte are important parameters in ASD anodization process. Generally, the increase in electrolyte concentration results in coarsening of the morphological features, while the nature of the electrolyte can change the composition of the oxide layer.[84] In facts, ASD is an important technique also for its ability to incorporate ions present in the electrolyte and, in this way, change the surface composition of the oxide layer. Due to the instantaneous melting and quenching of the surface, it is possible to incorporate in the titanium oxide layer ions present in the electrolyte. In facts, electrical breakdowns of an anode film produce high temperatures and pressures in discharge channels and around them, which results in the thermolysis of electrolyte components and their incorporation into growing coating structures.[83] Tuning the composition, it's a fundamental tool not only in corrosion resistance application, but also in biomedical and electronical applications. The first studies were performed on the incorporation of sodium and silicon in the oxide layer by the anodization in  $\text{Na}_2\text{SiO}_3$ . Maintaining the voltage over the 250 V in  $\text{Na}_2\text{SiO}_3$  and  $\text{Na}_2\text{PO}_4$ , the formation of the  $\text{TiS}_x$ , which is an incredibly corrosion resistant compound, has been detected.[83] Generally speaking, the ASD anodization in  $\text{Na}_2\text{SiO}_3$  containing electrolyte improves the corrosion resistance characteristics of the oxide due to the higher conductivity of these compounds that leads to a denser and more compact microstructure with respect to the ones that do not contain this salt. [86] However, it is important also to evaluate the potential at which the ASD is performed: in facts, at 400 V the formed layer is composed by a porous external layer enriched of sodium, silicon and oxygen which does not contribute to the corrosion resistance, and a compact inner oxide layer mainly composed by  $\text{TiO}_2$ . [83] Looking at another element, also the incorporation of zirconium is an important treatment that can be performed on the titanium surface. In facts, leaving the  $\text{TiO}_2$  immersed in aggressive media, the titanium oxide tends to dissolve in the solution in its hydrates form. The incorporation of Zr in the oxide layer can solve this weakness:  $\text{ZrO}_2$  has a greater stability in aqueous solutions and it increases the corrosion resistance of the bulk substrate. Another characteristic of zirconium is its capability to reduce the electrolyte resistivity, which leads to a reduction of the microarc power on the surface. Being the microarc energy discharge the main cause of the pore creation, a decreasing of its power causes the reduction of the pore dimensions and a more corrosion resistant surface.[87]

The incorporation of chlorides is another important tool to modify the behaviour of the oxide film. If on one hand, ASD in HCl after a pre-anodization with low alternating current creates a rough and thick oxide layer, on the other the use of  $\text{Cl}^-$  enriched electrolytes leads to the formation of the complex  $\text{TiCl}_4$  that causes the oxide cracking.[88] The first treatment can be applied in multi scale roughness application, while the second has to be avoided. Recently, also alumina becomes an important compound to be studied during the incorporation. This compound can increase the corrosion resistance of the porous layer through its filling and hindering effect. [38, 39] Looking at the biomedical applications, the incorporation of  $\text{P}^-$  and  $\text{Ca}^-$  ions in the oxide layer exhibits excellent osteointegration properties and it hinders the dissolution of titanium ions in the body fluid. Ticer (Ticer, ZL Microdent; TiUnite, Nobel Biocare Holding AB), a dental implant with anodically oxidized surface and the first among similar materials employed in clinical practice, was found to promote fast osteoblast cell differentiation and mineralization processes. Moreover, Ticer accelerates the integration with the bone, increases the bone/implant contact and improves primary and secondary stability of the implants.[91]

The modification of the oxide layer composition has an important application also in catalysts preparation. Heterogeneous catalysts are porous surfaces, mainly alumina and titania ( $\text{TiO}_2$ ) with active sites dispersed on their surface. ASD ensures the formation of oxide layers with controlled porosity and their conversion into target catalytically active coatings in a continuous one-pot process by choosing appropriate electrolyte compositions. PEO, in the catalyst production can be used as single and unique stage or as first stage followed by other treatments (impregnation in precursor solution, extraction pyrolysis etc). The first type ASD treated catalysts exhibit very good performances in the main catalytic processes as deep oxidation of propane-butane mixture, catalytic cracking reactions, phenol oxidation, while the second is mainly used in afterburning of exhaust gases of vehicles and industrial plants, combustion of diesel soot and biomass gasification.[92]

ASD treatment is also an important way to reduce the risk of fatigue failure due to fretting corrosion. In fact, mainly in biomedical application, the fatigue resistance of titanium alloy is an important issue in prosthesis design and production and an ASD treatment improves resistance characteristics. [93]

### ***2.6.3 Nanotubes production through anodization technique***

Nanoporous and tubular titania layers form on during anodization using fluoride containing electrolytes. The titania layers develop perpendicular to the metal substrate which can be self-organized under controlled conditions.[94] Titanium and titanium dioxide are readily

dissolved in fluoride-based electrolytes, particularly those containing hydrofluoric acid. In addition to field-assisted oxidation of porous/tubular layers, it is important to define the process of field-assisted dissolution leading to dissolution of the oxide preferentially at the pore/tube base, where the electric field is stronger. This implies that there is a constant dissolution rate of the anodic layer at the base of each pore. In a fluoride containing electrolyte the oxide dissolves leading to the formation of a titanium hexafluoride complex  $[\text{TiF}_6]^{2-}$ , which is stable in water. In Fig. 2.4 are sketched two possible forms of oxide layers obtained in different electrolytes.

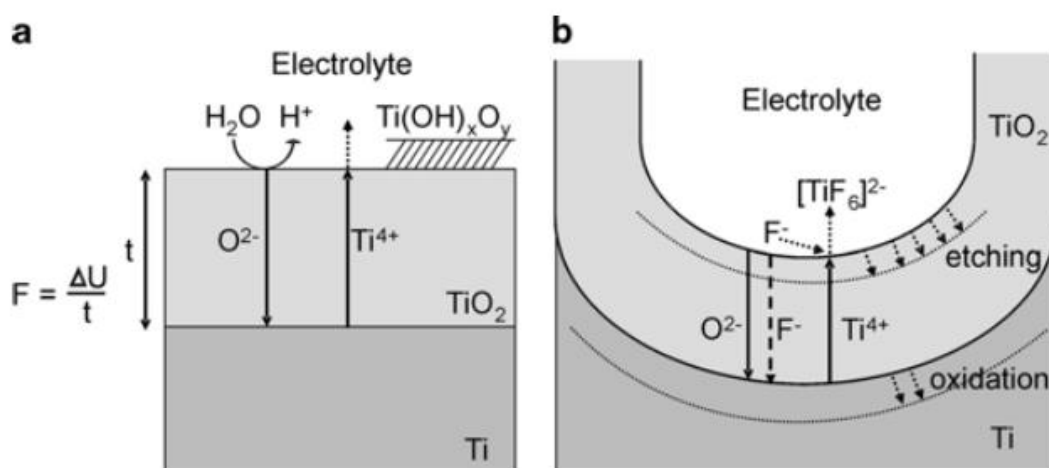


Figure 2.4 Schematic representation of oxide layer grown in absence of fluorides (a) and the mechanism of nanotubes formation in presence of fluorides (b). [70]

Hydrofluoric acid was the most-used electrolyte to dissolve the titanium oxide. In electrolyte solutions containing HF high ordered  $\text{TiO}_2$  nanotube arrays were prepared at low anodic potential of typically 5–20 V. However, the strong dissolubility of hydrofluoric acid limits the nanotube length to a maximum of about 500 nm. [70] The “second generation” of electrolytes was obtained when buffered neutral electrolytes containing NaF or  $\text{NH}_4\text{F}$  instead of HF were used and the importance of the pH was considered as factor for the nanotubes’ growth. The “third generation” nanotubes were grown in non-aqueous electrolytes: in facts, fluoride ions in water-based solutions are more aggressive than in organic media, which is the reason why the growth of the nanotubes in water is limited to lengths of a few microns. On the contrary, using optimized organic electrolyte systems, such as ethylene glycol, almost ideal hexagonally arranged nanotube arrays can be grown, with thickness of several hundreds of micrometers and tube diameters ranging from  $\mu\text{m}$  to hundreds  $\mu\text{m}$ . [95]

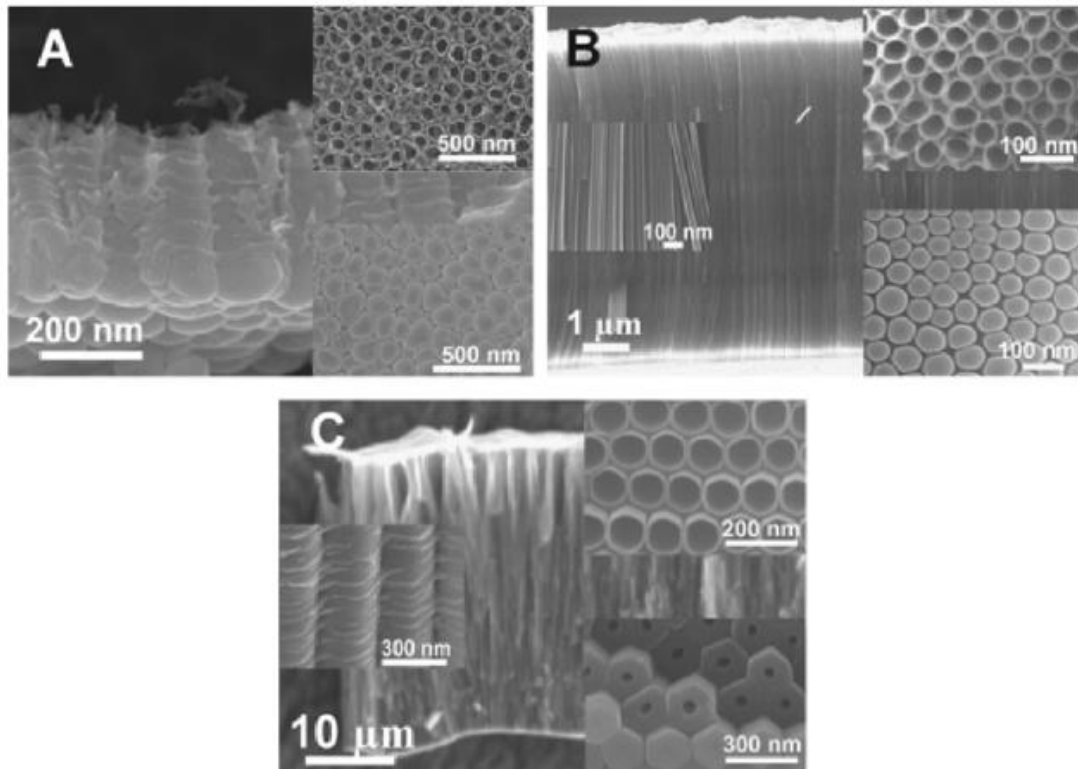


Figure 2.5 SEM images showing  $\text{TiO}_2$  nanotube layers grown with different electrolytes: typical morphology of nanotubes obtained with HF or acidic fluorides (A), with glycerol/fluoride electrolytes (B) and with ethylene glycol/fluoride electrolytes (C).[96]

The formed-oxide film is amorphous at low anodic potential and crystal at high potential. The crystal structure was reported to be anatase, rutile or the mixture of rutile and anatase.[96]

#### 2.6.4 Brief description of anodic oxide of other valve metals

In the following, a more detailed view of the main characteristics of anodized aluminium, magnesium, zirconium, niobium and tantalum are reported, to account of their technological interest in different fields, from bioengineering to electronics. For all the other valve metals, not described here, a similar behaviour can be found.

The protection or decoration of *aluminium* surfaces by anodization has been used commercially since at least 1923. Two forms of anodic aluminium oxide exist, the nonporous barrier oxide and the porous oxide. When Al is anodized in neutral or basic solutions ( $\text{pH} > 5$ ), a flat, nonporous, featureless insulating “barrier” oxide forms, the “barrier-type film (BTF). When Al is anodized in an acid [usually sulfuric ( $\text{H}_2\text{SO}_4$ ), oxalic ( $\text{H}_2\text{C}_2\text{O}_4$ ), or phosphoric ( $\text{H}_3\text{PO}_4$ ) acids], deep pores can form, with diameters varying between 5 and 100 nm and lengths up to several microns. The bottom of each pore also

consists of a thin “barrier layer” (10-100 nm thick) over the metallic Al surface; the pore diameter depends on pH, anodization voltage, and choice of acid. This porous structure has been called “pore-type film” (PTF) or “alumite”. [97] Anodic aluminium oxide (AAO) coating has attracted the scientists’ attention because of its self-organizing nature of vertical (cylindrical) pores in the form of hexagonal arrays, which provides a controlled and narrow distribution of pore diameters and inter-pore distances in addition to the possibility of forming the pores with extremely high aspect ratio. [98] When the pores are filled with metals or semiconductors in a subsequent alternating-current reductive electrolysis, these films can be fabricated into interesting magnetic recording, electronic, and electrooptical devices. A lot of research was conducted in the area of anodic oxidation of aluminium ever since its first industrial use. Their goal was to clarify the main principle behind the creation of oxide layer on the surface of aluminium part, specify the influences of individual input factors on thickness of oxide layer, geometry of oxide layer, its properties, also how to optimize the process of oxidation and last, but not least, creation of new electrolytes, which could reduce the cost and risks to health and environment. [99]

Regarding *magnesium* alloys, the first anodizing treatments, such as HAE and DOW-17, are now outdated since they use chromate or fluoride-containing electrolytes and produce coatings with reduced performance compared with more recent PEO processes such as KERONITE, TAGNITE, MAGOXID and ALGAN, which are more environmentally friendly. PEO of magnesium alloys is normally performed in silicate, phosphate and/or aluminate-containing alkaline electrolytes with the coating containing amorphous and/or crystalline phases such as MgO, Mg<sub>2</sub>SiO<sub>4</sub>, Mg<sub>3</sub>(PO<sub>4</sub>)<sub>2</sub> and Mg<sub>2</sub>AlO<sub>4</sub>. The thickness of the coating can easily achieve 50–100 μm, with an average growth rate of 1–5 μm min<sup>-1</sup>. A two- or three-layer structure is typically observed with a characteristic thin barrier layer, of a few hundred nanometres thickness, at the substrate/coating interface. Coatings can be formed under DC, AC or bipolar electrical regimes. In modern PEO technology, AC, pulsed DC and bipolar electrical regimes offer better control over plasma chemical processes compared with DC regimes, reducing adverse effects associated with the discharge under DC conditions and producing more uniform and less porous coatings [100]

As regarding *zirconium*, it finds applications as structural component in chemical reactors and in water-moderated nuclear reactors, as well as bioprosthetic implant, thanks to a good work ability combined with high strength also at high temperature, and good corrosion resistance, which can be further improved by anodic oxidation. [101] ZrO<sub>2</sub> coatings are commonly employed to further reduce corrosion rate, and especially in the production of biomedical implants the ASD process can be applied to produce crystalline films with tuneable composition. On the other hand, its oxide exhibits peculiar functional

properties, including high dielectric constant, luminescence and the possibility to obtain ionic conductivity – and related gas-sensing ability and suitability as solid electrolyte: therefore, ZrO<sub>2</sub> films gained interest in the production of optical and electronic devices.[102] Common electrolytes used in zirconium anodizing process are sulphate-based ones (H<sub>2</sub>SO<sub>4</sub>, Na<sub>2</sub>SO<sub>4</sub>, K<sub>2</sub>SO<sub>4</sub>), borate-based ones (ammonium borate), carbonate-based ones, caustic solutions (NaOH, KOH). Owing to the incorporation of electrolytic anions into the anodic films, oxidation kinetics and resulting optical and electrical properties of ZrO<sub>2</sub> mainly depend on the chemical nature of the electrolytic anions. [103] As in the case of titanium anodizing, all possible anodic oxides can be produced – barrier-type ZrO<sub>2</sub>, thick ceramic layers by ASD, and nanotubular oxides in presence of fluoride containing electrolytes. The crystal structure can also be tuned as a function of the electrolyte composition, being the cubic and monoclinic lattices the preferred crystal arrangements occurring.[104]

Also anodized *niobium* has attracted large attention, especially due to the high dielectric constant and high breakdown potential of the anodic oxide. In the early stages of research, Nb<sub>2</sub>O<sub>5</sub> was mostly studied as catalysts, sensors and electrochromic layers, while more recently the path was opened for applications in photocatalytic purification devices, batteries, solar cells and other electronic devices such as memristors.[54, 55] Anodizing is mainly performed in acid aqueous solutions (H<sub>2</sub>SO<sub>4</sub>, HNO<sub>3</sub>, H<sub>3</sub>PO<sub>4</sub>, HClO<sub>4</sub>, HF) and, more generally, in phosphate or fluoride-based electrolytes: as in the previously described anodizing processes, also on niobium the choice of electrolyte strongly affects the oxide morphology, with the formation of either compact barrier-type layers, or nanostructured porous layers.[107] Conversely to anodic ZrO<sub>2</sub>, which is mostly crystalline, anodic Nb<sub>2</sub>O<sub>5</sub> films maintain in a wider range of conditions an amorphous structure, linked with its high breakdown potential: field crystallization is generally achieved only at high voltages, as in the case of titanium anodizing. Once again, electrolyte ions such as phosphates or sulphates may be incorporated in the oxide during anodizing.[64]

Finally, anodized *tantalum* oxides present high relative permittivity and greater storage capacitance for the same thickness with respect to SiO<sub>2</sub>, which makes them particularly attractive to produce dielectric films for electronic industries.[108] Typical anodic processes for Ta are similar to those related to Nb anodizing, and also the results have close similarities, with a mostly amorphous nature and the possibility to produce self-ordered nanotubular structures in electrolytes containing fluoride ions. Taking into account the oxide composition, only high voltage anodizing usually leads to the modification of stoichiometry by incorporation of electrolyte ions; in the low voltage production of barrier films, the oxides can experience slight deviations from their original chemistry, but to a

negligible extent.[109] Conversely, Ta anodizing in  $H_3PO_4$  causes the incorporation of a substantial quantity of phosphate ions, with the peculiar formation of a double layered barrier-type structure with a more stoichiometric oxide close to the metal interface and one richer in phosphates close to the electrolyte; similar considerations were drawn in experimental works on zirconium anodizing in phosphate electrolytes.[110] As emerges from the quick overview given, valve metals behave similarly, and many features are repeated – for instance, the production of nanostructures in aggressive electrolytes that give rise to localized oxide dissolution.[64] In Fig. 2.6 are presented some SEM images of nanostructures grown on different metals.

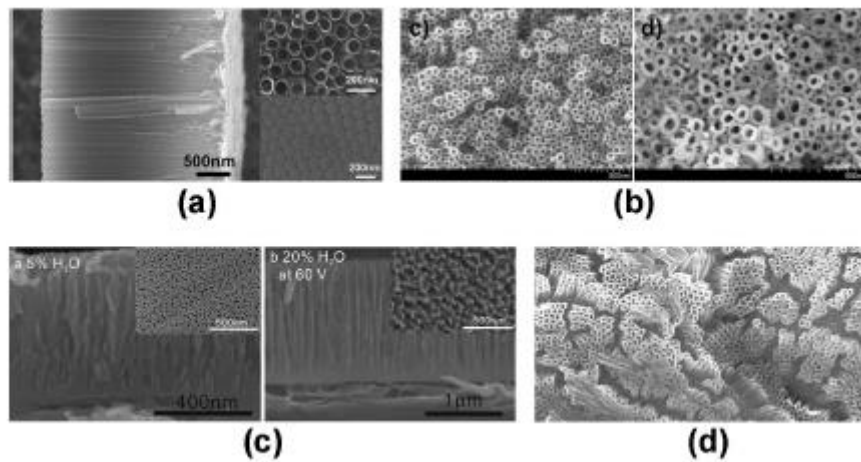


Figure 2.6 Anodic oxides with nanotubular morphology obtained on: **a)** titanium, **b)** zirconium, **c)** niobium and **d)** tantalum. [17]

## 2.7 Discontinuous anodizing

During discontinuous anodizing, in contrast with DC anodizing, current is not supplied continuously. Discontinuous anodizing defines all the anodic oxidation carried out with current waveform intersecting the zero. One of the easiest discontinuous waveforms is monopolar pulsed current, which alternates on-periods and off-periods. This anodizing regime is described by two parameters: duty cycle and frequency. The first, expressed as percentage, defines the ratio between on-time and total time, while the second defines the pulses frequency.

A positive duty cycle is the working time of positive pulse divided by the total time of the cycle and, to allow this, the instantaneous current density varies in time, with spikes, in Fig. 2.7, in correspondence of instantaneous rises and decreases of the potential.

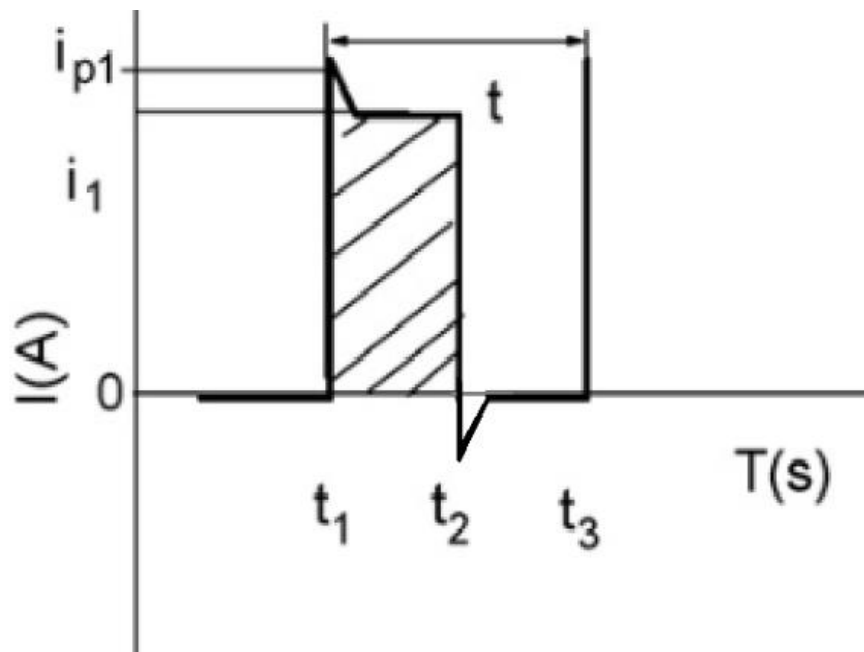


Figure 2.7 Sketch diagram of the unipolar current mode. [111]

The current can, not only vary between the positive spike and the zero, but also go negative, as depicted in Fig. 2.8. This is the case of bipolar pulsed regime.

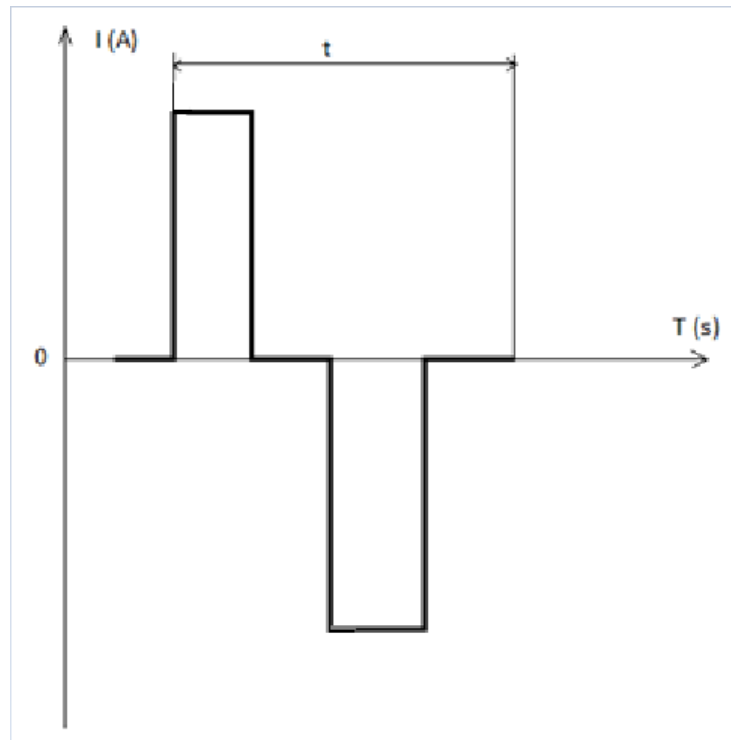


Figure 2.8 Sketch diagram of the bipolar current mode.

The anodization power supplies may differ with respect to the input signal control mode. There are some researches that use current as an input signal, in which the voltage increases in accordance with the increase of the coating resistance. The other option is to input constant amplitude, peak-to-peak or rms voltage and limit the maximum current. In this case, the current peak with the following current decay will be observed at the output as the impedance of the coating increases. In Fig. 2.9, all the possible applications and control modes technique are depicted.

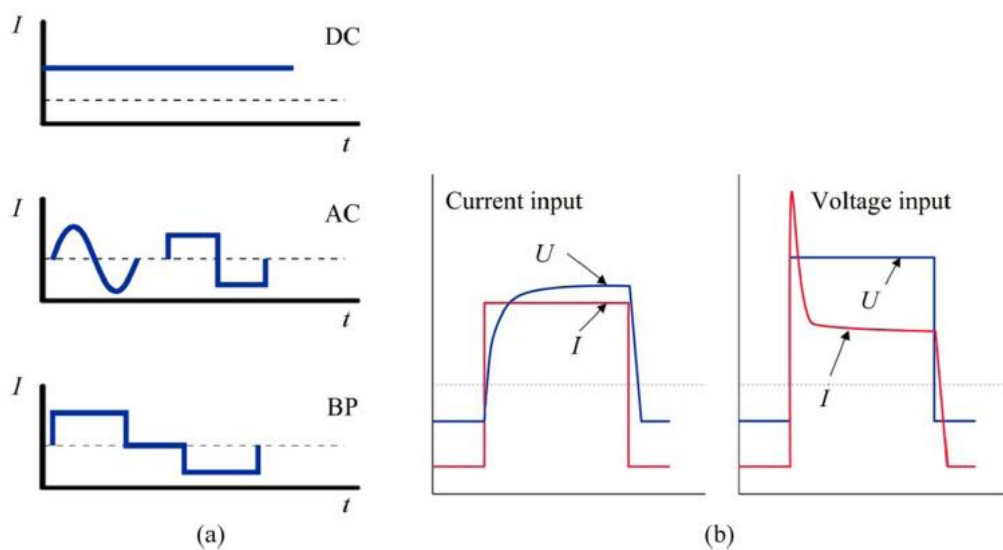


Figure 2.9 PEO current applications a) and control modes b). [64]

The bipolar mode has the advantage of two DC power supplies separately controlling the positive and negative pulses so it is easy to vary the duty cycle and time off period between the pulses. From the industrial point of view, this mode of control permits achievement of higher power and frequencies up to several thousand Hz.[112]

### ***2.7.1 Discontinuous anodizing on other metals***

This process can be applied on all the metals mentioned in paragraph 2.2 for traditional anodizing, but the most used one is magnesium. The main advantage is that, when the current is off or in the range of a negative pulse, sparks disappear, and melted areas are quenched by the electrolyte resulting in a less porous structure of the oxide layer, respect to traditional anodizing. The result is, in addition, that there is a cooling period among the intervals of current flowing to the anodic areas, so that a higher current density can be used, without increasing the electrolyte reaction on the oxide layer. This means that the burning of oxide film, that usually happens in the first stages of DC anodizing due to the continuous high temperature and sparks maintained on the surface of the sample, can easily be avoided. [113]

As a consequence, the most noticeable thing is that the overall current is lower respect to traditional anodizing, resulting in a more energetically favourable process; a reduction of 25-30% in power consumption is experienced. [113]

The characteristics of the coating, as thickness, morphology and structure are mainly determined by four parameters: final voltage, frequency, duty cycle and current density, from the most relevant to the lowest.

In the case of magnesium, it has been found that the duty cycle affects consistently the anodization only when the voltage is higher than 480 V. [111]

For small values of duty cycle, the appearance of the oxide is smooth and compact while increasing it, above 35%, it becomes rough with protuberances and depressions. This happens because gas bubbles, that are trapped in melted areas of the coating, evolve intensively.

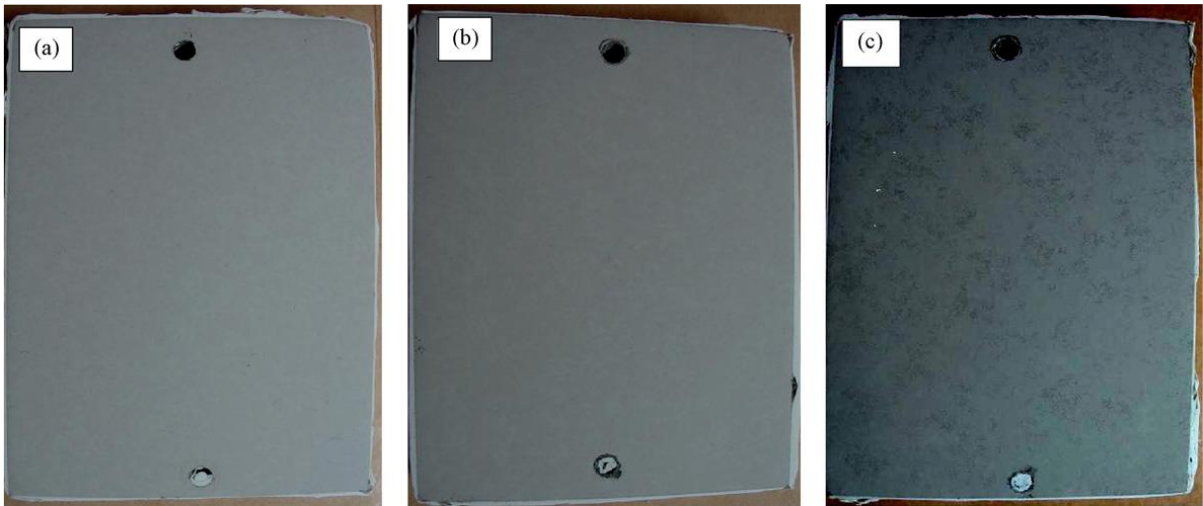


*Figure 2.10 Pictures of anodized AZ91HP, a magnesium alloy, at three duty cycles: a) 15%, b) 25%, c) 35%. All three at a final voltage of 480 V, current density 20 mA/cm<sup>2</sup> and frequency 600 Hz. [111]*

Keeping constant frequency, current density and anodizing time, the longer the working time in a cycle, the higher the temperature on the sample resulting in larger pore size and, consequently, the lower the corrosion resistance (Fig. 2.11). This means that the anodic reaction and water vaporization and electrolysis will intensify, which increase the thickness and porosity of the coating at the same time.

Considering the electrochemical nature of plasma electrolyte oxidation processes, voltage/current characteristics of the applied electricity may noticeably affect the coatings features. In this regard, several parameters such as state and polarity of current and voltage have been addressed in literature. Unipolar and bipolar current types are used for PEO treatment processes. Bipolar current has been more studied in achieving desirable corrosion properties. However, bipolar current type was stated to be of more efficiency than unipolar type. This may be due to fact that the coating produced in the unipolar state suffers from pores and defects created by entrapped gas within the coating. In comparison with unipolar pulse current, using bipolar pulse current improves plasma thermal conditions. It was seen that with accurate control of negative and positive pulses ratio, one may avoid very strong plasma discharge and consequently sudden extremely high temperatures. polarization, respectively. Films produced by bipolar pulses are usually thicker than those formed via unipolar pulses. Application of cathodic section to current during PEO process is effective in achieving a more dense and homogenous coating. Due to higher thickness and density, bipolar-made films provide a stronger protection against corrosion.[114]

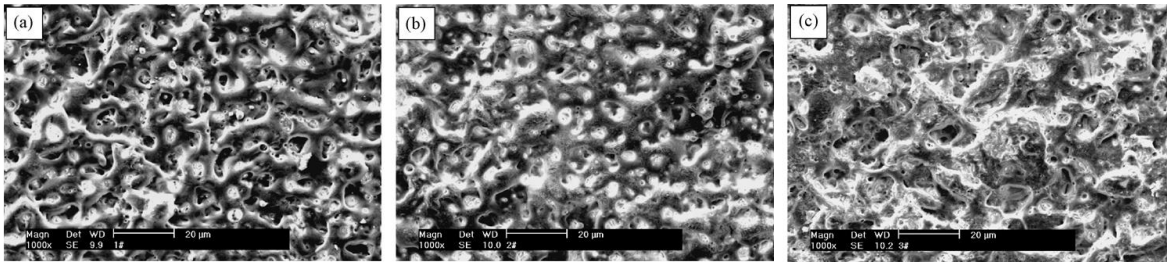


Figure 2.11 Surface morphologies of AZ91HP at three duty cycles: a) 15%, b) 25%, c) 35%. All three at a final voltage of 480 V, current density 20 mA/cm<sup>2</sup> and frequency 600 Hz. [111]

On the other hand, the longer the working time, the lower the pulse average current density which results in a lower final voltage after the same anodizing time, resulting in a higher corrosion resistance. It must be noted that, increasing the frequency, the coating thickness decreases; however, corrosion resistance parameters are independent on the thickness of the oxide layer, what really matters is the morphology of the layer. Indeed, when the final voltage is high enough (over 440 V [111]) to form the porosity, the oxide layer results thicker but the growing size of the pores causes a drop in the corrosion resistance of the sample. [111]. On the other hand, with a lower final voltage, the porosity results smaller and compact showing a much higher corrosion resistance. [111]

In the case of aluminium, pulsing from a high to a lower voltage, for example from 22 V to 15 V [115], increases both corrosion and abrasion resistance, improves thickness uniformity and increases oxide growth kinetics. The quality of the oxide film increases by increasing pulses frequency. In addition, hard coatings can be thicker with less energy with solution chilling.

R.O.Hussein et al. [116] studied the effects of the two different current modes: unipolar and bipolar ones. They found that using a bipolar mode the morphology and the porosity of the layer was smoother and more compact than with a unipolar mode. This behaviour can be explained with the classification of the different discharges that can take place on the oxide layer. This model assumes three types of discharge, types A, B and C. Type B discharges originate from the metal-oxide interface and are strong as a result of dielectric breakdown through the oxide layer creating cratered structures. Types A and C, originating from the oxide-electrolyte interface, are weaker than type B discharges, and occur as a result of gas discharges in micro pores in the oxide layer. The high temperature spikes correspond to the strongest discharges (B-type discharge) and they significantly affected the microstructure and morphology of the coating. The strongest discharges would make the coating more porous. So, the main effect of the bipolar current mode is a discharge disturbance, which avoids the development of long lived, very large microdischarges. By using the bipolar current mode there will be a balance of the discharge effect. The  $T_{off}$  duration should be

long enough for the local molten oxide to be cool down before another pulse were initiated, while the  $T_{on}$  provided time long enough for sintering and therefore thick and hard coating with minimum pores will be produced. Generally speaking, the introduction of the negative pulse and a pause ("time off") between the pulses, facilitates the quenching the microdischarges and prevents their transition into more powerful and destructive arc discharges. In another study, it has been shown that high frequency bipolar processes are more energy efficient than AC process and can offer the coating growth rate of  $\sim 3$  m/min and energy consumption of  $10\text{--}15$  (kW·h)/(m<sup>2</sup>·m).[117]

V.Dehnavi et al.[118] studied the effects of different *duty cycles* applied to the surface of 6061 aluminum alloy using a plasma electrolytic oxidation (PEO) process employing an unipolar pulsed direct current (DC) power mode in an alkaline electrolyte. They found that changing the duty cycle also the sparking or breakdown voltage as well as the maximum voltage eventually achieved were higher in samples treated with lower duty cycle (i.e. 20%) than with higher duty cycle (i.e. 80%) at the same frequency. Instead, no considerable difference in sparking and maximum voltage reached during PEO of samples treated at the same duty cycle but different frequencies. Also, on the surface are present differences between the samples anodized with different duty cycles: while lower duty cycles produced microdischarges with higher spatial density and lower intensity that causes smaller craters, high duty cycles create microdischarges stronger, even if their number is decreased, especially at longer times with bigger craters. In Fig. 2.12 the different microdischarge distributions and intensities are depicted. The different intensities and densities of microdischarge on the aluminium surface generates a dependence of thickness on the duty cycle chosen: the coating growth rate increases gradually with decreasing duty cycle at constant frequency. This increased growth rate at lower duty cycles could be linked to the fact that coating growth is the result of oxidized molten aluminium as it flows out through discharge channels and more discharges are involved at lower duty cycles. Varying the number and the intensity of the microdischarges also the distribution of some ions of the electrolyte can change: the higher the number of the microdischarges the more uniform would be the concentration of ions in the oxide layer (e.g. Si in this case).

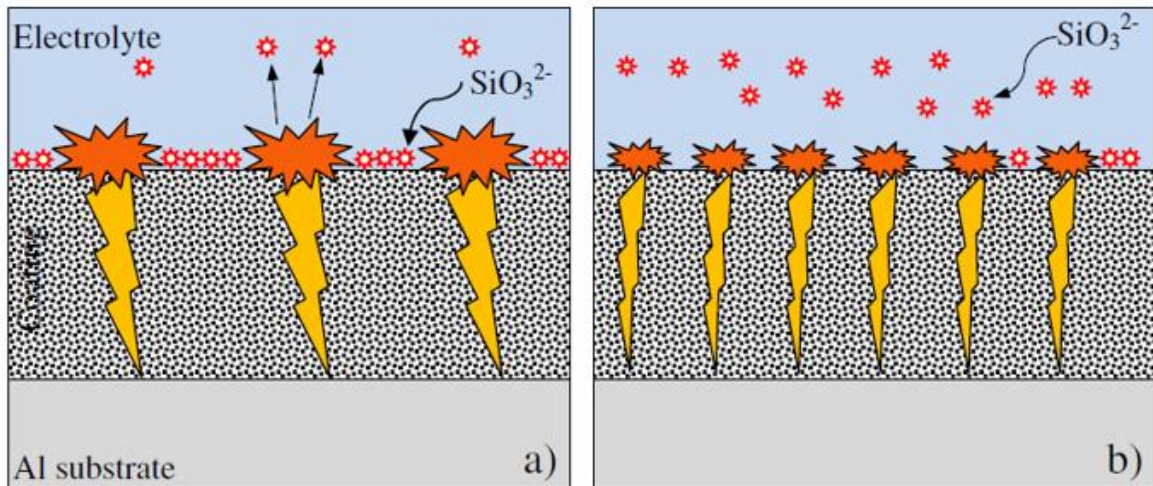


Figure 2.12 Diagram showing the effects of different duty cycles on the distribution of microdischarges. Figure a) represents the high duty cycles effect, while figure b) the low duty cycle effect. [66]

Another possible advantage of pulse anodizing can be found in the case of aluminium alloys containing copper or silicon. In the traditional anodizing process, an initial passivity of the anode takes place during polarization which leads to heating of the anode surface during the formation of the oxide film, ending with the burning of it. This problem can be overcome to some extent by superimposing an alternating current in the form of a ripple on the direct anodizing current. [113]

### 2.7.2 Discontinuous anodizing on titanium

On commercially pure titanium grade 4 samples it has been discovered that, with a lower *duty cycle*, the oxide layer results thicker, shows a higher degree of crystallinity, a homogeneous nano-pore size and distribution, and a more corrosion resistant passive oxide [119]; in addition, the quality of the resulting layer can be further improved keeping a high frequency.

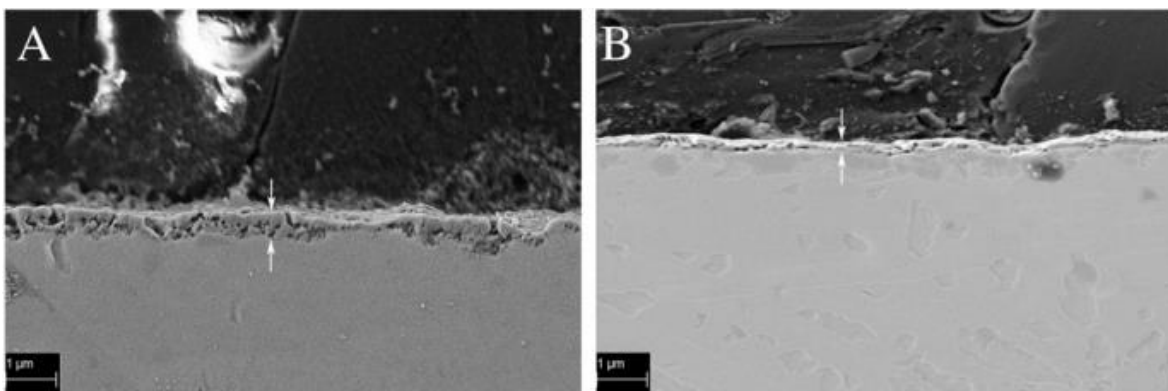


Figure 2.13 Representative SEM images at different duty cycles: A) 2%, B) 100%. [119]

The main result of pulse anodizing, mostly for high values of duty cycle, is the resulting nanoporous multi-layered structure manifesting in the oxide layer and this effect is even more evident prolonging the anodization time. In addition, pulse anodizing, respect to traditional, allows to reach the desired potential in a much shorter time. [120]

Pore sizes produced with pulsed current are smaller than those produced by galvanostatic or potentiostatic methods and are even smaller if the on time of the duty cycle is short, with a resulting dense pore nucleation and smaller pore growth. [121]

Also, a change in *frequency* has important results in the dimensions of the pores produced with discontinuous anodization. In facts, the higher the anodization frequency, the smaller the pores created. D.A. Torres-Ceròn et al. [122] tested Ti samples (ASME SB-265) in a water solution containing 8 g/L Na<sub>3</sub>PO<sub>4</sub> and 0.4 g/L NaOH using voltage pulses of 340 V for 10 minutes with a 10% duty cycle and frequencies of 1000, 1500 and 2000 Hz. Maintaining constant all the other parameters, it was seen a decreasing in the grain size approximately from 29 nm for 1000 Hz and 1500 Hz pulse frequencies until 21 nm for 2000 Hz. On the other hand, the pore surface density, number of micro-cavities per unit area, increases passing from 0.15 μm<sup>2</sup> for 1000 Hz, 0.27 μm<sup>2</sup> for 1500 Hz to 0.32 μm<sup>2</sup> for 2000 Hz. In this way, it is possible to deduce that the size of the micro-pores become smaller with increasing voltage pulse frequency in the PEO, thus the frequency controls the micro-discharges power through pulse activation time.[123] The possible explanation to this phenomenon is the shorter time of arcs discharge with high frequencies. In facts, frequency is defined as reciprocal of the time for one working cycle and the pulse on-time is shortened with frequency increasing. The shorter the pulse on-time, the less energy provided leading to weaker microdischarges with less lifetime In the bipolar pulses the more corrosion resistant layer can be explained by the sealing effect of the cathodic pulses after the anodic one. [83] Looking at even higher frequencies, i.e. 5000 Hz, but without duty cycles, Y.Wang et al [124] founded a particular surface structure of the anodized titanium. At low frequency, the film primarily consisted of rutile, anatase and hydroxyapatite. The large and small pores were relatively well separated and homogeneously distributed in the surface layer. At high frequency, the crystallinity decreased and there were many smaller pores on the wall of the larger ones and many inner pores in the film formed at high frequency. This morphology can be explained thinking that at a low frequency, such as 100 Hz, less electric breakdowns happened in a certain time, and the interval of every spark was about 10 ms, longer than the lifetime of the spark. So, the molten areas had enough time to be cooled and solidified before next pulse. But at a high frequency, such as 5000 Hz, the interval of every spark was about  $2 \times 10^{-4}$  s, less than the lifetime of the spark. So, there was not enough time for the molten areas to be cooled and solidified before next pulse. As it is known, the electrical conductivity of the TiO<sub>2</sub> increases significantly with the increase of the temperature, and the

electric breakdown often happens at the low insulating area. Secondary breakdown could happen many times in these molten areas due to the high conductivity. Many small pores were produced by the secondary breakdown in the large pores produced by the primary breakdown. So more and more small micro-pores existed in the large ones as the frequency increased,

However, it is possible to evaluate the influence of frequency and duty cycle in a combined way. The best corrosion performances were found with high frequency and duty cycle values near the 100%. [125] In fact, the high duty cycle value leads to a higher thickness due to the higher on time, while the high value of frequency causes the decrease in pore size and a more improved corrosion resistance. Gowtham et al. [125] obtain that the coating formed at 95% duty, 1000 Hz is compact, relatively smooth and deeper pores are absent, all good properties in a corrosion prevention prospective.

J.H. Wang et al. [126] studied the influence of *cumulative time of pulse width* in a single pulse voltage application. They found that the thickness of the ceramic coatings approximately linearly increases with the cumulative time of impulse width, while the single impulse width remained constant. On the other hand, single pulse energy remarkably influences the surface morphology of ceramic coating on Ti alloy. The sizes of oxide particles, micropores, and microcracks slightly increase with increasing impulse width and single pulse energy. However, the effects of single pulse energy on the micro-hardness and phase composition of ceramic coating are lesser than those of pulse frequency and duty cycle.

M.Babaei et al.[123] tried to study both the effect of frequency and *electrolyte concentration* on the layer morphology. If, on one hand, increasing the frequency the size of pores decreases, on the other, an increase of electrolyte concentration causes a change from a dense population of pores to smaller population of large-size pores uniformly distributed on the surface of the coating prepared at the same high frequency. It is observed that pore size tends to increase with increasing additive concentration. This phenomenon is associated with the decrease of electrolyte electrical resistivity when utilizing higher concentrated electrolytes. The decreasing in the electrolyte resistivity causes a higher micro discharge energy on the layer. Such strong electric sparks lead to an increased coating porosity. On the contrary, if this analysis is performed on samples treated at lower frequency, the differences are no more visible, due to the higher fluidity of the molten elements of the layer eliminates the micro discharge effect leading to a structure with large pore size.

Z.Yao et al.[127] worked on the influence of the *cathode current density* and of *cathode pulse width*. Generally speaking, cathode pulse has two main effects on the oxide layer: one is that the working electrode is under the low potential during the cathode process, which is suitable for the occurrence of some reduction reactions; therefore, it is generally

considered that the cathode process probably leads to the dissolution of some oxide phases on the coating surface, the other is that the cathode process influences the surface state of the electrode. Compared with the single-polar pulse mode, more Ti from the substrate dissolves and comes into the coating. In this way the proper cathode pulse is positive to form the coating. When the small cathode current density or cathode pulse width is applied, the positive effect of the cathode pulse is more than the negative effect. So, using the proper small cathode pulse it is possible to increase the thickness of the oxide layer, but if the cathode pulse is so strong that the destroying effect of the cathode pulse is more than the coating formation under the anode process, the thickness of the oxide layer is reduced or even the PEO process could be not occurring at all.

This kind of structure is important, for example, for the production of solar cells, photocatalysis, sensors and photonic crystals, where a highly ordered porous structure and high stability in acids are needed. Indeed, in the case of sensors, such oxide causes a change of phase by injection of a certain material into the pores, and, this change, can be detected by optical phenomena, as interference. [128]

In addition, by adjusting anodization waveforms, it is possible to modify crystallinity, colour and morphology without a subsequent heat treatment step, that otherwise would be necessary after traditional anodizing done with the same final voltage.

Another possible application for pulse anodizing is for the production of orthopedic and dental implants. Indeed, the naturally formed titanium oxide is not bioactive enough to form a bond with bone cells, because it is amorphous, while pulse anodizing allows to obtain a combination of rutile and anatase crystalline phase, that promotes the highest levels of antimicrobial effect, increases osteoblast attachment and does not adversely affect the biocompatibility. It is exactly the peculiar nanoporosity reached with this method that is beneficial for bone cell attachment and proliferation. [119]

## Chapter 3 - Materials and methods

In this work are involved mechanical, electrochemical and chemical methods for the experiment. For the superficial analysis have been used an electronic microscope, for the study of the morphology, and X-Ray diffraction, for the investigation of the oxide layer. Successively, to study the porosity, IMAGEJ, an image processing software, has been employed.

### 3.1 Original samples

The experiments have been performed on titanium grade 2, whose chemical composition and mechanical properties are listed in Table 3.1. Grade 2 is a commercially pure titanium and one of the most commonly used types.

Table 3.1 Chemical composition and mechanical characteristics of titanium grade 2.

Chemical Composition	Mechanical properties at room T
C: 0.10 max	Minimum tensile: 344 MPa
Fe: 0.30 max	Minimum yield: 276 MPa
H: 0.015 max	Hardness (Vickers): 145
N: 0.03 max	Tensile modulus: 103 GPa
O: 0.25 max	Poisson's ratio: 0.34-0.10
Ti: remaining	

Square samples of 10x10x1.6 mm have been cold-cut from a titanium grade 2 plate, to remove grease and dust an ultrasonic cleaning in ethanol has been completed in 4 minutes and then they have been rinsed in distilled water. The ultrasonic cleaning has been performed putting the samples in a beaker, filled with alcohol, in vertical position to favour the detachment of any solid debris. It is important to perform the procedure on samples with the same surface characteristics, so they have been mechanically polished with 100, 400 and 800 grit SiC papers. Samples have been held in place by a weak adhesive on a hard-aluminium holder and pressed manually against a rotating abrasive disc of abrasive paper. Surface preparation has been completed with a second ultrasonic ethanol cleaning for 5 minutes.

The values of roughness of the so-prepared samples resembles that of titanium as received from the producer, allowing to reproduce the conditions of implementation in field.

The samples prepared in this way will be referred to as “as is” (AI).

## **3.2 Surface analysis**

### **3.2.1 SEM**

A scanning electron microscope StereoScan 360 has been used to capture a magnified image of the samples in order to investigate their morphology.

### **3.2.2 XRD**

To analyse the crystallinity of the oxide layers, it has been used an X-RD technique, with a diffractometer model Phillips PW 1830, able to generate a Cu-K $\alpha$  radiation with a wavelength of 0.154 nm. This technique does not allow the measurement of absolute crystalline fraction, but it is able to determine if anatase or rutile crystalline phases are present in more than 2% fraction and, through Spurr-Meyer equation, the relative amount of each crystalline phase.

### **3.2.3 Optical microscope**

An optical microscope LEICA DL ML has been used to capture a magnified image of the samples, in order to observe the grains.

## **3.3 Analysis of porosity**

To obtain a clear image of the porosity, ImageJ, version 1.52a, has been employed. ImageJ is a Java-based image processing program developed at the National Institutes of Health and the Laboratory for Optical and Computational Instrumentation (LOCI, University of Wisconsin).

Once opened the SEM image with ImageJ, first of all, the dimension has been converted from pixel to metric, then the picture has been cropped and increasing values of threshold have been applied, in particular have been used the following values: 20, 25, 30, 35, 40, 45, 50, 60, 70, 80, 90, 100, 110, 120, 130, 140, 150 and 160. This is because the original image is in 8 bits, this means that the colours used for the pictures are  $2^8$  (256) while the software needs a binary image to be able to analyse it.

Considering the image below, a threshold of 90 has been applied, on a maximum of 256, this means that the software must consider black the first 90 shades of grey and white all the rest of the picture, then it gives back a mask in binary.

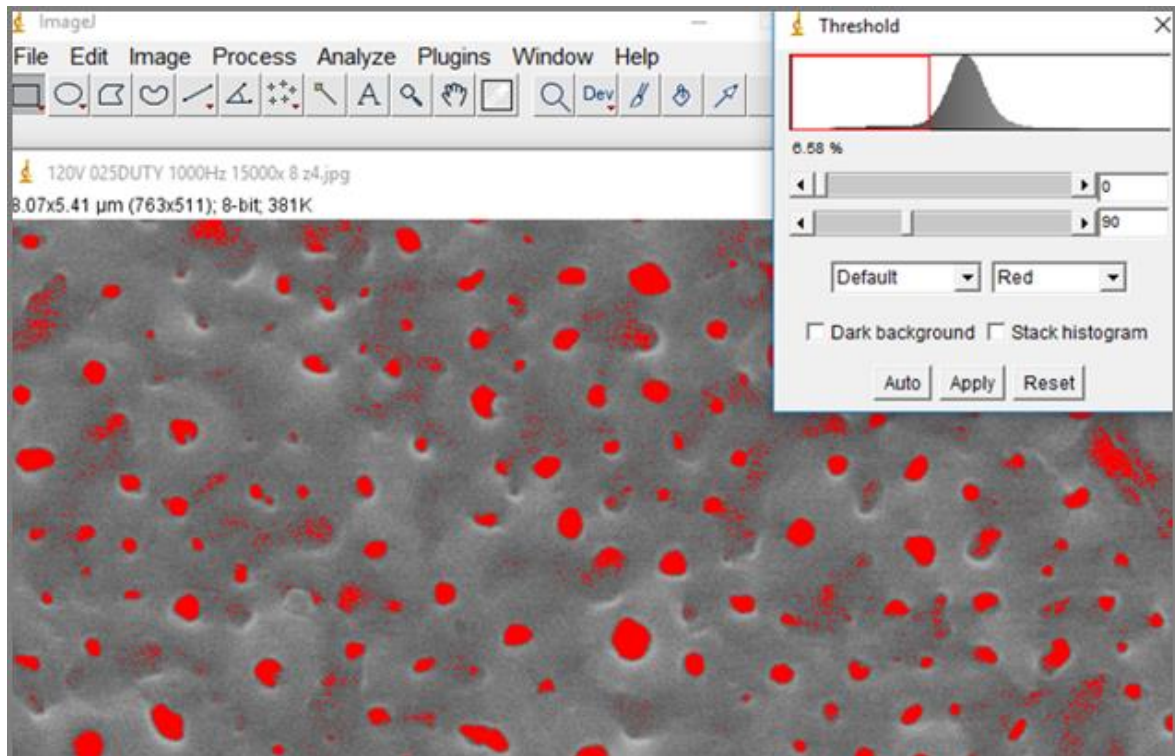


Figure 3.1 SEM picture of an anodized sample with applied a threshold of 90.

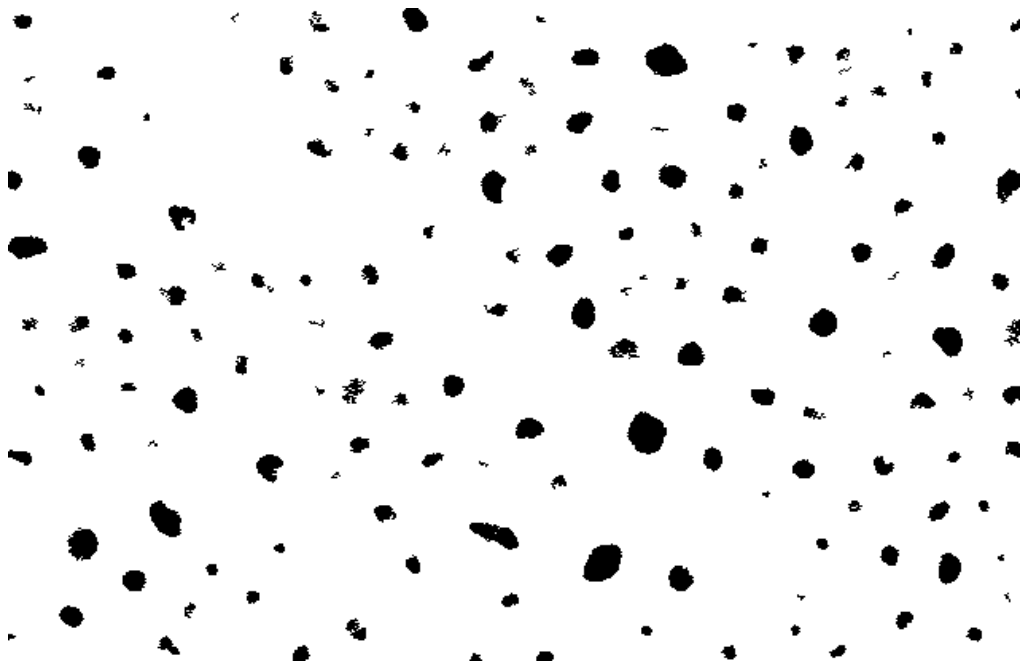


Figure 3.2 Binary mask of a sample with applied a threshold of 90.

As the threshold is increased, the program considers bigger and bigger areas of the pores, until it starts to involve also the surroundings. To solve this problem, a maximum area has to be imposed at the beginning of the analysis for each picture, so that anything bigger would be eliminated. This value is obtained by circulating the maximum visible pore and using the command analyze, the program gives back the value of its area in  $\mu\text{m}^2$ .

This process has been repeated for each value of threshold and all the masks obtained are stacked. The resulting image is, then, eroded, cutting one or two pixels, and dilated, again of one or two pixels, to de-noise the image. “Erode” and “Dilate” are filters already present in the commands of the software.

This final process allows to eliminate false pores resulting from shadow zones.

Eventually, the final negative and binary image has been superimposed to the initial one, to see the accuracy of the recognition.

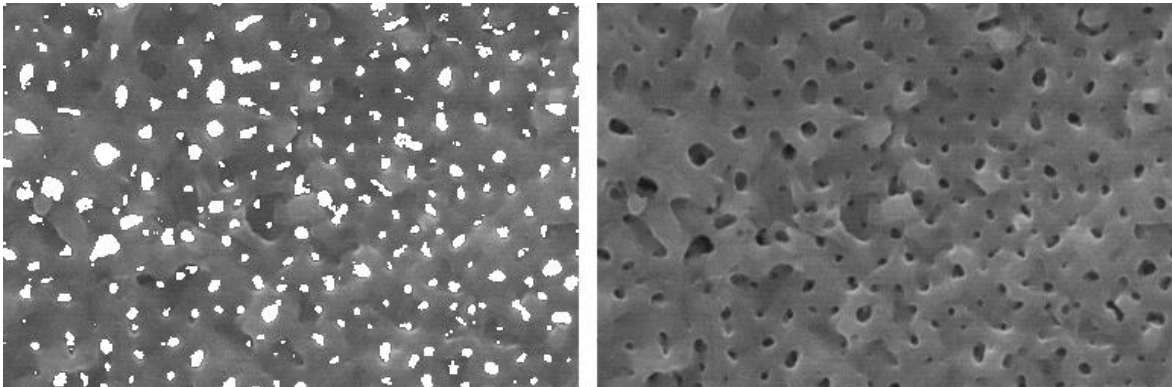


Figure 3.3 Final negative and binary image of a sample superimposed to the initial one and original image.

In addition, the procedure gives back, for each image, a table with a list of all the pores identified in the process with the dimension, that will be used for the statistical analysis.

To automatize this process, a macro, displayed below, has been created.

```

1 //-----PARAMETRI DI ANALISI-----
2 minsize = 0.001;
3 maxsize = 0.200;
4 mincirc = 0.60;
5 thresholdarray = newArray(20,25,30,35,40,45,50,60,70,80,90,100,110,120);
6 //
7 //Ottengo percorso e nome del file
8 directory = getDirectory("image");
9 name = getTitle();
10 ingrandimento = -1;
11 /* per n da 3 a 5 cerca n cifre prima di una x,
12 se le trovi esegui il codice e ricava l'ingrandimento*/
13 for (n=3;n<=5;n++)
14 {
15 if (matches(name, ".* [0-9]{n}x.*"))
16 {
17 if (indexOf(name, "x ")>=0)
18 {
19 posizionex = indexOf(name, "x ");
20 }
21 else
22 {
23 posizionex = indexOf(name, "x.");
24 }
25 ingrandimento = substring(name, posizionex-n, posizionex);
26 }
27 };
28 if (ingrandimento<0)
29 print("Nessun fattore di ingrandimento di 3-5 cifre trovato nel nome");
30 //setta la scala con l'ingrandimento trovato
31 dist = 0.0053 * ingrandimento;
32 run("Set Scale...", "distance=dist known=1 unit=um");
33 //SetTool("rectangle");
34 makeRectangle(4, 69, 636, 411);
35 run("Crop");
36 saveAs("TIFF", directory+name+" crop");
37 /* ciclo for per ogni elemento dell'array
38 applica autocontrasto, applica il threshold corrispondente
39 all'i-esimo elemento dell'array converte in una maschera
40 filtrando le particelle per dimensione e circolarità */
41 for (i=0; i<thresholdarray.length; i++){
42 j = thresholdarray[i];
43 open(directory+name+" crop"+"."+i+".tif");
44 //run("Brightness/Contrast...");
45 run("Enhance Contrast", "saturated=0.35");
46 run("Apply LUT");
47 setAutoThreshold("Default");
48 //run("Threshold...");
49 setThreshold(0, j);
50 setThreshold(0, j);
51 //setThreshold(0, j);
52 setOption("BlackBackground", false);
53 run("Convert to Mask");
54 run("Analyze Particles...", "size=minsize-maxsize circularity=mincirc-1.00
55 show=Masks display clear summarize");
56 saveAs("TIFF", directory+name+" crop"+j);
57 close();
58 close();
59 };
60 close();
61 for (i=0; i<thresholdarray.length; i++){
62 j = thresholdarray[i];
63 open(directory+name+" crop"+"."+j+".tif");
64 };
65 //Crea lo stack delle immagini ottenute con threshold
66 run("Images to Stack", "name=Stack title=[] use");
67 selectWindow("Stack");
68 run("Z Project...", "projection=[Max Intensity]");
69 selectWindow("Stack");
70 selectWindow("MAX_Stack");
71 run("Open");
72 saveAs("Tiff", directory+name+" crop"+" Stack e open");
73 //Analizzo lo stack così ottenuto e salvo i risultati in un CSV
74 run("Analyze Particles...", "size=minsize-maxsize circularity=mincirc-1.00
75 show=Nothing display clear");
76 selectWindow("Results");
77 saveAs("Measurements", directory+name+" Results.csv");
78 close();
79 close();
80 //Aprò lo stack e lo sottraggo all'immagine iniziale
81 open(directory+name+" crop"+" Stack e open.tif");
82 open(directory+name+" crop.tif");
83 selectWindow(name+" crop Stack e open.tif");
84 run("invert");
85 imageCalculator("Subtract create", name+" crop"+" Stack e open.tif", name+" crop.tif");
86 selectWindow("Result of " + name + " crop Stack e open.tif");

```

Figure 3.4 Transcription of the macro used to automatize the ImageJ process.

In the first lines can be found the main parameters: minimum size, maximum size and minimum circularity, that should be identified and modified for each SEM image. The macro, then, identifies the magnification written in the title of the image, in order to set the scale and crop the image, eliminating the data bar. After that, it creates a new image for each threshold value, stacks all the images, applies erode and dilate filters, analyses the dimension of each particle and finally creates a binary image superimposed to the original one and the table with pore dimensions listed.

## 3.4 Potentiodynamic testing

### 3.4.1 Electrolyte

In literature, [44, 129] it is reported that among all the possible halides anions, Ti suffers pitting corrosion only in bromides. This phenomenon is an effect which has been attributed to Br<sup>-</sup> adsorption at sites associated with impurity inclusions containing either Al and Si or Fe. In a previous work of the group, all the halides were tested in order to find which one was the more aggressive with respect to the titanium chemically treated.[130] Indeed, all the halides anions were introduced as sodium salts so to ensure the total independence of the corrosion resistance to the cation. The corrosion resistance behaviour of the oxide layer followed the literature indications and the sodium bromide came out as optimal aggressive solution with a concentration of 0.5 M. Starting from these results, the samples anodized with ASD process at 150 V were tested, but the improved corrosion resistance and the thicker oxide layer made the solution too weak to be used as testing corrosion agent. In fact, the potentiodynamic tests went out of scale. Being the supposed corrosion resistance of discontinuously anodically treated samples higher than the classical ASD treatment, it was necessary to find new test solution.

- *NaF*: it is reported that lower breakdown voltages have been observed in bromide and iodide solutions, whereas higher values are known for fluoride.[131] Moreover, owing to the cosmotrope character of F<sup>-</sup>, a much higher potential needs to be applied, say around 90 V/MSE, to observe an apparent breakdown before sparking.[132]
- *K<sub>3</sub>[Fe(CN)<sub>6</sub>]*: as it has been reported in the literature, no breakdown of the passive film on titanium was observed with the two redox anions hexacyanoferrate III [Fe(CN)<sub>6</sub>]<sup>3-</sup> and hexacyanoferrate II [Fe(CN)<sub>6</sub>]<sup>4-</sup>. [4, 5] However due to their oxidizing nature, ferrocyanide anions were tested.
- *FeCl<sub>3</sub>*: in literature, it has been already indicated that Br<sup>-</sup> and I<sup>-</sup> were found to be more efficient than Cl<sup>-</sup> (requiring a greater potential) for the breakdown of the passive film on titanium.[132] However, the presence of an oxidizing metal ion (i.e. Iron in this case) causes

severe pitting conditions. This severity increases following this trend: no addition > FeCl<sub>2</sub> > FeCl<sub>3</sub> > CuCl<sub>2</sub>. [134]

- *NaBr*: as already said, bromides result to be the more aggressive halides for titanium, suggesting a strong chemical interaction between the titanium oxide film surface and bromine ions. This strong corrosion aggressiveness is also linked to the nature of this anion which is chaotropic. In fact, it is reported [132] that the chaotropic anions, except the case of SCN<sup>-</sup>, allow the breakdown of passivity to be effective at relatively low or moderate potentials, whereas it is very hard or even not possible for the kosmotropic anions.

All these anions were tested also in different conditions of temperature (i.e. 25°C and 50 °C) and pH (i.e. 7 and 0) to find an effective aggressive solution.

### 3.4.2 Setup

Samples corrosion resistance to bromides containing solutions have been characterized with potentiodynamic tests performed with MetroOhm Autolab Potentiostat M204. Open circuit potential (OCP) has been recorded after 1 h of sample exposition to the testing solution with a potassium chloride saturated silver/silver chloride reference electrode (SSC). Then potential has been scanned from 100 mV below the OCP up to 8 V SSC at 20 mV/min. Anodic current and potential difference between metal and reference electrode have been registered with Nova® 2.1.1 software. Tests have been performed in 1 L cell, filled with a 0.5 M sodium bromide solution.

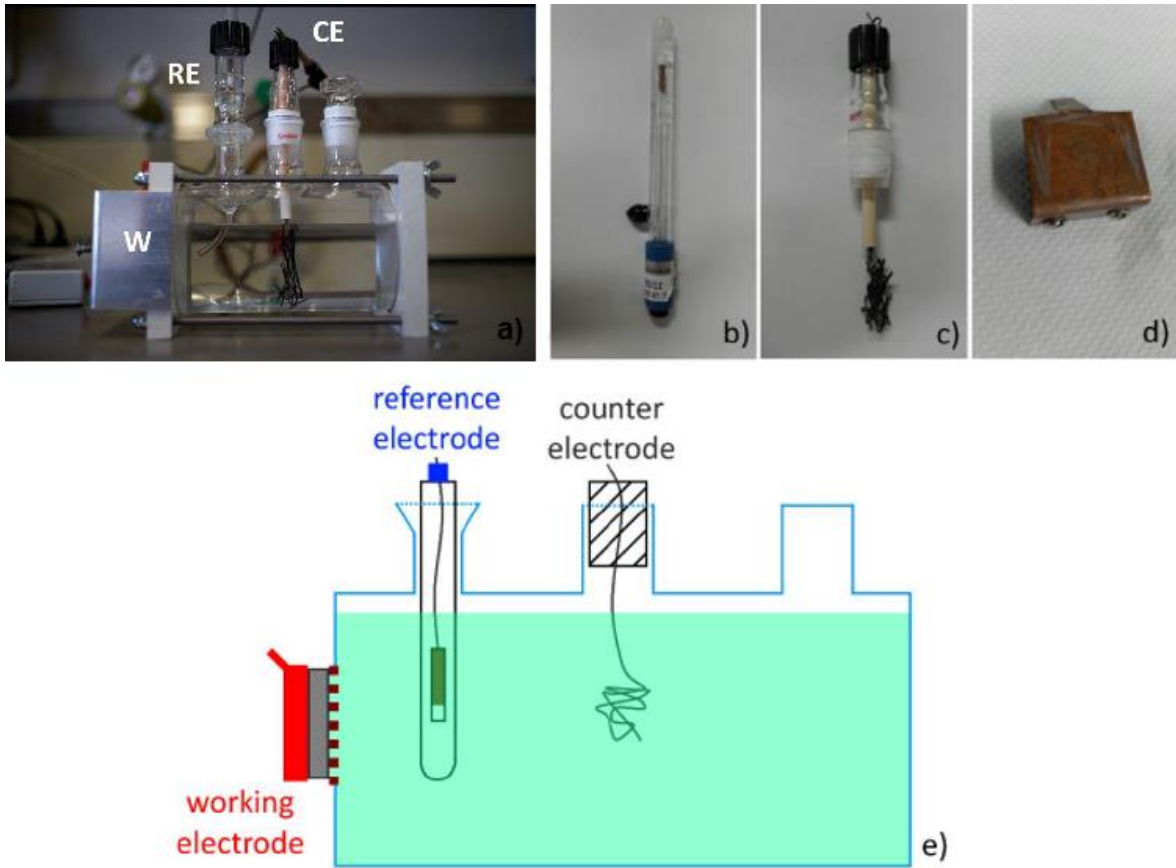


Figure 3.5 Potentiodynamic test setup. a) glass cell, b) reference electrode, c) counter electrode, d) copper contact for working electrode, e) schematics of a cell ready to work. [135]

### 3.4.3 Finalizing anodising setup

#### 3.4.3.1 Equipment

As power supply, for the anodization, has been used Asterion AST 751.



Figure 3.6 Asterion AST 751.

The maximum applicable power is 750 W and it is possible to work in different regimes: DC, AC and AC+DC. Two DC output ranges are provided, 0-250 V/0-500 V and two AC/AC+DC output ranges, 0-200 V/0-400 V with a frequency range of 16-1000 Hz. A wide range of AC and DC loads can be powered, including reactive loads (inductive and capacitive) running at full rated apparent power, and non-linear loads drawing current with high crest factor, up to 5:1.

As shown in the picture below, the instrument can work in galvanostatic or potentiostatic regime choosing from the steady state panel, the first possibility is the one of choice for this thesis work.



Figure 3.7 Steady state panel.

In the same panel it is possible to select the output mode, among AC, DC and AC+DC and then the voltage range. Depending on the voltage range selected it will affect the maximum current reachable, according to the third Ohm's Law:

$$P = VI \quad 5)$$

The maximum dispensable power is 750 W, as a consequence, when working in AC or AC+DC regime above 200 V, the maximum current is lower respect to the one allowed when working below 200 V; it is the instrument itself that evaluates the current limit depending on the range of potential set.

For this thesis work it has been necessary to work in both ranges.

Waveform generation includes standard *sine wave* and *square wave*, and extensive programmability to produce complex waveforms based on harmonics or arbitrary parameter value/time relations, for our purposes it has been created *duty cycles* at different values. A transient generator could combine sequences of voltage, frequency and wave shape to simulate real-world AC or DC disturbances and automate a complex profile of power stimulus to the unit under test.

The power analyser utilizes DSP-based digitization of output parameters to implement measurement functions spanning single parameter values (voltage/current/frequency), power characteristics (true/apparent power, crest factor, power factor), and advanced computation using fast Fourier transform (FFT) derivation of the harmonics and distortion contained in the voltage and current waveforms.

### 3.4.3.2 Testing, problems and solution

Before defining the optimal setup for the anodization, have been investigated several other options.

- The first attempt has been made following the standard procedure, that is: a square titanium plate of 20x20x1.9 mm held by a titanium tweeze, connected to the anode and immersed in 1L of sulphuric acid 0.5 M, in a glass beaker with a titanium net as cathode.

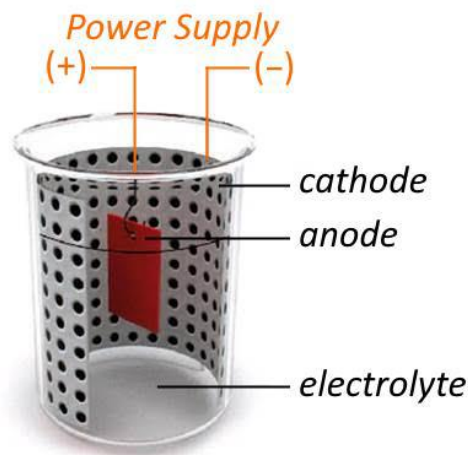


Figure 3.8 Schematics of an electrochemical cell for anodization. [13]

It has been noticed that, when the potential rose above 150 V, the current needed for a surface of 8 cm<sup>2</sup> exceeded the security value imposed by the power supply and stopped.

- Several electrolytes have been tested, to try to solve the problem: starting from sulphuric acid 0.5 M mixed with 0.4 g/L of sodium hydroxide, to other acids as phosphoric 0.5 M, to salts as ammonium sulphate, sodium hydrogen phosphate, ammonium tetrafluoroborate, ammonium phosphate, sodium sulphate and potassium sulphate (all 0.5 M). No useful results have been noticed and so it has been decided to keep using sulphuric acid, the standard electrolyte for anodization, and try to lower the necessary current by shielding one of the two faces of the sample.

- Scotch tapes as *Teflon* and *Kapton* have been applied on one side of the samples and then have been immersed in the electrolyte but the wetting caused the detachment from the surface before the reaching of the final potential.
- *Silicone* and *insulating silicon fat* have been applied on one side of the samples and left to dry the day before the test, but the wetting and the rising temperature of the electrolyte caused the detachment from the surface before reaching the final potential.
- A polymeric cell, made of PLA, has been designed and then 3D printed. The cell would have contained the sample, exposing only one face to the electrolyte, as shown in the pictures below.



Figure 3.9 Design of the polymeric cell with the sample mounted in.

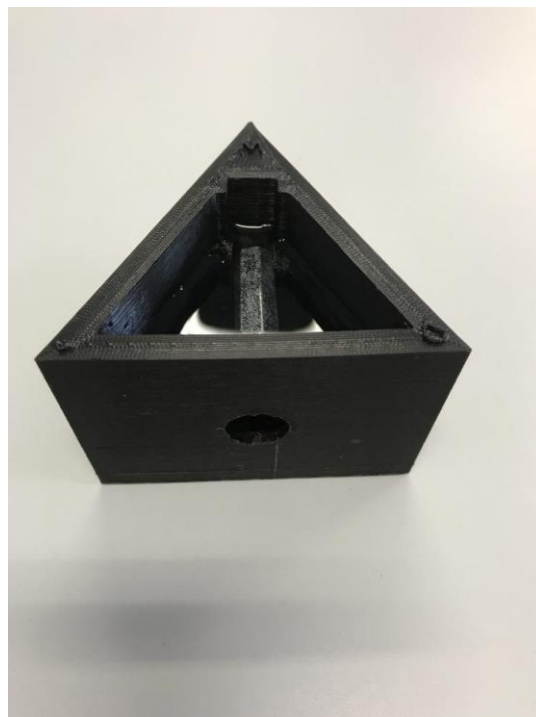


Figure 3.10 PLA cell.

An iron bolt has been used to keep the sample pressing on the o-ring and so insulating the inside of the cell from the electrolyte. After sealing the inside of the cell with silicone, it has been tried and a potential of 200 V has been reached but, when the sample has been taken off, a crevice corrosion has been found on it, in correspondence of the o-ring. A flat o-ring has been used, creating a new cell with a slot for it, but with this new solution, the electrolyte permeated inside the cell corroding the bolt and causing an electric fault. Beside this problem, the increasing temperature of the system, when around 200 V, caused the o-ring to melt and stick to the cell, making it impossible to be used again.

- Considering that the main problem was the spike of current when starting a cycle, a new shape of the wavefunction has been created. To reach the potential set, a ramp has been included, instead of an abrupt step.

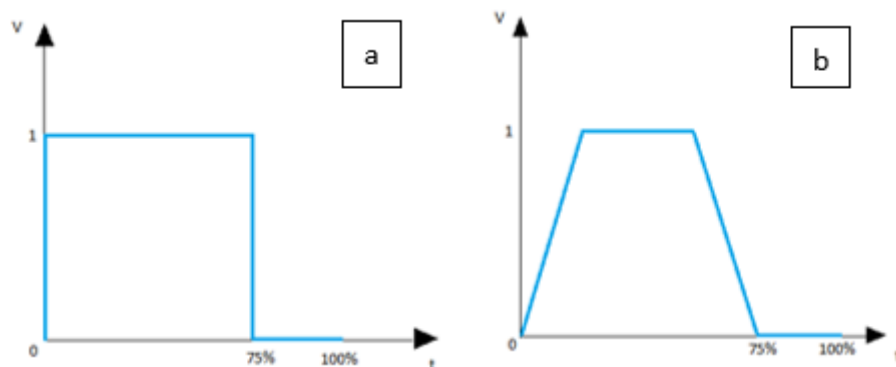


Figure 3.11 a) Abrupt duty cycle and b) duty cycle with ramp.

This solution helped to get a lower spike of current, even with a surface of 8 cm<sup>2</sup>, but not enough to reach the potential of interest.

The final adopted solution, to keep the spikes of current under control, has been to use smaller samples, of 10x10x1.9 mm, so that it was no more necessary to shield one face and it was possible to use the standard anodization method depicted in Fig. 3.8, and duty cycles with a ramp. This solution made necessary to customize also the cell for the potentiodynamic test, as the area for the corrosion test has been shrunk.

# Chapter 4 – Results

## 4.1 Material characterization results

### 4.1.1 Superficial roughness

Three of the samples, immediately after polishing, each with a different value of SiC paper, have been analysed in terms of superficial roughness and the results are reported in the tables below.

The parameters reported for each sample are:

- **Average maximum profile peak height  $R_{PM}$** , that is the average of the successive values of maximum profile peak heights calculated over the evaluation length.
- **Roughness average  $R_A$** , that is the arithmetic average of the absolute values of the profile heights over the evaluation length.
- **Average maximum height of the profile  $R_{ZDIN}$** , that is the average of the successive values of  $R_{TI}$  (maximum heights within a sampling length) calculated over five sampling lengths within the evaluation length.

Besides  $R_A$ , that is hardly affected by the individual peaks or valleys being the mean value of the whole profile, the other two parameters chosen are reported to express an idea of the shape of the profile.  $R_{ZDIN}$ , in fact, represents the distance between the average line crossing the five highest peaks and the average line crossing the five lowest valleys.  $R_{PM}$ , being the average distance between the highest points of the evaluation lengths and the mean line, displays a further image of the deviation from the average.

Table 4.1 Superficial roughness results in  $\mu\text{m}$  of the sample polished with a 320 grit SiC paper.

SAMPLE n° 1	
$R_{pm}$	1.091
$R_a$	0.266
$R_{zdin}$	2.052

Table 4.2 Superficial roughness results in  $\mu\text{m}$  of the sample polished with a 600 grit SiC paper.

SAMPLE n° 2	
$R_{pm}$	0.842

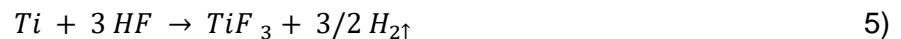
$R_a$	0.198
$R_{z\text{din}}$	1.550

Table 4.3 Superficial roughness results in  $\mu\text{m}$  of the sample polished with a 1200 grit SiC paper.

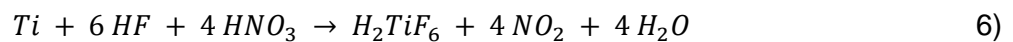
SAMPLE n° 3	
$R_{pm}$	0.998
$R_a$	0.336
$R_{z\text{din}}$	2.084

### 4.1.2 Metallurgy test results

In order to be observed at the optical microscope, some of the titanium samples have been chemically attacked by an acid solution to increase the appearance of grain boundaries and observe the phases. By changing the dimension of the grains, it is possible to change also the pitting potential in potentiodynamic tests [90]. The solution used would corrode uniformly the surface of the sample, following the reaction below, for this reason it should contain fluoride ions.



The most effective one, as reported in the literature [91, 92] is the **Kroll's solution**, whose composition is 2 mL HF, 4 mL HNO<sub>3</sub>, 94 mL H<sub>2</sub>O [91], and it works following the reaction:



Nitric acid has been added in order to dilute the solution and decrease its dangerousness, but also to stabilize it and increase the corrosion rate.

Depending on the duration of the attack it is possible to obtain a better contrast or a more detailed image; in fact, the shorter times reveal more detail, while longer etching times result in more contrast. As etching time increases, indeed, the details result lost in the contrast [91]. It must be noted, in addition, that longer expositions cause an excessive corrosion of the samples. Micrographies of samples attacked by the Kroll's solution with different etching durations are shown in Fig. 4.1, 4.2, 4.3, 4.4, 4.5 and 4.6.

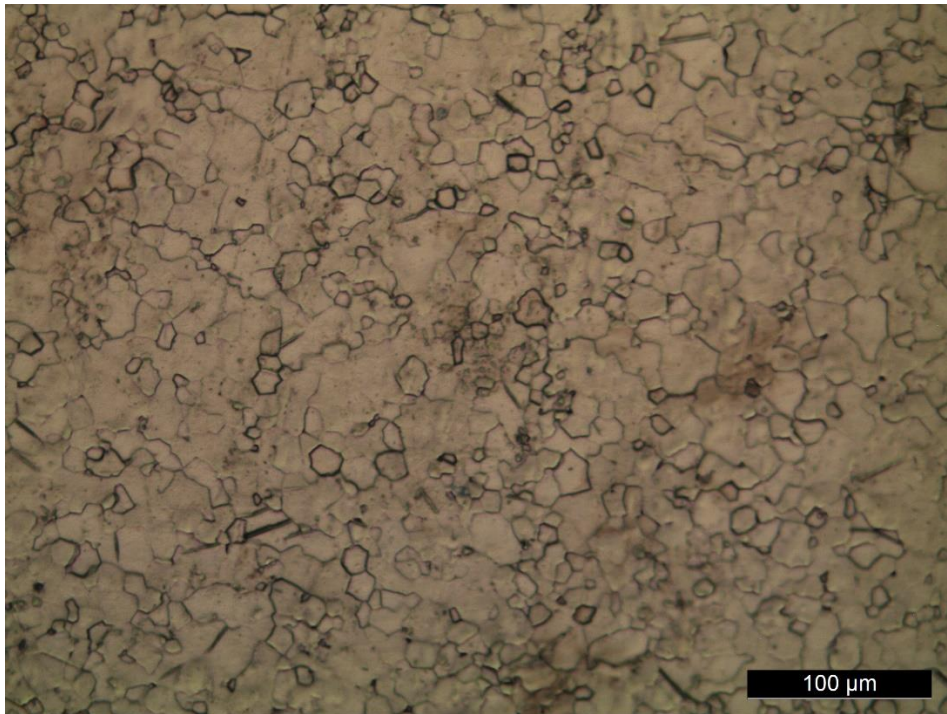


Figure 4.1 CP titanium sample exposed to Kroll's solution at room temperature for 45 seconds.

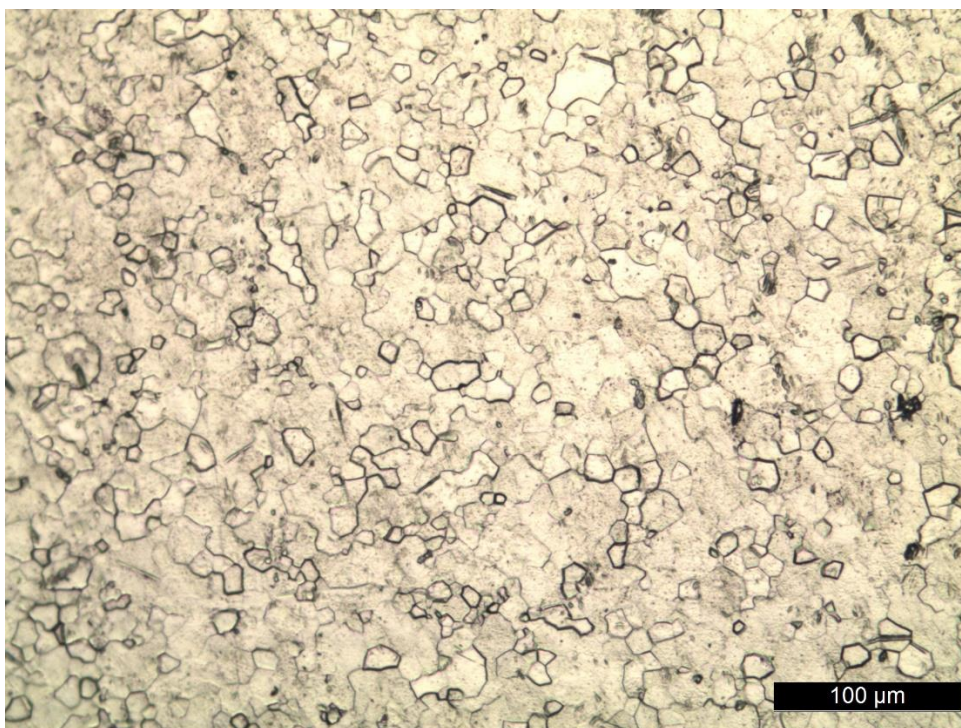
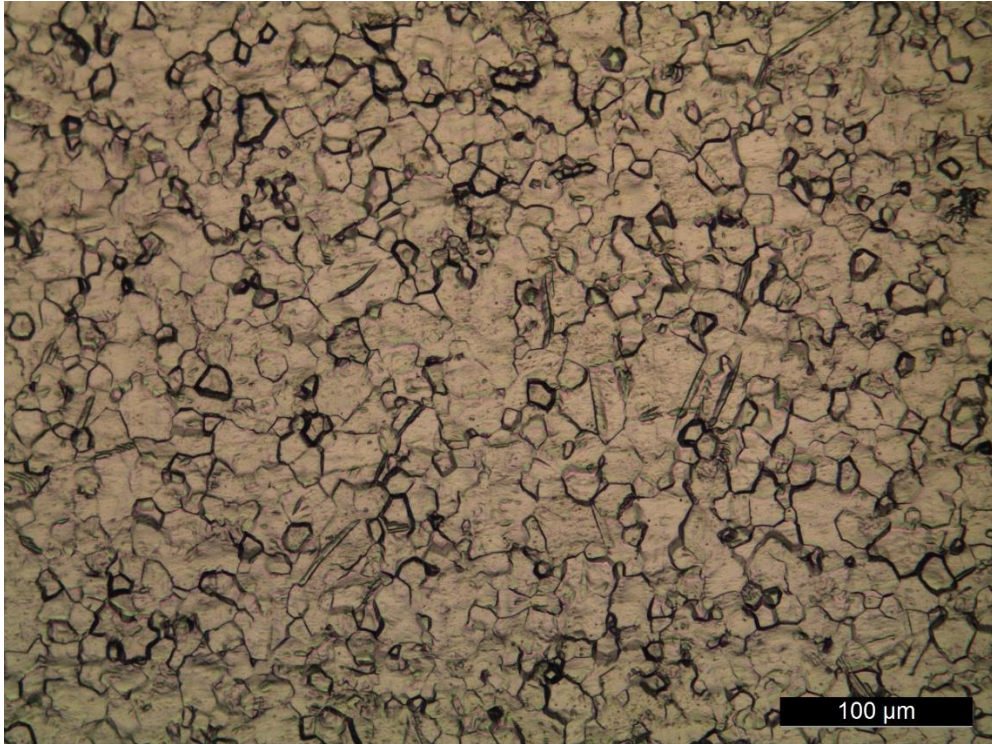
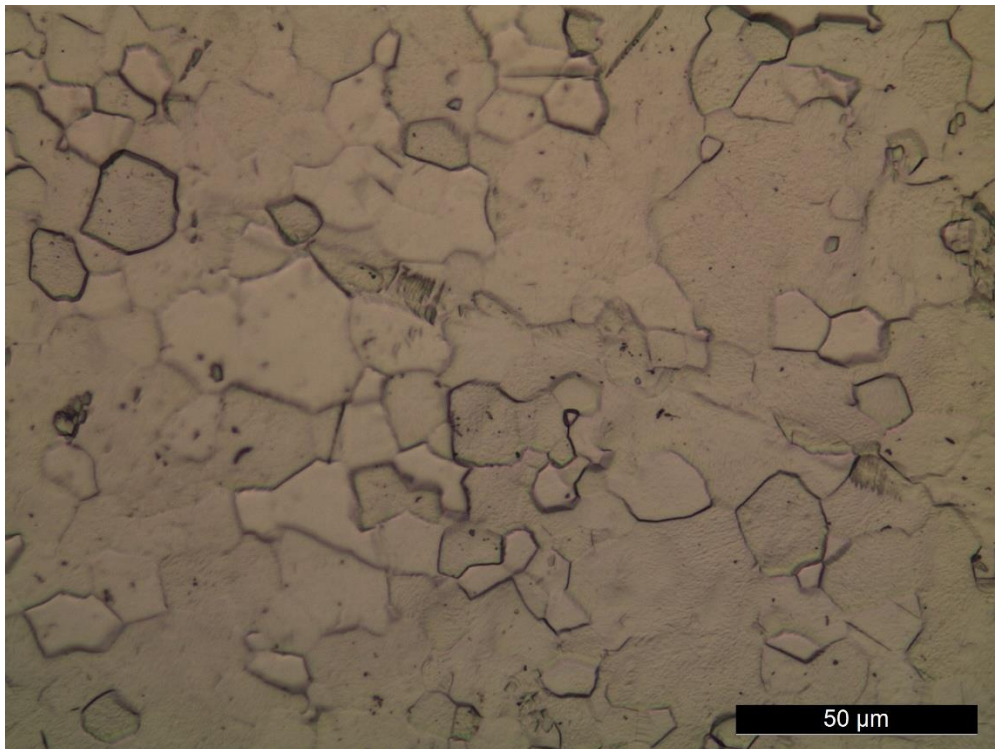


Figure 4.2 CP titanium sample exposed to Kroll's solution at room temperature for 60 seconds.



*Figure 4.3 CP titanium sample exposed to Kroll's solution at room temperature for 75 seconds.*



*Figure 4.4 CP titanium sample exposed to Kroll's solution at room temperature for 45 seconds.*

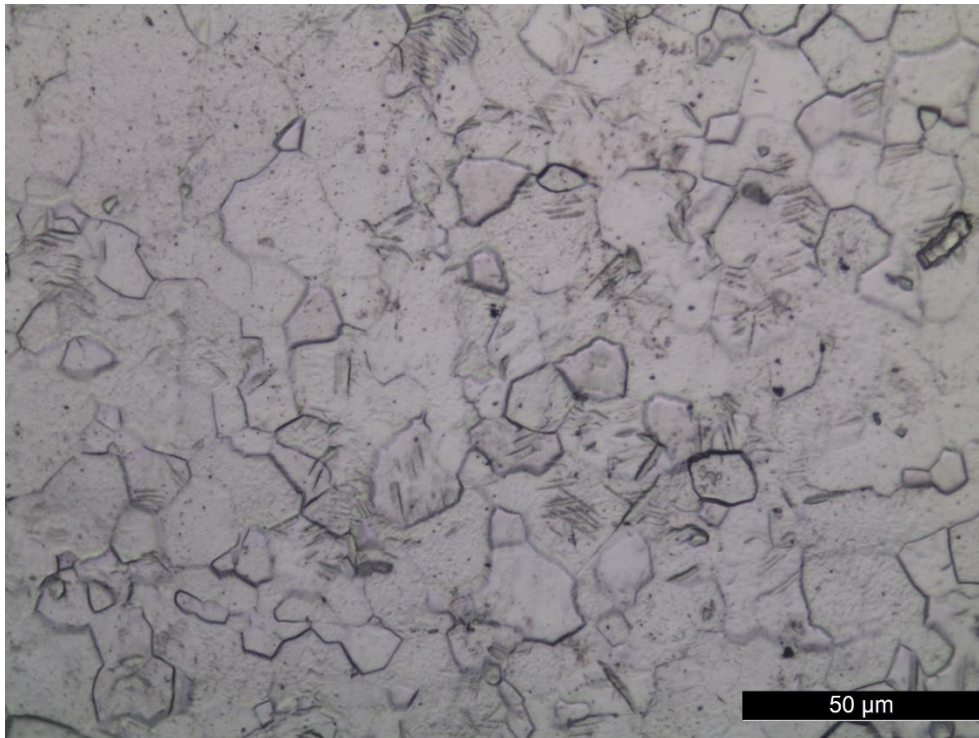


*Figure 4.5 CP titanium sample exposed to Kroll's solution at room temperature for 60 seconds.*

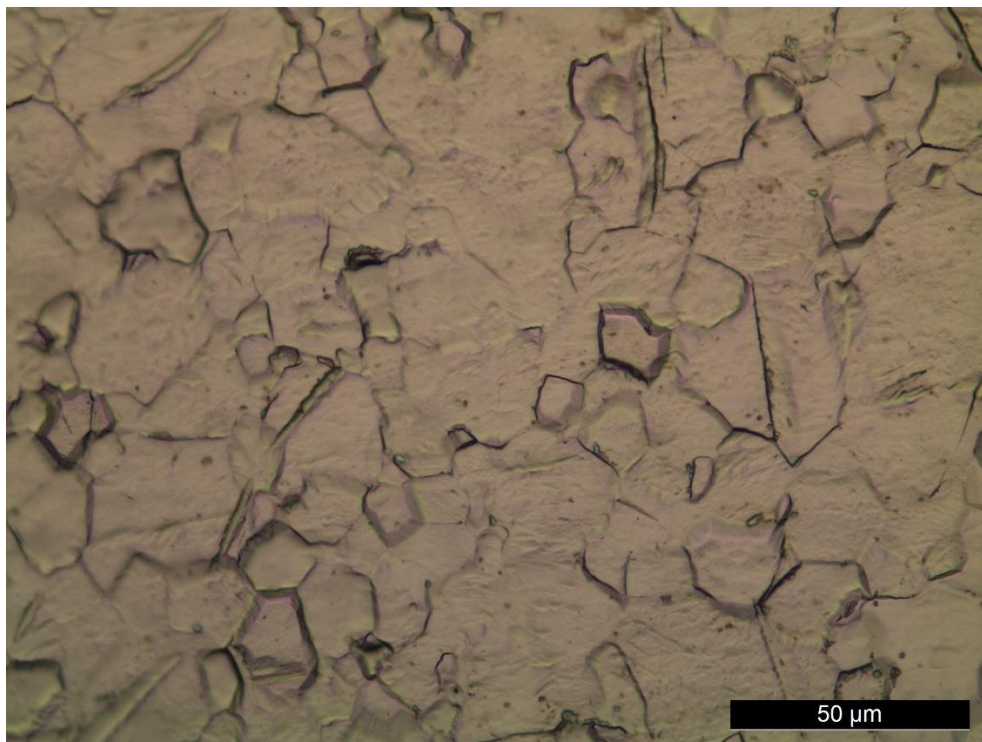


*Figure 4.6 CP titanium sample exposed to Kroll's solution at room temperature for 75 seconds.*

Observing the grains at in Figures 4.1,4.2 and 4.3, it can be noted that the alpha grains are mixed to beta grains, while in Figures 4.4, 4.5 and 4.6, at a higher magnification, alpha lamellas can be observed inside the beta grains.

The images obtained have been analysed with ImageJ and the results are reported in the table below.

*Table 4.4 Analysis of grain dimensions, areas in  $\mu\text{m}^2$ .*

Duration of acid attack	45 seconds	75 seconds
<b>Average</b>	134.8	125.1
<b>Standard Deviation</b>	87.1	76.5
<b>Minimum</b>	30.1	39.9
<b>Maximum</b>	351.7	348.4

## **4.2 Test electrolyte**

As reported in paragraph 3.4.1, titanium suffers pitting corrosion only in bromides and the optimal aggressive solution found is sodium bromide in a concentration of 0.5 M. However, the improving corrosion resistance shown by the anodized samples required a stronger corrosive agent. For this reason, the possible electrolytes were tested in different conditions: first different concentrations, then different temperatures and pH.

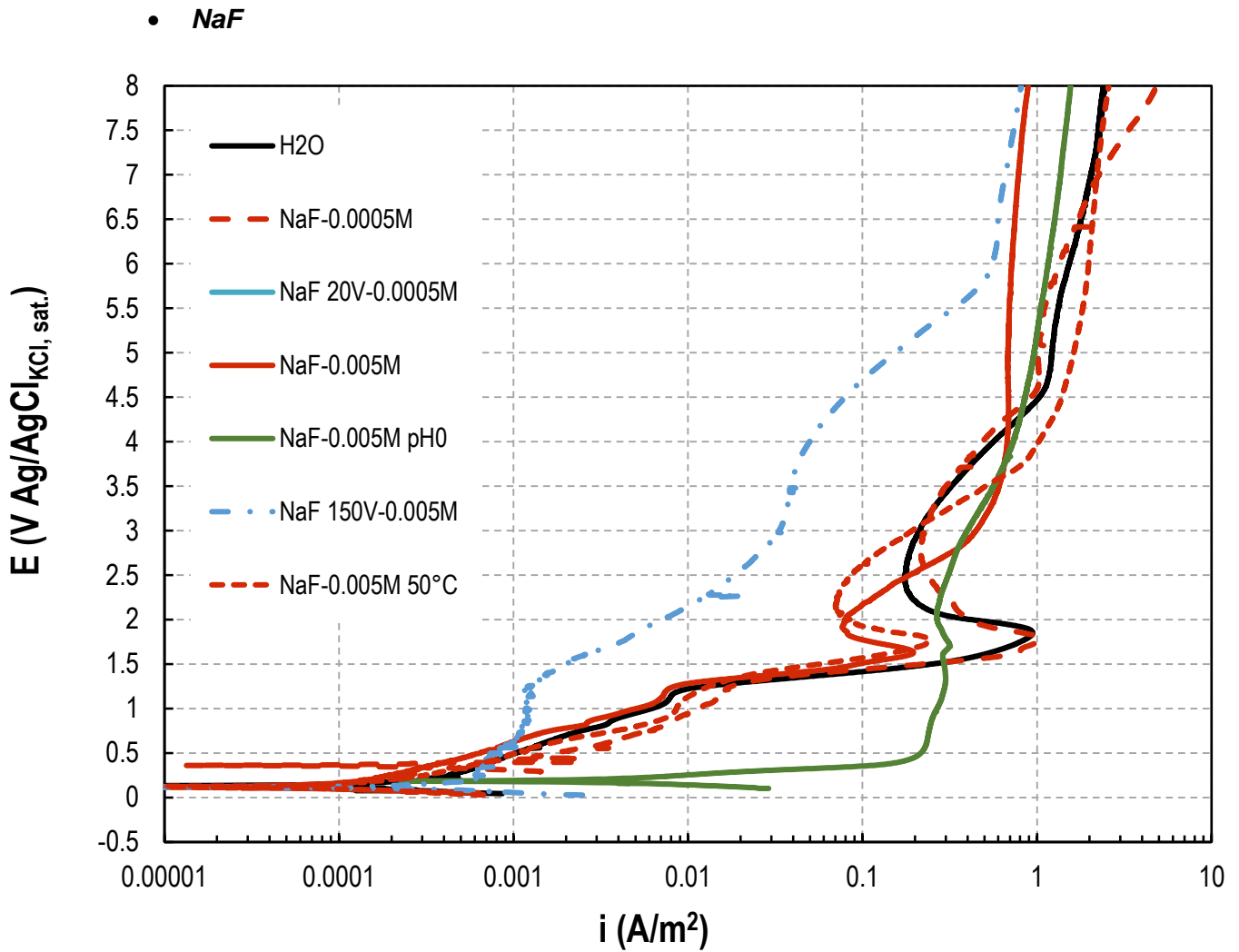


Figure 4.7 Potentiodynamic curves of samples anodized at 20 V and 150 V and tested in NaF at different molarities, temperatures and pH.

As can be noted from the potentiodynamic tests, NaF exhibits a strong aggressiveness on titanium, but it results in an active behaviour of the metal with high current densities with no pitting in all the tested conditions. Increasing temperature, an increase in corrosion rate with higher current densities is visible. Moreover, a decrease in pH, going toward a very acid pH (i.e. 0), causes an increase in the aggressiveness. However, an anodization treatment of 150 V or even of 20 V decreases strongly the corrosion rate. For these reasons, the NaF is not suitable to discriminate between samples with different corrosion.

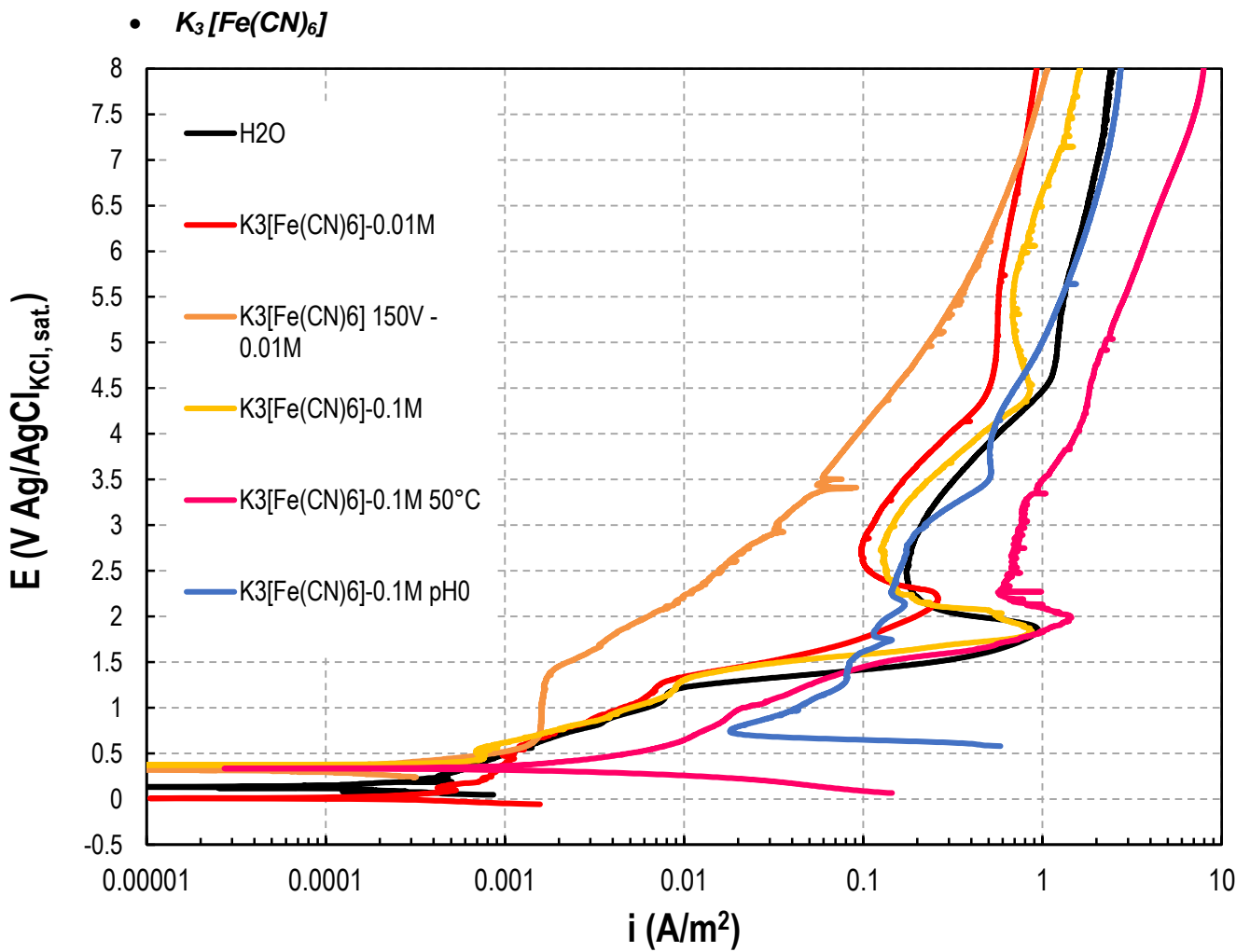


Figure 4.8 Potentiodynamic curves of samples anodized at 150 V and tested in  $K_3[Fe(CN)_6]$ .

As in the case of fluorides, also ferrocyanides cause an aggressive attack on the titanium surface with high current densities, but no pitting is present. Increasing temperature, it is possible to see a noticeable increasing in the corrosion rate. An acidic pH causes an increasing in the aggressiveness of the solution, with a really active metallic surface.

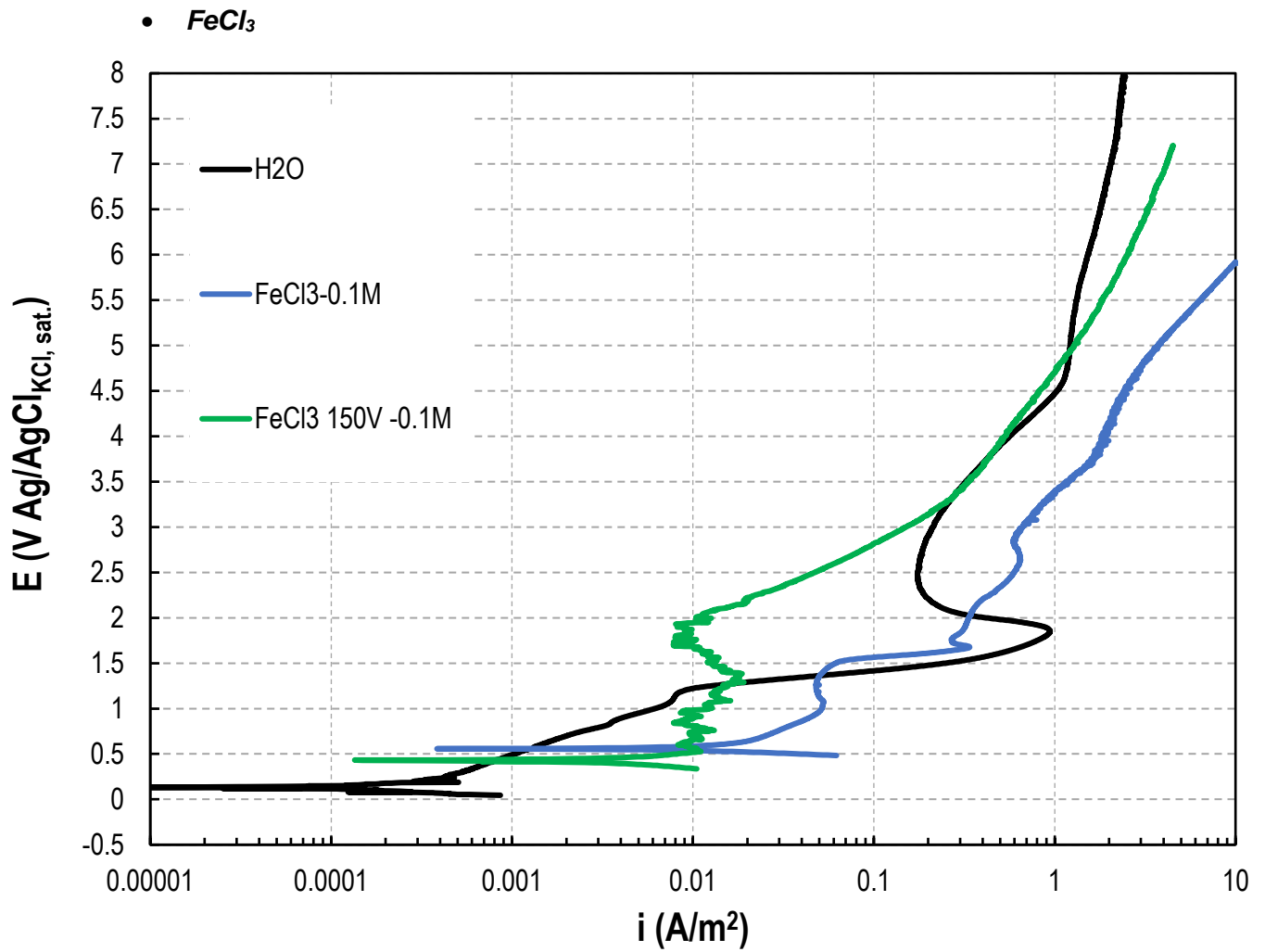


Figure 4.9 Potentiodynamic curves of samples anodized at 150 V and tested in  $FeCl_3$ .

The electrolyte containing  $FeCl_3$  does not exhibit any tendency to pitting corrosion, even if the metal surface is active with high current densities, even at room temperature. Applied to the anodized sample, the corrosion rate is still very high, but with no localized corrosion.

- **NaBr**

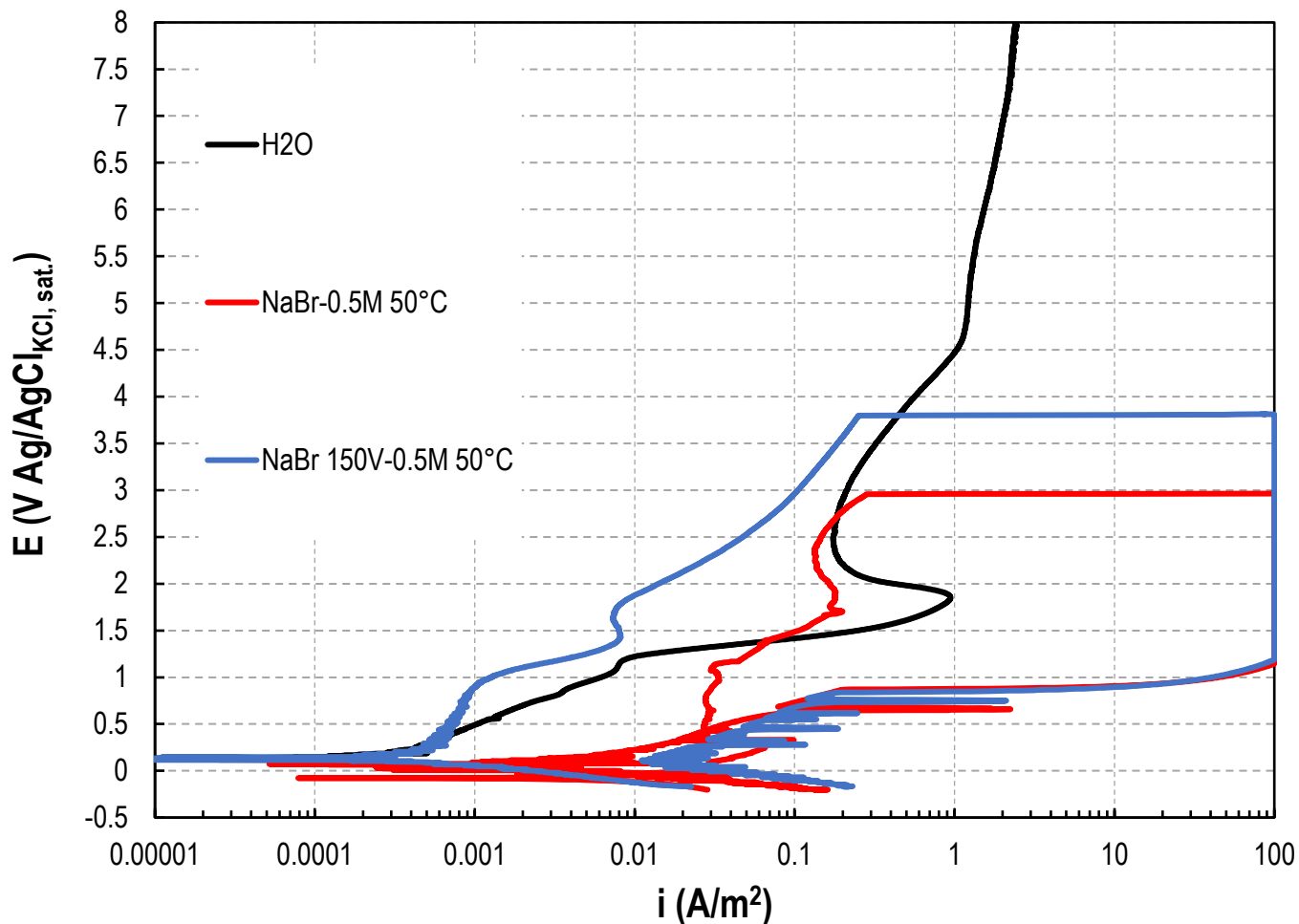


Figure 4.10 Potentiodynamic curves of samples anodized at 150 V and tested in NaBr.

Being NaBr already tested [130] as electrolyte for titanium corrosion with an optimal concentration of 0.5 M, in these tests the electrolyte was used in a more aggressive condition to reach a more effective corrosion behaviour. In fact, the electrolyte alone was not able to dissolve the oxide layer formed during the anodization of titanium. Increasing the temperature, it is possible to obtain conditions so that the pitting corrosion is present, even with anodized samples.

For this reason, NaBr at a temperature of 50°C has been chosen as electrolyte of the potentiodynamic tests.

## 4.3 Anodizing

### 4.3.1 Test details

Al samples have been anodized with the method described in paragraph 3.4.3 and the details of the experiments performed are reported in the table below. All the tests have been performed with a growing ramp of the potential of 0.5 V/s.

Table 4.5 Experiments performed.

Waveform	Voltage (V)	Freq. (Hz)	$i_{peak}$ (A)	$i_{plateau}$ (A)	$\Delta T(^{\circ}C)$
DC	220	-	-	2.4	9
DC	160	-	-	0.8	2
DC	120	-	-	0.36	0
Duty 25%	220	1000	6	6	7
Duty 25%	160	1000	4.5	3	2
Duty 25%	120	1000	2.8	1.7	2
Duty 25%	220	20	7	7	8
Duty 25%	160	20	3	2.4	0
Duty 25%	120	20	1.4	0.6	0
Duty 75%	220	1000	6.5	4.6	4
Duty 75%	160	1000	3.4	1.3	3
Duty 75%	120	1000	2	0.4	0
Duty 75%	220	20	2	1.4	14
Duty 75%	160	20	1.8	0.7	0
Duty 75%	120	20	1.2	0.6	0
DC	220	-	-	2.4	14
DC	160	-	-	0.8	2
DC	120	-	-	0.36	0
Duty 25%	220	1000	6	6	3
Duty 25%	160	1000	4.5	3	0
Duty 25%	120	1000	2.8	1.7	0
Duty 25%	220	20	7	7	7
Duty 25%	160	20	3	2.4	1
Duty 25%	120	20	1.4	0.6	1
Duty 75%	220	1000	6.5	4.6	16
Duty 75%	160	1000	3.4	1.2	1
Duty 75%	120	1000	2	0.4	2

<b>Duty 75%</b>	220	20	2	1.4	8
<b>Duty 75%</b>	160	20	1.8	0.7	0
<b>Duty 75%</b>	120	20	1.2	0.6	0

### 4.3.2 Surface morphology

All the samples have been observed at the SEM, taking, for each one, more than one picture in a different zone and the porosity has been investigated with ImageJ.

Below are reported some of the above-mentioned pictures.

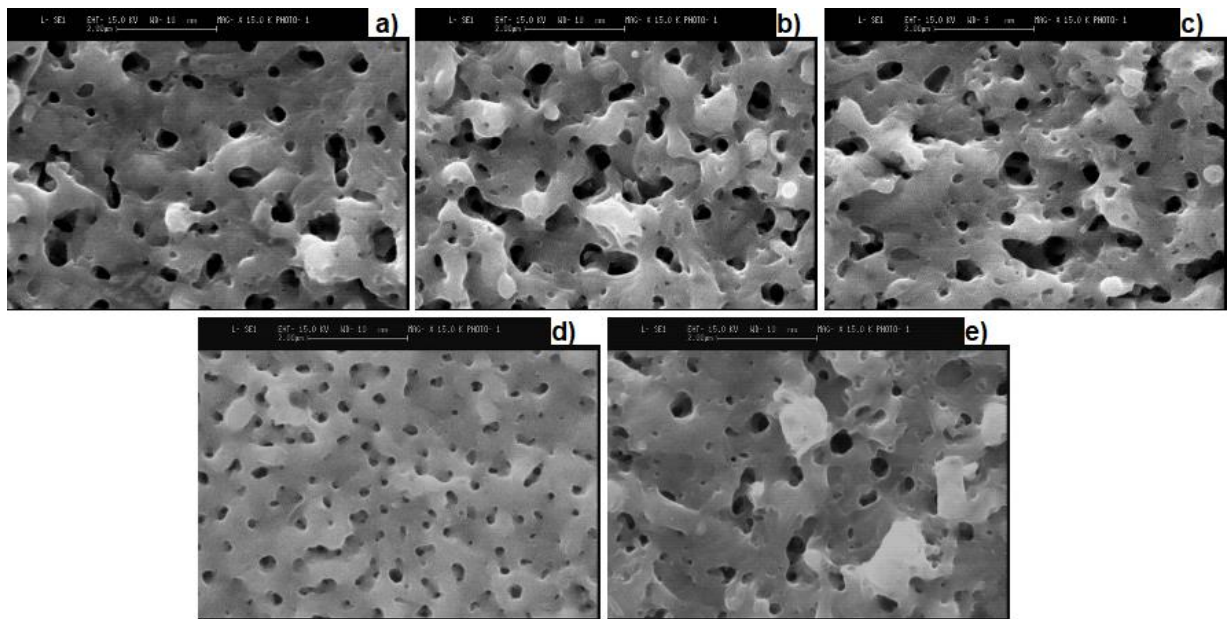


Figure 4.11 SEM pictures of the samples anodized at a final voltage of **220 V** and a) Duty cycle 25% 20 Hz, b) Duty cycle 25% 1000 Hz, c) Duty cycle 75% 20 Hz, d) Duty cycle 75% 1000 Hz and e) DC

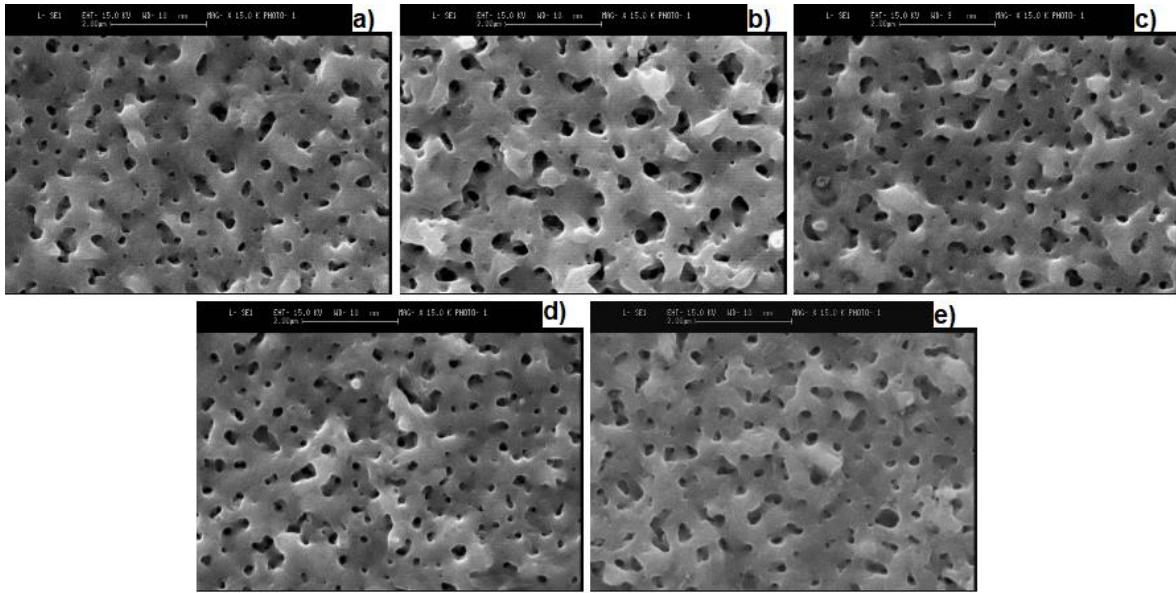


Figure 4.12 SEM pictures of the samples anodized at a final voltage of **160 V** and a) Duty cycle 25% 20 Hz, b) Duty cycle 25% 1000 Hz, c) Duty cycle 75% 20 Hz, d) Duty cycle 75% 1000 Hz and e) DC.

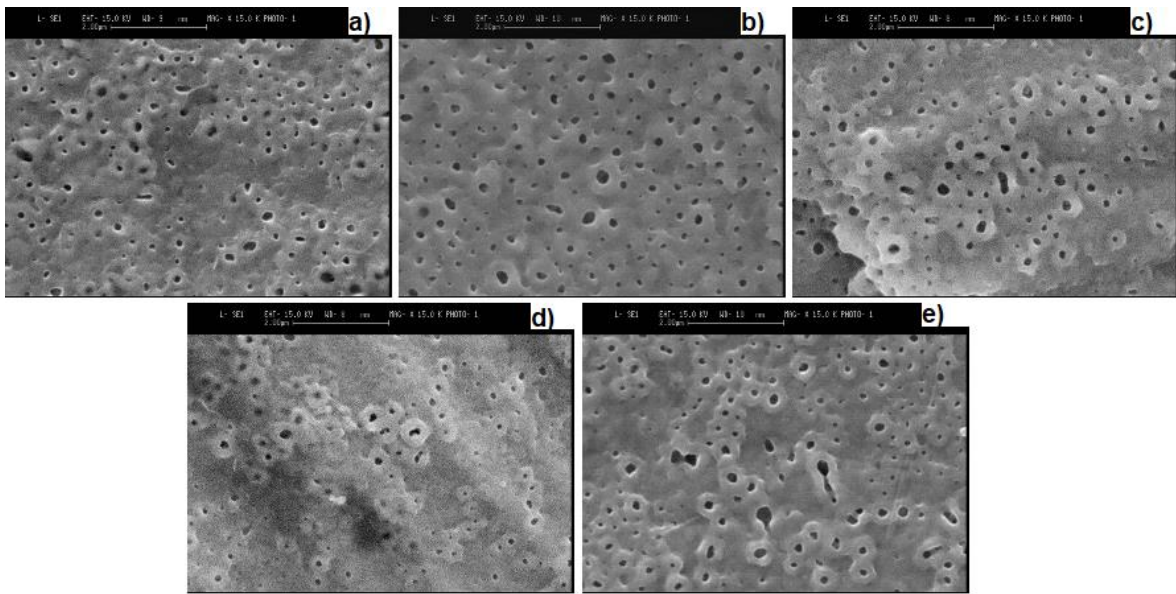


Figure 4.13 SEM pictures of the samples anodized at a final voltage of **120 V** and a) Duty cycle 25% 20 Hz, b) Duty cycle 25% 1000 Hz, c) Duty cycle 75% 20 Hz, d) Duty cycle 75% 1000 Hz and e) DC.

### 4.3.3 Samples crystallinity

The composition of the oxide layer has been studied through the XRD analysis. It is known that the peaks of the anatase and rutile crystalline phases are identified with the angles  $2\theta = 25.5$  and  $2\theta = 27.5$  respectively. The analysis has been performed varying the three main variables of the process, i.e. voltage, duty cycle and frequency, in order to understand the effect of each of them on the oxide. Due to the complexity of the three dimensions dependence problem, the results will be presented below, fixing two variables and changing only one.

- *Change in voltage with constant duty and frequency*

The first comparison is performed between the samples anodized with frequency equal to zero and direct current.

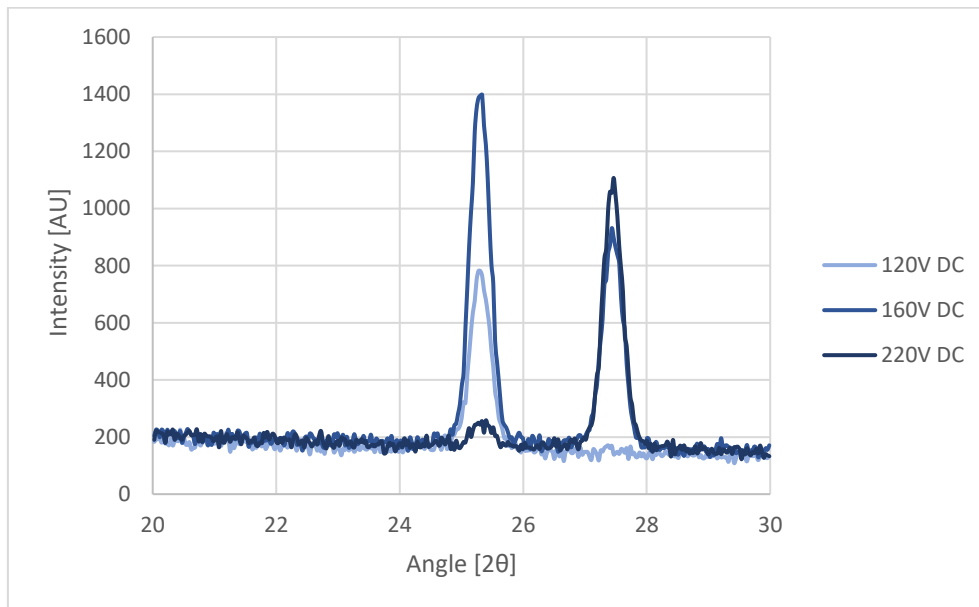


Figure 4.14 XRD analysis of anodized titanium at 120 V, 160 V and 220 V in DC.

The second comparison is performed between the samples anodized with a duty cycle of 25% and a frequency of 20 Hz at 120 V, 160 V and 220 V.

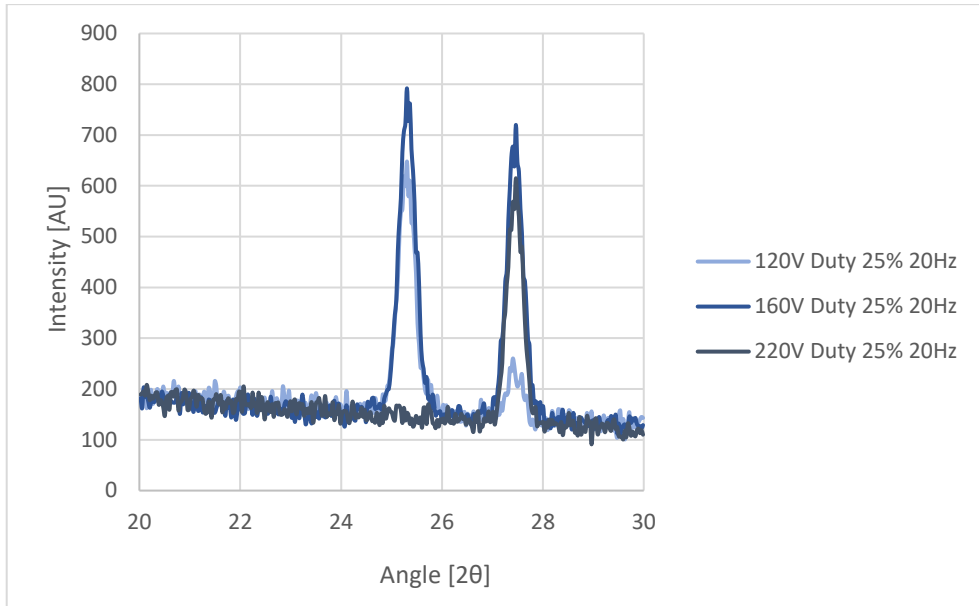


Figure 4.15 XRD analysis of titanium anodized with a duty cycle of 25% and a frequency of 20 Hz at 120 V, 160 V and 220 V.

The third comparison is between samples anodized with a 25% duty cycle and a frequency of 1000 Hz at 120 V, 160 V and 220 V.

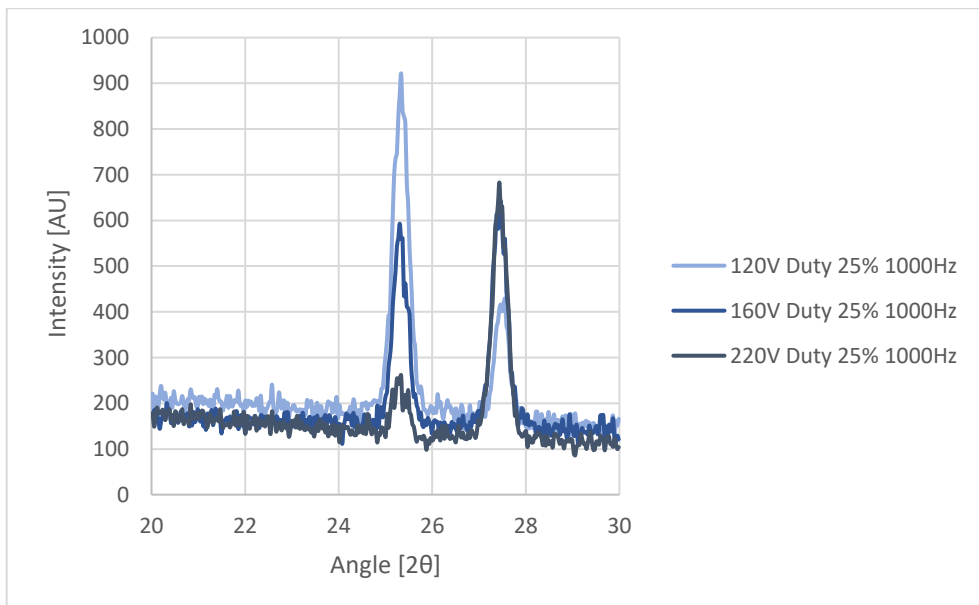


Figure 4.16 XRD analysis of titanium anodized with a duty cycle 25% and a frequency 1000Hz at 120 V, 160 V and 220 V.

Increasing the duty cycle percentage, it is possible to compare the last two groups of anodization with a duty cycle of 75% and frequencies of 20 Hz and 1000 Hz for the fourth and the fifth groups respectively.

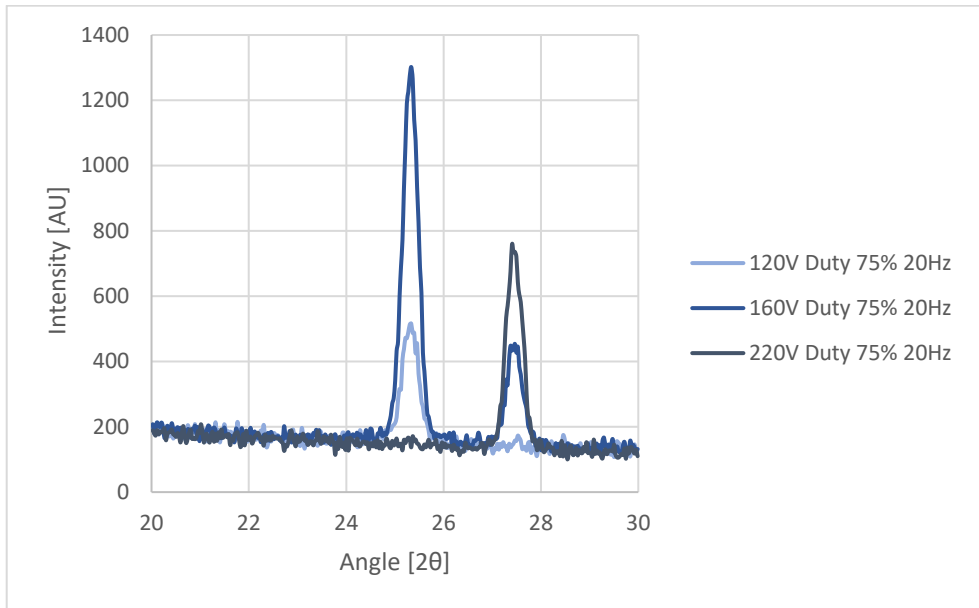


Figure 4.17 XRD analysis of titanium anodized with a duty cycle 75% and a frequency 20Hz at 120 V, 160 V and 220 V.

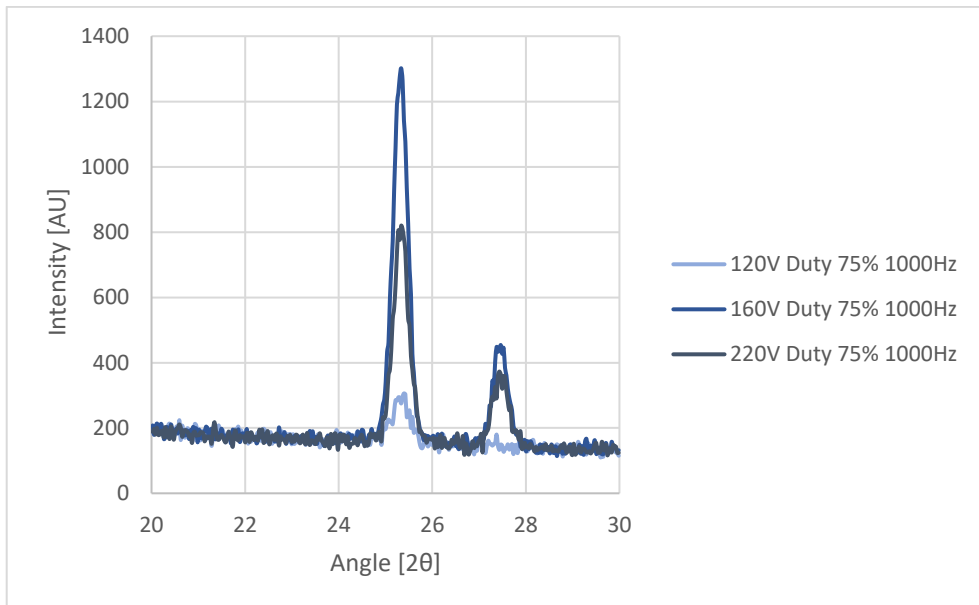
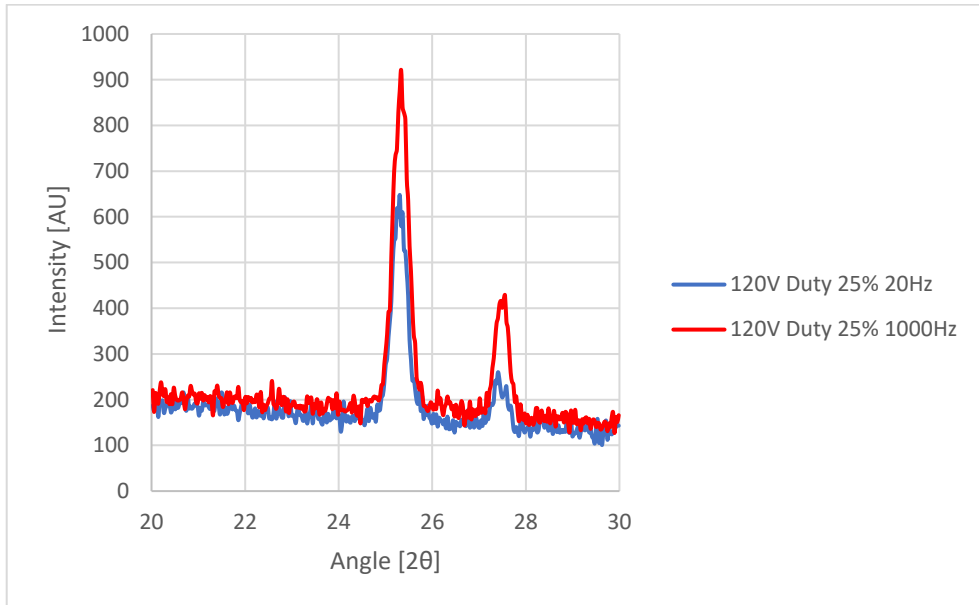


Figure 4.18 XRD analysis of titanium anodized with a duty cycle 75% and a frequency 1000Hz at 120 V, 160 V and 220 V.

- *Change in frequency with constant duty and voltage*

In the first group are collected all the sample anodized at a voltage of 120 V and a duty cycle of 25%.



*Figure 4.19 XRD analysis of titanium anodized with a duty cycle 25% and at 120 V with 1000 Hz and 20 Hz.*

In the second group are collected the samples anodized with a voltage of 160 V and a duty cycle of 25%.

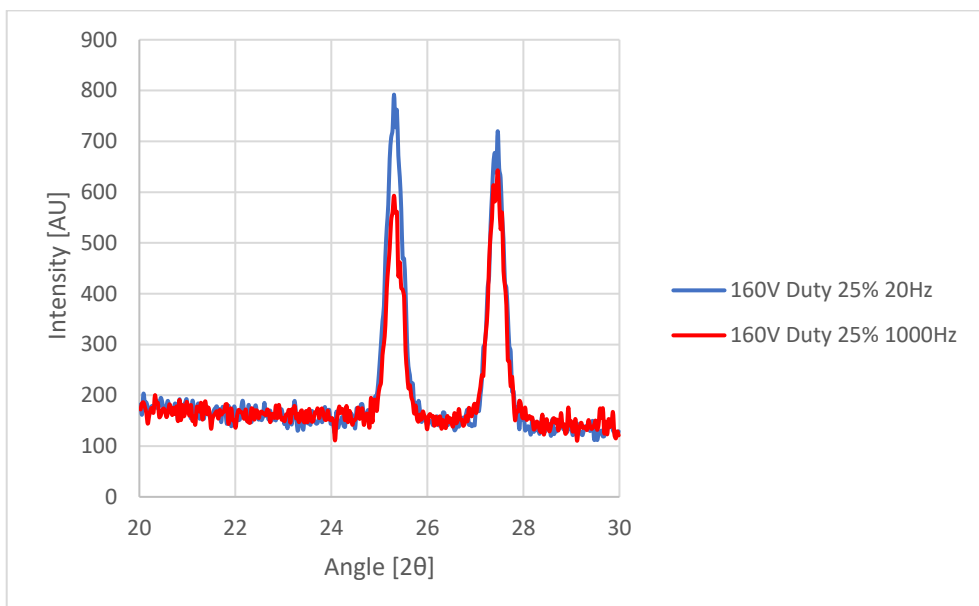


*Figure 4.20 XRD analysis of titanium anodized with a duty cycle 25% and at 160 V with 1000 Hz and 20 Hz.*

In the third group the samples anodized at 220 V and 25% of duty cycle, but at different frequencies.

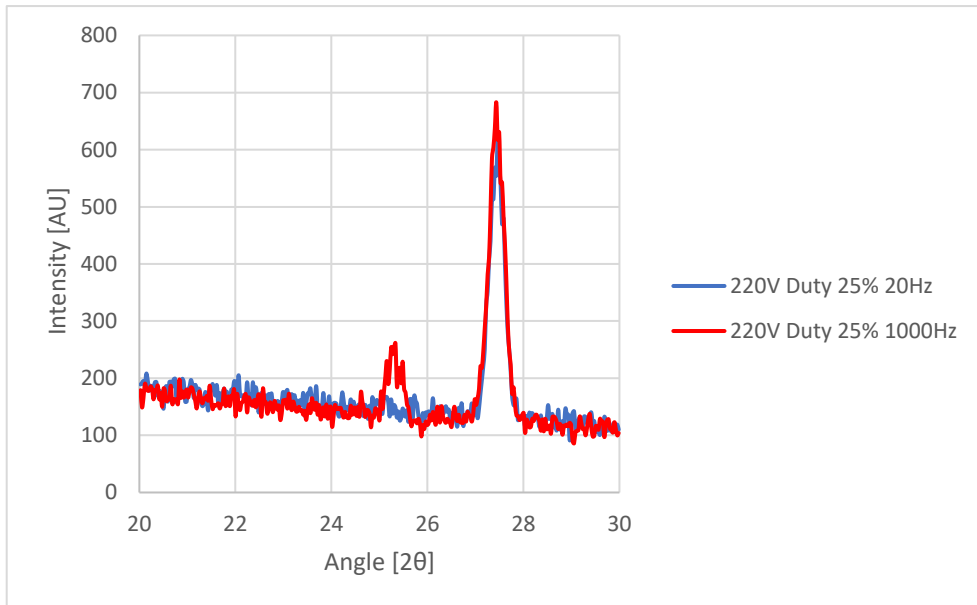


Figure 4.21 XRD analysis of titanium anodized with a duty cycle 25% and at 220 V with 1000 Hz and 20 Hz.

With this graph, all the samples anodized with a duty cycle of 25% have been shown. In the next pages there are all the sample anodized with a duty of 75%.

This is the first group of the sample anodized with a duty cycle of 75%. The voltage used is 120 V and the effects of the frequency are compared.

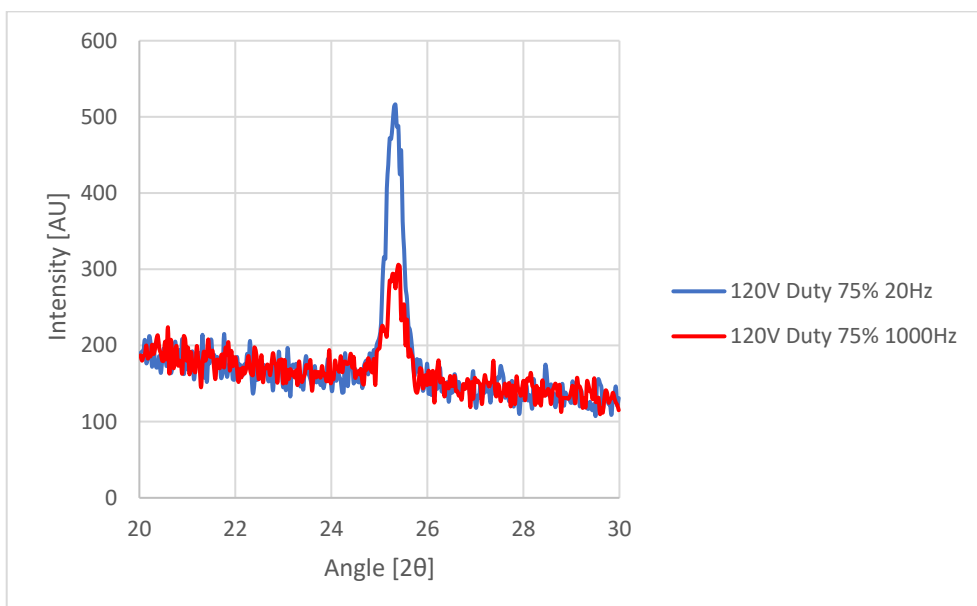


Figure 4.22 XRD analysis of titanium anodized with a duty cycle 75% and at 120 V with 1000 Hz and 20 Hz.

In this group the samples anodized at 160 V and 75% of duty cycle with different frequencies are shown.

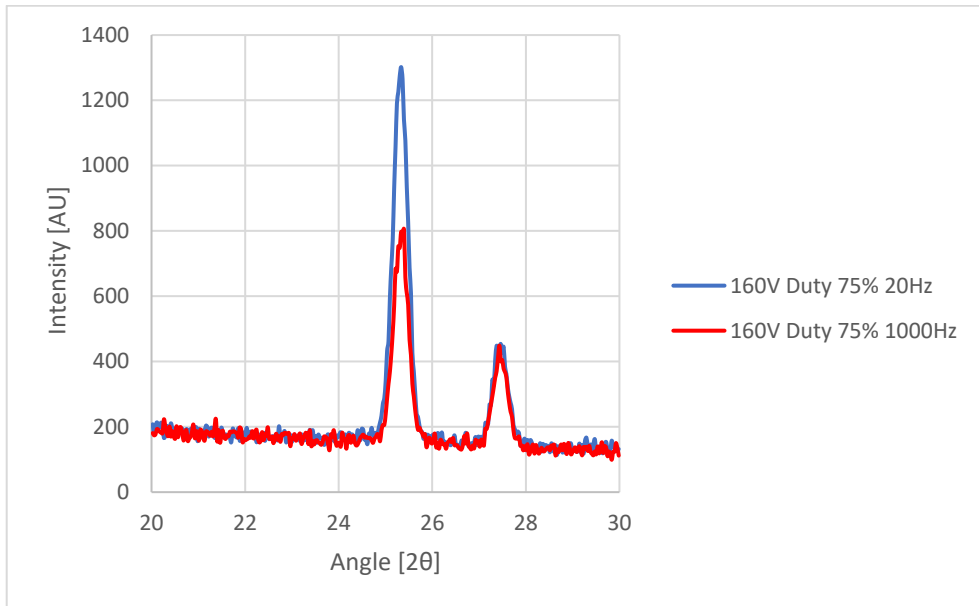


Figure 4.23 XRD analysis of titanium anodized with a duty cycle 75% and at 160 V with 1000 Hz and 20 Hz.

This is the last graph of this section and it shows the samples anodized at 220 V with 75% duty cycle and different frequencies.

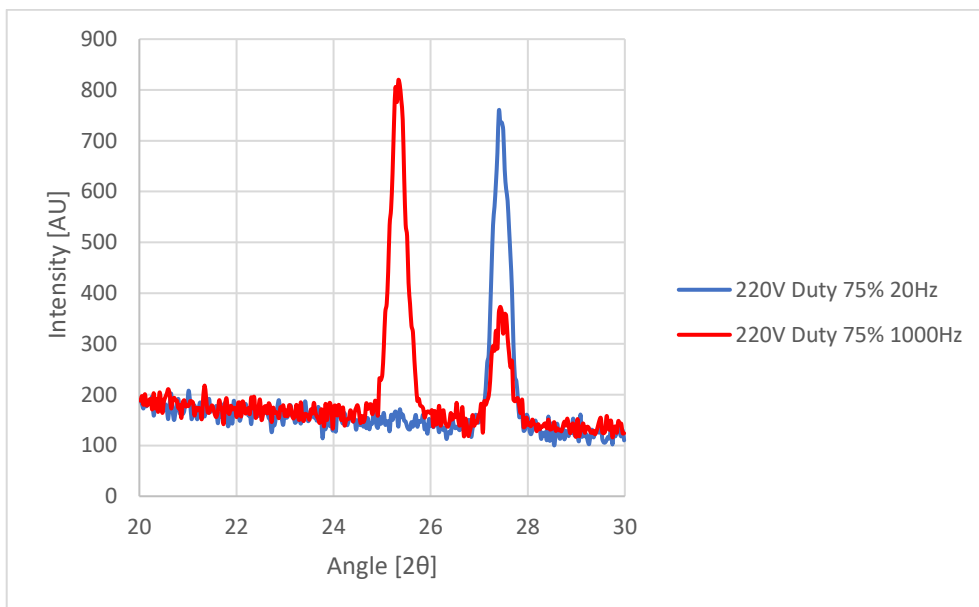
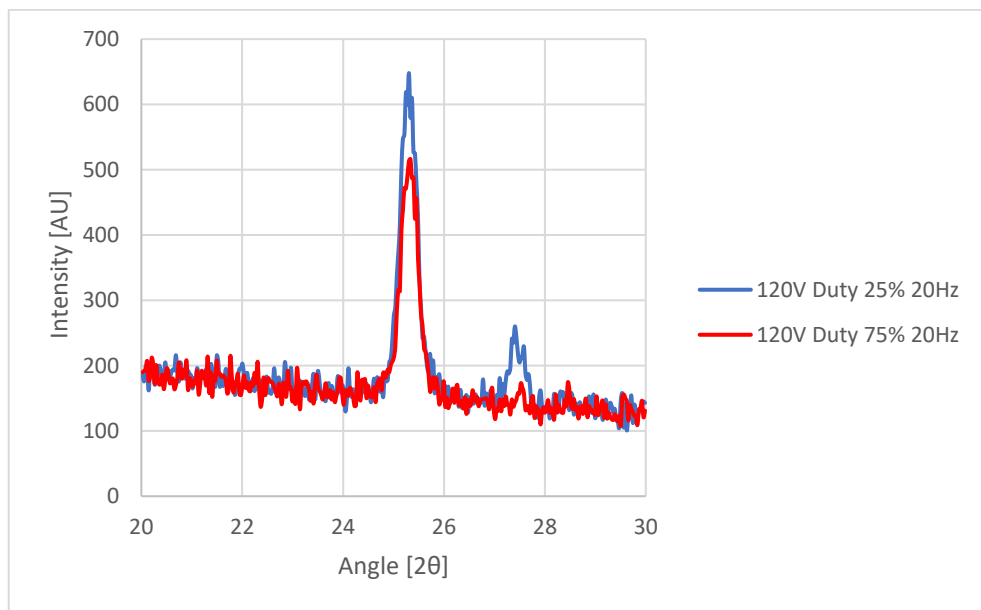


Figure 4.24 XRD analysis of titanium anodized with a duty cycle 75% and at 220 V with 1000 Hz and 20 Hz.

- *Change in duty cycle with constant frequency and voltage*

The first set of graphs shows all the samples anodized at 120 V, 160 V and 220 V with 20 Hz of frequency and different duty cycles, while the last three graphs show the sample anodized at the same conditions but with 1000Hz of frequency.

In this graph are shown the XRD test results of the samples anodized at 120 V with 20 Hz of frequency and different duty cycles.



*Figure 4.25 XRD analysis of titanium anodized with 20 Hz of frequency at 120 V with 25% and 75% of duty cycle.*

In this figure the trend of the sample anodized at 160 V with 20 Hz of frequency and different duty cycles are shown.

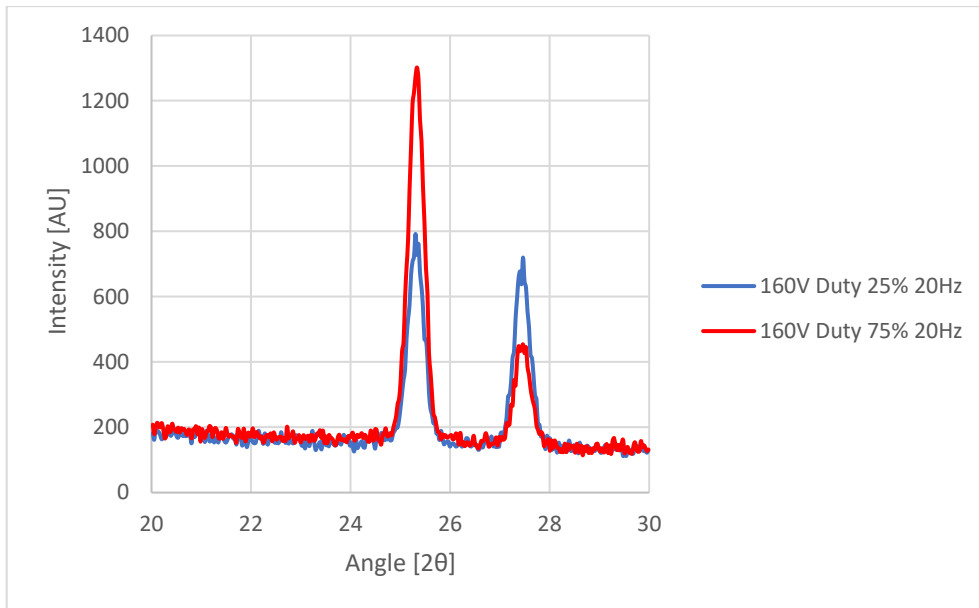


Figure 4.26 XRD analysis of titanium anodized with 20 Hz of frequency at 160 V with 25% and 75% of duty cycle.

This is the last figure of the set and it represents the XRD analysis of samples anodized at 220 V and 20 Hz with different duty cycles.

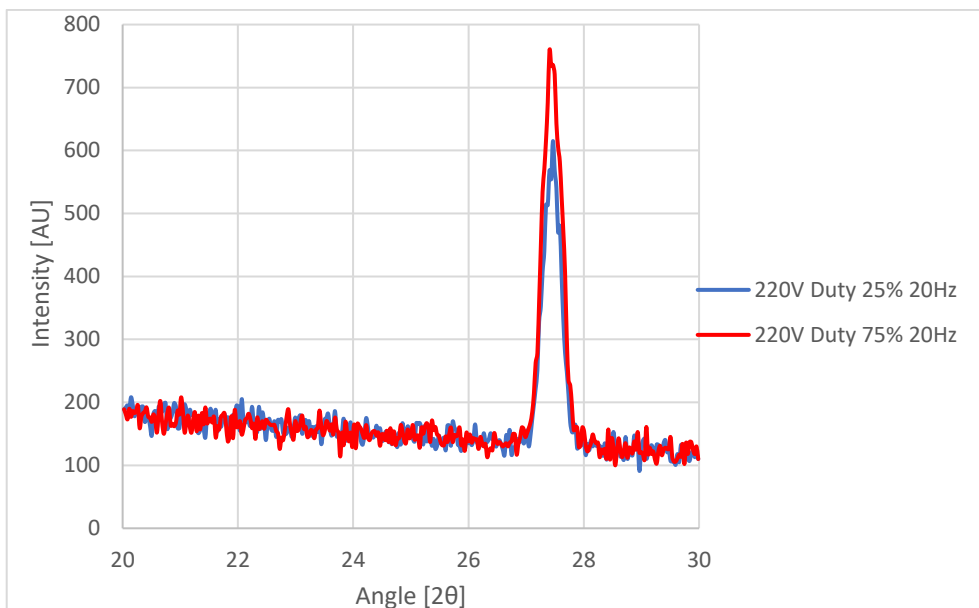


Figure 4.27 XRD analysis of titanium anodized with 20 Hz of frequency at 220 V with 25% and 75% of duty cycle.

In this figure the trends of the samples anodized at 120 V and 1000 Hz with different duty cycles are represented.

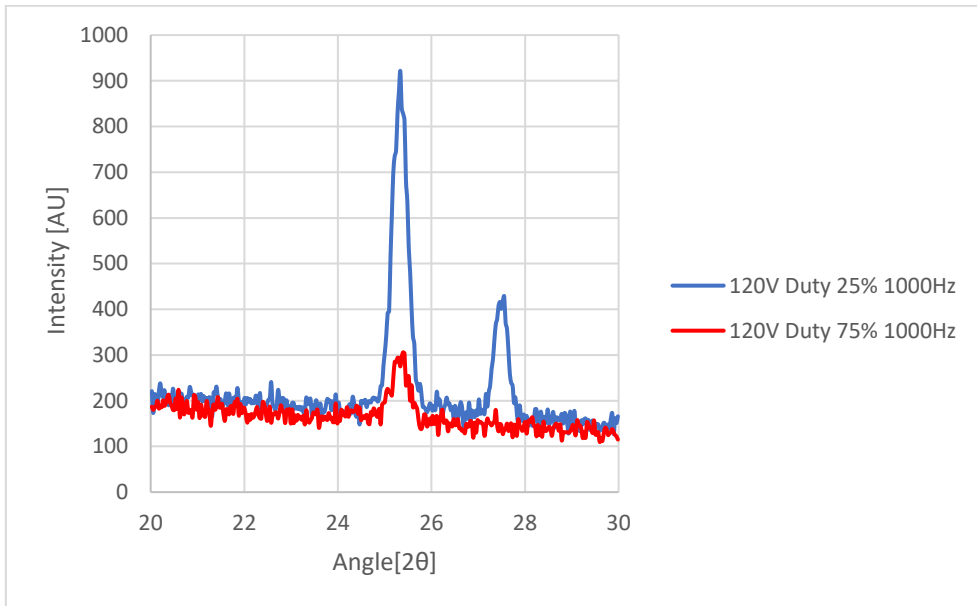


Figure 4.28 XRD analysis of titanium anodized with 1000 Hz of frequency at 120 V with 25% and 75% of duty cycle.

Changing the voltage to 160 V, here below it is reported the XRD results of the samples anodized with 1000 Hz and different duty cycles.

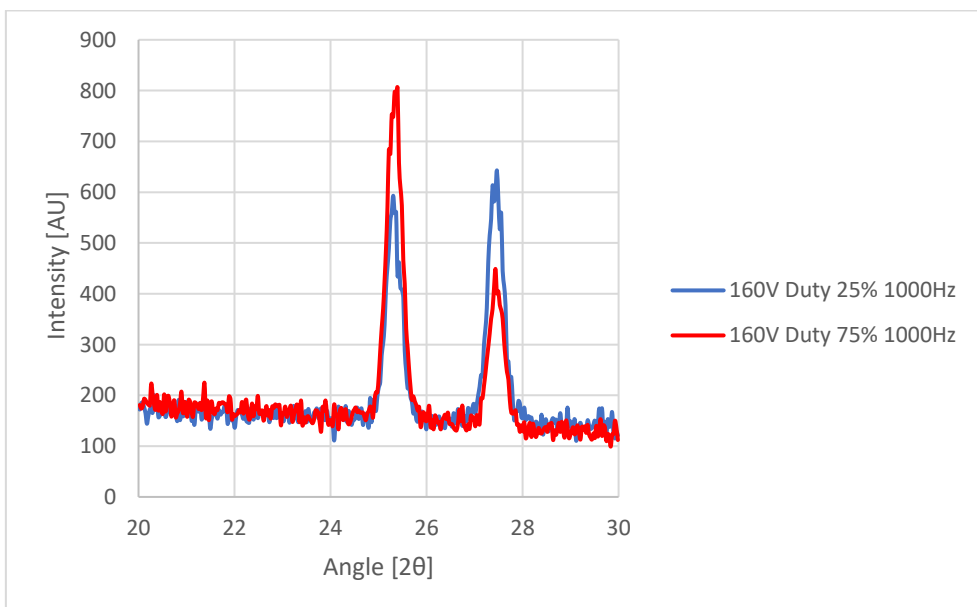


Figure 4.29 XRD analysis of titanium anodized with 1000 Hz of frequency at 160 V with 25% and 75% of duty cycle.

This is the last figure of the section and it represents the XRD results of the samples anodized at 220 V with 1000 Hz of frequency and different duty cycles.

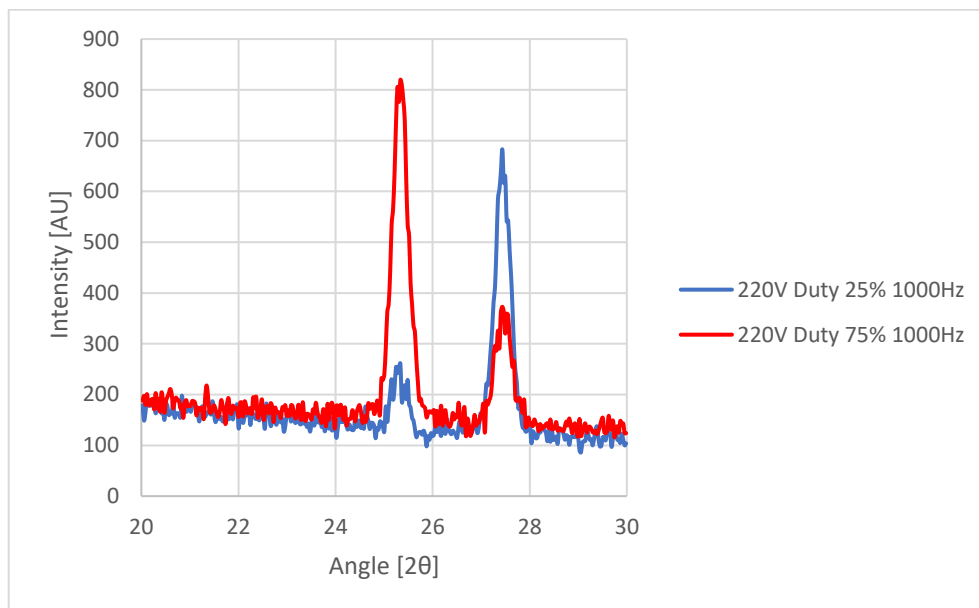


Figure 4.30 XRD analysis of titanium anodized with 1000 Hz of frequency at 220 V with 25% and 75% of duty cycle.

### 4.3.4 Potentiodynamic tests results

The corrosion resistance of the samples has been studied through a potentiodynamic test. Due to the complexity of the three dimensions dependence problem, the results will be presented in groups, fixing two variables and changing only one.

- *Change in voltage with constant duty and frequency*

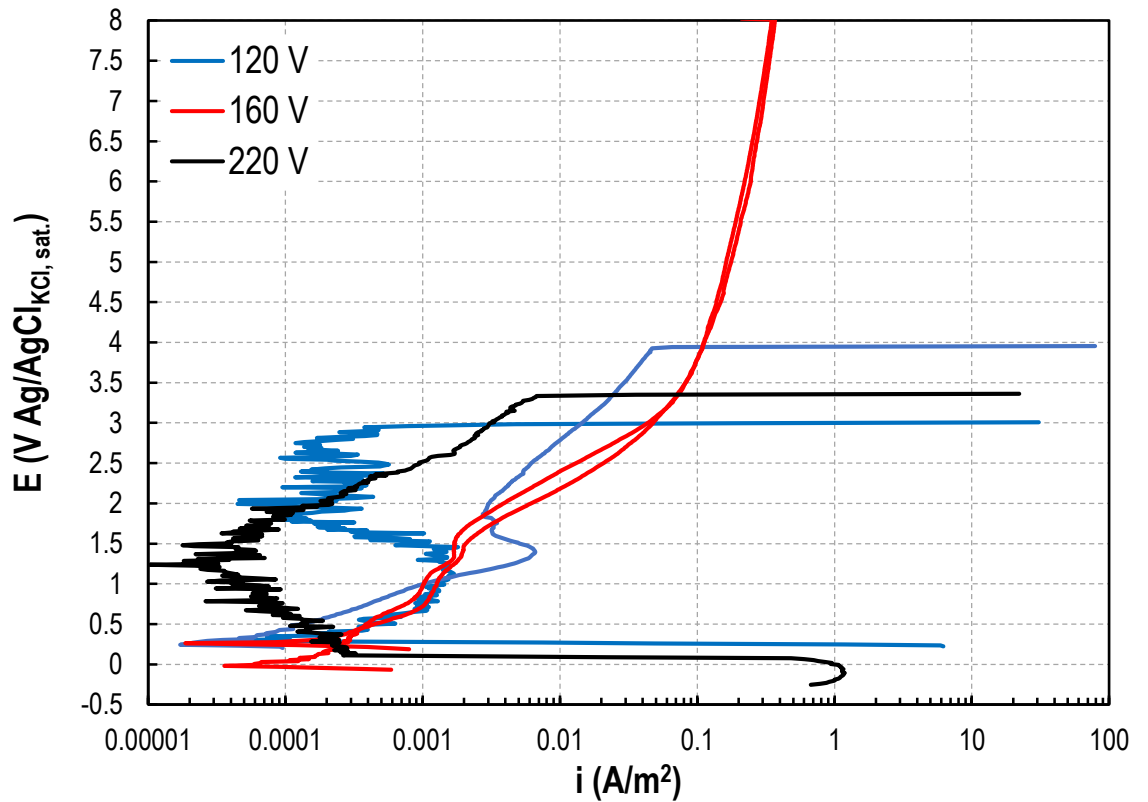


Figure 4.31 Potentiodynamic tests results of DC anodization.

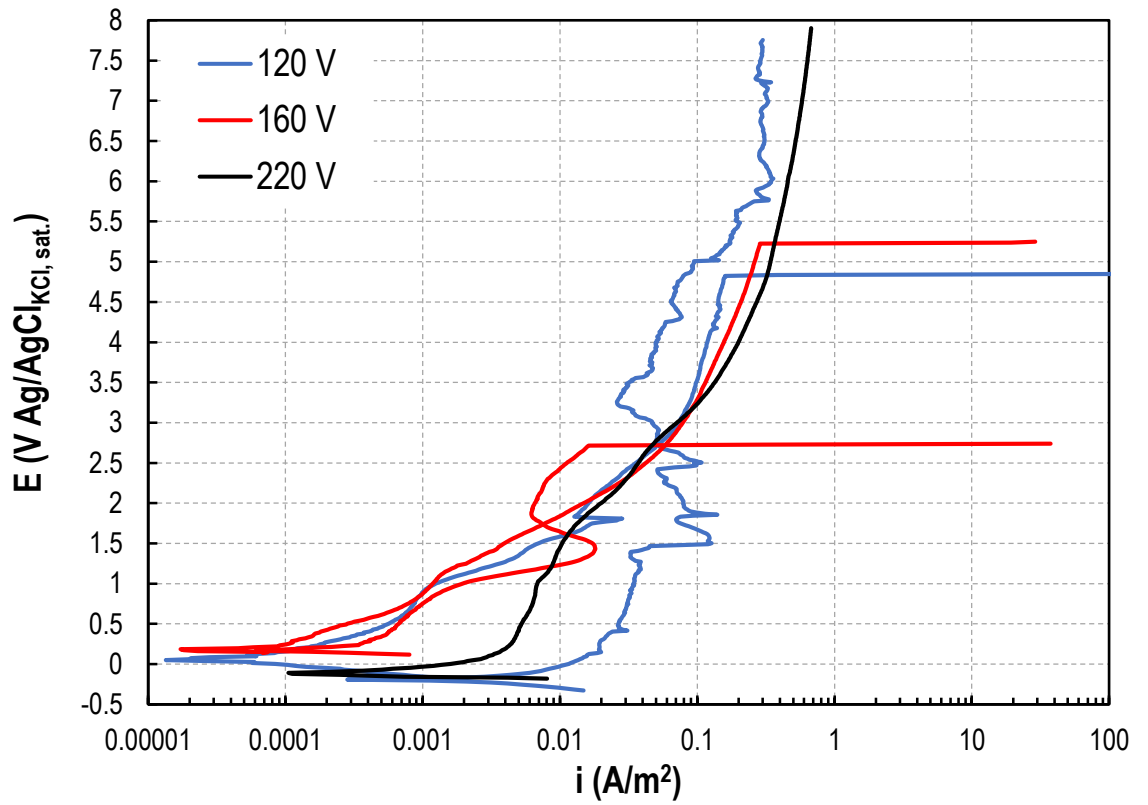


Figure 4.32 Potentiodynamic tests results of anodization with duty cycle 25% and frequency 1000 Hz.

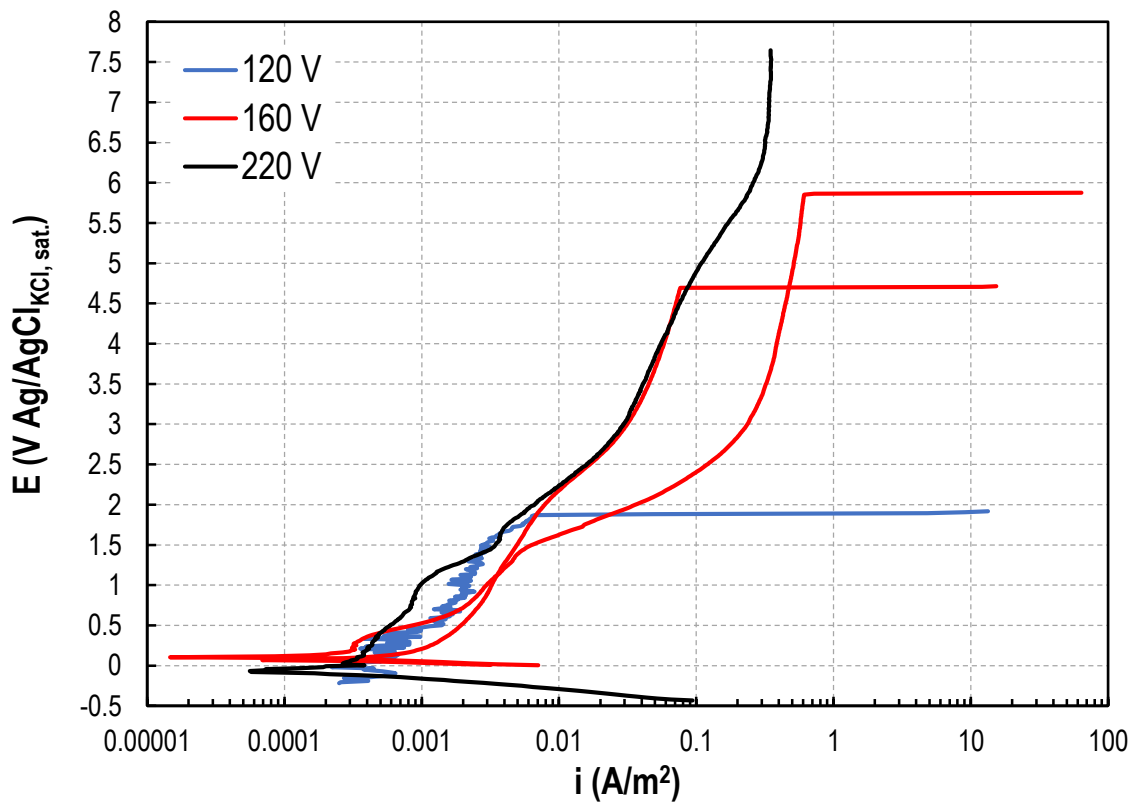


Figure 4.33 Potentiodynamic results of anodization with duty cycle 25% and frequency 20 Hz.

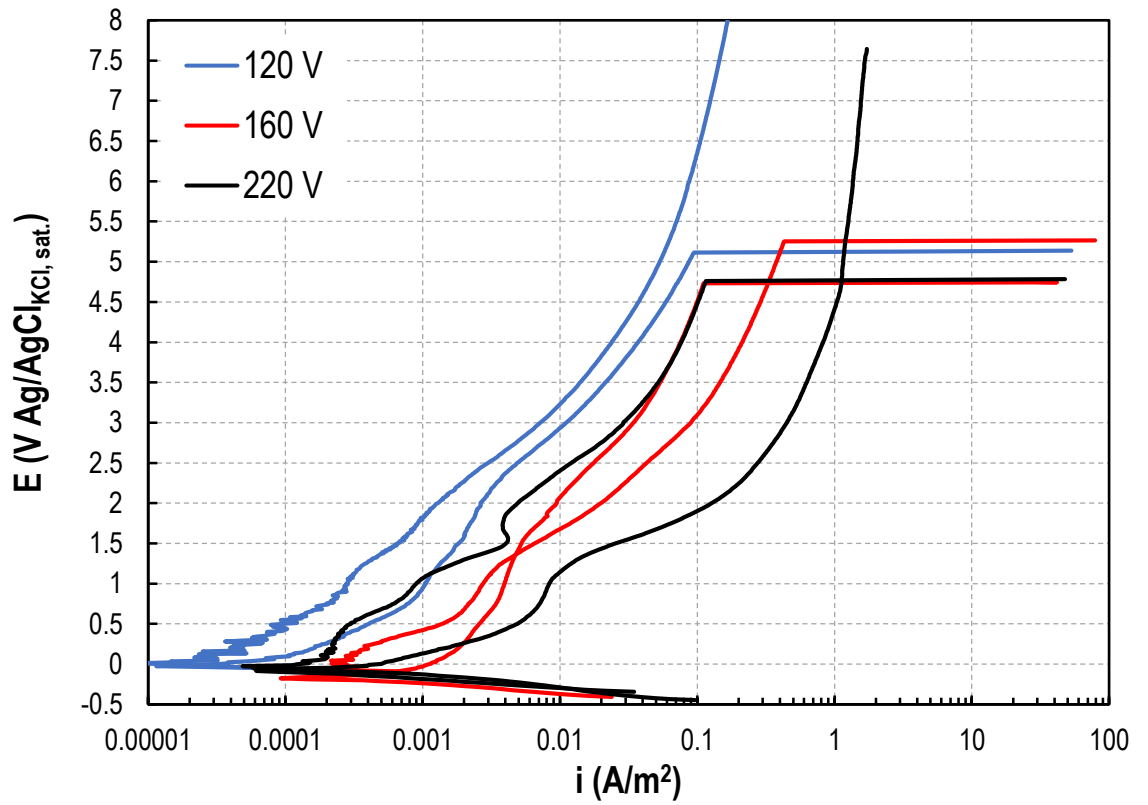


Figure 4.34 Potentiodynamic tests results of anodization with duty cycle 75% and frequency 1000 Hz.

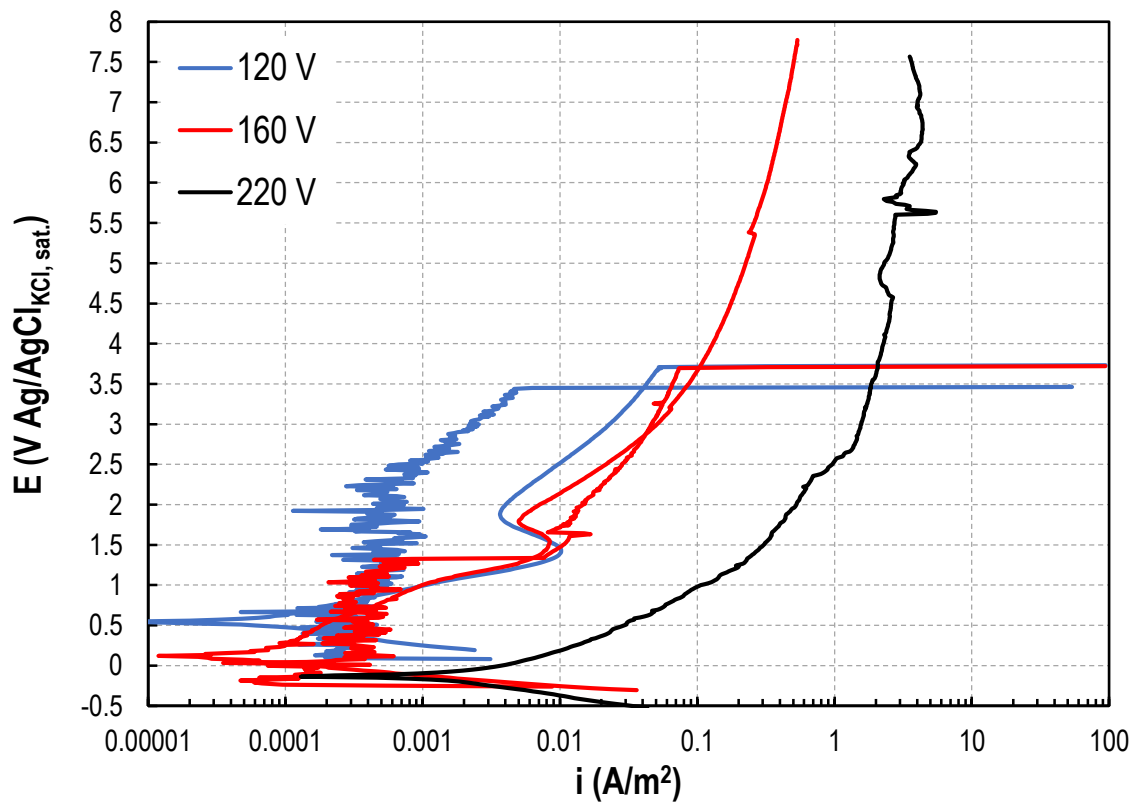


Figure 4.35 Potentiodynamic tests results of anodization with duty cycle 75% and frequency 20 Hz.

- Change in duty with constant voltage and frequency

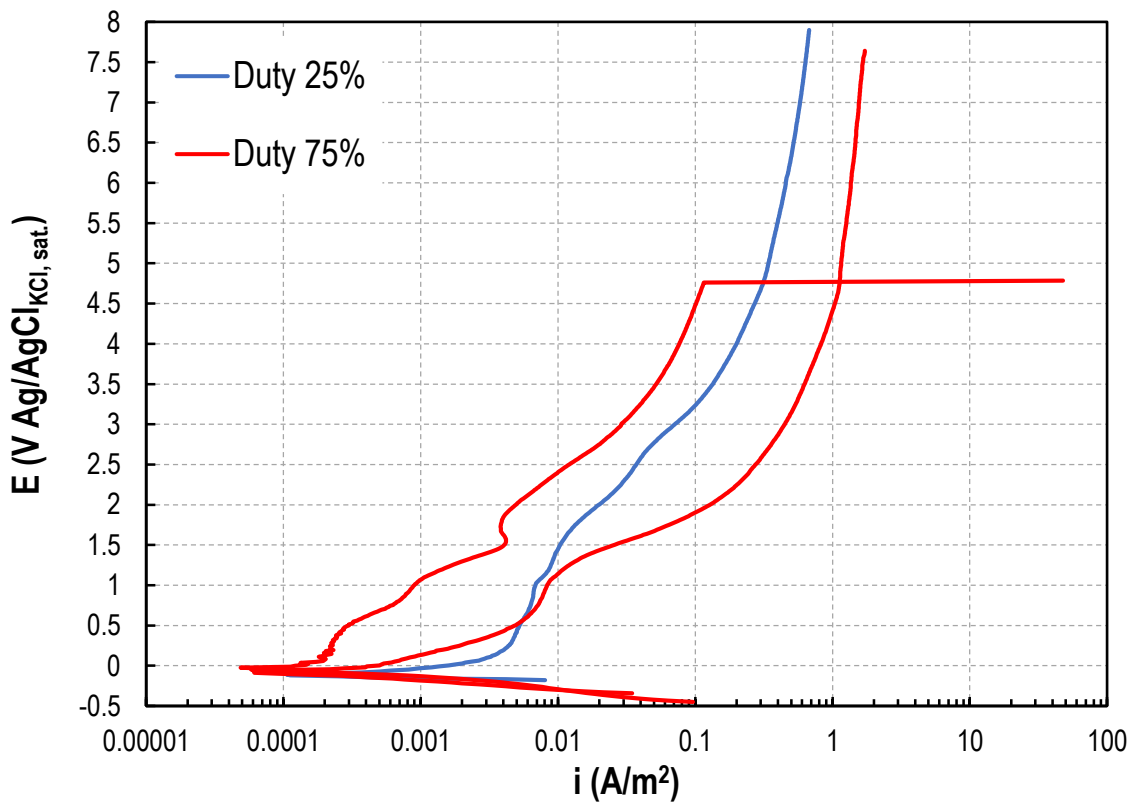


Figure 4.36 Potentiodynamic tests results of anodization with voltage 220 V and frequency 1000 Hz.

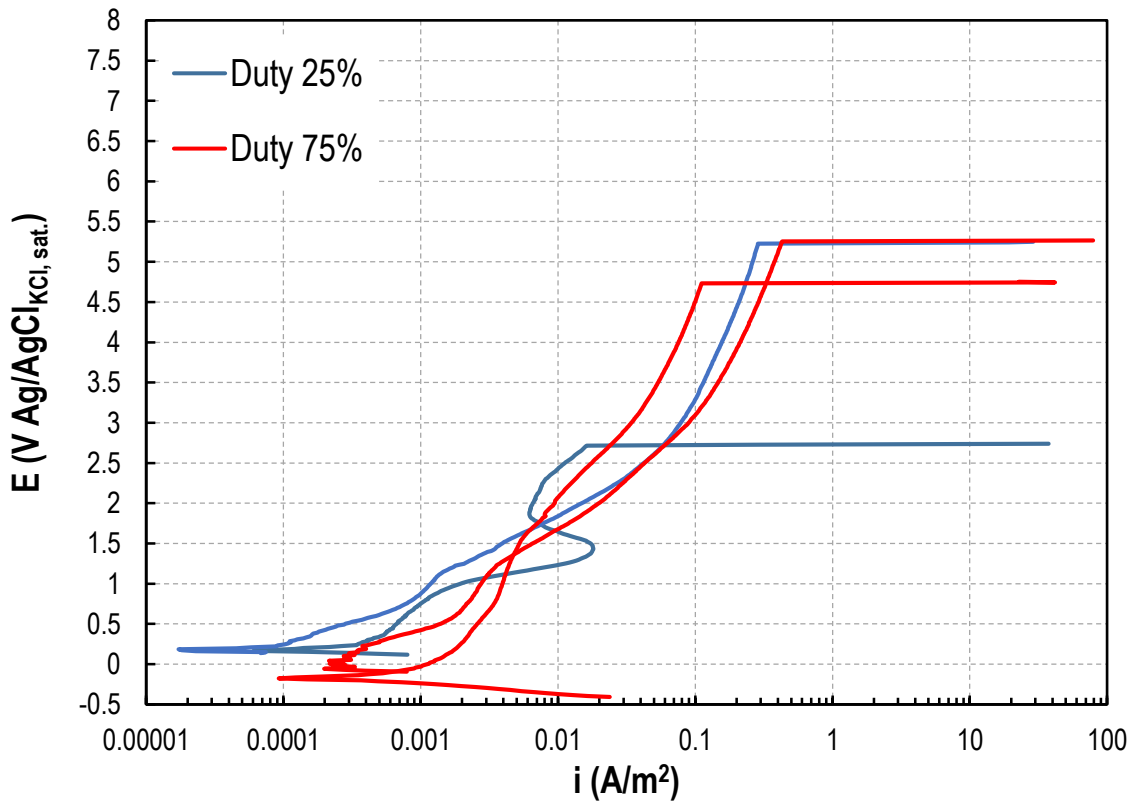


Figure 4.37 Potentiodynamic results of anodization with voltage 160 V and frequency 1000 Hz.

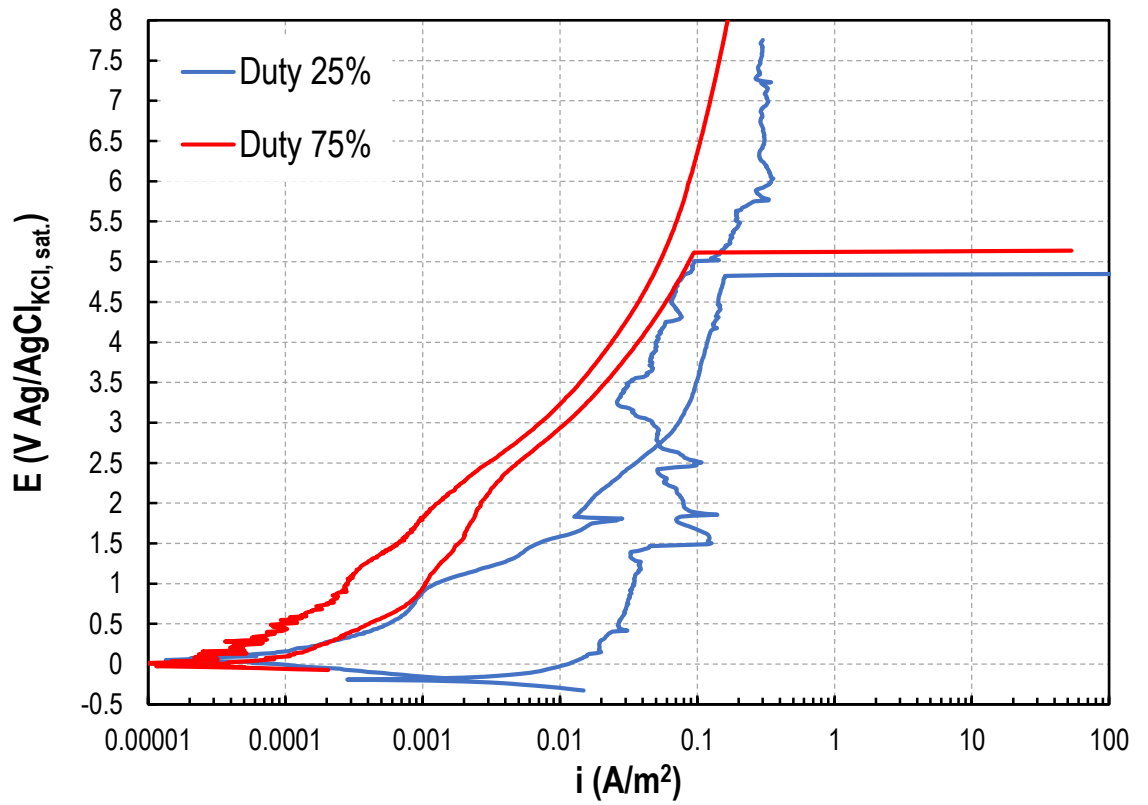


Figure 4.38 Potentiodynamic tests results of anodization with voltage 120 V and frequency 1000 Hz.

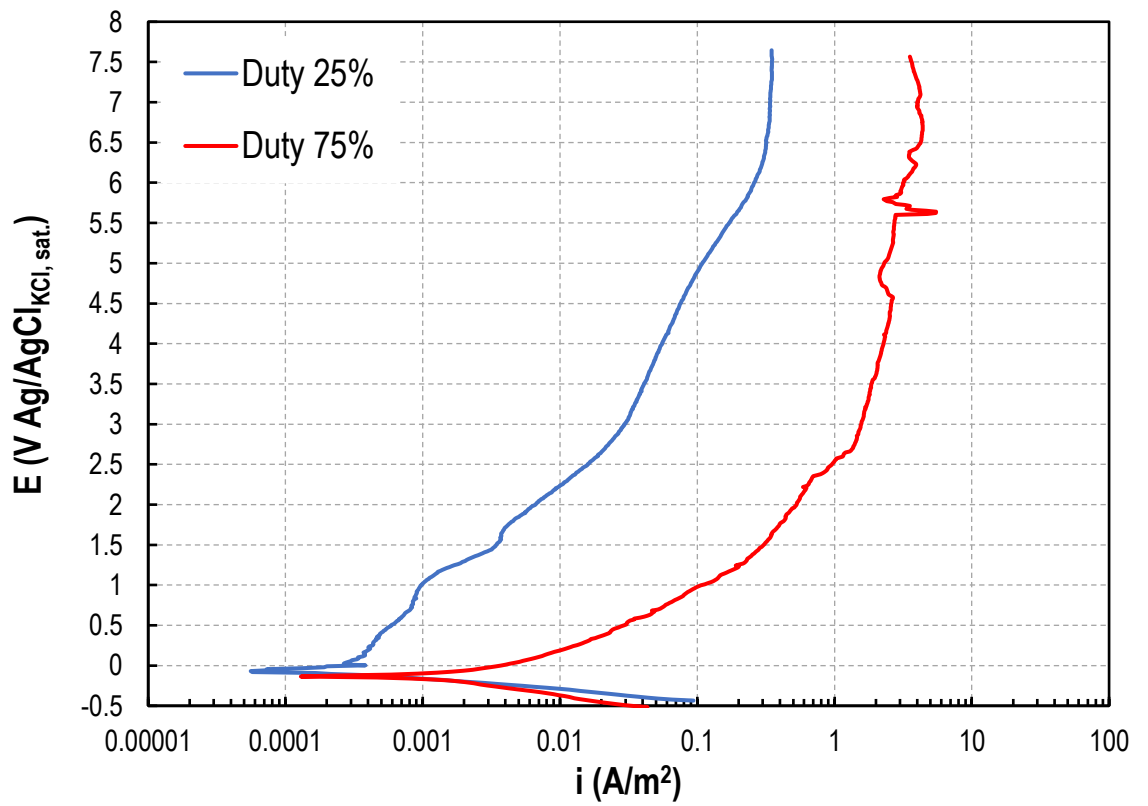


Figure 4.39 Potentiodynamic tests results of anodization with voltage 220 V and frequency 20 Hz.

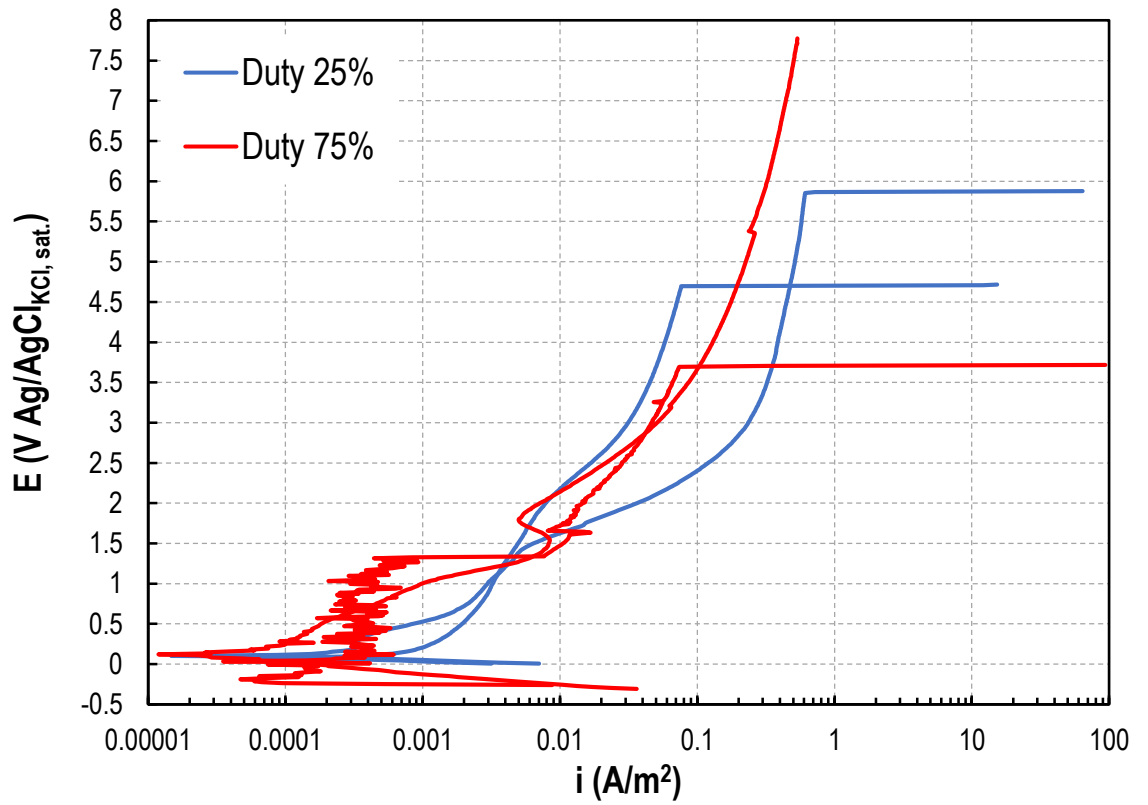


Figure 4.40 Potentiodynamic tests results of anodization with voltage 160 V and frequency 20 Hz.

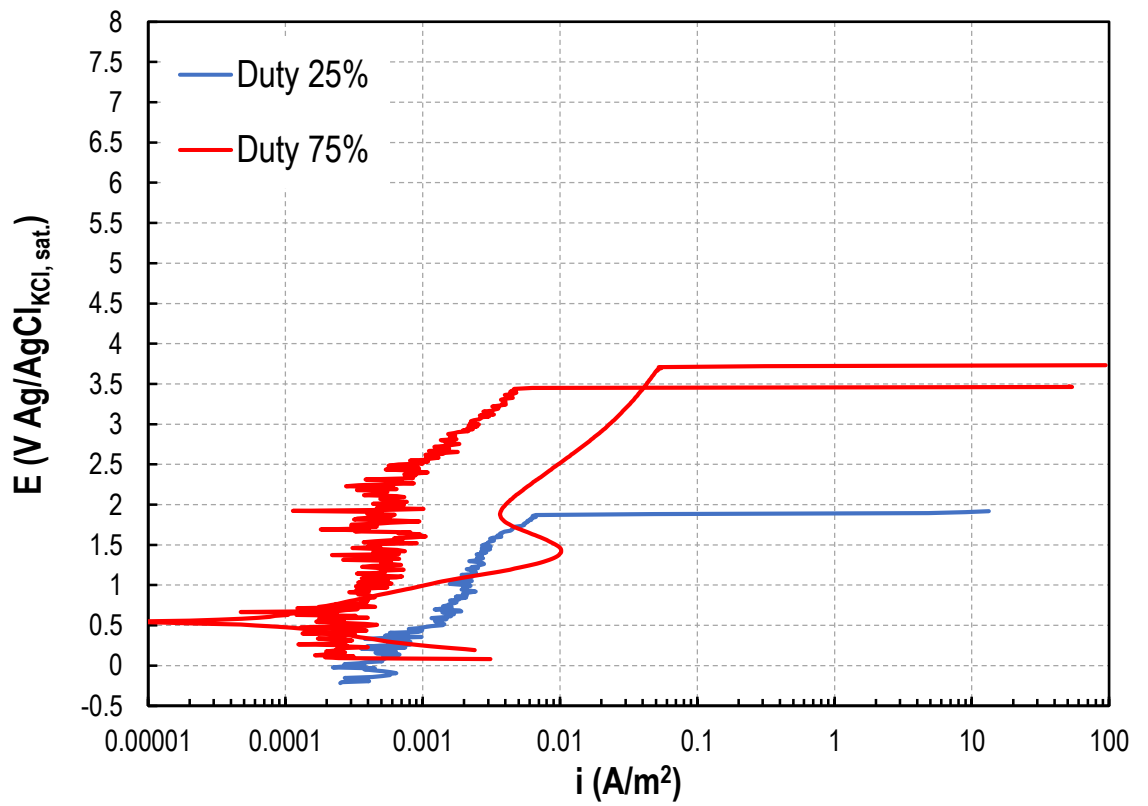


Figure 4.41 Potentiodynamic tests results of anodization with voltage 120 V and frequency 20 Hz.

- Change in frequency with constant duty and voltage

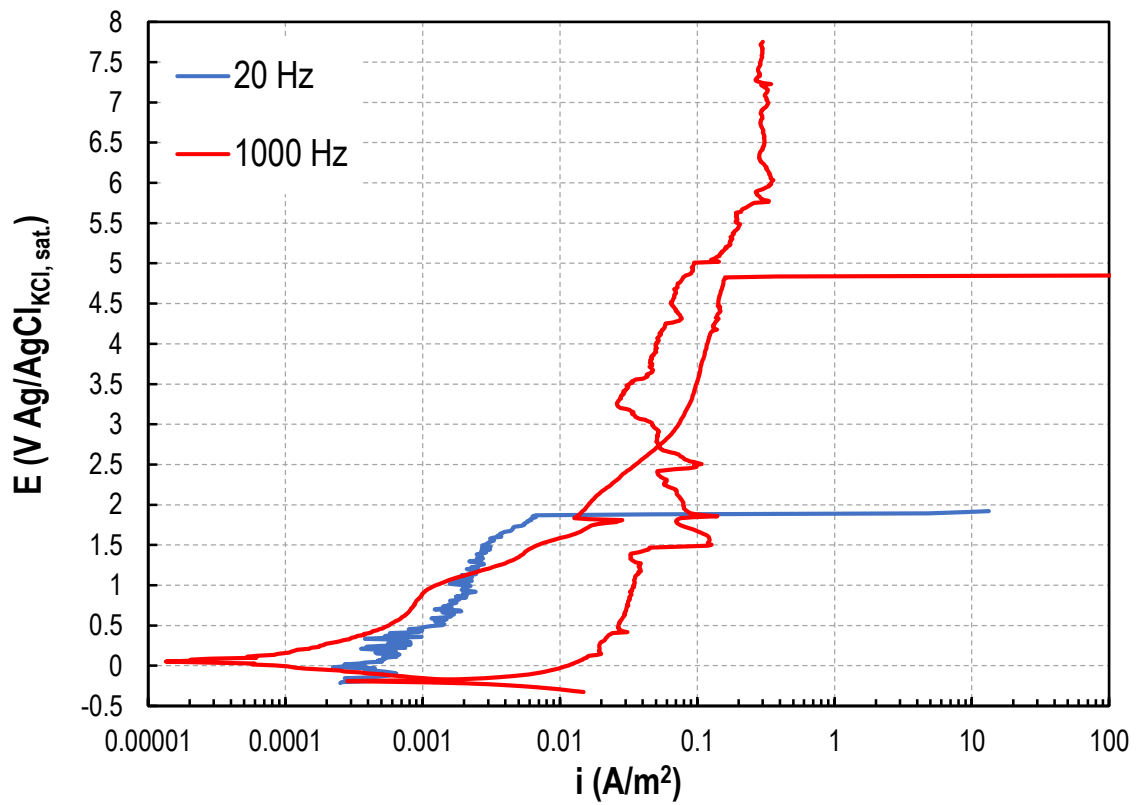


Figure 4.42 Potentiodynamic tests results of anodization with voltage 120 V and duty cycle 25%.

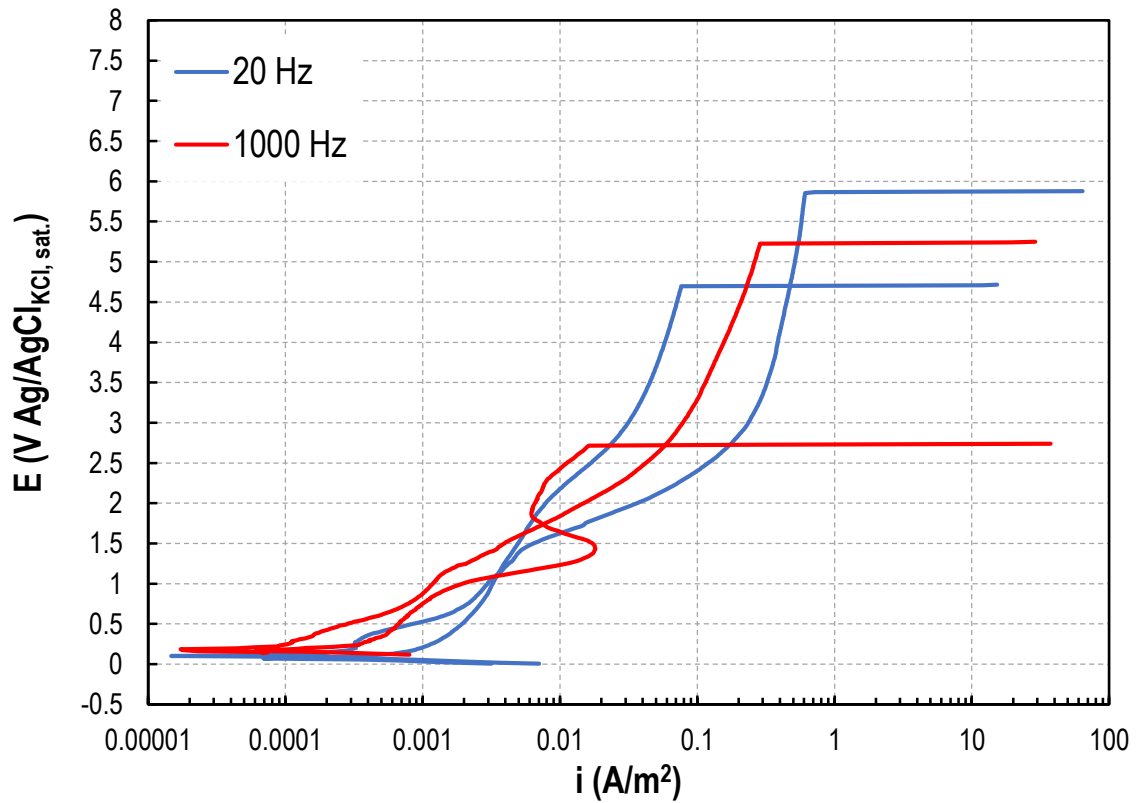


Figure 4.43 Potentiodynamic tests results of anodization with voltage 160 V and duty cycle 25%.

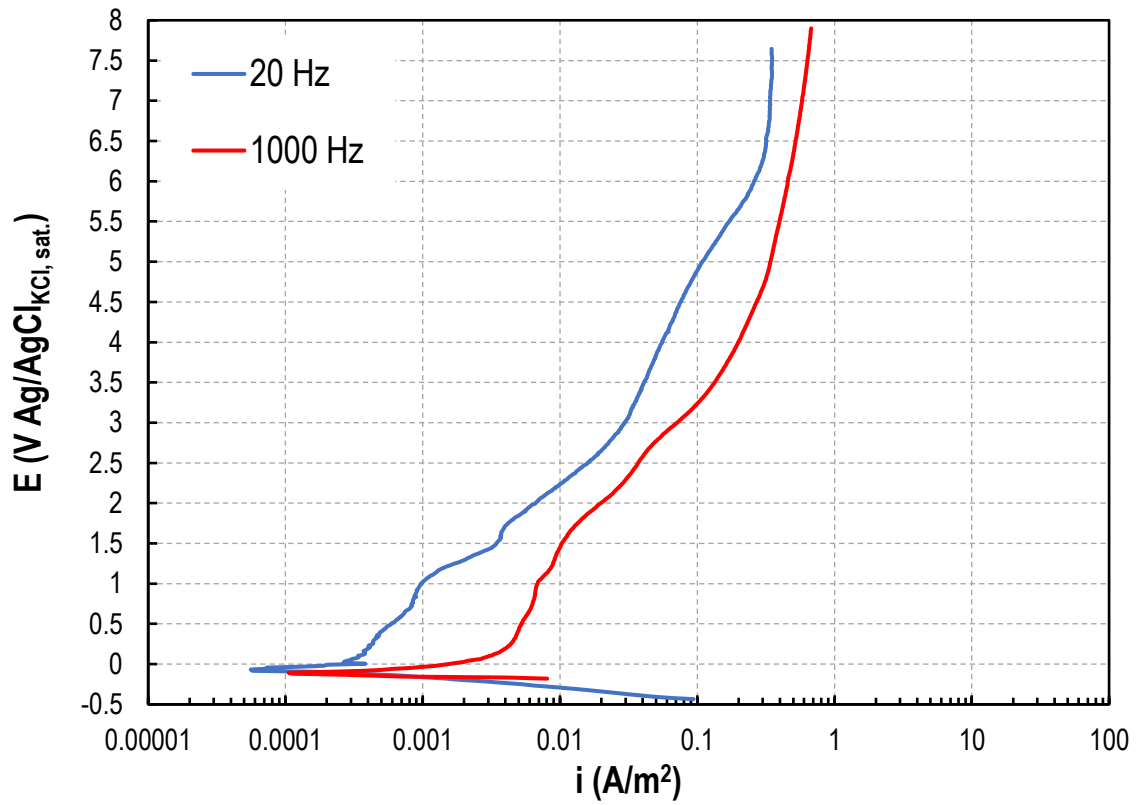


Figure 4.44 Potentiodynamic tests results of anodization with voltage 220 V and duty cycle 25%.

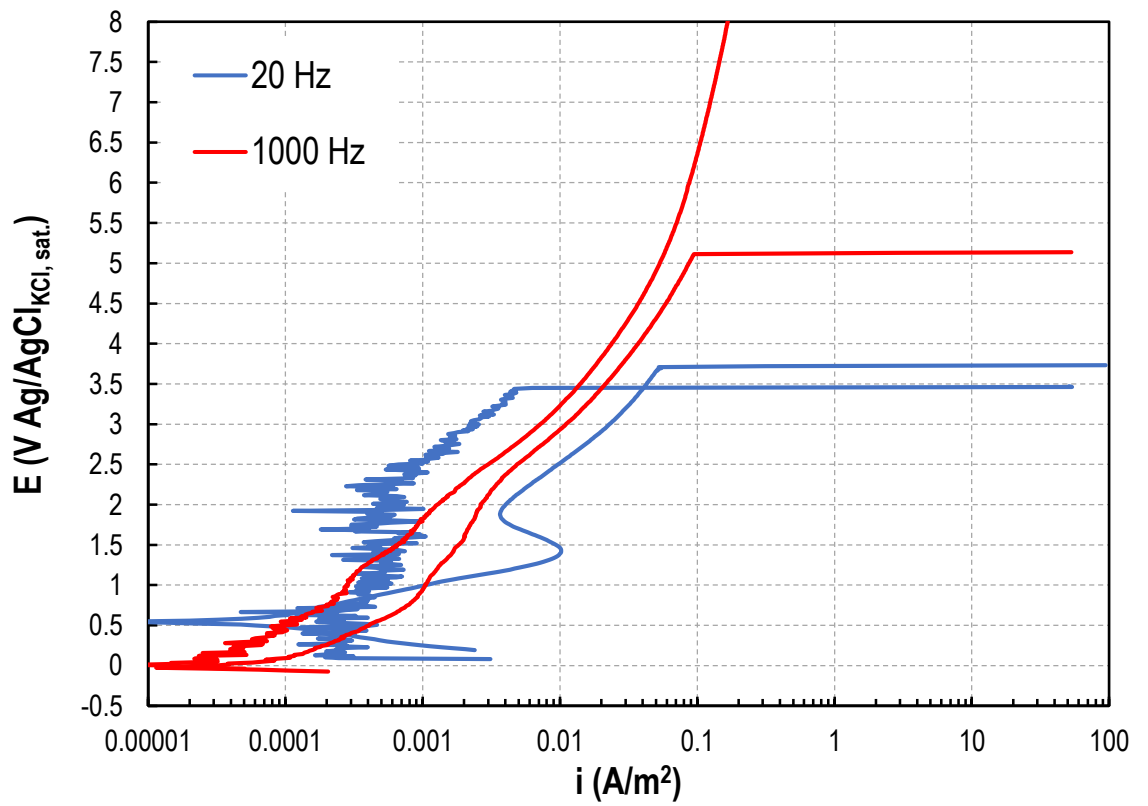


Figure 4.45 Potentiodynamic tests results of anodization with voltage 120 V and duty cycle 75%.

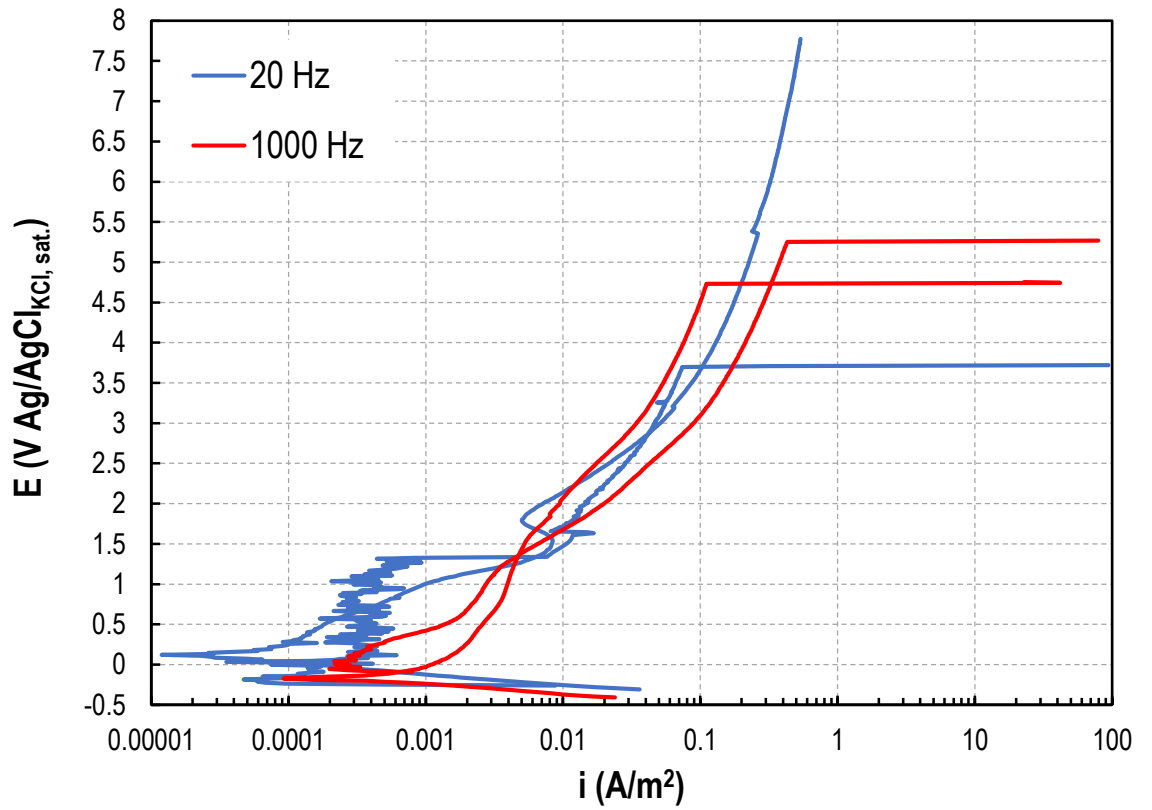


Figure 4.46 Potentiodynamic tests results of anodization with voltage 160 V and duty cycle 75%.

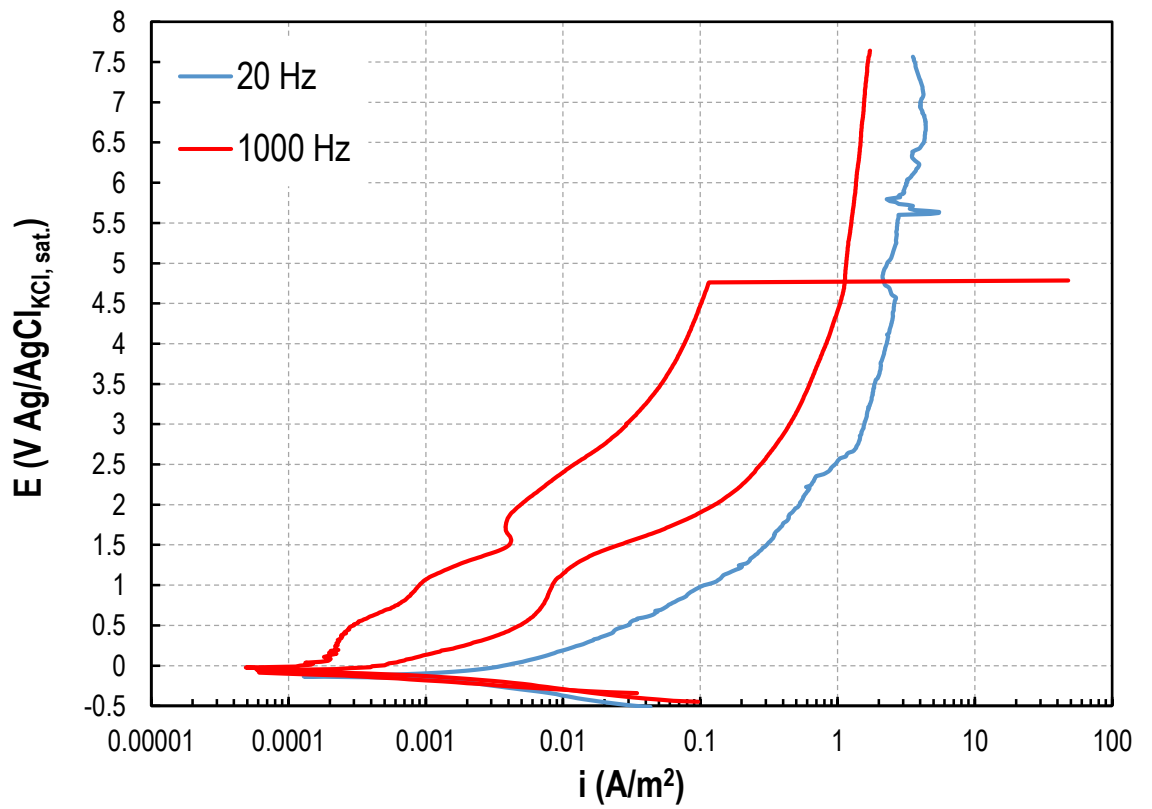


Figure 4.47 Potentiodynamic tests results of anodization with voltage 220 V and duty cycle 75%.

# Chapter 5 – Discussion

## 5.1 Morphology

The distribution density of the areas of the pores has been analysed statistically. The analysis has been performed varying the three main variables of the process, i.e. voltage, duty cycle and frequency, in order to understand the effect of each of them on the oxide.

The curve is normalized, this means that the area below it is equal to one. The probability to find a pore area in an interval of interest can be evaluated through the integral among the extremes of the interval.

In Figure 5.1, 5.2 and 5.3 a comparison among DC, duty 25% at different frequencies is presented.

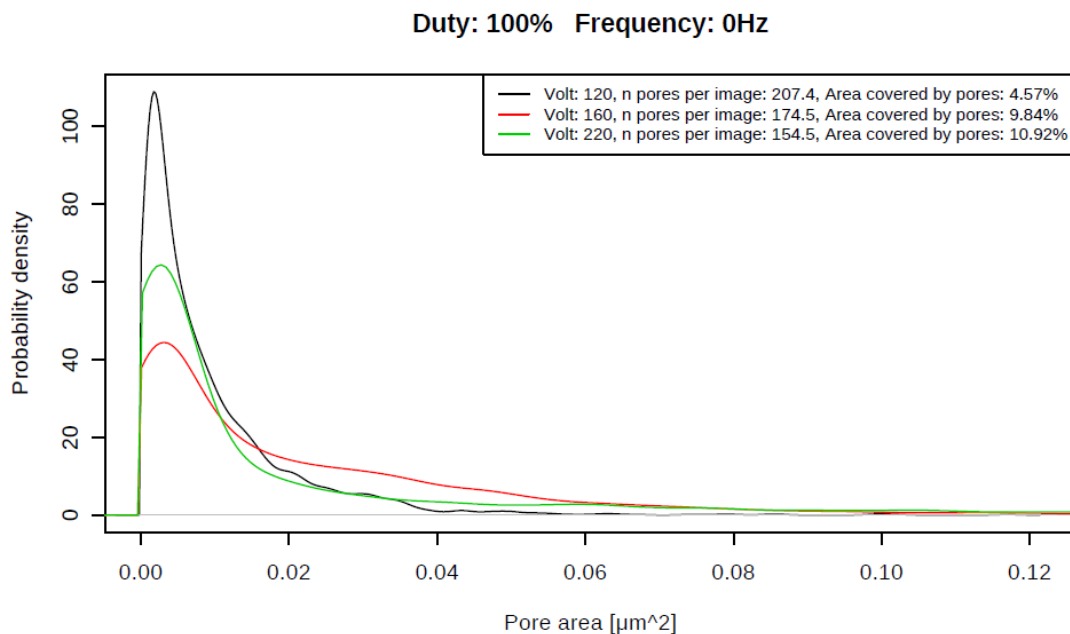


Figure 5.1 Density curves of samples anodized with DC.

**Duty: 25% Frequency: 20Hz**

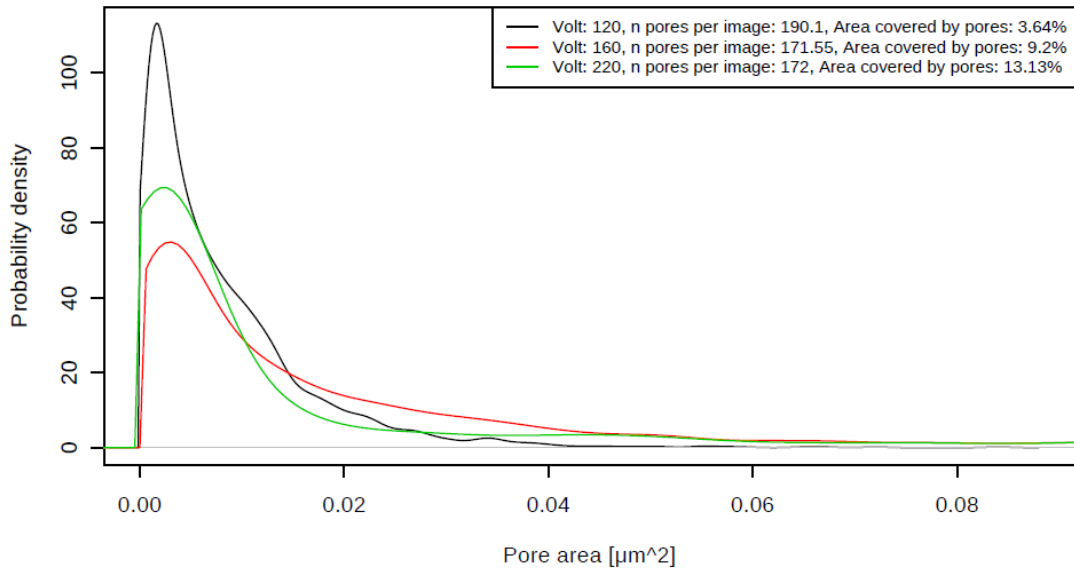


Figure 5.2 Density curves of samples anodized with duty 25% and frequency 20 Hz.

**Duty: 25% Frequency: 1000Hz**

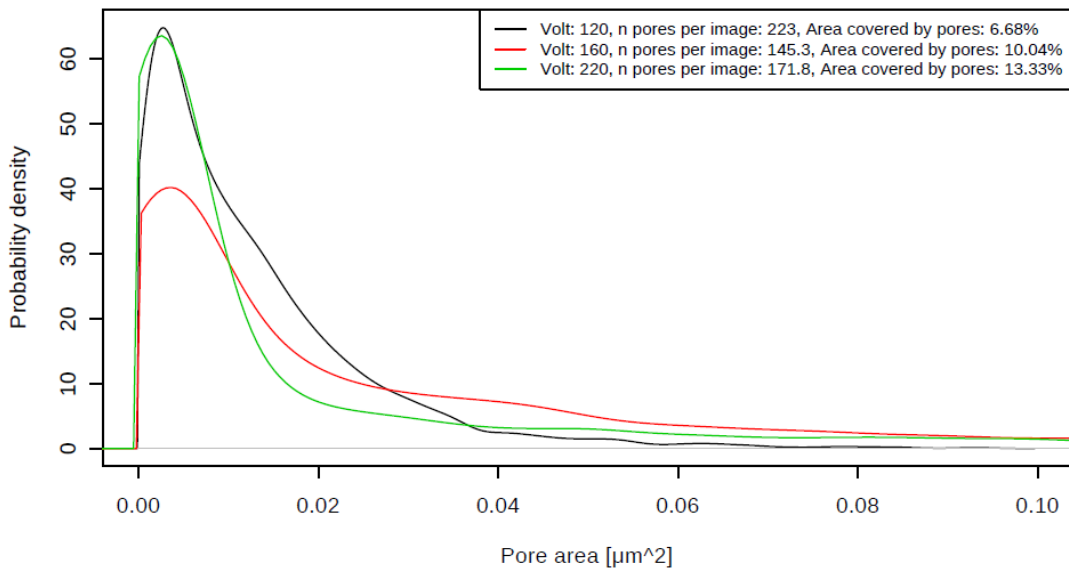


Figure 5.3 Density curves of samples anodized with duty 25% and frequency 1000 Hz.

Shifting from a DC anodizing to a duty cycle 25% with a frequency of 20 Hz, it can be noted that the area covered by the pores is lower, at voltages equal to 120 V and 160 V, in the pulsed case. Although, it can be found a different behaviour when the voltage is 220 V, the area covered by pores is larger in the case of duty cycle than in the DC. In facts, there is a lower value of the area covered by pores due to the less voltage applied at low frequency.

Increasing the frequency, differently from the previous situation, the same duty cycle but with a frequency of 1000 Hz causes a major area covered by pores respect to the DC case, in all the three voltages. So, increasing the polarization depolarization velocity, the power supplied causes an increase in the average covered by pores also at low potentials.

A comparison among DC and duty 75% at a frequency of 20 Hz and 1000 Hz can be made looking at Figure 5.1, 5.4 and 5.5.

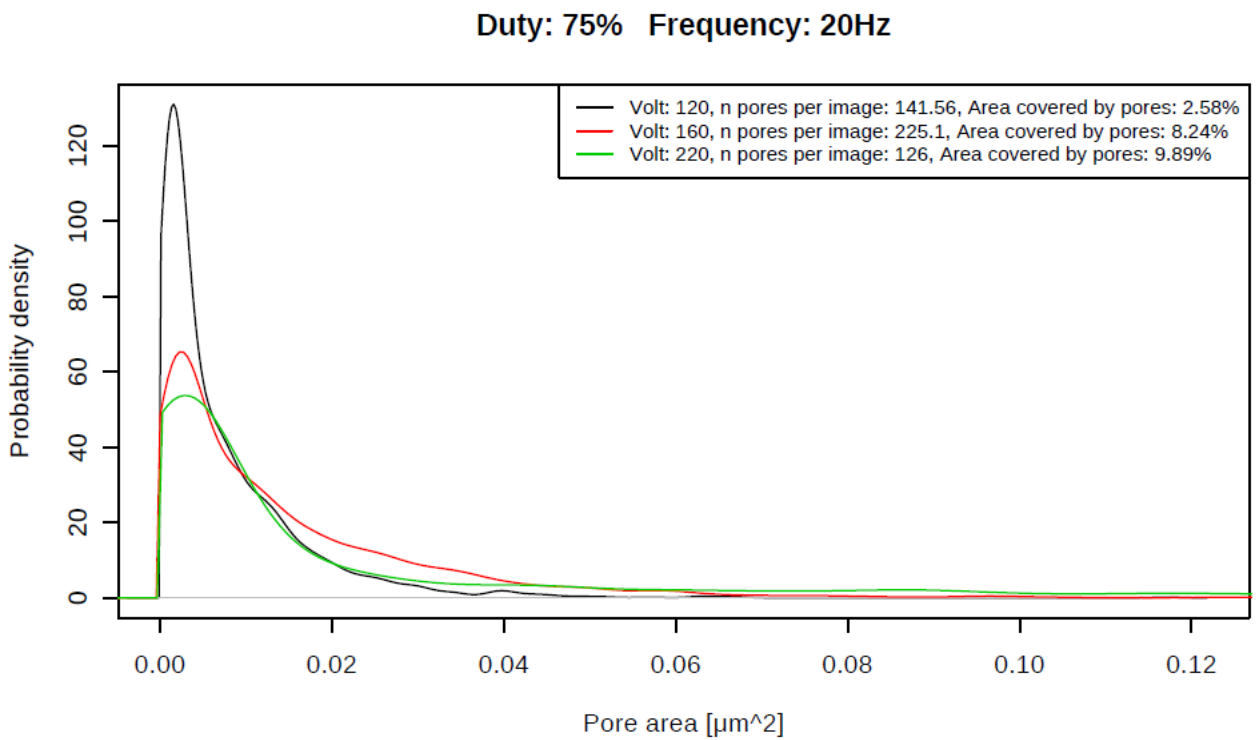
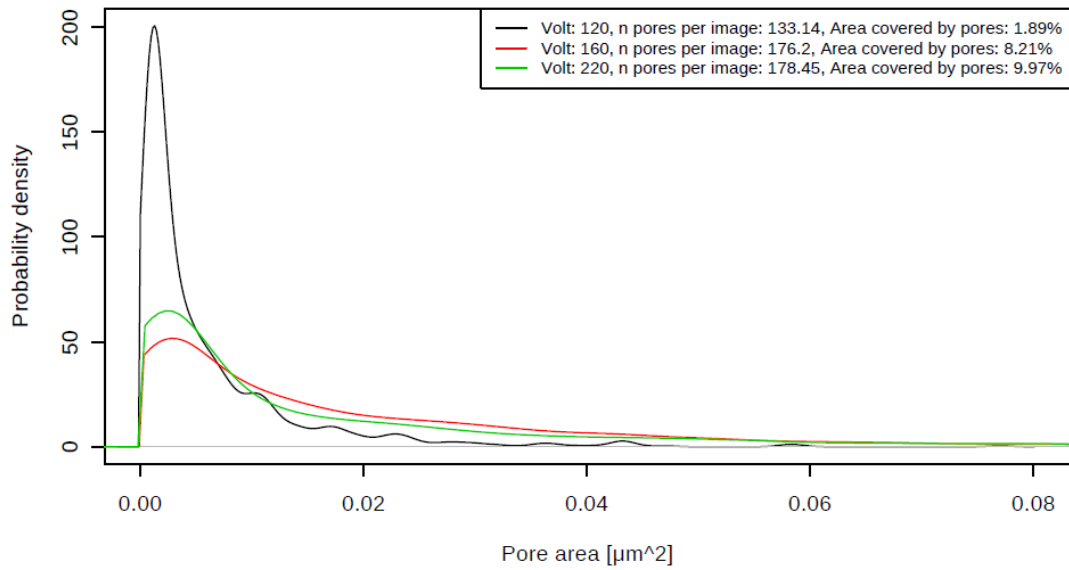


Figure 5.4 Density curves of samples anodized with duty 75% and frequency 20 Hz.

**Duty: 75% Frequency: 1000Hz**



*Figure 5.5 Density curves of samples anodized with duty 75% at frequency 1000 Hz.*

In this case, for all the three voltages the area covered by pores is lower on the samples anodized with the duty cycle 75% with respect to the DC anodization; in addition, in the case of voltage 120 V the DC case is the double of the duty 75% with both frequencies. Increasing the frequency, the effect of the duty cycle on the area covered by pores is stronger than at low frequency.

A comparison among DC and both duties at the frequencies of 1000 and 20 Hz and voltage 120 V can be made looking at Figure 5.6, 5.7 and 5.8.

Volt: 120 Frequency: 0Hz

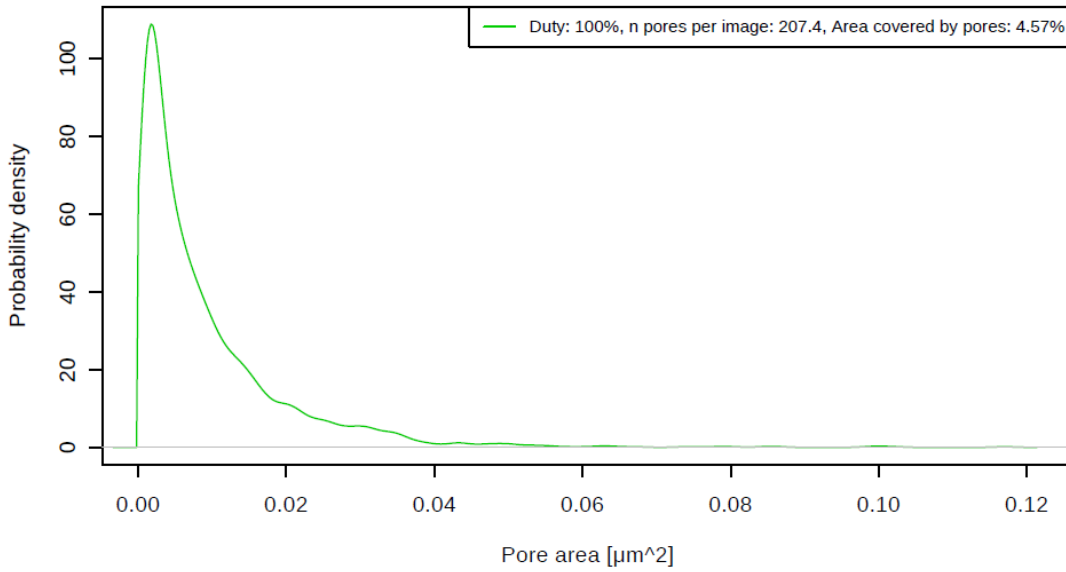


Figure 5.6 Density curve of samples anodized with DC at voltage 120 V.

Volt: 120 Frequency: 1000Hz

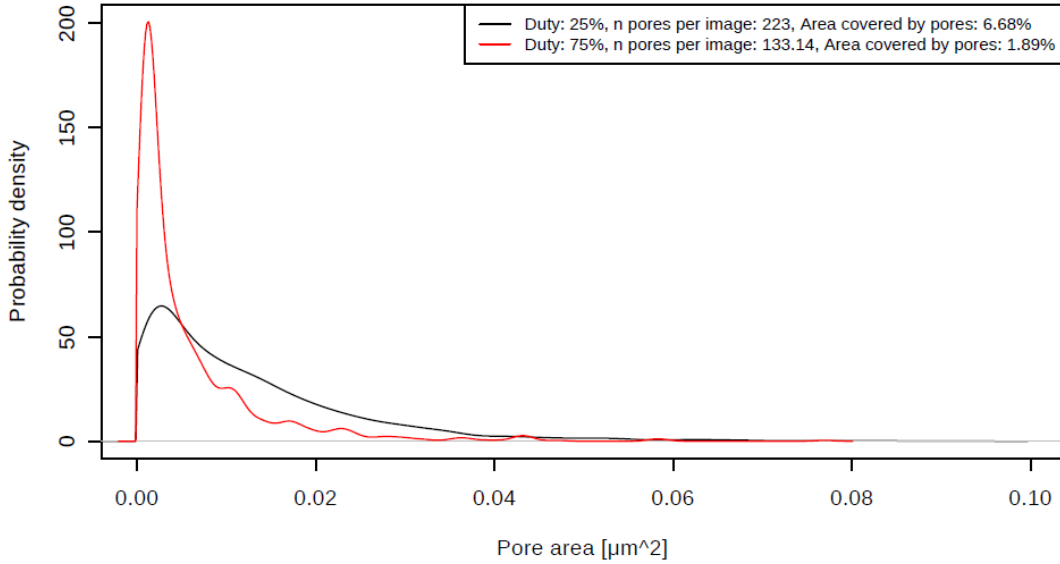


Figure 5.7 Density curves of samples anodized with both duties at frequency 1000 Hz and voltage 120 V.

Volt: 120 Frequency: 20Hz

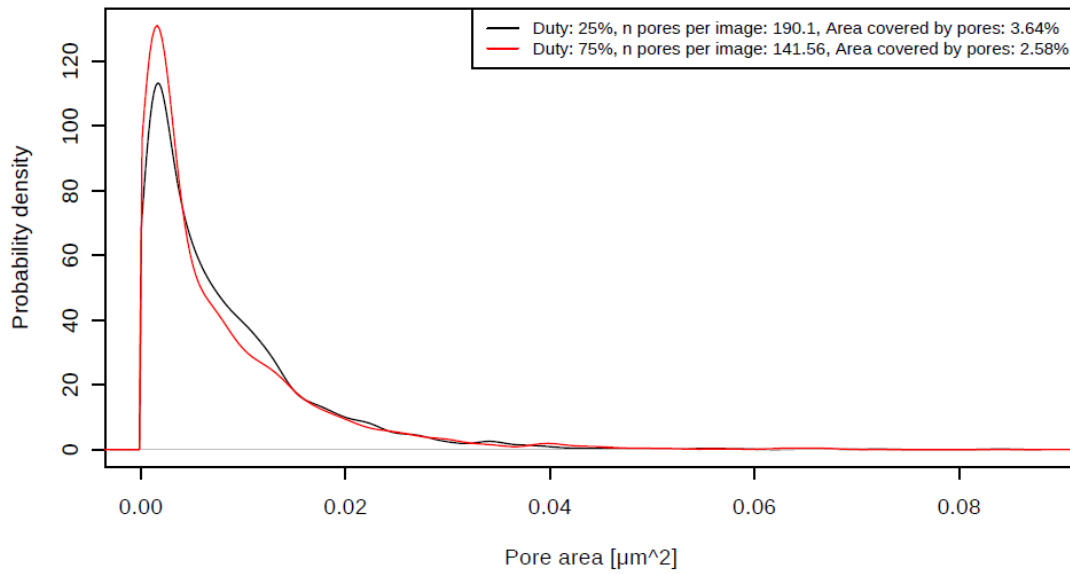


Figure 5.8 Density curves of samples anodized with both duties at frequency 20 Hz and voltage 120 V.

For a frequency of 1000 Hz, as can be noticed from the area covered by the pores written in the pictures, that the duty cycle 25% presents a porosity higher than the DC, while in the duty cycle 75% it is significantly lower, coherently with what said before.

At frequency 20 Hz, the two duty cycles present a similar curve, with the duty 75% showing a smaller area covered by pores, and in both cases it is lower respect to DC.

A comparison among DC and both duties at a frequency of 20 Hz and voltage 160 V can be made looking at Figure 5.9 and 5.10.

**Volt: 160 Frequency: 0Hz**

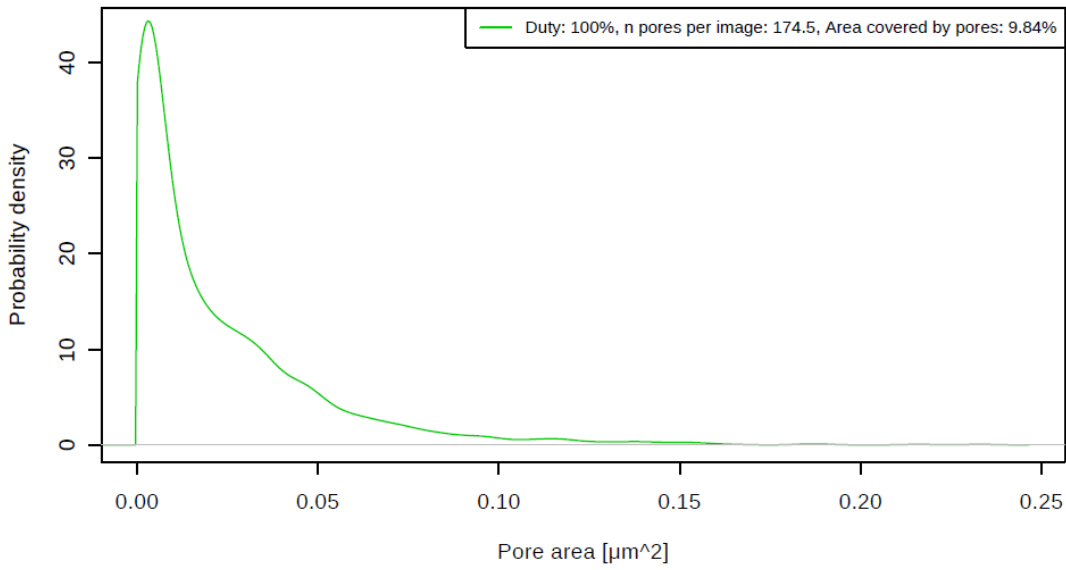


*Figure 5.9 Density curve of samples anodized with DC at voltage 160 V.*

**Volt: 160 Frequency: 20Hz**

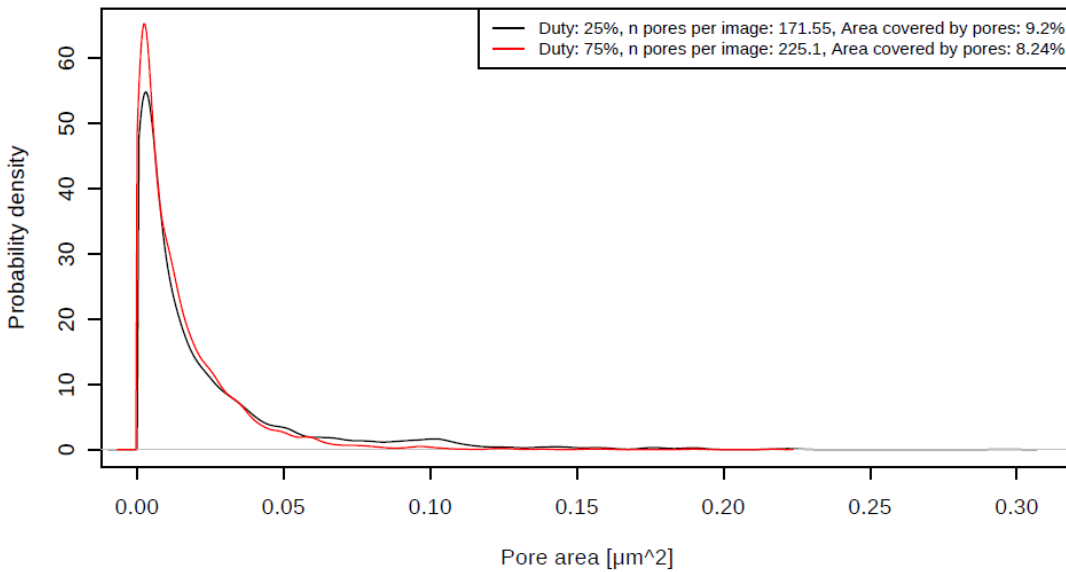


*Figure 5.10 Density curves of samples anodized with both duties at frequency 20 Hz and voltage 160 V.*

Increasing the voltage, at frequency 20 Hz, the two duties still present an area covered by pores lower than the DC even though the difference is small in the case of the duty 25%, but bigger in the case of duty 75%.

A comparison among DC and both duties at a frequency of 20 Hz and voltage 220 V can be made looking at Figure 5.11 and 5.12.

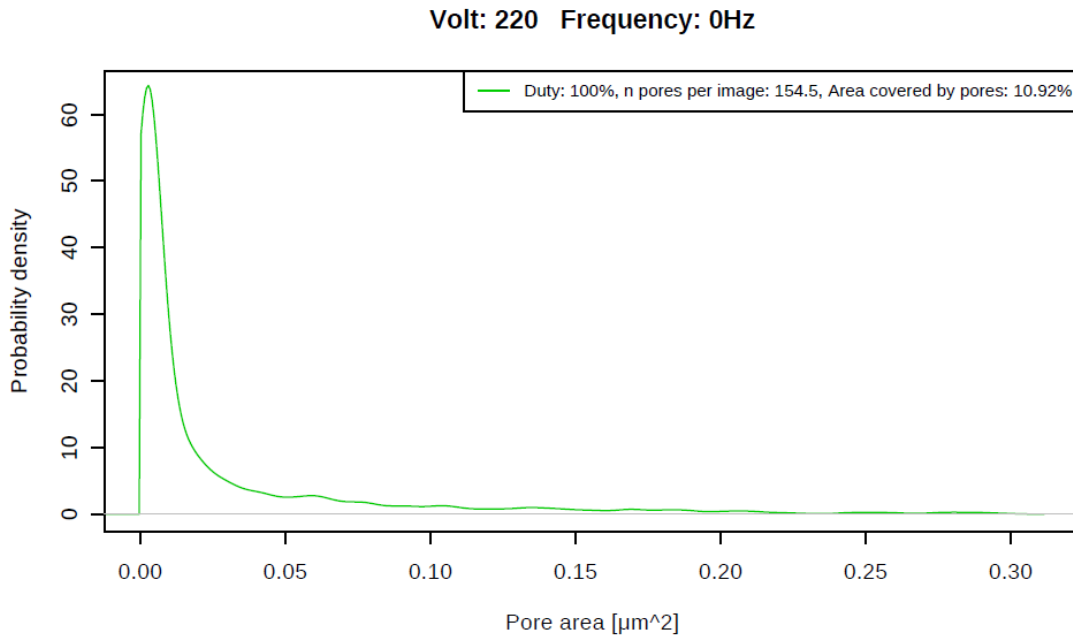


Figure 5.11 Density curve of samples anodized with DC and voltage 220 V.

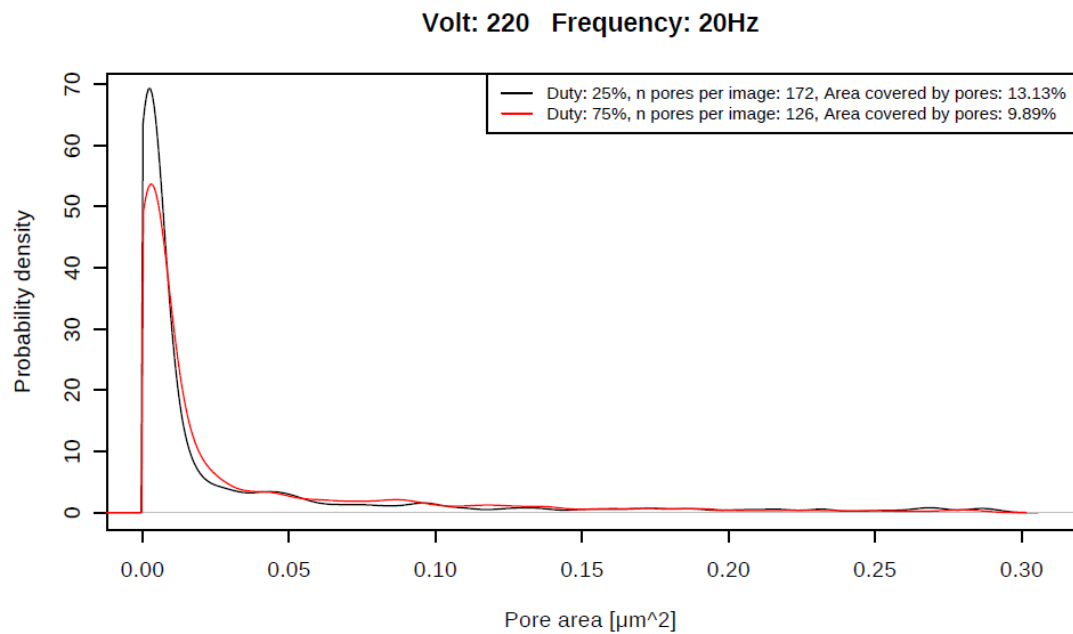
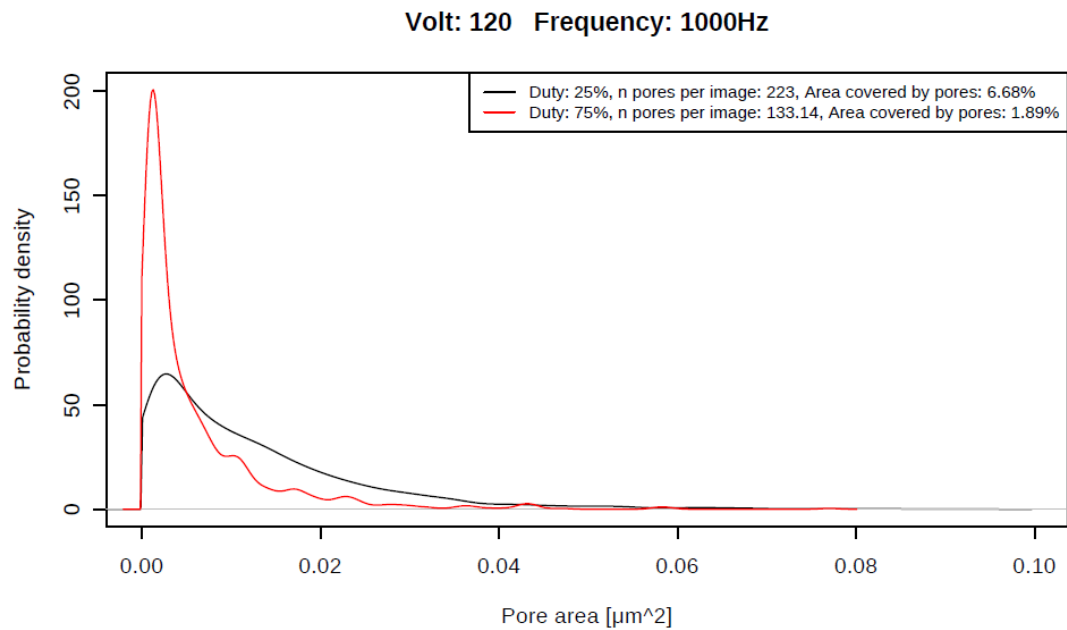


Figure 5.12 Density curves of samples anodized with both duties at frequency 20 Hz and voltage 220 V.

Reaching a voltage of 220 V, at frequency 20 Hz, the duty 25% presents an area covered by pores that is bigger than the DC, while the duty 75% is still under the DC value.

A comparison among DC and both duties at a frequency of 1000 Hz and voltage 120 V can be made looking at Figure 5.6 and 5.13.



*Figure 5.13 Density curves of samples anodized with both duties at frequency 1000 Hz and voltage 120 V.*

With a frequency of 1000 Hz and a voltage of 120 V, the area covered by pores for the duty 25% is much bigger respect to DC while is still smaller for the duty 75%, as reported above. A comparison among DC and both duties at a frequency of 1000 Hz and voltage 160 V can be made looking at Figure 5.9 and 5.14.

Volt: 160 Frequency: 1000Hz

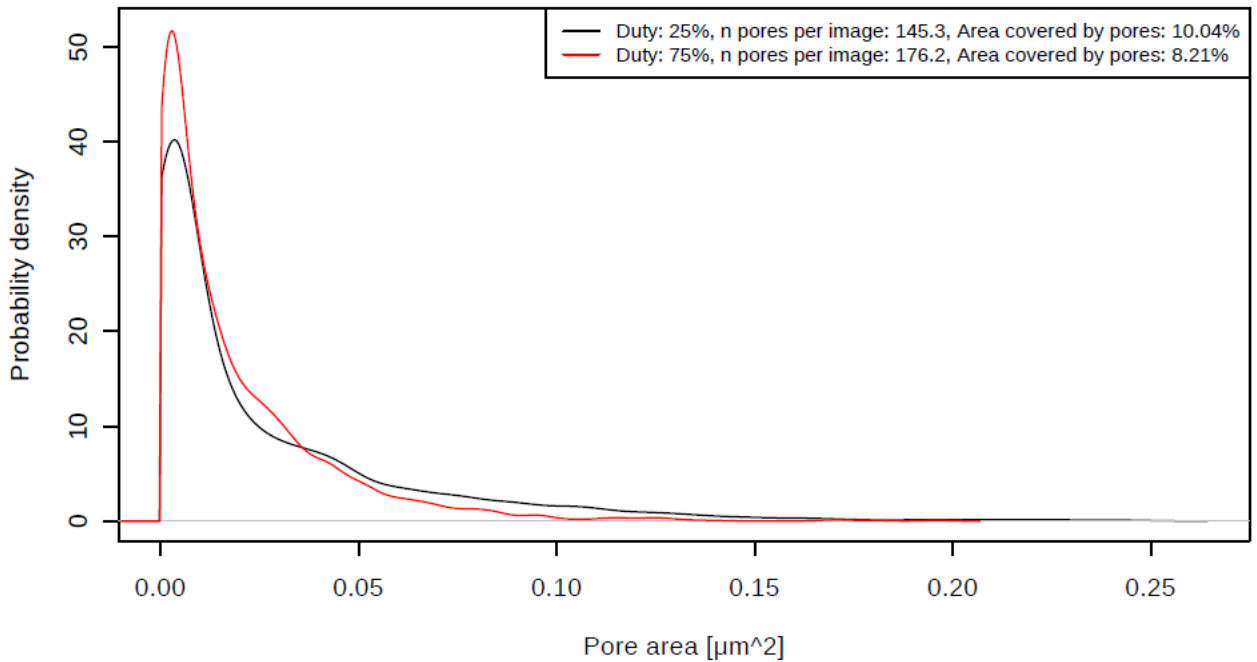


Figure 5.14 Density curves of samples anodized with both duties at frequency 1000 Hz and voltage 160 V.

Increasing the voltage to 160 V, the situation remains similar to the case of voltage 120 V. In fact, the area covered by pores is smaller for the duty 75%, followed by the DC case and the biggest one is the case of the duty 25%.

A comparison among DC and both duties at a frequency of 1000 Hz and voltage 220 V can be made looking at Figure 5.11 and 5.15.

Volt: 220 Frequency: 1000Hz

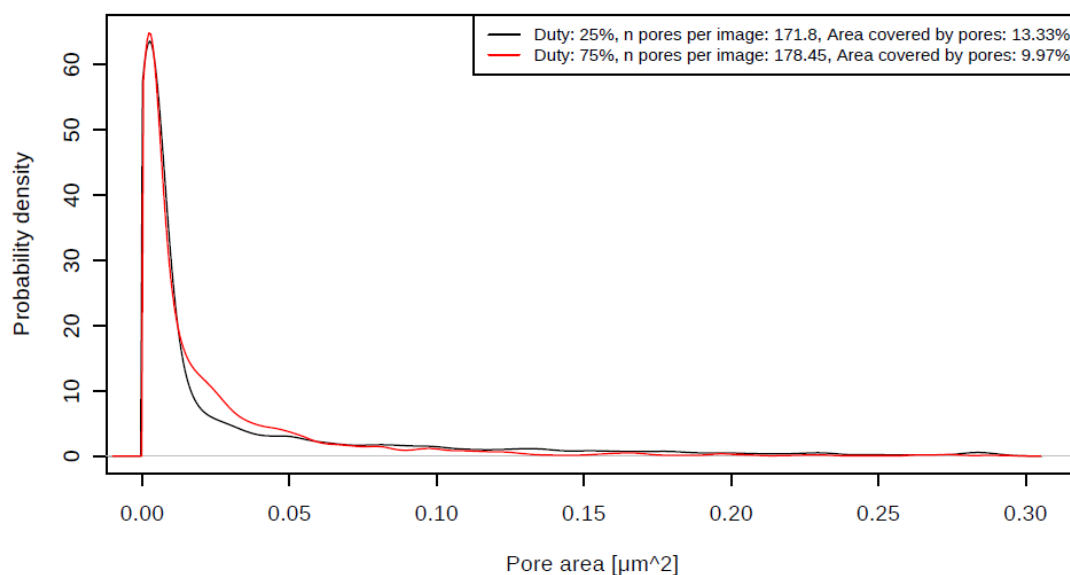


Figure 5.15 Density curves of samples anodized with both duties at frequency 1000 Hz and voltage 220 V.

Even in this case, reaching the maximum voltage of 220 V, the situation remains unchanged respect to the last two cases. In particular, the duty 75% shows the smallest area covered by pores, followed by the DC case and the biggest area covered is presented by the duty 25%.

In general, increasing the duty cycle to 75%, the area covered by pores results lower respect to both DC and duty 25%, in the same conditions, for each value of frequency and voltage.

When the value of the duty is lower, the situation depends on both frequency and voltage. In particular, for low frequency values and a voltage up to 160 V the area covered by pores is smaller respect to DC, in the same conditions. Increasing the voltage and keeping the same frequency, the tendency is inverted. At higher frequencies, for each value of voltage, the area covered by pores is bigger respect to DC, in the same conditions.

In conclusion, to have the lowest porosity possible, defined as the percentage of surface covered by pores, it is necessary to anodize at 120 V with a duty 75% and a frequency of 1000 Hz, obtaining the minimum value of 1.89%. On the other hand, to obtain a thicker oxide film it is possible to anodize at 220 V, the porosity, however, will increase from 1.89%, the minimum value, to 9.89% the minimum possible value for the voltage defined, with duty cycle 75% and frequency 20 Hz. In the same conditions of voltage and duty cycle but with a frequency of 1000 Hz, the porosity is only slightly larger, going from 9.89% to 9.97%.

## 5.2 Crystallinity

Looking at the results shown in paragraph 4.3.3, it is possible to analyse the trends of the anatase and rutile phase, in order to understand the effects of any parameter on the oxide composition.

- *Change in voltage with constant duty and frequency*

The first comparison was performed between the samples anodized with frequency equal to zero and direct current. Through the XRD results it was possible to calculate the area under the curves for each phase and compare them.

Table 5.1 Areas under the XRD curves for crystallinity phase of the oxide layer.

SAMPLE	ANATASE	RUTILE
120 V	264.99	1.605
160V	460.08	284.475
220V	19.275	346.455

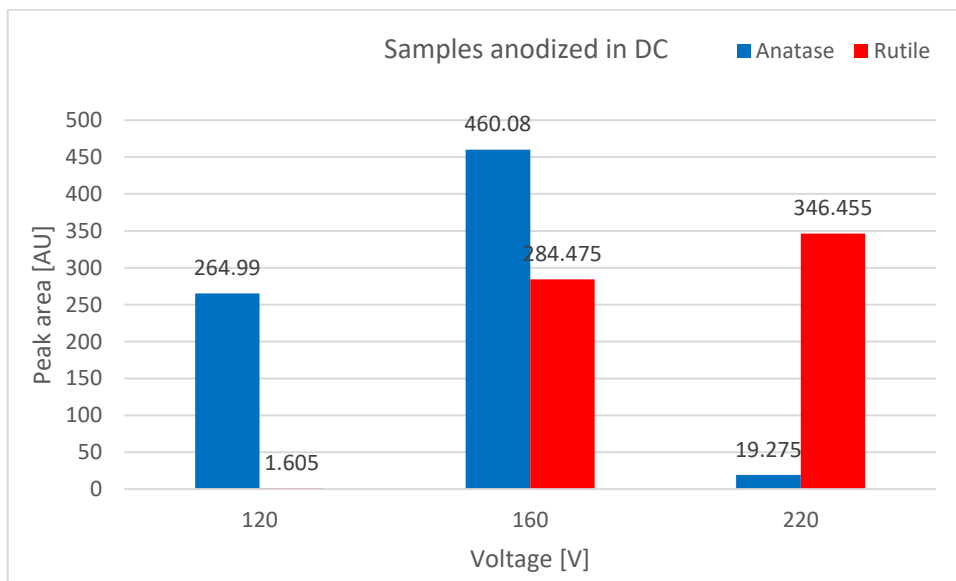


Figure 5.16 Areas of the anatase and rutile curves of anodized titanium at 120 V, 160 V and 220 V in DC.

This is the most studied case, where the crystallinity changes increasing the voltage applied to the sample during the anodization. As reported in many references [24,36], the anatase phase first increases and then decreases increasing the voltage, while the rutile phase, more thermodynamically stable than anatase, increases increasing the voltage. This analysis confirms the references' trend for the crystallinity of the oxide.

The second comparison was performed between the samples anodized with a duty cycle of 25% and a frequency of 20 Hz at 120 V, 160 V and 220 V. The differences are more evident if the numerical results of the areas under the curves are compared than simply looking at the XRD curves:

*Table 5.2 Areas under the XRD curves for crystallinity phase of the oxide layer of the anodized titanium with 25% duty cycle and a frequency of 20 Hz at 120 V, 160 V and 220 V.*

SAMPLES	ANATASE	RUTILE
<b>120V 25DUTY 20HZ</b>	191.52	25.965
<b>160V 25DUTY 20HZ</b>	246.675	179.7
<b>220V 25DUTY 20HZ</b>	ABSENT	154.755

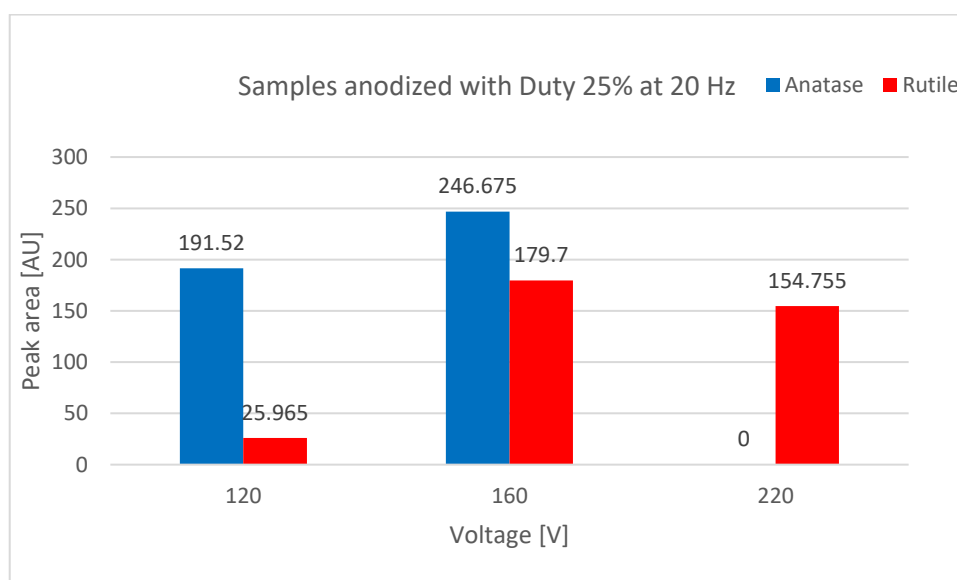


*Figure 5.17 Areas of anatase and rutile curves of titanium anodized with a duty cycle of 25% and a frequency of 20 Hz at 120 V, 160 V and 220 V.*

Using a duty cycle for the anodization different trends are present. The rutile is already present at 120 V, while in the classical DC anodization it was absent. Moreover, the two peaks are more similar at 160 V and the anatase is absent at 220 V, while a little peak was still present in the classical DC anodization. However, the most evident difference is the trend of the rutile phase: while in the DC anodization it increases increasing the voltage, changing the duty cycle it presents a maximum at 160 V and then it decreases.

Even if the area values are of the same order of magnitude with respect to the DC anodized curves, the maximum values for the second graph are lower (i.e. 1398 for the

DC anodized samples, instead of 398 for the duty 25% and 20 Hz frequency samples at 160 V). This result in wider and less pronounced peaks.

The third comparison is between samples anodized with a 25% duty cycle and a frequency of 1000 Hz at 120 V, 160 V and 220 V.

The areas under the curves are shown in Tab.5.4.

*Table 5.3 Areas under the XRD curves for crystallinity phase of the oxide layer of the anodized titanium with 25% duty cycle and a frequency of 1000 Hz at 120 V, 160 V and 220 V.*

SAMPLES	ANATASE	RUTILE
<b>120V 25DUTY 1000HZ</b>	280.035	101.97
<b>160V 25DUTY 1000HZ</b>	190.815	169.725
<b>220V 25DUTY 1000HZ</b>	62.73	201.06

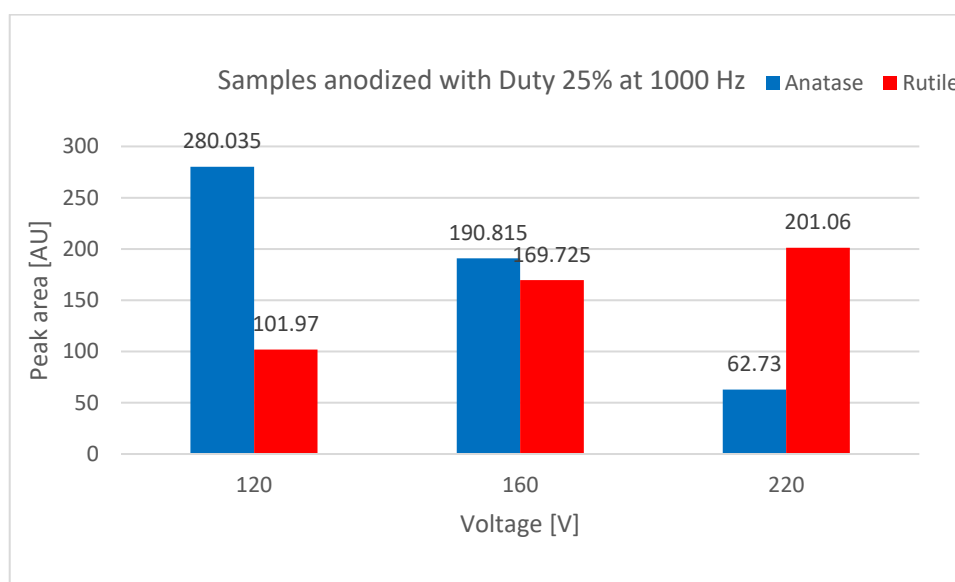


*Figure 5.18 Areas of anatase and rutile curves of titanium anodized with a duty cycle of 25% and a frequency of 1000 Hz at 120 V, 160 V and 220 V.*

Looking at the XRD curves reported in Fig.4.16, some differences are still present both with the standard DC anodization and the 25% duty cycle at 20 Hz. With respect with the first group, the rutile phase is present also at 120 V and it is more important at 160 V, with a splitting of the oxide between the two phases near to the 50%. With respect to the second case, the anatase is still present at 220 V and the curves are more pronounced and less wide.

However, also the trends of the areas are different: first of all, anatase does not present anymore a trend with a maximum, but it decreases constantly increasing the voltage, while both in the DC and 25% duty cycle at 20 Hz it presented a maximum at 160 V.

On the contrary, the rutile phase continuously increases like in the DC case and in contrast with the 25% duty cycle at 20 Hz.

Increasing the duty cycle percentage, it is possible to compare the last two groups of anodization with a duty cycle of 75% and frequencies of 20 Hz and 1000 Hz for the fourth and the fifth groups respectively.

*Table 5.4 Areas under the XRD curves for crystallinity phase of the oxide layer of the anodized titanium with 75% duty cycle and a frequency of 20 Hz at 120 V, 160 V and 220 V.*

SAMPLES	ANATASE	RUTILE
<b>120V 75DUTY 20HZ</b>	177.9	ABSENT
<b>160V 75DUTY 20HZ</b>	440.295	132.45
<b>220V 75DUTY 20HZ</b>	ABSENT	225.315

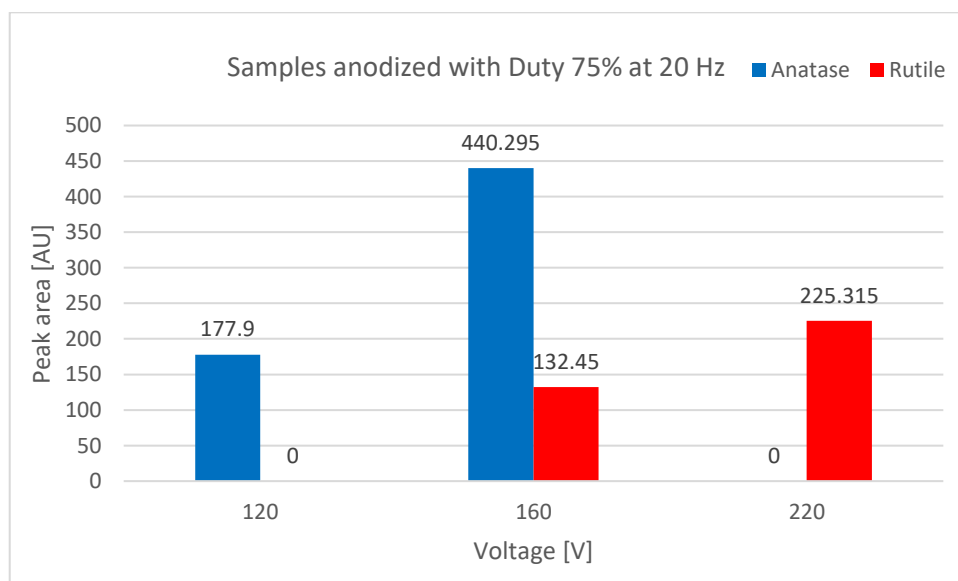


*Figure 5.19 Areas of anatase and rutile curves of titanium anodized with a duty cycle of 75% and a frequency of 20 Hz at 120 V, 160 V and 220 V.*

Starting from the XRD curves shown in Fig.4.16 and increasing the duty cycle percentage, the peaks are more pronounced and less wide than with lower duty cycle. It seems that increasing the duty cycle the curves are more similar to the DC trends. The main differences with the DC standard anodization are: the lower growth of the rutile phase at 160 V and a lower value of the rutile at 220 V.

However, to numerically evaluate the effect of the change of duty, it is important to analyse the trends of the areas under the curves. As for the DC case, the anatase trend exhibits a maximum at 160 V, but it is more pronounced, while the rutile phase continuously increases. The main difference with the lower duty at the same frequency is the trend of the rutile phase, which does no more present a maximum trend.

The last group of this section is characterized by a 75% duty cycle and a frequency of 1000 Hz.

The areas under the curves are reported in Tab.5.6:

*Table 5.5 Areas under the XRD curves for crystallinity phase of the oxide layer of the anodized titanium with 75% duty cycle and a frequency of 1000 Hz at 120 V, 160 V and 220 V.*

SAMPLES	ANATASE	RUTILE
<b>120V 75DUTY 1000HZ</b>	77.145	21.435
<b>160V 75DUTY 1000HZ</b>	259.095	99.165
<b>220V 75DUTY 1000HZ</b>	274.275	96.645

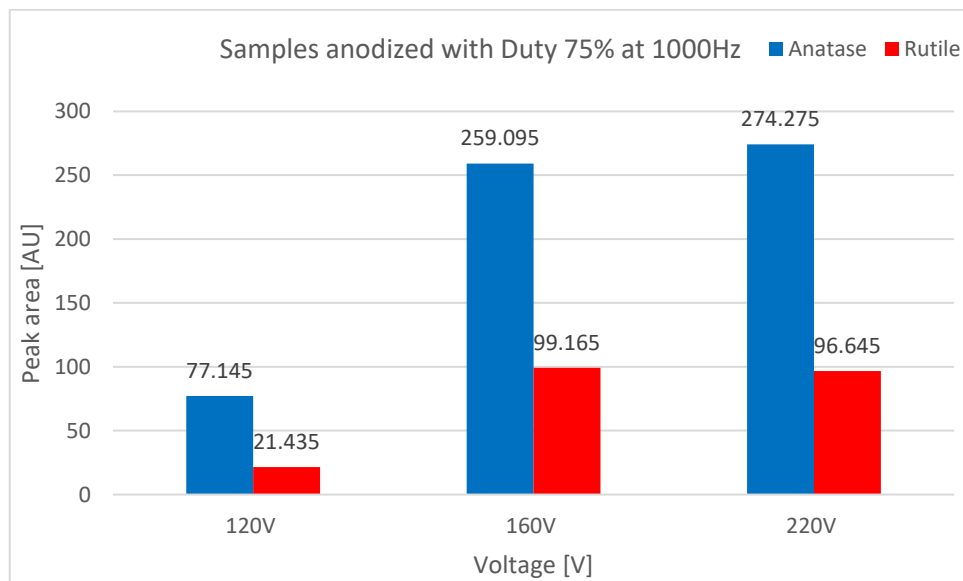


*Figure 5.20 Areas of anatase and rutile curves of titanium anodized with a duty cycle of 75% and a frequency of 1000 Hz at 120 V, 160 V and 220 V.*

As it is possible to see in Fig.4.18, in this case the anatase peak is less pronounced at 120 V than in the classical DC anodization, while at 160 V the anatase peak are more similar. The peak of rutile is less intense at 220 V and it is not the only phase present at this voltage. In facts, the more significant difference is that at 220 V the anatase peak is

still present and anatase is the most present phase. The peaks are more pronounced and not wide like with lower duty cycles.

The differences in the trends are more visible from the areas under the XRD curves, as is shown in Fig.5.20. In opposition to all the previous trends, the anatase phase increases increasing the voltage even if between the last two voltages the growth is less rapid. On the other hand, also rutile presents a different trend, with a stabilization after the 160 V.

- *Change in frequency with constant duty and voltage*

In the first group are collected all the sample anodized at a voltage of 120 V and a duty cycle of 25%.

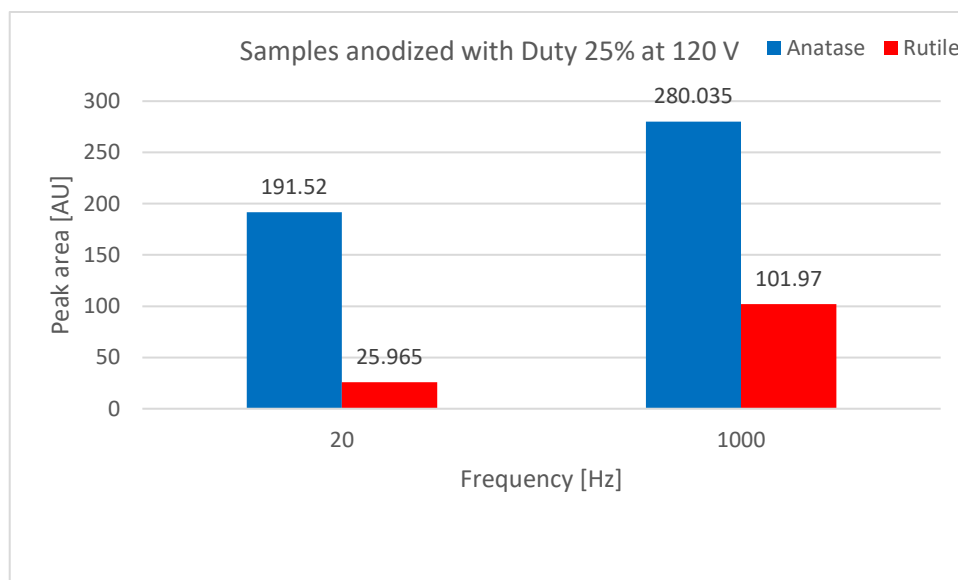


*Figure 5.21 Areas of anatase and rutile curves of titanium anodized with a duty cycle of 25% and a voltage of 120 V at 20 Hz and 1000 Hz.*

Looking at Fig.4.19 increasing the frequency, the peaks of anatase and rutile seems to be more pronounced, while at lower frequency the curves are wider. So, the presence of the two crystal phases, increasing the frequency, is in both cases accentuated.

However, analysing the trends of the areas under the curves (Fig.5.21), in this case increasing the frequency maintaining the same duty cycle and voltage the areas of both anatase and rutile increases too.

In the second group are collected the samples anodized with a voltage of 160 V and a duty cycle of 25%.

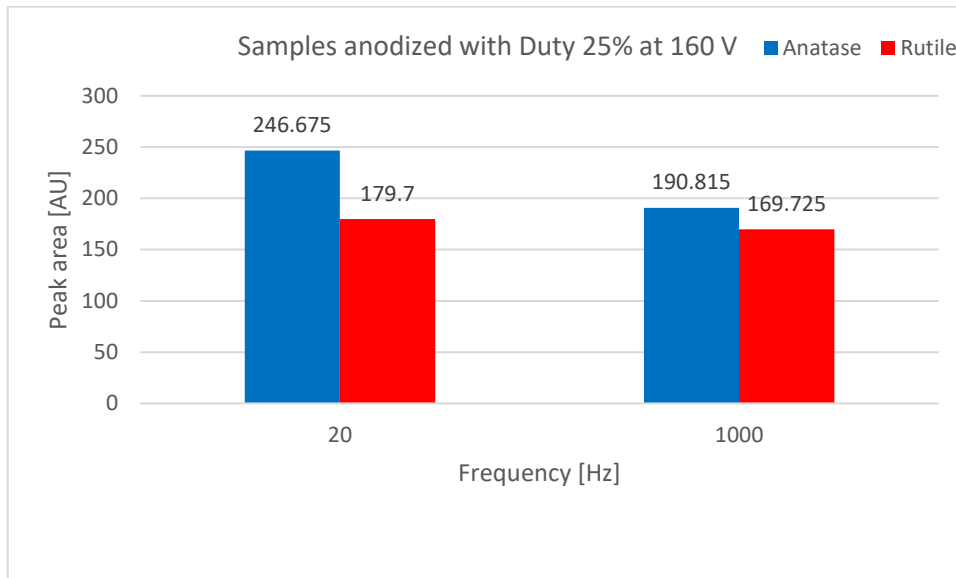


*Figure 5.22 Areas of anatase and rutile curves of titanium anodized with a duty cycle of 25% and a voltage of 160 V at 20 Hz and 1000 Hz.*

Looking at Fig.4.20, in this case, the frequency has an opposite effect on the phase composition of the oxide layer. Increasing the frequency at 160 V, the peaks of anatase and rutile are both lower, but they also present a different distribution. In fact, the rutile phase at high frequency exceeds the anatase phase and even at lower frequency its peaks value is very similar to the anatase one (i.e. 792 of anatase and 720 of rutile).

The numerical results of the areas under the curves (Fig.5.22) are saying that the anatase phase is still the predominant phase at both the frequency even if the rutile peak exceeds the anatase one. This means that the anatase peak is wider than the rutile one. In contrast to the trends of anatase and rutile at 120 V and 25% duty cycle, both phases decrease increasing the frequency.

In the third group the samples anodized at 220 V and 25% of duty cycle, but at different frequencies.

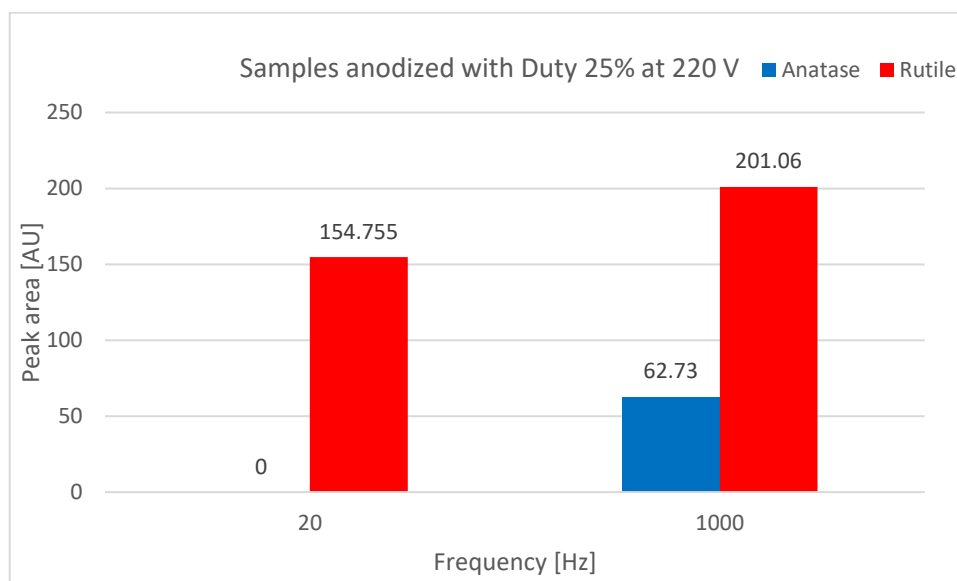


*Figure 5.23 Areas of anatase and rutile curves of titanium anodized with a duty cycle of 25% and a voltage of 220 V at 20 Hz and 1000 Hz.*

At high voltages, the frequency does not modify the prevalence of rutile phase on the anatase phase. In Fig.4.21 it is possible to see that both the distributions exhibit a prevalence of rutile phase over anatase. However, at high frequency the anatase phase is not eliminated, but is still present besides the high anodization voltage. Being the frequency the reciprocal of the working time, a high frequency results in a short working time which causes a stop in the micro arcs propagation and an instantaneous freeze of the phase composition of the oxide. The rapid stop and quench of the oxide layer can be the cause of the presence of the anatase phase still at so high anodization voltages.

The trends of the areas confirm the increasing of both the phases increasing the frequency and the presence of the anatase phase even at 220 V with 1000 Hz of frequency, while with low frequency it is absent.

With this graph, all the samples anodized with a duty cycle of 25% have been shown. In the next pages there are all the sample anodized with a duty of 75%.

This is the first group of the sample anodized with a duty cycle of 75%. The voltage used is 120 V and the effects of the frequency are compared.

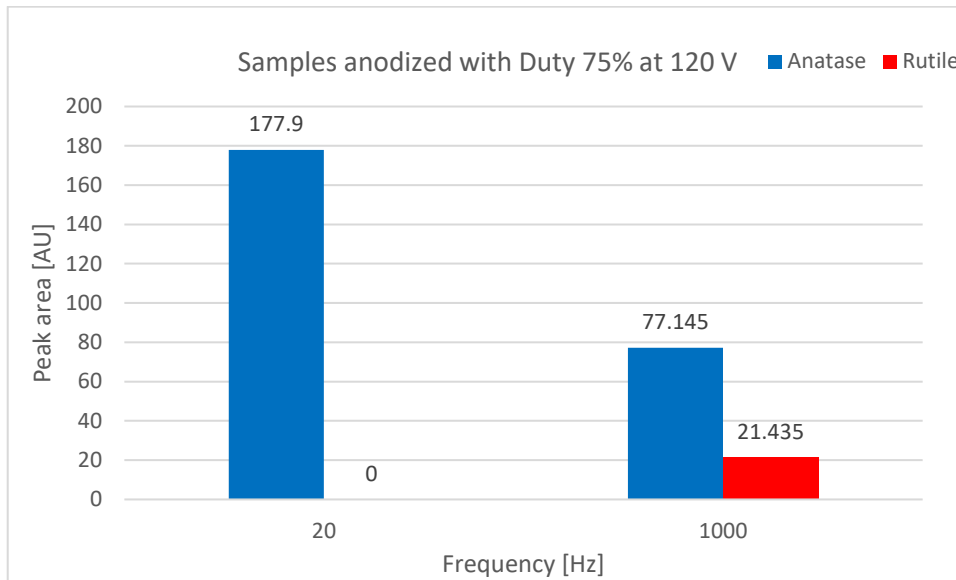
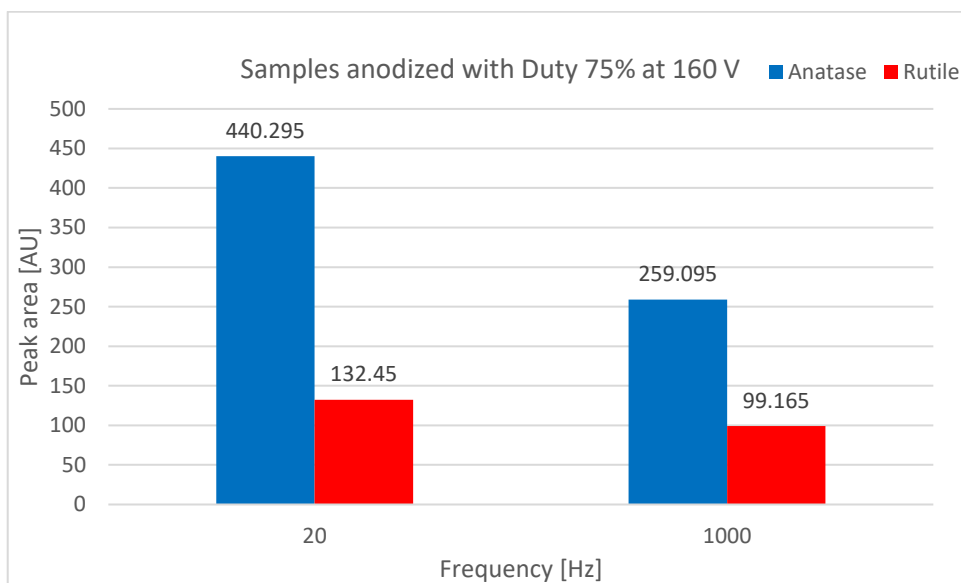


Figure 5.24 Areas of anatase and rutile curves of titanium anodized with a duty cycle of 75% and a voltage of 120 V at 20 Hz and 1000 Hz.

Looking at Fig.4.22 the change in duty cycle causes the total absence of the rutile phase at both high and low frequencies, fact that has already happened for the DC anodization. This trend at low voltages can support the idea of the approaching of the curves to the DC trend increasing the duty percentage. However, increasing the frequency the peak is lower while at high frequency it is more pronounced. This is in contrast with the trends observed in the case of duty 25%. It seems that the effect of the change of duty cycle is dominant over the change of frequency for what concerns the phase distribution.

Looking at the area distributions, shown in Fig.5.24, while the anatase phase decreases strongly, the rutile phase increases, but with a very low value (i.e. 21.435). The first trend is in contrast with what happened at the same frequencies and voltage with a duty cycle of 25%.

In this group the samples anodized at 160 V and 75% of duty cycle with different frequencies are shown.



*Figure 5.25 Areas of anatase and rutile curves of titanium anodized with a duty cycle of 75% and a voltage of 160 V at 20 Hz and 1000 Hz.*

In Fig.4.23 the XRD results are shown and, in this case, the two rutile peaks are identical both at lower and higher frequency. On the contrary, the anatase peaks are different: while at high frequency it is less pronounced, with low frequency the peak is well-defined with values very similar to the DC anodization.

The analysis of the areas under the curves reflects the trends of the peaks: the rutile values are very similar (i.e. 132.45 and 99.165) and the value of the anatase phase at low frequency is very similar to the one of the DC anodization (i.e. 460.08). In both cases increasing the frequency, the areas of both rutile and anatase decrease like in the 25% duty cycle anodizations at the same voltage.

These are the last graphs of this section and they show the areas of the samples anodized at 220 V with 75% duty cycle and different frequencies.

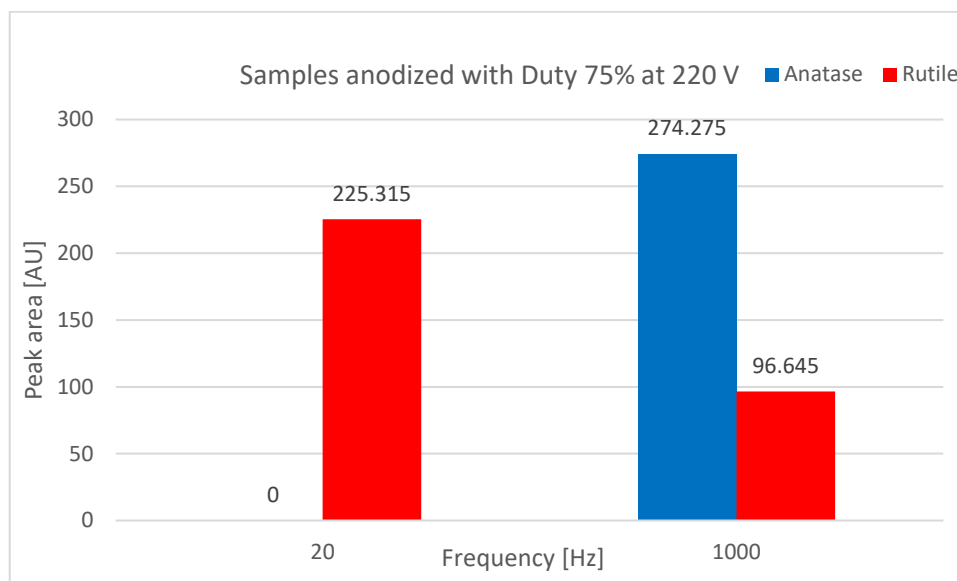


*Figure 5.26 Areas of anatase and rutile curves of titanium anodized with a duty cycle of 75% and a voltage of 220 V at 20 Hz and 1000 Hz.*

Just looking at the trend of the XRD results (Fig.4.24), at high voltages the effect of frequency is stronger and more evident than at lower voltages. When the frequency is high the anatase phase is still present at high voltages, while the rutile phase is just a minor part. On the contrary at low frequencies the anatase phase is absent. Low frequencies imply a long working time and a longer time for the micro arc discharge to convert the anatase phase into the rutile one. Increasing the duty cycle and decreasing the frequency the trends are more and more similar to the DC anodization trends.

Analysing the areas under the curves (Fig.5.26), it is possible to see that the anatase phase increases, increasing the frequency even at very high voltages, like in this case 220 V, while in the DC anodization the anatase after a maximum tends to decrease at high voltages. With respect to the 25% duty cycle, the trend of the anatase is confirmed (it increases in both conditions), while the rutile is now the opposite. In facts, with a duty cycle of 25% the rutile phase increases, while with a duty of the 75% it decreases.

- *Change in duty cycle with constant frequency and voltage*

The first set of graphs shows all the samples anodized at 120 V, 160 V and 220 V with 20 Hz of frequency and different duty cycles, while the last six graphs show the areas under the curves of the samples anodized at the same conditions but with 1000Hz of frequency.

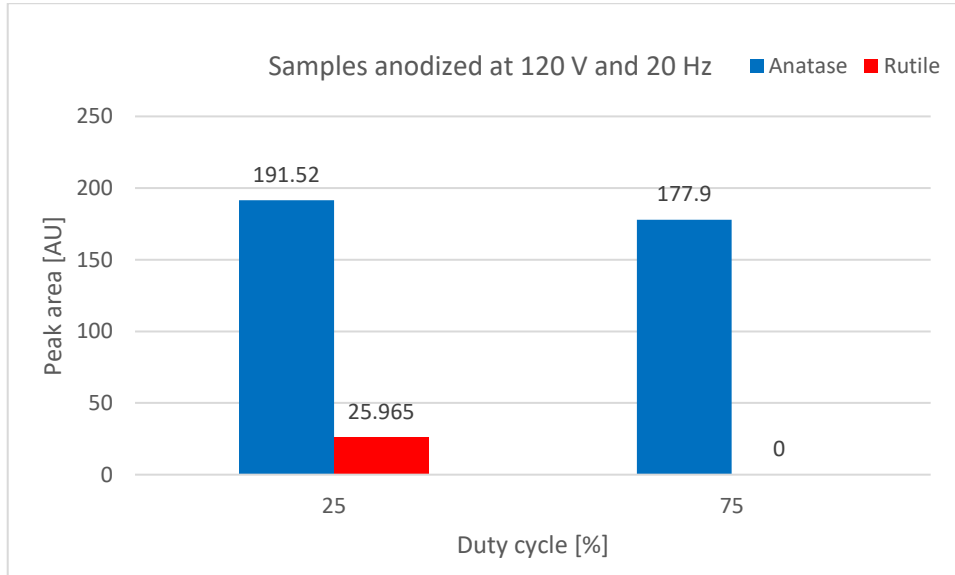


*Figure 5.27 Areas of anatase and rutile curves of titanium anodized with 20 Hz of frequency at 120 V with 25% and 75% duty cycle.*

In Fig.4.25, the XRD curves show some differences between the two duty cycles applied. The most important is the presence of the rutile phase even at 120 V with a duty cycle of the 25% which is in contrast with the DC trend, and its absence at the same voltage but with a duty cycle higher (i.e. 75%). However, both the peaks are lower, increasing the duty cycle.

Analysing the trends of the areas under the XRD curves (Fig.5.27), the trends of the XRD curves are confirmed. The rutile phase is present at lower duty cycle, but it is absent at higher duty. This trend confirms the hypothesis that, increasing the duty cycle at low frequency the oxide behaviour, and also its crystallinity, approaches the DC trend. In fact, the rutile phase is absent at 120 V in the DC anodization like with a duty of 75%. It is important to remember that in this comparison, the samples are anodized both at low frequency, so with long working time.

In the next figure the samples anodized at 160 V with frequency of 20 Hz and duty cycles of 25% and 75% are analysed.

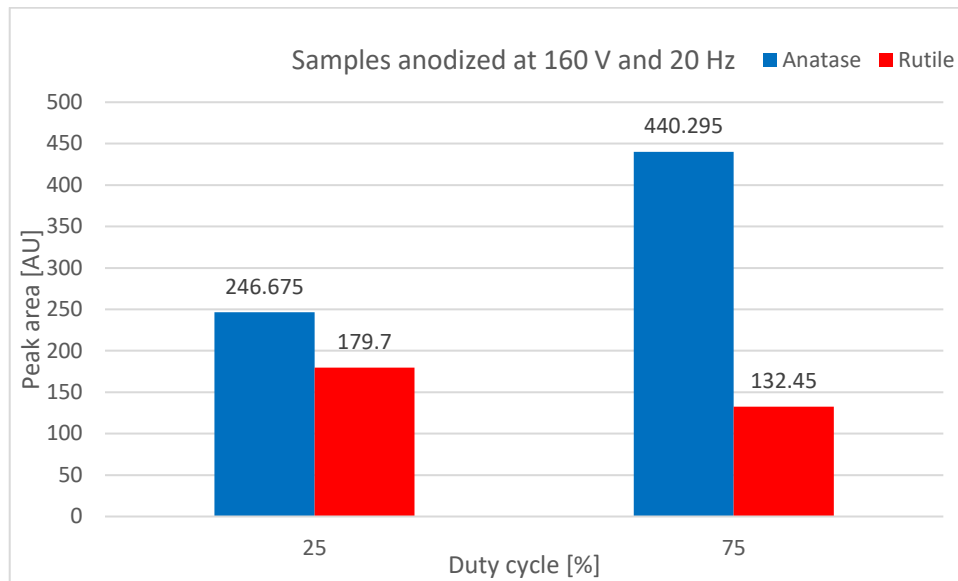


*Figure 5.28 Areas of anatase and rutile curves of titanium anodized with 20 Hz of frequency at 160 V with 25% and 75% duty cycle.*

In Fig.4.26, the differences between the two duty cycles are evident, while the lower duty presents a distribution which is almost equal for anatase and rutile, the higher duty presents a more pronounced peak for the anatase and a lower peak for the rutile with a clear difference between the two. At low frequency and high duty cycle, the trend is still similar to the DC trend.

The analysis of the distribution of the areas under the XRD curves, confirms the analysis of the trends. The anatase and rutile phase at low duty cycle is almost the same (i.e. 246.675 and 179.7), while increasing the duty cycle the difference is more remarkable. To numerically confront the data, it is just possible to look at the area of the DC areas at 160 V (i.e. 460.08 for the anatase and 284.475 for the rutile) which are close to the 75% duty areas at 20 Hz (i.e. 440.295 and 132.45 for anatase and rutile respectively).

In the last graph at this frequency (20 Hz) the samples anodized at 220 V and with duty of 25% and 75% are shown.

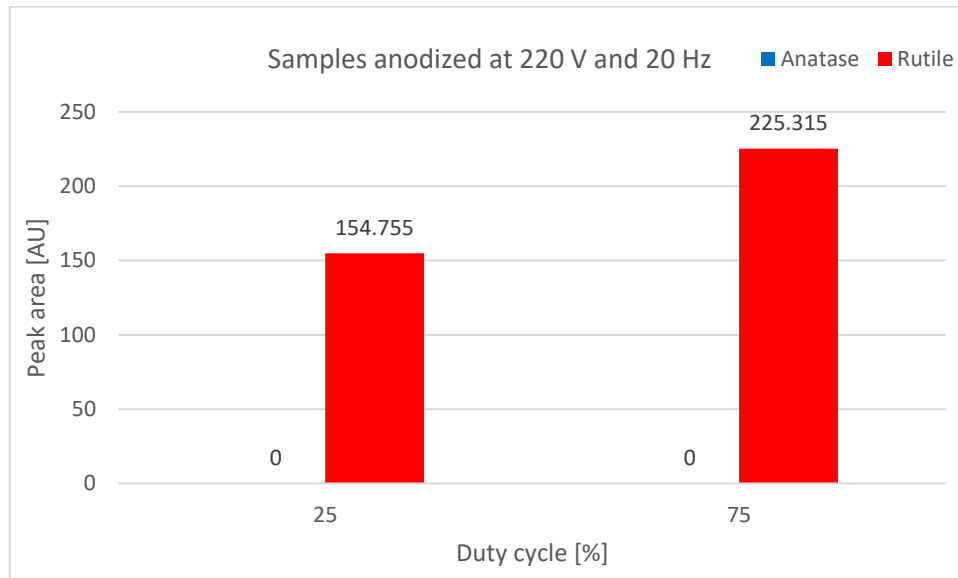


*Figure 5.29 Areas of anatase and rutile curves of titanium anodized with 20 Hz of frequency at 220 V with 25% and 75% duty cycle.*

From the Fig.4.27, it is possible to derive the absence of the anatase phase for both the samples and so it is possible to say that at so high voltages and temperature in the composition of the oxide the rutile phase prevails, independently from the duty cycle used. However, the peak of the rutile phase is higher at higher duty cycle.

To numerically evaluate the trends of the areas, in Fig.5.29, the areas under the curves are shown. Even in this case the higher duty cycle exhibits a trend more similar to the DC one. In facts, the area of the rutile in the DC anodization was 346.455 while with a duty cycle of 75% it is equal to 225.315 which is closer to the DC value than the value of the 25% duty cycle anodization.

In the last three graphs the trends of rutile and anatase areas will be shown at a frequency of 1000 Hz and voltages of 120 V, 160 V and 220 V with different duty cycles.

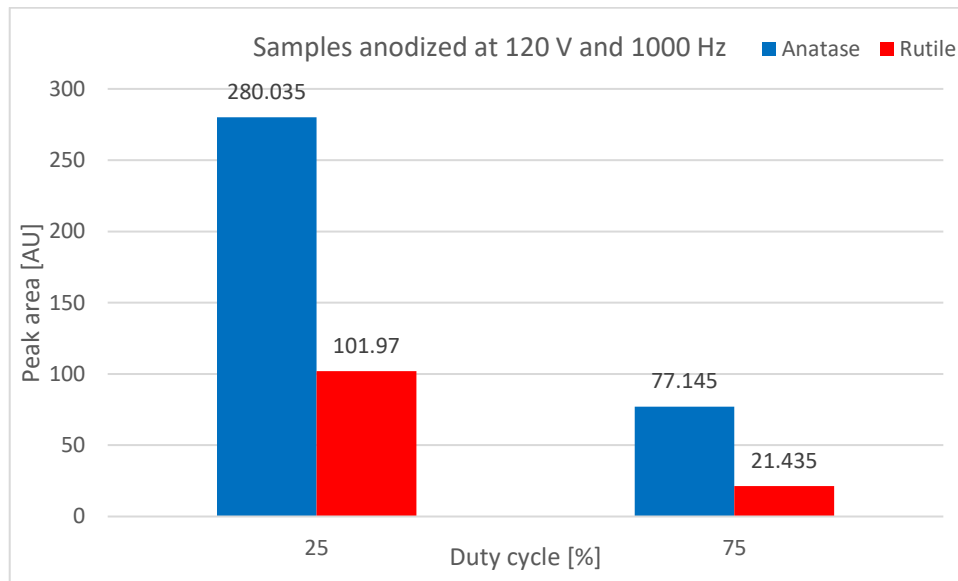


*Figure 5.30 Areas of anatase and rutile curves of titanium anodized with 1000 Hz of frequency at 120 V with 25% and 75% duty cycle.*

From Fig.4.28, it is possible to see that the effect of frequency at low voltages is strong: the rutile phase is already present even at 120 V, while at lower frequency (i.e. 20 Hz) it is absent. The two peaks of the anatase and rutile phase with a low duty cycle (i.e. 25%) are both higher and more pronounced than the ones at higher duty (i.e. 75%).

Looking at the analysis of the areas, the results of the duty 75% are no more similar to the DC ones, but the increasing of the frequency decreases strongly the value of anatase phase. So, the frequency modifies the distribution of the phases changing the working time on the samples and even if the sample is anodized for the 75% of the time, the on-off speed (set with the frequency value) decreases the overall working time. For lower duty cycle, the increasing of the velocity of the on-off increases the values of both anatase and rutile.

In this graph is presented the distributions of the areas of rutile and anatase anodized at different duty cycles but with voltage equal to 160 V and 1000 Hz.

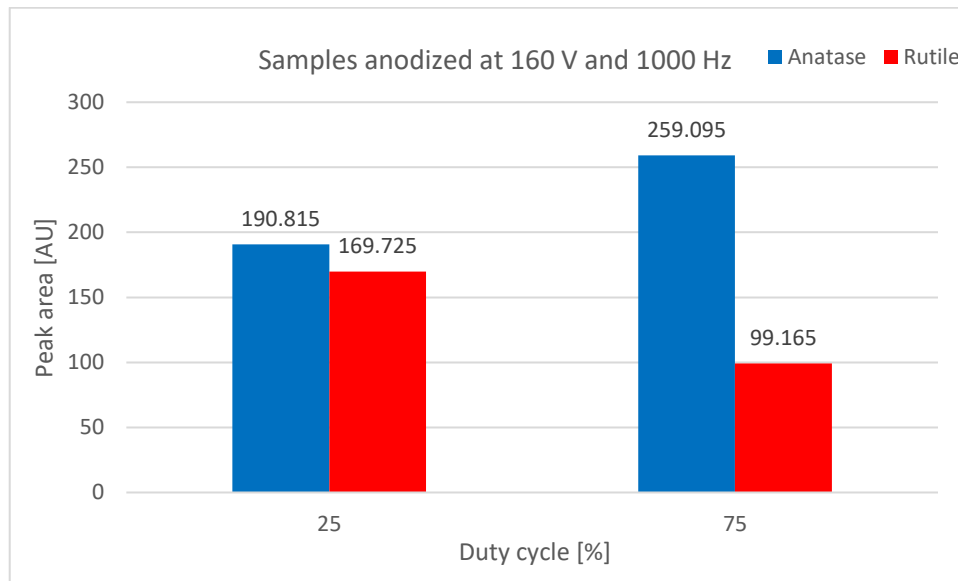


*Figure 5.31 Areas of anatase and rutile curves of titanium anodized with 1000 Hz of frequency at 160 V with 25% and 75% duty cycle.*

Increasing the voltage, it is possible to see in Fig.4.29, that the rutile phase increases for both the duty cycles, while the peak of anatase is less pronounced than the one at 120 V. However, the distribution between the two duty cycles is different: at low duty the difference between the two peaks is less pronounced and the anatase peak is as high as the rutile one, while at higher duty cycles (like 75%), the difference between the two peaks is remarkable and the anatase peak is higher than the rutile one. The increasing of frequency causes a decrease in the anatase value for both the duties (the maximum value of the sample anodized at 20 Hz and 75% of duty cycle is 1265 AU, while at higher frequency it is 805 AU. For the samples anodized at 20Hz and 25% of duty cycle the maximum was 772 AU and at higher frequency it is 602 AU), while the rutile phase is on both cases increased. It is possible that a high velocity of on-off keeps the temperature low and the rutile phase which is more thermodynamically stable is so more favourite.

Analysing the areas distributions, (Fig.5.31) the trends are confirmed and the difference between the peaks of the anatase and rutile are more pronounced at 75% of duty.

In the last graph, the samples anodized at 220 V and 1000 Hz with different duties are analysed.

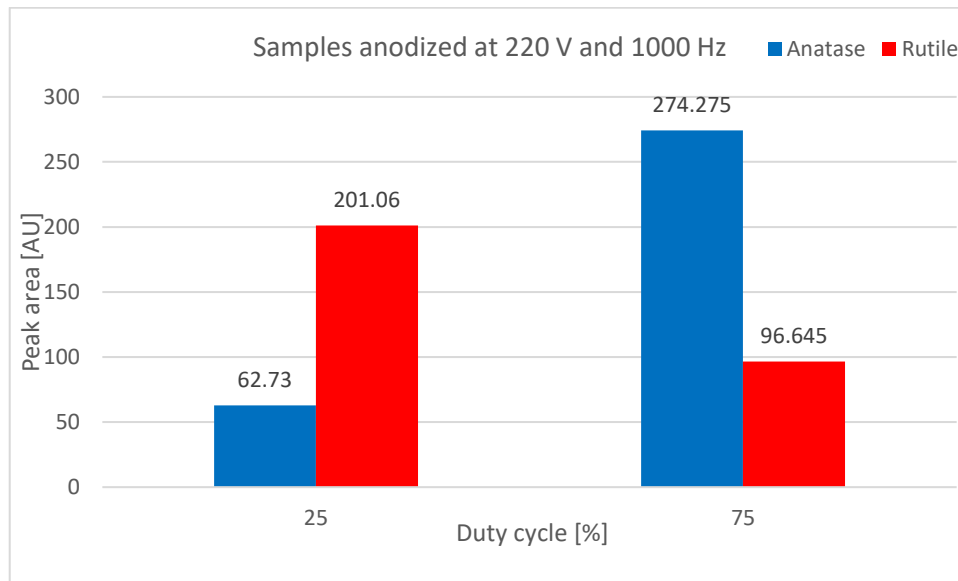


*Figure 5.32 Areas of anatase and rutile curves of titanium anodized with 1000 Hz of frequency at 220 V with 25% and 75% duty cycle.*

In Fig.4.30, the curves of samples anodized at 220 V and 1000 Hz at different duties are shown. The curves appear different, with the rutile phase which prevails in the lower duty cycle and the anatase phase which prevails in the higher duty. At high frequency and voltages, the effect of duty cycle is stronger than at lower frequency or at lower voltages.

Also, the analysis of the areas confirms this trend with the anatase phase that prevails with high duty cycles. This is in contrast to what happens at low frequency, where the only phase present was the rutile at so high voltages. So, the presence of the anatase even at 220 V can be explained by the velocity of the stop and quench of the oxide layer, while the different distribution of the two phases is dependent on the duty chosen.

### 5.3 Corrosion resistance

After all the corrosion tests, it is now important to numerically compare the different curves and the corrosion resistance of each sample. The corrosion data, organized fixing two variable and varying only one, will be analysed in the following paragraphs.

- *Change in voltage with constant duty cycle and frequency*

In the first set of data (Tab.5.7, 5.8, 5.9) all the sample anodized at different voltages in DC are collected:

*Table 5.6 Pitting potentials, current densities and number of the sample anodized in DC at 120 V, 160 V and 220 V.*

SETTINGS	PITTING POTENTIAL [V]	CURRENT DENSITY [A/M <sup>2</sup> ]	NUMBER OF THE SAMPLE
DC-120 V	3,904	0,0457	21
DC-120 V	2,91	0,000476	6
DC-160 V	--	--	20
DC-160 V	--	--	5
DC-220 V	3,236	0,006687	3

*Table 5.7 Current densities and number of the sample anodized in DC at 120 V, 160 V and 220 V and a potential equal to 1 V.*

SETTINGS	POTENTIAL [V]	CURRENT DENSITY [A/m <sup>2</sup> ]	NUMBER OF THE SAMPLE
DC - 120 V	1	0,001	21
DC - 120 V	1	0,0014	6
DC - 160 V	1	0,00103	20
DC - 160 V	1	0,00127	5
DC - 220 V	1	4,47E-05	3

*Table 5.8 Current densities and number of the sample anodized in DC at 120 V, 160 V and 220 V and a potential equal to 2 V.*

SETTINGS	POTENTIAL [V]	CURRENT DENSITY [A/M <sup>2</sup> ]	NUMBER OF THE SAMPLE
DC - 120 V	2	0,00306	21
DC - 120 V	2	0,00009	6
DC - 160 V	2	0,00389	20
DC - 160 V	2	0,00619	5
DC - 220 V	2	0,0001959	3

It is possible to see from the pitting potential that while the 160 V DC anodization is immune from pitting corrosion, the 120 V and 220 V are subjected to pitting corrosion. The pitting potentials are in between 2.91 V and 3.904 V and the samples are corroded by the bromide solution. The fact that the 220 V sample is corroded (with a low pitting potential) is due to the porosity of the oxide layer that is higher than the 160 V. In facts, looking at Fig.5.1 it is possible to see that the porosity of the sample anodized with 120 V is the higher between the three, while the 220 V is in the middle and the 160 V is the lower. However, the behaviour of the anodized titanium in bromide is, generally, better and better increasing the voltage. It is not possible to determine if the heating of the solution of bromide is the cause of the change of behaviour at high anodization voltages, because of the unique test performed. From the 1 V and 2 V current densities it is possible to see that the 220 V is less active than the 160 V and 140 V being its values (Tab.5.8 and Tab.5.9) lower. These data can suggest that the pitting signal present at 220 V can be the result of an inhomogeneity in the sample itself that causes pitting initiation.

In the figure below are shown the average of the current densities at the pitting potential, at 1 V and 2 V and their standard deviations.

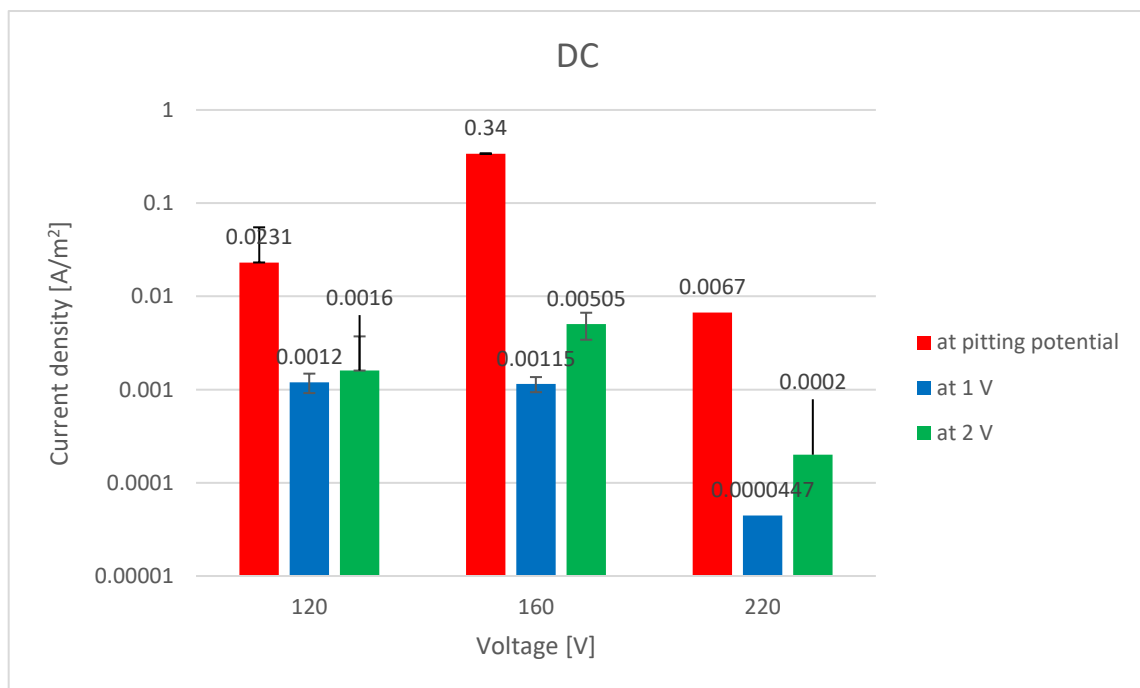


Figure 5.32 Average of the current densities at 1 V, 2 V and at pitting potential with standard deviations.

From the figure below, it can be deduced that the 160 V anodization exhibits the highest activity among all the other samples. Even if the 220 V pits at a quite low potential, its activities are the lowest among all the others.

In this tables are shown the corrosion test data of the samples anodized at 120 V, 160 V and 220 V with duty cycle of 25% and a frequency of 20 Hz.

*Table 5.9 Pitting potentials, current densities and number of the sample anodized with duty cycle of 25% and a frequency of 20 Hz at 120 V, 160 V and 220 V.*

SETTINGS	PITTING POTENTIAL [V]	CURRENT DENSITY [A/M <sup>2</sup> ]	NUMBER OF THE SAMPLE
DUTY 25% - 120 V - 20HZ	1,89	0,005589	27
DUTY 25% - 160 V - 20 HZ	4,643	0,083	11
DUTY 25% - 160 V - 20HZ	5,816	0,6054	26
DUTY 25% - 220 V - 20 HZ	--	--	10

*Table 5.10 Current densities and number of the sample anodized with duty cycle of 25% and a frequency of 20 Hz at 120 V, 160 V and 220 V at 1 V.*

SETTINGS	POTENTIAL [V]	CURRENT DENSITY [A/M <sup>2</sup> ]	NUMBER OF THE SAMPLE
DUTY 25%-120V- 20Hz	1	0,00215	27
DUTY 25% - 160 V - 20 HZ	1	0,003228	11
DUTY 25%-160V- 20HZ	1	0,002973	26
DUTY 25% - 220 V - 20 HZ	1	0,000969	10

*Table 5.11 Current densities and number of the sample anodized with duty cycle of 25% and a frequency of 20 Hz at 120 V, 160 V and 220 V at 2 V.*

SETTINGS	POTENTIAL [V]	CURRENT DENSITY [A/M <sup>2</sup> ]	NUMBER OF THE SAMPLE
DUTY 25%-120V- 20Hz	2	--	27
DUTY 25% - 160 V - 20 HZ	2	0,0078879	11
DUTY 25%-160V- 20HZ	2	0,0363	26
DUTY 25% - 220 V - 20 HZ	2	0,00661	10

Inserting a duty cycle and a frequency (i.e. 25% and 20 Hz) the trend is different than the DC corrosion test trends. Here, the 220 V is the more resistant from the pitting corrosion while the 120 V is the more subjected to pitting. This behaviour can be attributed to the decreasing of the current density circulating on the sample which moves the resistance of the oxide from 160 V to 220 V with respect to the DC samples. However, this trend is in contrast with the porosity of the samples (Fig.5.2): in facts, not only the porosity increases increasing the voltage, but also the dimensions of the pores change. The higher the voltage the bigger are the pores while their number is of the same order of magnitude (i.e. 190, 171.55 and 172 for 120 V, 160 V and 220 V respectively). It seems that the presence of bigger pores does not influence the corrosion resistance, maybe due to the thicker oxide layer at high voltages and the increasing of the diffusional resistances, but more tests have to be performed.

Looking at the current densities at 1 V and 2 V (Tab.5.12 and Tab.5.11), fixing duty cycle and frequency the sample anodized at 220 V is always the less active in accord to the pitting data. Increasing the potential, the corrosion resistance increases.

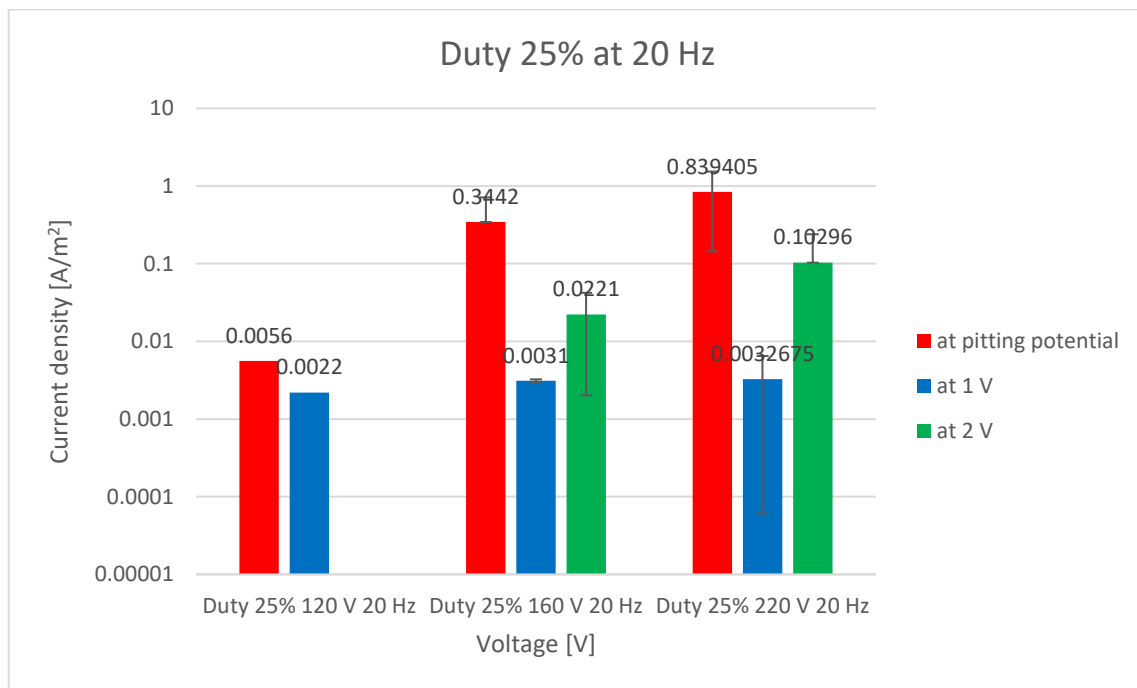


Figure 5.33 Average of the current densities at 1 V, 2 V and at pitting potential with corresponding standard deviations of samples anodized at 120 V, 160 V and 220 V with 20 Hz and 25% duty cycle.

The trend of the current densities is increasing, increasing the voltage of anodization at low duty cycle and low frequency. This fact confirms the previous analysis, but it can also deduced that the 220 V is the most active among all the other.

In the following table are collected some meaningful data of the sample anodized at 1000 Hz and 120 V, 160 V and 220 V with a duty cycle of 25%.

*Table 5.12 Pitting potentials, current densities and number of the sample anodized with duty cycle of 25% and a frequency of 1000 Hz at 120 V, 160 V and 220 V.*

SETTINGS	PITTING POTENTIAL [V]	CURRENT DENSITY [A/M <sup>2</sup> ]	NUMBER OF THE SAMPLE
DUTY 25% - 120 V - 1000 Hz	4,743	0,1547	24
DUTY 25% - 120 V - 1000 HZ	--	--	8
DUTY 25% - 160 V - 1000 HZ	2,716	0,01684	7
DUTY 25% - 160 V -1000 HZ	5,19004	0,2828	23
DUTY 25% - 220 V - 1000 Hz	--	--	22

*Table 5.13 Current densities and number of the sample anodized with duty cycle of 25% and a frequency of 1000 Hz at 120 V, 160 V and 220 V at 1 V.*

SETTINGS	POTENTIAL [V]	CURRENT DENSITY [A/M <sup>2</sup> ]	NUMBER OF THE SAMPLE
DUTY 25% - 120 V - 1000 Hz	1	0,001248	24
DUTY 25% - 120 V - 1000 HZ	1	0,03548	8
DUTY 25% - 160 V - 1000 HZ	1	0,001961	7
DUTY 25% - 160 V -1000 HZ	1	0,001184	23
DUTY 25% - 220 V - 1000 HZ	1	0,00682388	22

Table 5.14 Current densities and number of the sample anodized with duty cycle of 25% and a frequency of 1000 Hz at 120 V, 160 V and 220 V at 2 V.

SETTINGS	POTENTIAL [V]	CURRENT DENSITY [A/M <sup>2</sup> ]	NUMBER OF THE SAMPLE
DUTY 25% - 120 V - 1000 Hz	2	0,01618	24
DUTY 25% - 120 V - 1000 HZ	2	0,07969	8
DUTY 25% - 160 V - 1000 HZ	2	0,006506	7
DUTY 25% - 160 V -1000 HZ	2	0,0011845	23
DUTY 25% - 220 V - 1000 HZ	2	0,019939	22

Looking at the pitting potentials (Tab.5.13), the data are not clear: in facts of the two 120 V just one presents pitting while the other is not affected by pitting corrosion. However, the graph (Fig.4.32) of the sample immune from pitting (i.e. 8) is very disturbed and its reliability can be questionable. Looking at the porosity (Fig.5.3), it increases with the voltage as for the 25% duty cycle, but the distribution of the dimension of the pore is different. Here (i.e. at 1000 Hz), the pores are more homogeneous and the porosity curve is less wide for the 160 V and 220 V than at 20 Hz, but the comparison between different frequency will be analysed in detailed in the following pages. So, just looking at porosity and pitting potential, it seems that the increasing of the porosity does not influence the corrosion resistance, because both increases increasing the anodization voltage with this duty cycle. However, it is important to remember that the porosity is not sufficient to characterize the corrosion phenomenon because increasing the potential also the thickness of the oxide layer increases and it results in a higher corrosion resistance.

The current densities at 1 V and 2 V give back another important information: the 220 V curve is the most active at 1 V, except for the sample number 8, and also at 2 V is very active, but its activity never results in a pitting initiation.

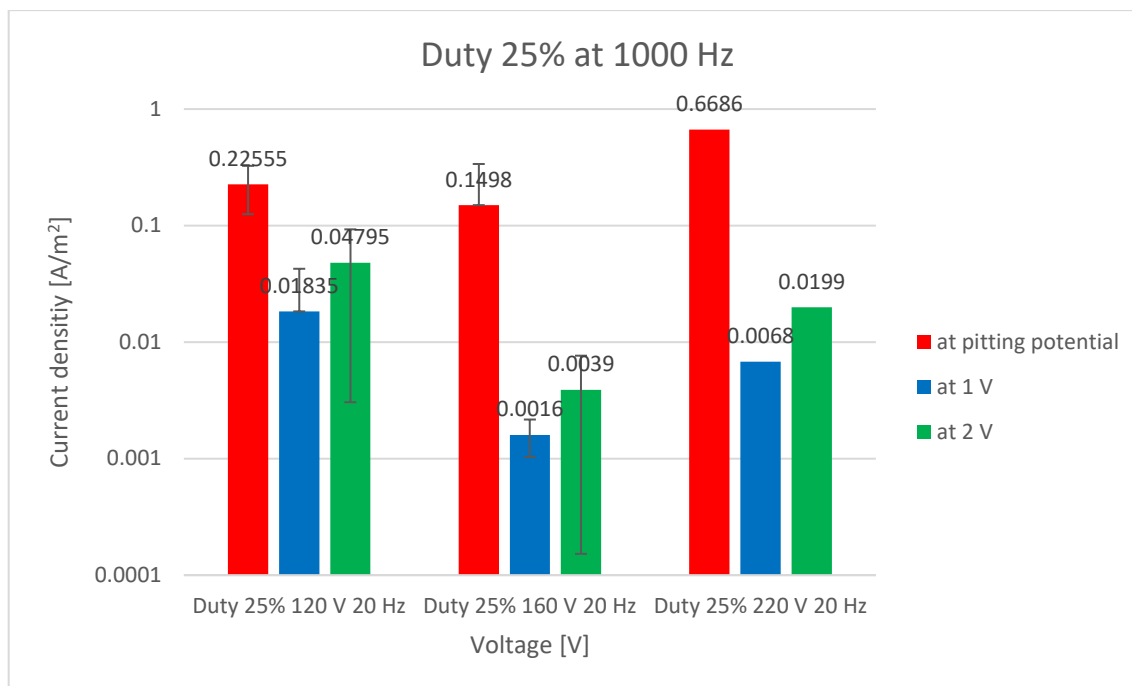


Figure 5.34 Average of the current densities at 1 V, 2 V and at pitting potential with corresponding standard deviations of samples anodized at 120 V, 160 V and 220 V with 1000 Hz and 25% duty cycle.

Increasing the frequency, the current densities are more similar and the differences are smoothed out. However, the current densities of the 120 V are now the highest among the three treatments.

In the next tables are collected all the corrosion data of the samples anodized with a duty of 75% and different voltages and frequency. First, all the sample with frequency of 20 Hz will be compared, then the sample with frequency of 1000 Hz.

Table 5.15 Pitting potentials, current densities and number of the sample anodized with duty cycle of 75% and a frequency of 20 Hz at 120 V, 160 V and 220 V.

SETTINGS	PITTING POTENTIAL [V]	CURRENT DENSITY [A/M <sup>2</sup> ]	NUMBER OF THE SAMPLE
DUTY 75% - 120 V - 20Hz	3,3885	0,0048056	33
DUTY 75% - 120 V - 20 HZ	3,6949	0,05478	18
DUTY 75%-160V- 20 HZ	3,6585	0,07263	32
DUTY 75% - 160 V- 20 HZ	--	--	17
DUTY 75% - 220 V -20HZ	--	--	16

Table 5.16 Current densities and number of the sample anodized with duty cycle of 75% and a frequency of 20 Hz at 120 V, 160 V and 220 V at 1 V.

SETTINGS	POTENTIAL [V]	CURRENT DENSITY [A/M <sup>2</sup> ]	NUMBER OF THE SAMPLE
DUTY 75% - 120 V - 20Hz	1	0,000718	33
DUTY 75% - 120 V - 20 HZ	1	0,001044	18
DUTY 75%-160V-20 HZ	1	0,000332	32
DUTY 75% - 160 V- 20 HZ	1	0,0009948	17
DUTY 75% - 220 V -20HZ	1	0,1064	16

Table 5.17 Current densities and number of the sample anodized with duty cycle of 75% and a frequency of 20 Hz at 120 V, 160 V and 220 V at 2 V.

SETTINGS	POTENTIAL [V]	CURRENT DENSITY [A/M <sup>2</sup> ]	NUMBER OF THE SAMPLE
DUTY 75% - 120 V - 20Hz	2	0,0007017	33
DUTY 75% - 120 V - 20 HZ	2	0,004004	18
DUTY 75%-160V-20 HZ	2	0,014279	32
DUTY 75% - 160 V- 20 HZ	2	0,0071337	17
DUTY 75% - 220 V -20HZ	2	0,5278	16

Looking at the pitting potentials of this set of data, it is possible to say that increasing the potential also the pitting corrosion is less probable. However, the 220 V (i.e. sample number 16) is the most active among the five sample, but its activity does not result in a pitting formation. Increasing the duty cycle the pitting potential of the 120 V is higher and it is very similar for both the tests. This can be caused by the increasing of the current density circulating on the sample increasing the duty cycle. It is important to remember that higher the current density, thicker is the oxide layer. The two 160 V samples present a discordant behaviour, when in one case the pitting is near to the one of the 120 V (i.e. 3.6585 and 3.6949 for the 160 V and 120 V respectively) and in the other it is absent. The sample 32 starts with an activity which is lower to the one of the sample 17, but then its activity exceeds its and results in a pitting initiation. The porosity increases increasing the voltage as for the previous cases and the pore distributions are wide for the 160 V and 220 V while narrow for

the 120 V. They are similar to the curves of the samples anodized with 25% duty cycle and the same frequency and voltages. (Fig.5.4)

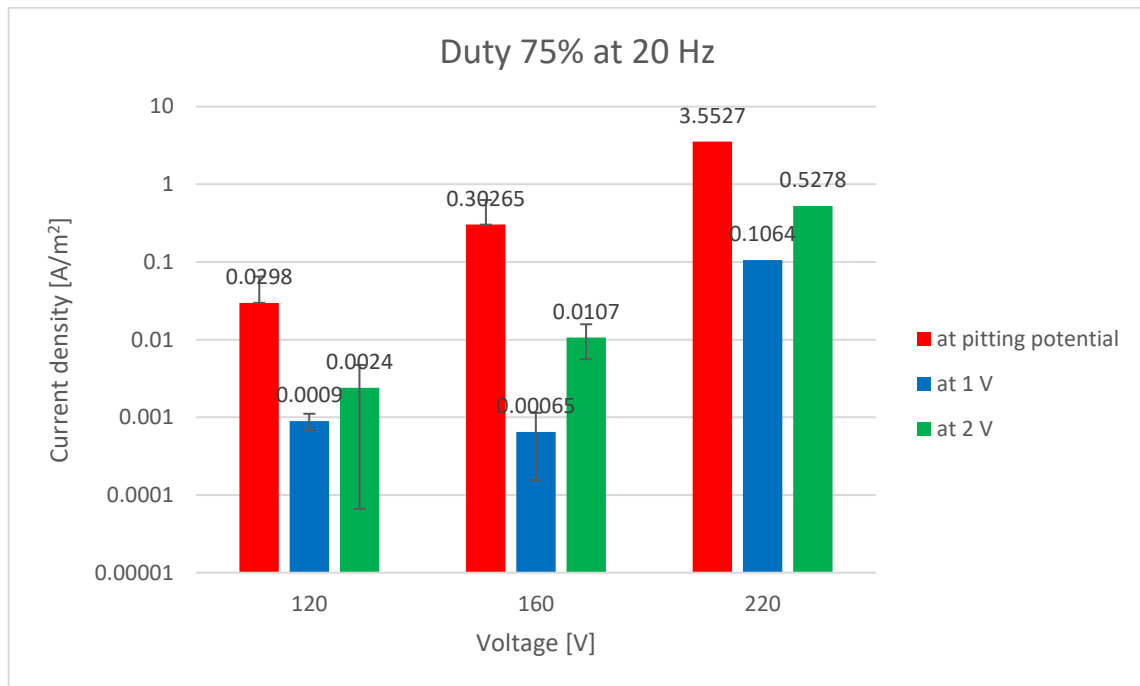


Figure 5.35 Average of the current densities at 1 V, 2 V and at pitting potential with corresponding standard deviations of samples anodized at 120 V, 160 V and 220 V with 20 Hz and 75% duty cycle.

At high duty cycles (see also the following case), the current density at pitting potential increases increasing the voltages, meaning that the samples are more and more active due to increasing of the porosity of the oxide. Also the current densities at 1 V and 2 V increase increasing the voltage confirming the previous trend.

The last comparison is performed with samples anodized with different voltages but the same 75% duty cycle and 1000 Hz of frequency.

Table 5.18 Pitting potentials, current densities and number of the sample anodized with duty cycle of 75% and a frequency of 1000 Hz at 120 V, 160 V and 220 V.

SETTINGS	PITTING POTENTIAL [V]	CURRENT DENSITY [A/M²]	NUMBER OF THE SAMPLE
DUTY 75% - 120 V - 1000 Hz	--	--	14
DUTY 75% - 120 V - 1000 HZ	5,102	0,0936	30
Duty 75%-160V-1000Hz	5,193	0,416	29
Duty 75% - 160 V - 1000 HZ	4,7236	0,1134	15

<b>Duty 75 %- 220 V - 1000Hz</b>	4,72366	0,1134	13
<b>Duty 75% - 220 V - 1000 Hz</b>	--	--	28

*Table 5.19 Current densities and number of the sample anodized with duty cycle of 75% and a frequency of 1000 Hz at 120 V, 160 V and 220 V at 1 V.*

<b>SETTINGS</b>	<b>POTENTIAL [V]</b>	<b>CURRENT DENSITY [A/M<sup>2</sup>]</b>	<b>NUMBER OF THE SAMPLE</b>
<b>Duty 75% - 120 V - 1000 HZ</b>	1	0,0002981	14
<b>Duty 75% - 120 V - 1000 HZ</b>	1	0,0010589	30
<b>Duty 75% - 160 V - 1000 HZ</b>	1	0,00275	29
<b>Duty 75% - 160 V - 1000 HZ</b>	1	0,003946	15
<b>Duty 75% - 220 V - 1000 HZ</b>	1	0,000899	13
<b>Duty 75% - 220 V - 1000 HZ</b>	1	0,008354	28

*Table 5.20 Current densities and number of the sample anodized with duty cycle of 75% and a frequency of 1000 Hz at 120 V, 160 V and 220 V at 2 V.*

<b>SETTINGS</b>	<b>POTENTIAL [V]</b>	<b>CURRENT DENSITY [A/M<sup>2</sup>]</b>	<b>NUMBER OF THE SAMPLE</b>
<b>DUTY 75%- 120 V - 1000 HZ</b>	2	0,001293	14
<b>Duty 75% - 120 V - 1000 HZ</b>	2	0,0026237	30
<b>Duty 75% - 160 V - 1000 HZ</b>	2	0,0199	29
<b>Duty 75% - 160 V - 1000 HZ</b>	2	0,009493	15
<b>Duty 75% - 220 V - 1000 HZ</b>	2	0,004924	13
<b>Duty 75% - 220 V - 1000 HZ</b>	2	0,12763	28

Analysing the pitting potentials and the current densities at 1 V and 2 V, the results are controversial: between the two 120 V and the two 220 V, just one for each anodization settings presents pitting corrosion while the other is immune. Starting from the 120 V, the sample 14 is the less active and the more resistant to pitting corrosion (Fig.4.34), while the sample 30 pits at 5.102 V, near to the pitting potential of the two 160 V. The two 160 V are similar and their pitting potential is near 5 V. The increased resistance of the 120 V can be linked with the decreasing of the area occupied by pores on the oxide surface (Fig.5.5) with respect to both the DC case and the 25% duty cycle at the same frequency (i.e. 1.89, 4.57 and 3.64 for the 75%, DC and the 25% respectively). On the other hand, the porosity of the 160 V and 220 V do not present a remarkable decrease. Looking at the current densities at 1 V and 2 V, the two samples that present pitting are the less active at 1 V, while at 2 V the number 28 is the more active while the 14 has an activity of the same order of magnitude of the other samples.

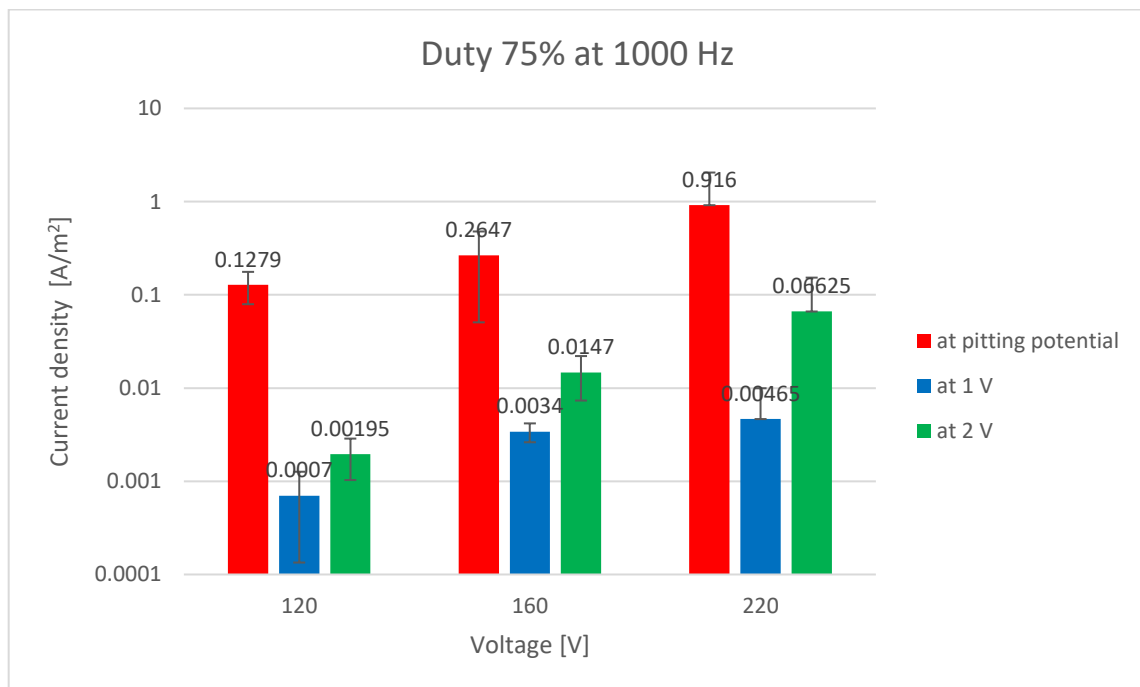


Figure 5.36 Average of the current densities at 1 V, 2 V and at pitting potential with corresponding standard deviations of samples anodized at 120 V, 160 V and 220 V with 1000 Hz and 75% duty cycle.

As for the previous case the current densities increase increasing the voltages, but the differences between the treatment are less pronounced due to the effects of frequency.

Looking at the four cases together, it seems that frequency and duty cycles have two different effect on the oxide layer and depending on which one prevails, the corrosion resistance trend is different. For example the trend with a maximum of the DC and with a minimum of 25% at 1000 Hz cases and the crescent trend of the 75% (both 1000 and 20 Hz) and the 25% at 20 Hz.

- *Change in frequency with constant duty cycle and voltage*

In the first set all the samples anodized at 120 V and 25% duty cycle are analysed.

*Table 5.21 Pitting potentials, current densities and number of the sample anodized with duty cycle of 75% and a frequency of 1000 Hz at 120 V, 160 V and 220 V.*

SETTINGS	PITTING POTENTIAL [V]	CURRENT DENSITY [A/M <sup>2</sup> ]	NUMBER OF THE SAMPLE
DUTY 25% - 120 V – 20 HZ	1,89	0,005589	27
DUTY 25% - 120 V - 1000 HZ	4,743	0,1547	24
DUTY 25% - 120 V - 1000 HZ	--	--	8

*Table 5.22 Current densities and number of the sample anodized with duty cycle of 75% and a frequency of 1000 Hz at 120 V, 160 V and 220 V at 1 V.*

SETTINGS	POTENTIAL [V]	CURRENT DENSITY [A/M <sup>2</sup> ]	NUMBER OF THE SAMPLE
DUTY 25% - 120 V – 20 HZ	1	0,00215	27
DUTY 25% - 120 V - 1000 HZ	1	0,001248	24
DUTY 25% - 120 V - 1000 HZ	1	0,03548	8

*Table 5.23 Current densities and number of the sample anodized with duty cycle of 75% and a frequency of 1000 Hz at 120 V, 160 V and 220 V at 2 V.*

SETTINGS	POTENTIAL [V]	CURRENT DENSITY [A/M <sup>2</sup> ]	NUMBER OF THE SAMPLE
DUTY 25% - 120 V -20 HZ	2	--	27
DUTY 25% - 120 V - 1000 HZ	2	0,01618	24
DUTY 25% - 120 V - 1000 HZ	2	0,07969	8

At low duty cycle and voltage, the effects of the frequency are more remarkable: the pitting potential is increased increasing the frequency from 1.89 V to 4.473 V and in the last sample (i.e. number 8) the pitting is no more present. Looking at the morphology data (Fig.5.7 and Fig.5.8), the frequency has an important impact on the distribution and on the area of the

pores. At low frequency the pores are more homogeneous and the area is less than at high frequency. However, the corrosion data are saying that even if the area of the pores at 1000 Hz is greater, the corrosion resistance is higher. Maybe the number of the pores influences more the corrosion resistance than just the area analysed alone. However, more tests have to be performed to analyse the real dependences between the anodizing settings and the corrosion resistance of the sample.

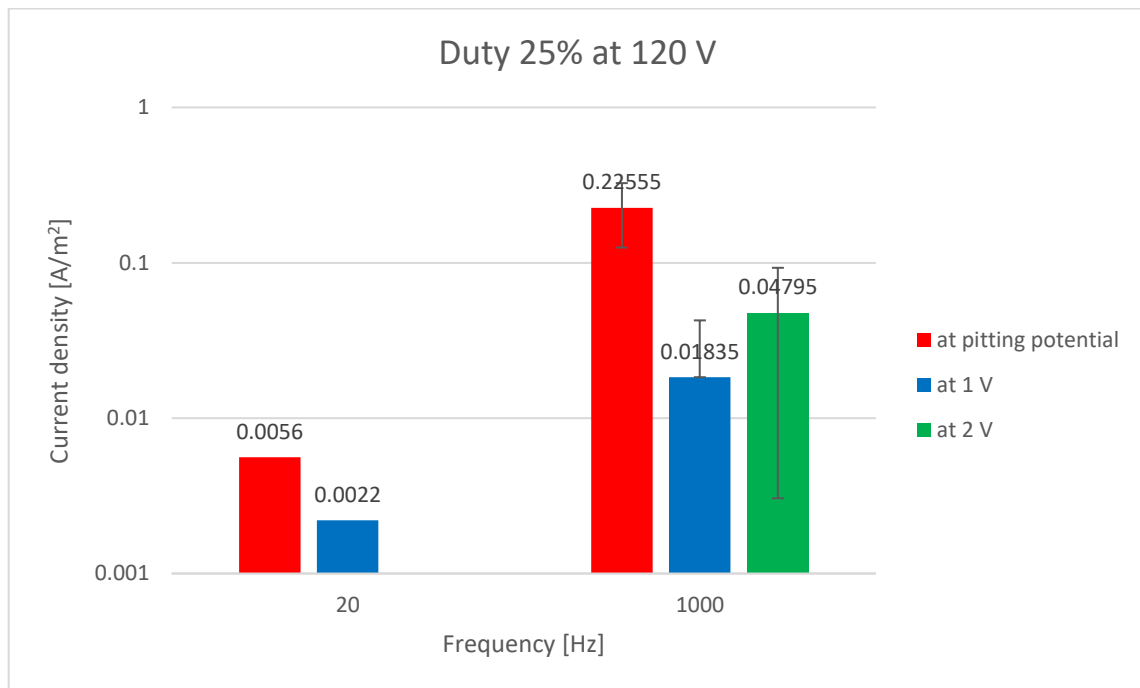


Figure 5.37 Average of the current densities at 1 V, 2 V and at pitting potential with corresponding standard deviations of samples anodized at 120 V with 25% duty cycle.

The increasing of the frequency causes an increasing of the current densities and of the activity of the samples, due to the increasing of the porosity.

In the next comparison all the samples anodized at 160 V and 25% duty are analysed:

Table 5.24 Pitting potentials, current densities and number of the sample anodized with duty cycle of 75% and a frequency of 1000 Hz at 120 V, 160 V and 220 V.

SETTINGS	PITTING POTENTIAL [V]	CURRENT DENSITY [A/M <sup>2</sup> ]	NUMBER OF THE SAMPLE
DUTY 25% - 160 V - 20 HZ	4,643	0,083	11
DUTY 25% - 160 V - 20 HZ	5,816	0,6054	26
DUTY 25% - 160 V - 1000 HZ	2,716	0,01684	7
DUTY 25% - 160 V - 1000 HZ	5,19004	0,2828	23

Table 5.25 Current densities and number of the sample anodized with duty cycle of 75% and a frequency of 1000 Hz at 120 V, 160 V and 220 V at 1 V.

SETTINGS	POTENTIAL [V]	CURRENT DENSITY [A/M <sup>2</sup> ]	NUMBER OF THE SAMPLE
DUTY 25% - 160 V - 20 HZ	1	0,003228	11
DUTY 25% - 160 V - 20 HZ	1	0,002973	26
DUTY 25% - 160 V - 1000 HZ	1	0,001961	7
DUTY 25% - 160 V - 1000 HZ	1	0,001184	23

Table 5.26 Current densities and number of the sample anodized with duty cycle of 75% and a frequency of 1000 Hz at 120 V, 160 V and 220 V at 2 V.

SETTINGS	POTENTIAL [V]	CURRENT DENSITY [A/M <sup>2</sup> ]	NUMBER OF THE SAMPLE
DUTY 25% - 160 V - 20 HZ	2	0,0078879	11
DUTY 25% - 160 V - 20 HZ	2	0,0363	26
DUTY 25% - 160 V - 1000 HZ	2	0,006506	7
DUTY 25% - 160 V - 1000 HZ	2	0,0011845	23

In this case the effects of frequency are no more clear and there is no difference between the two frequencies (i.e. 20 Hz and 1000 Hz). Moreover, the differences between the two

treatment are absent also in the morphology, where the area of the pores and their distribution are similar (Fig.5.10 and Fig.5.14). So, the corrosion behaviour of the samples anodized at different frequencies at this duty cycle and voltage (i.e. 160 V and 25%) can be ascribed to a so similar superficial morphology. However, there is an inversion on the trend of the number of pores: while at the lower voltage (i.e. 120 V) the 1000 Hz sample presents a higher number of pores, at 160 V the higher frequency sample has a lower number of pores. Increasing the number of the tests, it will be possible to understand if the number of pores more or less important than the total area of the pores.

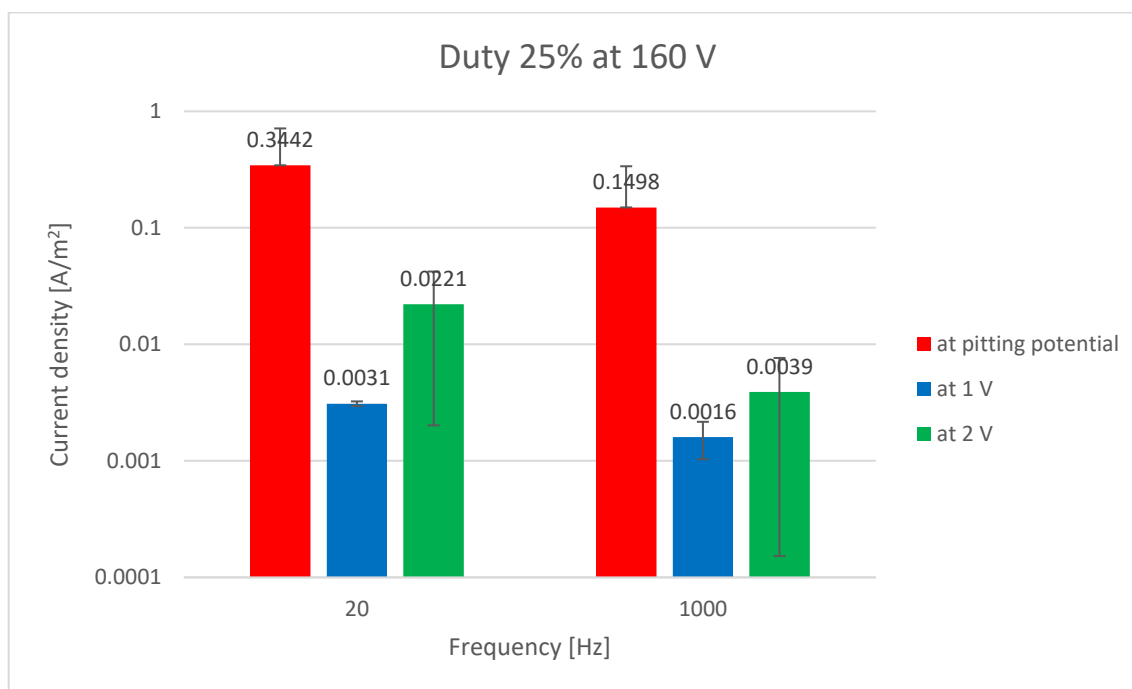


Figure 5.38 Average of the current densities at 1 V, 2 V and at pitting potential with corresponding standard deviations of samples anodized at 160 V with 25% duty cycle.

Increasing the voltage, the effects of the frequency as already said are less evident but the trend is opposite with respect to the 160 V.

In this set are collected all the corrosion data about samples anodized at 220V and duty 25% with different frequencies.

Table 5.27 Pitting potentials, current densities and number of the sample anodized with duty cycle of 75% and a frequency of 1000 Hz at 120 V, 160 V and 220 V.

SETTINGS	PITTING POTENTIAL [V]	CURRENT DENSITY [A/M <sup>2</sup> ]	NUMBER OF THE SAMPLE
DUTY 25% - 220 V - 20 HZ	--	--	10
DUTY 25% - 220 V - 1000 HZ	--	--	22

Table 5.28 Current densities and number of the sample anodized with duty cycle of 25% and a frequency of 1000 Hz at 120 V, 160 V and 220 V at 1 V.

SETTINGS	POTENTIAL [V]	CURRENT DENSITY [A/M <sup>2</sup> ]	NUMBER OF THE SAMPLE
DUTY 25% - 220 V - 20 HZ	1	0,000969	10
DUTY 25% - 220 V - 1000 HZ	1	0,00682388	22

Table 5.29 Current densities and number of the sample anodized with duty cycle of 25% and a frequency of 1000 Hz at 120 V, 160 V and 220 V at 2 V.

SETTINGS	POTENTIAL [V]	CURRENT DENSITY [A/M <sup>2</sup> ]	NUMBER OF THE SAMPLE
DUTY 25% - 220 V - 20 HZ	2	0,00661	10
DUTY 25% - 220 V - 1000 HZ	2	0,019939	22

Also in this case, it is not possible to see a concrete difference between the two behaviours, but it is possible to note that the high frequency sample is more active than the low frequency one. Looking at the morphology of the samples (Fig.5.15 and Fig.5.12), the distributions are similar and the area occupied by the pores are identical. Although, increasing the voltage, the difference between the number of pores of the samples at the two frequencies increases, it does not produce any effect on the corrosion behaviours.

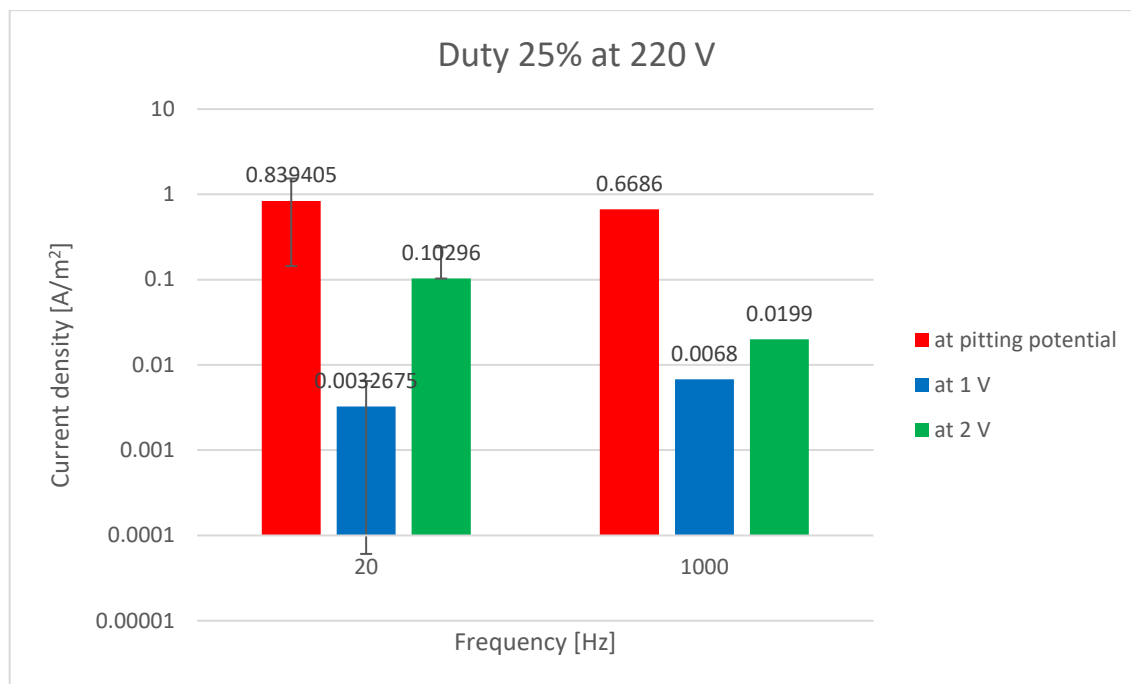


Figure 5.39 Average of the current densities at 1 V, 2 V and at pitting potential with corresponding standard deviations of samples anodized at 220 V with 25% duty cycle.

The 220 V follows the 160 V with a 1000 Hz lower than the 20 Hz.

In the next comparison all the samples anodized with duty 75% and at 120 V, 160 V and 220 V are compared with different frequencies.

Table 5.30 Pitting potentials, current densities and number of the sample anodized with duty cycle of 75% and a frequency of 1000 Hz at 120 V, 160 V and 220 V.

SETTINGS	PITTING POTENTIAL [V]	CURRENT DENSITY [A/M <sup>2</sup> ]	NUMBER OF THE SAMPLE
DUTY 75% - 120 V - 20 HZ	3,3885	0,0048056	33
DUTY 75% - 120 V - 20 HZ	3,6949	0,05478	18
DUTY 75% - 120 V - 1000 HZ	--	--	14
DUTY 75% - 120 V - 1000 HZ	5,102	0,0936	30

Table 5.31 Current densities and number of the sample anodized with duty cycle of 75% and a frequency of 1000 Hz at 120 V, 160 V and 220 V at 1 V.

SETTINGS	POTENTIAL [V]	CURRENT DENSITY [A/M <sup>2</sup> ]	NUMBER OF THE SAMPLE
DUTY 75% - 120 V - 20 HZ	1	0,000718	33
DUTY 75% - 120 V - 20 HZ	1	0,001044	18
DUTY 75% - 120 V - 1000 HZ	1	0,0002981	14
DUTY 75% - 120 V - 1000 HZ	1	0,0010589	30

Table 5.32 Current densities and number of the sample anodized with duty cycle of 75% and a frequency of 1000 Hz at 120 V, 160 V and 220 V at 2 V.

SETTINGS	POTENTIAL [V]	CURRENT DENSITY [A/M <sup>2</sup> ]	NUMBER OF THE SAMPLE
DUTY 75% - 120 V - 20 HZ	2	0,0007017	33
DUTY 75% - 120 V - 20 HZ	2	0,004004	18
DUTY 75% - 120 V - 1000 HZ	2	0,001293	14
DUTY 75% - 120 V - 1000 HZ	2	0,0026237	30

As for the samples anodized at lower duty cycle (i.e.25%) the effects of the frequency are more appreciable at lower voltages. In facts, the pitting potentials of samples reported in Tab.5.30. are increased by the increasing of the frequency and the corrosion behaviour of the sample is improved. Maybe the rapid stop of the current on the sample gives no time to the sparks to diffuse and to create big pores on the surface but the rapid quenching of the melting oxide improved the corrosion resistance. In facts, in Fig.5.7 and 5.8 it is possible to see that the increasing of the frequency decreases the area covered by pores and the beneficial effects are visible also in the corrosion behaviour.

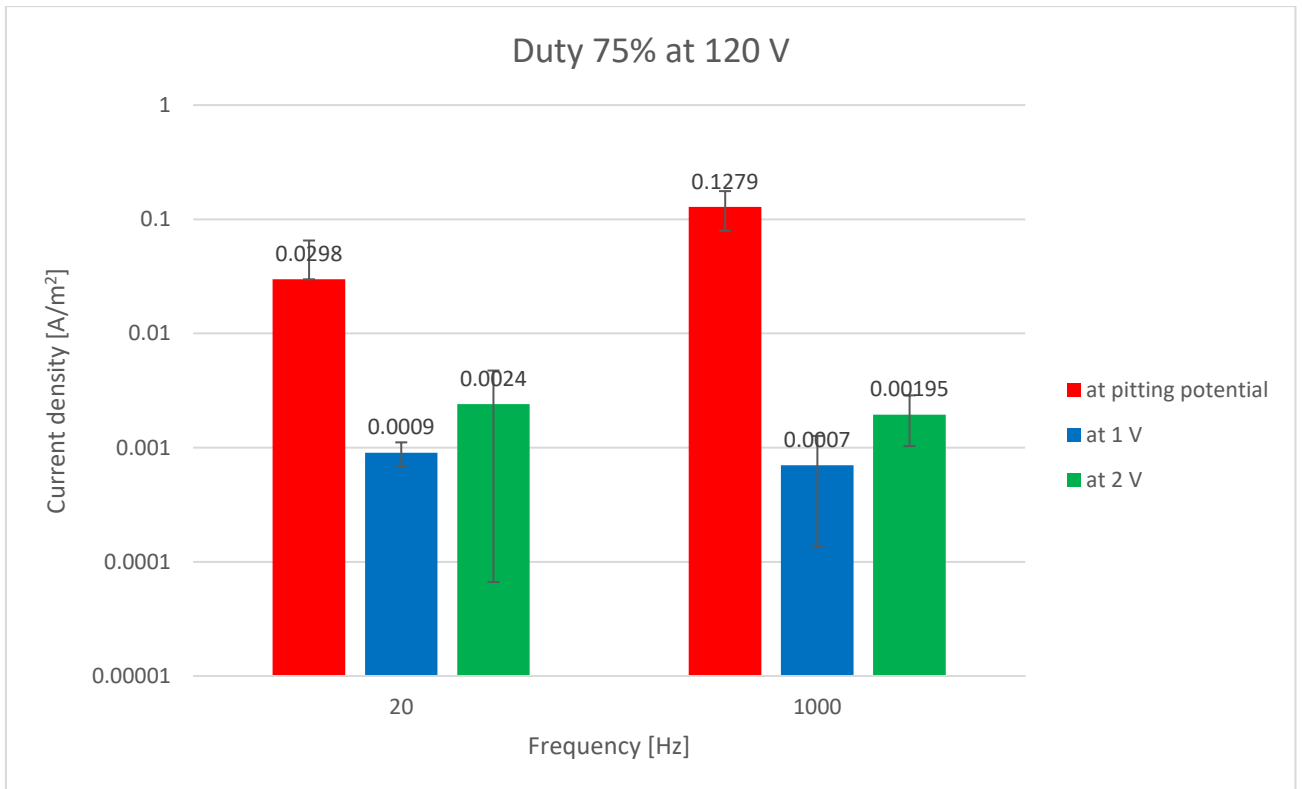


Figure 5.40 Average of the current densities at 1 V, 2 V and at pitting potential with corresponding standard deviations of samples anodized at 220 V with 25% duty cycle.

Increasing the duty cycle, the trend returns similar to the 120 V and 25% with a increasing of the current density increasing the frequency.

Increasing the voltage, the sample anodized at 160 V are collected and commented.

Table 5.33 Pitting potentials, current densities and number of the sample anodized with duty cycle of 75% and a frequency of 1000 Hz at 120 V, 160 V and 220 V.

SETTINGS	PITTING POTENTIAL [V]	CURRENT DENSITY [A/M <sup>2</sup> ]	NUMBER OF THE SAMPLE
DUTY 75% - 160 V - 20 HZ	3,6585	0,07263	32
DUTY 75% - 160 V - 20 HZ	--	--	17
DUTY 75% - 160 V - 1000 HZ	5,193	0,416	29
DUTY 75% - 160 V - 1000 HZ	4,7236	0,1134	15

Table 5.34 Current densities and number of the sample anodized with duty cycle of 75% and a frequency of 1000 Hz at 120 V, 160 V and 220 V at 1 V.

SETTINGS	POTENTIAL [V]	CURRENT DENSITY [A/M <sup>2</sup> ]	NUMBER OF THE SAMPLE
DUTY 75% - 160 V - 20 HZ	1	0,000332	32
DUTY 75% - 160 V - 20 HZ	1	0,0009948	17
DUTY 75% - 160 V - 1000HZ	1	0,00275	29
DUTY 75% - 160 V - 1000 HZ	1	0,003946	15

Table 5.35 Current densities and number of the sample anodized with duty cycle of 75% and a frequency of 1000 Hz at 120 V, 160 V and 220 V at 2 V.

SETTINGS	POTENTIAL [V]	CURRENT DENSITY [A/M <sup>2</sup> ]	NUMBER OF THE SAMPLE
DUTY 75% - 160 V - 20 HZ	2	0,014279	32
DUTY 75% - 160 V - 20 HZ	2	0,0071337	17
DUTY 75%- 160 V – 1000 HZ	2	0,0199	29
DUTY 75% - 160 V - 1000 HZ	2	0,009493	15

Increasing the voltages, the beneficial effects are no more clear on the sample surface, but looking at the potentiodynamic graphs, Fig.4.35, the sample number 17 is very disturbed and its reliability can be discussed. However, even if more tests have to be performed to understand the real effect of the frequency at high voltages, the morphology reports that while the total areas of the pores are very similar, the number of the pores is higher for the sample anodized at lower frequency. So, if only the sample 32 is taken in consideration, being the total area of the pores very similar, the difference of 1 V between the pitting potentials is to be ascribed to the number of the pores.

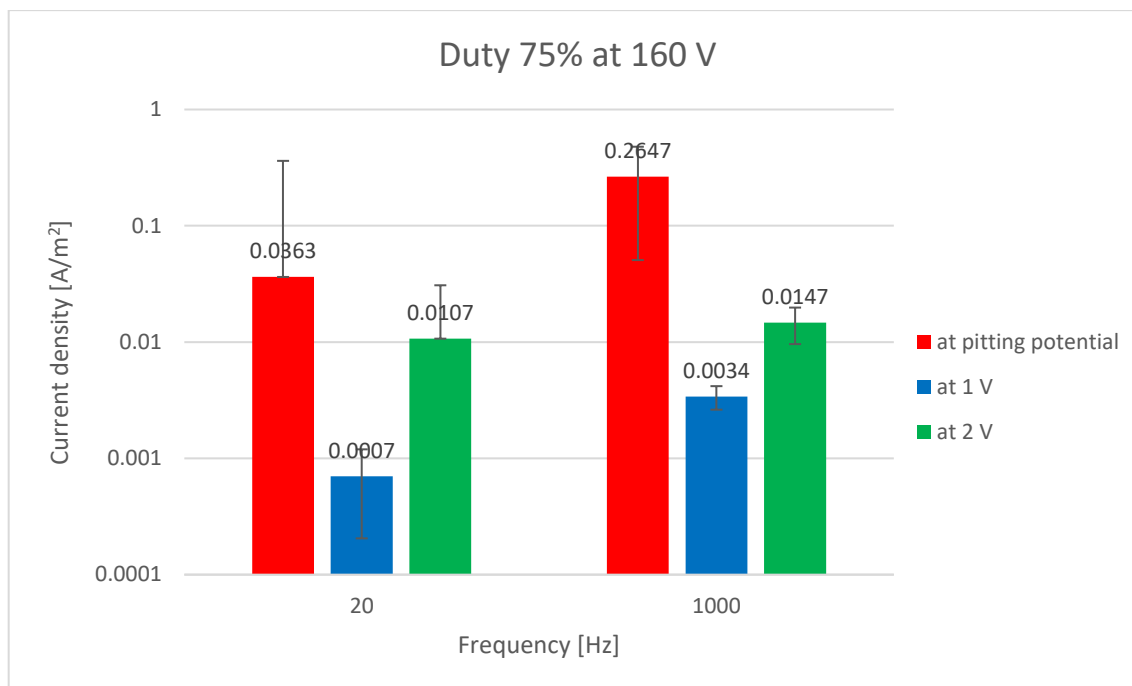


Figure 5.41 Average of the current densities at 1 V, 2 V and at pitting potential with corresponding standard deviations of samples anodized at 160 V with 75% duty cycle.

As for the 120 V and 75%, the trends of all the current densities increase increasing the frequency, showing an higher activity of the samples anodized at higher frequency.

In the last comparison all the samples anodized at 220 V and 75% at different frequencies.

Table 5.36 Pitting potentials, current densities and number of the sample anodized with duty cycle of 75% and a frequency of 1000 Hz at 120 V, 160 V and 220 V.

SETTINGS	PITTING POTENTIAL [V]	CURRENT DENSITY [A/M <sup>2</sup> ]	NUMBER OF THE SAMPLE
<b>DUTY 75% - 220 V -20HZ</b>	--	--	16
<b>DUTY 75% - 220 V -1000HZ</b>	4,72366	0,1134	13
<b>DUTY 75% - 220 V -1000 HZ</b>	--	--	28

Table 5.37 Current densities and number of the sample anodized with duty cycle of 75% and a frequency of 1000 Hz at 120 V, 160 V and 220 V at 1 V.

SETTINGS	POTENTIAL [V]	CURRENT DENSITY [A/M <sup>2</sup> ]	NUMBER OF THE SAMPLE
DUTY 75% - 220 V -20HZ	1	0,1064	16
DUTY 75% - 220 V - 1000HZ	1	0,000899	13
DUTY 75% - 220 V -1000 HZ	1	0,008354	28

Table 5.38 Current densities and number of the sample anodized with duty cycle of 75% and a frequency of 1000 Hz at 120 V, 160 V and 220 V at 2 V.

SETTINGS	POTENTIAL [V]	CURRENT DENSITY [A/M <sup>2</sup> ]	NUMBER OF THE SAMPLE
DUTY 75% - 220 V – 20 HZ	2	0,5278	16
DUTY 75 % - 220 V - 1000HZ	2	0,004924	13
DUTY 75% - 220 V -1000 HZ	2	0,12763	28

As for the duty 25%, at high voltages the differences between the corrosion resistance of the sample is no more visible. Also the morphology of the sample does not say anything about the superficial effects of the change of frequency, being the distributions and the area of the pores very similar. The only parameter which is still different is the number of pores, but at high voltages the pores become more and more similar to nanogrooves and the limits of one pore are no more defined.

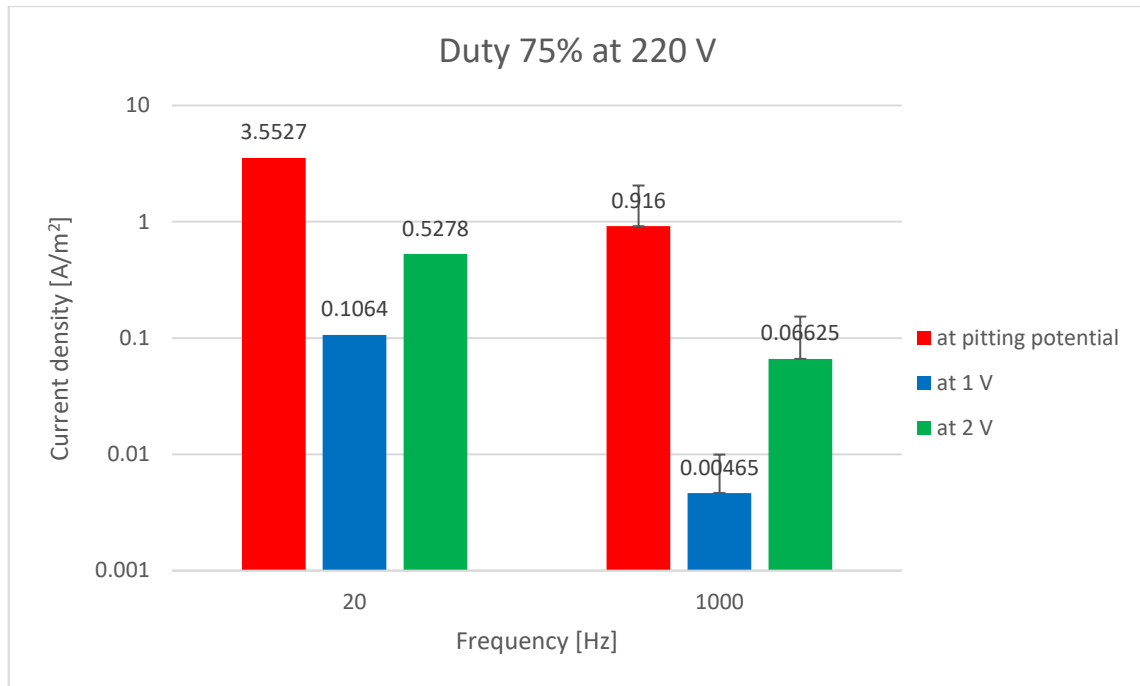


Figure 5.42 Average of the current densities at 1 V, 2 V and at pitting potential with corresponding standard deviations of samples anodized at 220 V with 75% duty cycle.

When the voltage is increased the trend is inversed and at higher frequency the current densities are lower than at lower frequency.

- *Change in duty cycle with constant frequency and voltage*

The first group of data collects together the corrosion resistance results of sample anodized at 120 V and 20 Hz at different duty cycles.

Table 5.39 Pitting potentials, current densities and number of the sample anodized with frequency of 20 Hz and different duty cycles at 120 V.

SETTINGS	PITTING POTENTIAL [V]	CURRENT DENSITY [A/M <sup>2</sup> ]	NUMBER OF THE SAMPLE
DUTY 25%-120V-20HZ	1.89	0.005589	27
DUTY 75% - 120 V - 20HZ	3.3885	0.0048056	33
DUTY 75% - 120 V - 20 HZ	3.6949	0.05478	18

Table 5.40 Current densities and number of the sample anodized with different duty cycles and a frequency of 20 Hz at 120 V at 1 V.

SETTINGS	POTENTIAL [V]	CURRENT DENSITY [A/M <sup>2</sup> ]	NUMBER OF THE SAMPLE
DUTY 25%-120V-20HZ	1	0.00215	27
DUTY 75% - 120 V - 20HZ	1	0.000718	33
DUTY 75% - 120 V - 20 HZ	1	0.001044	18

Table 5.41 Current densities and number of the sample anodized with different duty cycles and a frequency of 20 Hz at 120 V at 2 V.

SETTINGS	POTENTIAL [V]	CURRENT DENSITY [A/M <sup>2</sup> ]	NUMBER OF THE SAMPLE
DUTY 25%-120V-20HZ	2	--	27
DUTY 75% - 120 V - 20HZ	2	0.0007017	33
DUTY 75% - 120 V - 20 HZ	2	0.004004	18

At low voltages the effects of the duty cycle are more remarkable and the pitting potential is lower for lower duty cycle. However, the pitting potential of the 75% is similar to the DC pitting potential and it confirms the approaching of the corrosion resistance high duty trend to the DC one. Looking at the porosity of the sample, the 25% duty cycle has a higher number of pores and also the area covered by pores is higher. These data confirm the corrosion resistance results where the higher porosity leads to a weaker corrosion resistance. Looking at the activities of the sample, the 25% duty cycle is the more active at 1 V.

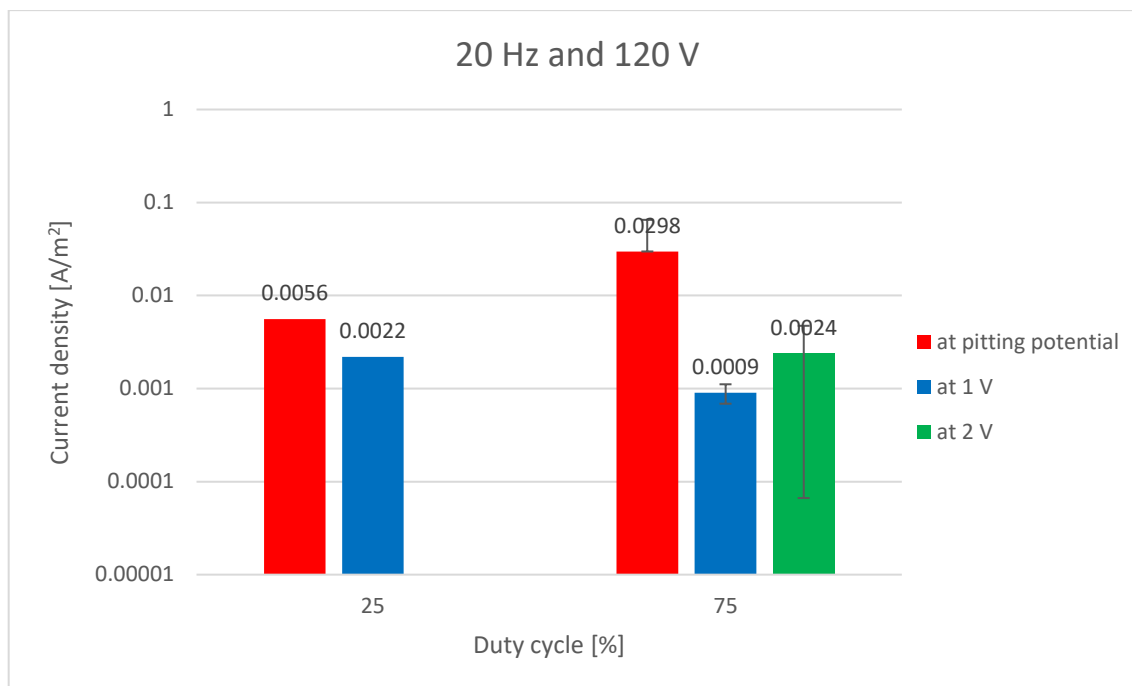


Figure 5.43 Average of the current densities at 1 V, 2 V and at pitting potential with corresponding standard deviations of samples anodized at 120 V with 20 Hz.

In the second comparison the samples anodized at 160 V and 20 Hz are compared.

Table 5.42 Pitting potentials, current densities and number of the sample anodized with frequency of 20 Hz and different duty cycles at 160 V.

SETTINGS	POTENTIAL [V]	CURRENT DENSITY [A/M <sup>2</sup> ]	NUMBER OF THE SAMPLE
DUTY 25% - 160 V - 20 HZ	4.643	0.083	11
DUTY 25%-160V-20HZ	5.816	0.6054	26
DUTY 75%-160V-20 HZ	3.6585	0.07263	32
DUTY 75% - 160 V-20 HZ	--	--	17

Table 5.43 Current densities and number of the sample anodized with different duty cycles and a frequency of 20 Hz at 160 V at 1 V.

SETTINGS	POTENTIAL [V]	CURRENT DENSITY [A/M <sup>2</sup> ]	NUMBER OF THE SAMPLE
DUTY 25% - 160 V - 20 HZ	1	0.003228	11
DUTY 25%-160V-20HZ	1	0.002973	26

<b>DUTY 75%-160V- 20 HZ</b>	1	0.000332	32
<b>DUTY 75% - 160 V- 20 HZ</b>	1	0.0009948	17

Table 5.44 Current densities and number of the sample anodized with different duty cycles and a frequency of 20 Hz at 160 V at 2 V.

SETTINGS	POTENTIAL [V]	CURRENT DENSITY [A/M <sup>2</sup> ]	NUMBER OF THE SAMPLE
<b>DUTY 25% - 160 V - 20 HZ</b>	2	0.0078879	11
<b>DUTY 25%-160V- 20HZ</b>	2	0.0363	26
<b>DUTY 75%-160V- 20 HZ</b>	2	0.014279	32
<b>DUTY 75% - 160 V- 20 HZ</b>	2	0.0071337	17

Increasing the voltage, the effects of the duty cycles are no more visible and just one over two samples presents a complete corrosion resistance while the other pits at low potential. The trends are similar also in the porosity where both area and number of pores are similar.

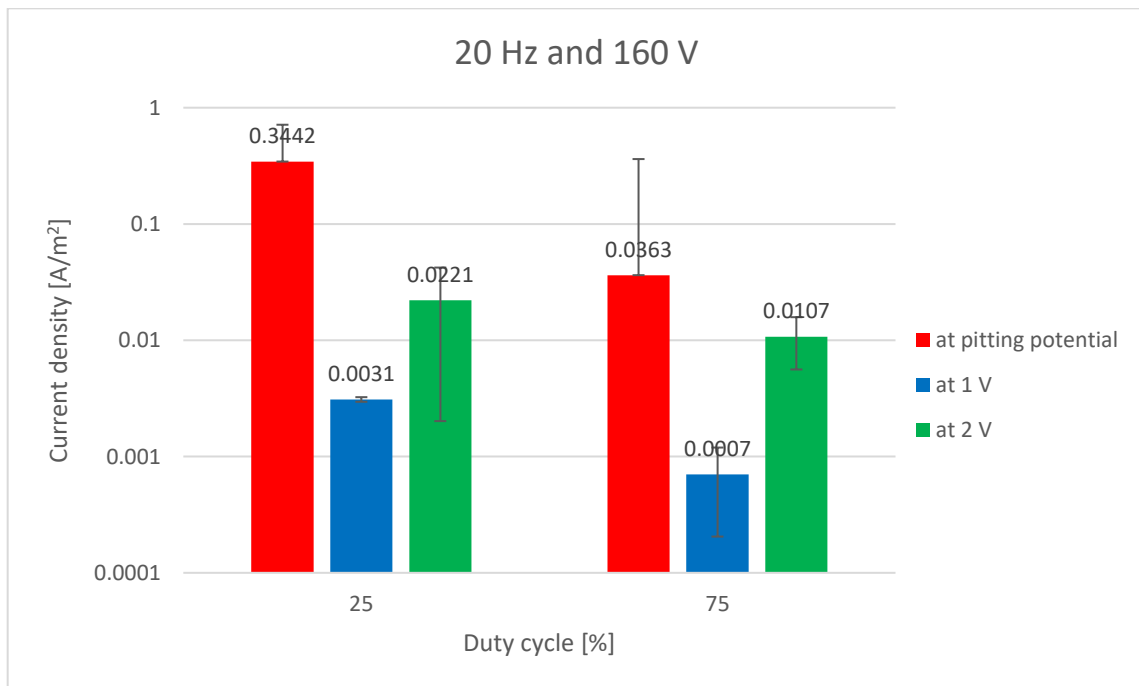


Figure 5.44 Average of the current densities at 1 V, 2 V and at pitting potential with corresponding standard deviations of samples anodized at 160 V with 20 Hz.

The last comparison at this frequency is performed on samples anodized at 220 V.

*Table 5.45 Pitting potentials, current densities and number of the sample anodized with frequency of 20 Hz and different duty cycles at 220 V.*

SETTINGS	POTENTIAL [V]	CURRENT DENSITY [A/M <sup>2</sup> ]	NUMBER OF THE SAMPLE
DUTY 25% - 220 V - 20 HZ	--	--	10
DUTY 25% - 220 V - 20 HZ	5,4949	1,33111	25
DUTY 75% - 220 V -20HZ	--	--	16

*Table 5.46 Current densities and number of the sample anodized with different duty cycles and a frequency of 20 Hz at 220 V at 1 V.*

SETTINGS	POTENTIAL [V]	CURRENT DENSITY [A/M <sup>2</sup> ]	NUMBER OF THE SAMPLE
DUTY 25% - 220 V - 20 HZ	1	0.000969	10
DUTY 25% - 220 V - 20 HZ	1	0.005535	25
DUTY 75% - 220 V -20HZ	1	0.1064	16

*Table 5.47 Current densities and number of the sample anodized with different duty cycles and a frequency of 20 Hz at 220 V at 2 V.*

SETTINGS	POTENTIAL [V]	CURRENT DENSITY [A/M <sup>2</sup> ]	NUMBER OF THE SAMPLE
DUTY 25% - 220 V - 20 HZ	2	0.00661	10
DUTY 25% - 220 V - 20 HZ	2	0.19932	25
DUTY 75% - 220 V -20HZ	2	0.5278	16

At high voltages the effects of the different duty cycles is less visible and both the duties lead to high corrosion resistance (i.e. absence of pitting potential or high pitting voltages). Looking at the porosity the area covered by pores and the number of pores are very similar, fact that can explain the similar corrosion resistance of the samples. (Fig.5.12) Regarding the activities of the samples at 1 V, the two anodized at low duty cycles are of the same order of magnitude while the one at high duty cycle is two orders bigger than the

other two. The higher activity of the sample anodized at high duty cycle is confirmed also at 2 V where it presents the highest activity.

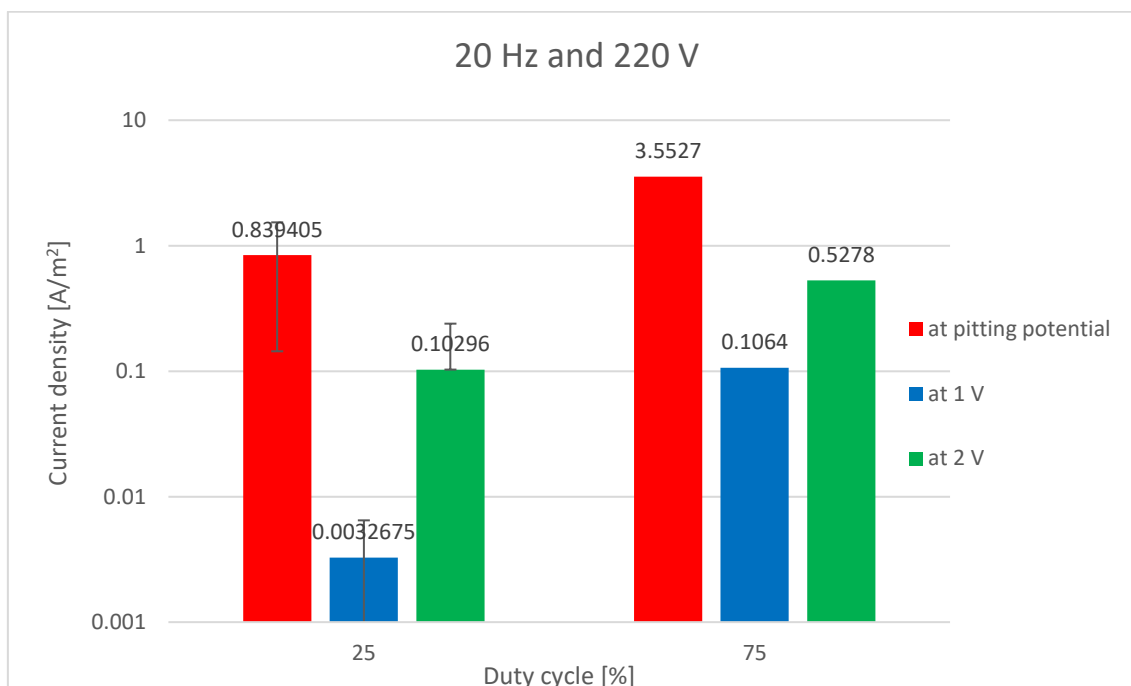


Figure 5.45 Average of the current densities at 1 V, 2 V and at pitting potential with corresponding standard deviations of samples anodized at 220 V with 20 Hz.

In the last section all the samples anodized at 1000 Hz of frequency and different duty cycles will be analysed.

Table 5.48 Pitting potentials, current densities and number of the sample anodized with frequency of 1000 Hz and different duty cycles at 120 V.

SETTINGS	POTENTIAL [V]	CURRENT DENSITY [A/M <sup>2</sup> ]	NUMBER OF THE SAMPLE
DUTY 25% - 120 V - 1000 HZ	4.743	0.1547	24
DUTY 25% - 120 V - 1000 HZ	--	--	8
DUTY 75% - 120 V - 1000 HZ	--	--	14
DUTY 75% - 120 V - 1000 HZ	5.102	0.0936	30

Table 5.49 Current densities and number of the sample anodized with different duty cycles and a frequency of 1000 Hz at 120 V at 1 V.

SETTINGS	POTENTIAL [V]	CURRENT DENSITY [A/M <sup>2</sup> ]	NUMBER OF THE SAMPLE
DUTY 25% - 120 V - 1000 HZ	1	0.001248	24
DUTY 25% - 120 V - 1000 HZ	1	0.03548	8
DUTY 75% - 120 V - 1000 HZ	1	0.0002981	14
DUTY 75% - 120 V - 1000 HZ	1	0.0010589	30

Table 5.50 Current densities and number of the sample anodized with different duty cycles and a frequency of 1000 Hz at 120 V at 2 V.

SETTINGS	POTENTIAL [V]	CURRENT DENSITY [A/M <sup>2</sup> ]	NUMBER OF THE SAMPLE
DUTY 25% - 120 V - 1000 HZ	2	0.01618	24
DUTY 25% - 120 V - 1000 HZ	2	0.07969	8
DUTY 75% - 120 V - 1000 HZ	2	0.001293	14
DUTY 75% - 120 V - 1000 HZ	2	0.0026237	30

Increasing the frequency with respect to the 20 Hz, a common trend is no more present and both the conditions present the 50% of the sample with pitting at a similar voltage. So, just looking at the corrosion data, it is possible to think at a surface appearance analogue between the two duty cycles. Actually, the porosity analysis is telling another story: while the low duty sample presents at this frequency a high area covered by pores and a high number of pores, at high duty cycle the number of pore and the area covered by pore is low. Probably the porosity is not the only parameter to be taken into account, but also the crystallinity and other events mainly linked with the tests have to be considered. In this way more tests have to be performed. The activities of the samples are quite similar at 1 V, while at 2 V the samples anodized at higher duty are less active (one order lower than the 25% duty).

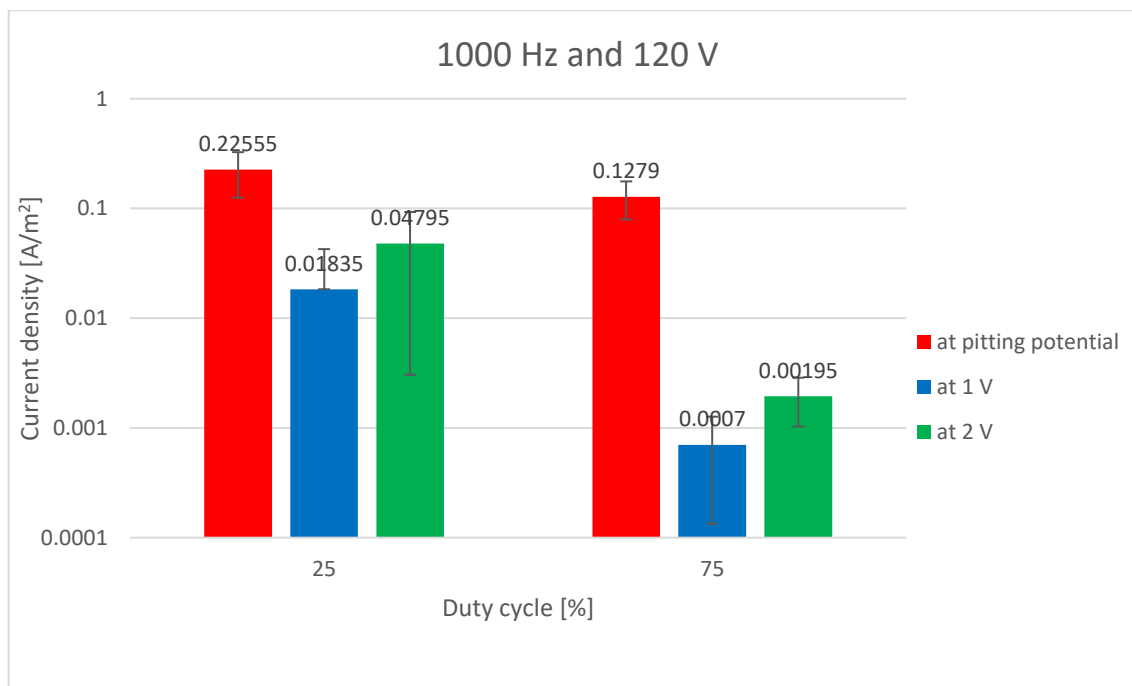


Figure 5.46 Average of the current densities at 1 V, 2 V and at pitting potential with corresponding standard deviations of samples anodized at 120 V with 1000 Hz.

The samples anodized at 160 V and 1000 Hz of frequency will be now compared and analysed.

Table 5.51 Pitting potentials, current densities and number of the sample anodized with frequency of 1000 Hz and different duty cycles at 160 V.

SETTINGS	POTENTIAL [V]	CURRENT DENSITY [A/M <sup>2</sup> ]	NUMBER OF THE SAMPLE
DUTY 25% - 160 V - 1000 HZ	2.716	0.01684	7
DUTY 25% - 160 V - 1000 HZ	5.19004	0.2828	23
DUTY 75% - 160 V - 1000 HZ	5.193	0.416	29
DUTY 75% - 160 V - 1000 HZ	4.7236	0.1134	15

Table 5.52 Current densities and number of the sample anodized with different duty cycles and a frequency of 1000 Hz at 160 V at 1 V.

SETTINGS	POTENTIAL [V]	CURRENT DENSITY [A/M <sup>2</sup> ]	NUMBER OF THE SAMPLE
DUTY 25% - 160 V - 1000 HZ	1	0.001961	7
DUTY 25% - 160 V -1000 HZ	1	0.001184	23
DUTY 75%- 160 V – 1000 HZ	1	0.00275	29
DUTY 75% - 160 V - 1000 HZ	1	0.003946	15

Table 5.53 Current densities and number of the sample anodized with different duty cycles and a frequency of 1000 Hz at 160 V at 2 V.

SETTINGS	POTENTIAL [V]	CURRENT DENSITY [A/M <sup>2</sup> ]	NUMBER OF THE SAMPLE
DUTY 25% - 160 V - 1000 HZ	2	0.006506	7
DUTY 25% - 160 V -1000 HZ	2	0.0011845	23
DUTY 75% - 160 V – 1000 HZ	2	0.0199	29
DUTY 75% - 160 V - 1000 HZ	2	0.009493	15

Also in this case, the increasing of the frequency with respect to the 20 Hz brings to a not clear trend of the corrosion resistance of the samples even at different duty cycle. It is possible that the effects of the frequency prevail on the duty ones. In facts, the pitting potentials and the activities of the samples at different duty cycles are very similar. However, the porosity (Fig.5.14) reveals an approaching of the 25% duty to the 75% increasing the voltages independently from the frequency. (Fig.5.14 and 5.10)

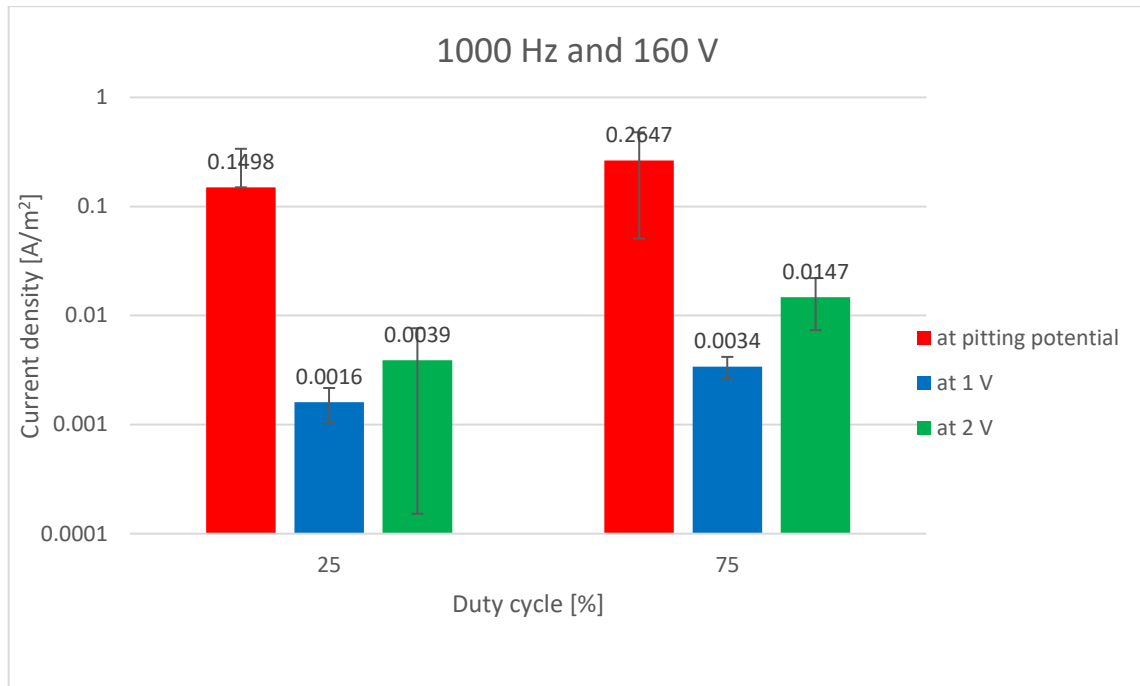


Figure 5.47 Average of the current densities at 1 V, 2 V and at pitting potential with corresponding standard deviations of samples anodized at 160 V with 1000 Hz.

The last comparison is performed between the samples anodized at 220 V and 1000 Hz.

Table 5.54 Pitting potentials, current densities and number of the sample anodized with frequency of 1000 Hz and different duty cycles at 220 V.

SETTINGS	POTENTIAL [V]	CURRENT DENSITY [A/M <sup>2</sup> ]	NUMBER OF THE SAMPLE
DUTY 25% - 220 V - 1000 HZ	--	--	22
DUTY 75 %- 220 V - 1000 HZ	4.72366	0.1134	13
DUTY 75% - 220 V -1000 HZ	--	--	28

Table 5.55 Current densities and number of the sample anodized with different duty cycles and a frequency of 1000 Hz at 220 V at 1 V.

SETTINGS	POTENTIAL [V]	CURRENT DENSITY [A/M <sup>2</sup> ]	NUMBER OF THE SAMPLE
DUTY 25% - 220 V - 1000 HZ	1	0.00682388	22
DUTY 75 %- 220 V -1000 HZ	1	0.000899	13
DUTY 75% - 220 V -1000 HZ	1	0.008354	28

Table 5.56 Current densities and number of the sample anodized with different duty cycles and a frequency of 1000 Hz at 220 V at 2 V.

SETTINGS	POTENTIAL [V]	CURRENT DENSITY [A/M <sup>2</sup> ]	NUMBER OF THE SAMPLE
DUTY 25% - 220 V - 1000 HZ	2	0.019939	22
DUTY 75% - 220 V - 1000 HZ	2	0.004924	13
DUTY 75% - 220 V - 1000 HZ	2	0.12763	28

In this case the differences between the duties are disappeared as in the two previous cases and the corrosion resistances of the samples are similar. At 1 V, the activities are of the same order of magnitude, while at 2 V they become dissimilar with a discrepancy of two order between the samples of the same repeatability. The porosity shows a quite identical size distribution of the pores of the samples, with also area and number of pores similar.

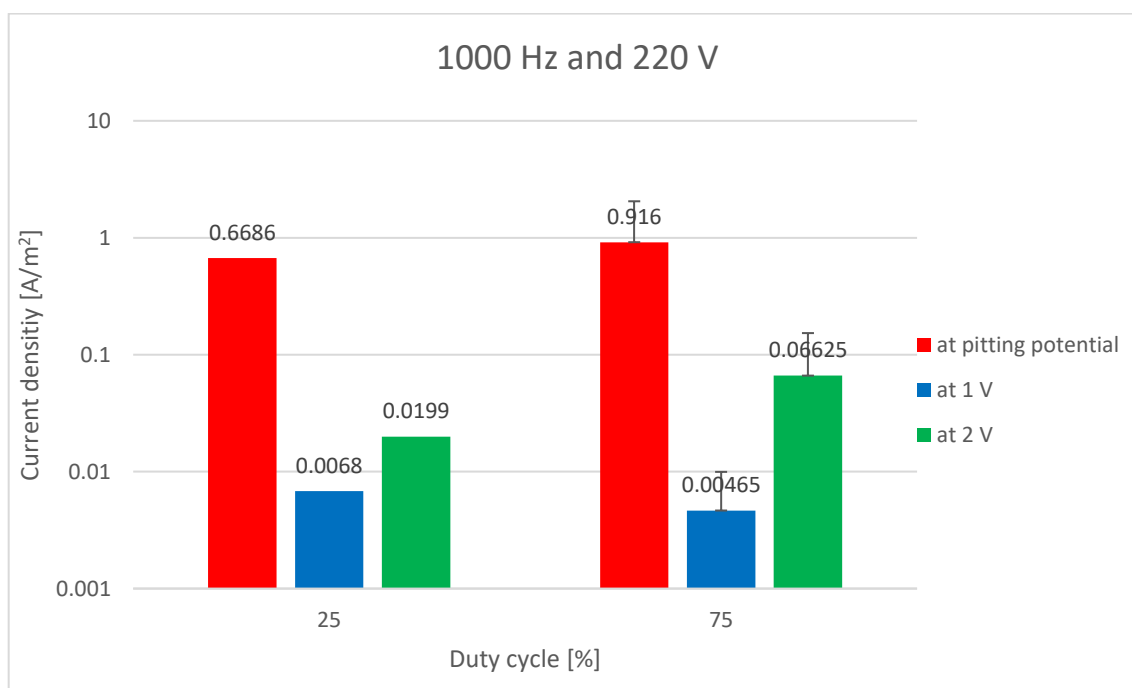


Figure 5.48 Average of the current densities at 1 V, 2 V and at pitting potential with corresponding standard deviations of samples anodized at 220 V with 1000 Hz.

### 5.3.1 Correlation among crystallinity, porosity and corrosion resistance

In the following pages a comparison between the results in terms of crystallinity, porosity and corrosion resistance is presented, varying one parameter at a time while keeping fixed the other two.

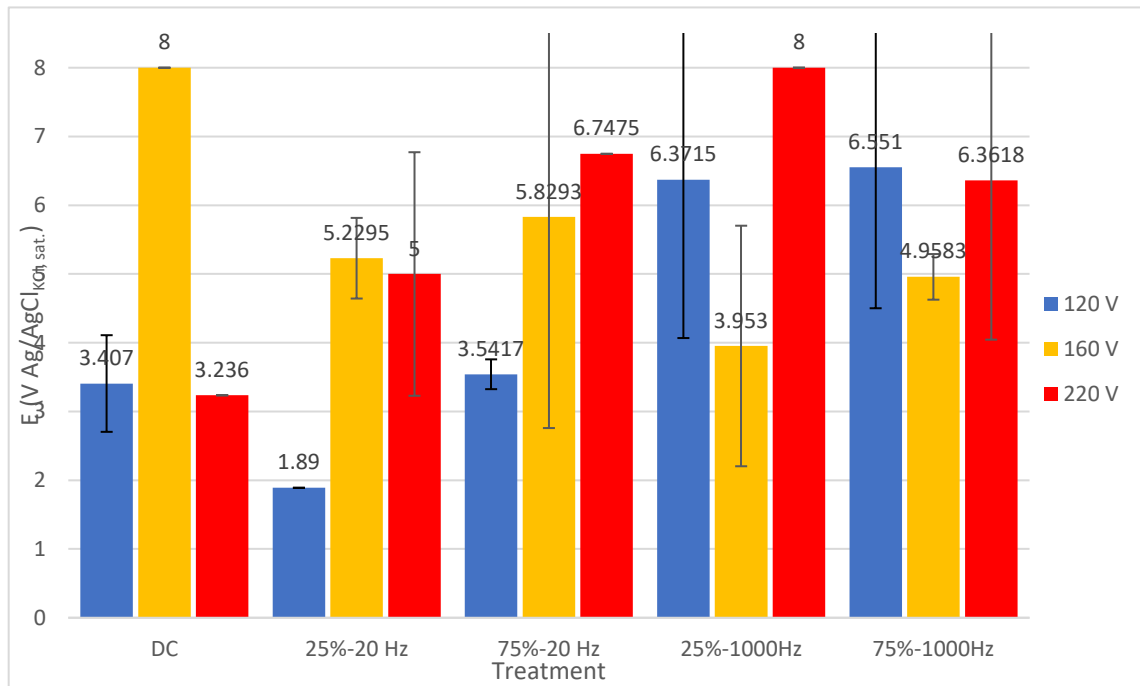


Figure 3.49 Comparison of pitting potentials with different treatments.

The pitting potentials represented in Fig.5.49, are derived as average of the pitting potentials of the two data come out from the repeatability. When the sample does not present pitting, it was taken as value 8 V, the maximum voltage detected from the instrument. So, the value present in Fig.5.49 equal to 8 V are evaluation in which the minimum was considered.

Analysing the voltages one by one, the 120 V exhibits a strong improvement of the corrosion resistance changing the frequency from 20 Hz to 1000 Hz with a pitting potential that increases of about 3 V with respect to the DC. However, the differences between the duty cycles are not so clear in this case. It is only possible to note that the increasing of the duty cycle at 20 Hz improves the corrosion resistance of the sample bringing it near to the DC one. So, comparing the duty cycles, the higher one results in the best corrosion resistance. At 160 V, the trend is opposite and the increasing of the frequency does not

produce any beneficial effect on the corrosion resistance. However, the improvement of the corrosion resistance with the duty cycle is confirmed and between the two duty the 75% results always in a better corrosion resistance. The last voltage tested (i.e.220 V) exhibits the best improvements in corrosion resistance with an increasing till 5 V of the pitting potential with respect to the DC in the case of 25% and 1000 Hz. Unfortunately, the effects of the frequency and duty cycles are not so clear: in facts, looking at the 25% increasing the frequency the corrosion resistance is improved, while looking at the 75% it is the opposite. Also, the increasing of the duty does not produce an univocal effect but at low frequency it improves the corrosion resistance while at high frequency it reduces the corrosion resistance.

As it was already done for all the partial results, the pitting potentials are now compared with the porosity of the sample to have a global view on the phenomena ongoing on the oxide layer.

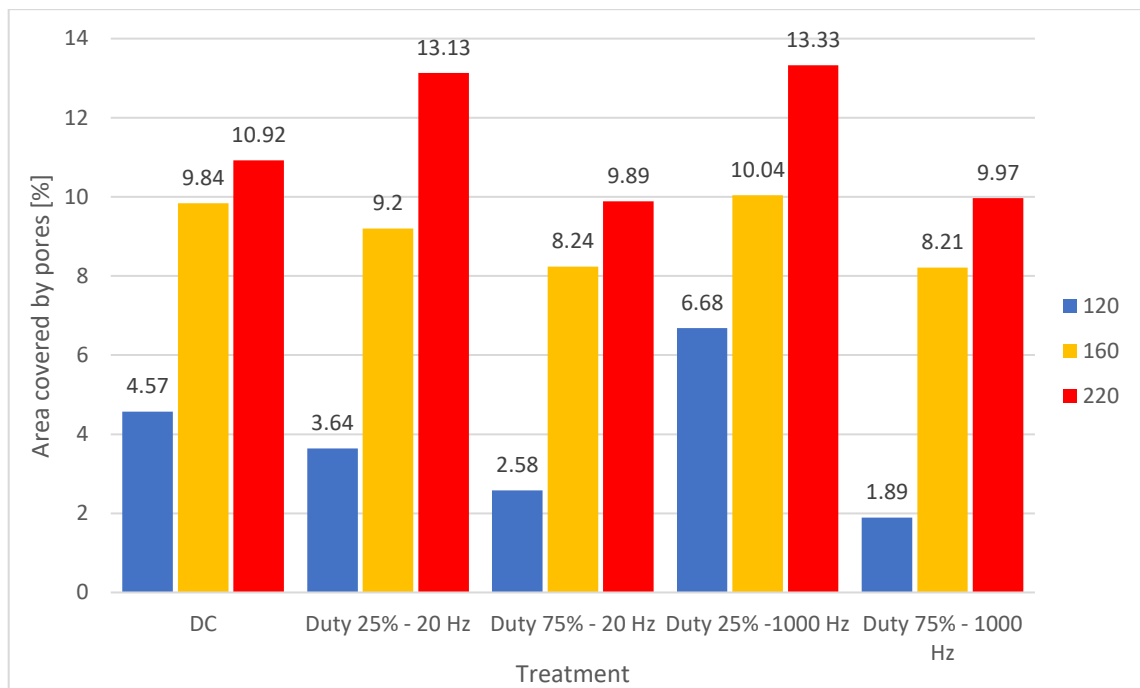


Figure 5.50 Area covered by pores of samples anodized at 120 V, 160 V and 220 V with different treatments.

The best results in terms of corrosion resistance is given by the sample anodized at 220 V with a duty of 25% and a frequency of 1000 Hz, but, as already said in the analysis of the partial data, it is not the less porous. On the contrary, the sample is one of the two most porous samples. This confirms the fact that corrosion is not directly connected to the porosity, but other factors have to be taken into account as the thickness or the nature of the oxide layer. However, from the Fig.5.50 it is possible to derive a trend in the porosity

of the sample anodized at different voltages. In facts, looking at the three different voltages, the porosity increases in all cases increasing the voltage.

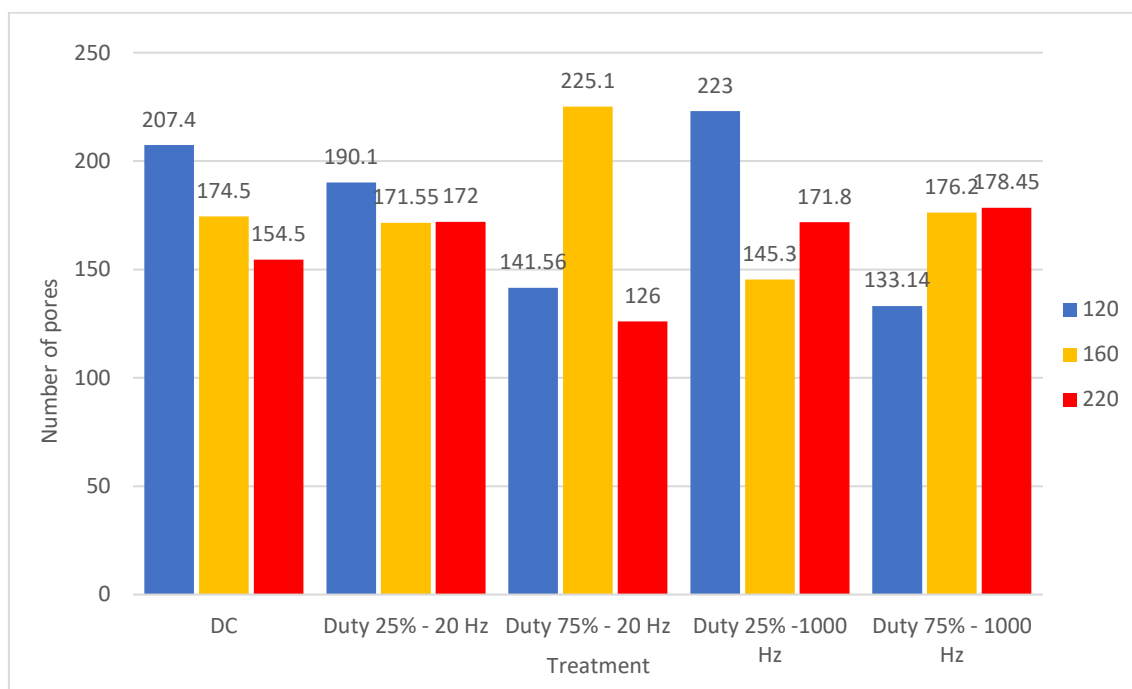


Figure 5.51 Number of pores with different treatments

Looking at the Fig.5.51, the sample with the highest corrosion resistance is one of the samples with the highest number of pores among all the sample analysed. This is another example of how complicated the corrosion resistance dependence is. In facts, even if the area covered by pores and their number are both very high (these two factors influence the diffusivity of the aggressive media), the corrosion resistance is high. This phenomenon can be explained with the increasing of the thickness of the oxide layer, but more tests have to be performed.

Comparing the figures 5.52 and 5.51, it can be noticed that the number of pores and the anatase phase for low voltages, as 120 V, follow the same trend with a maximum at 25% duty and 1000 Hz. This is due to the production of the anatase phase with the voltage that is linear till the passage in the ASD range where other factors play an important role and the pores are no more limited to the oxide surface. As said, all the other voltages do not present any correlation between the crystallinity phase and the number of the pores.

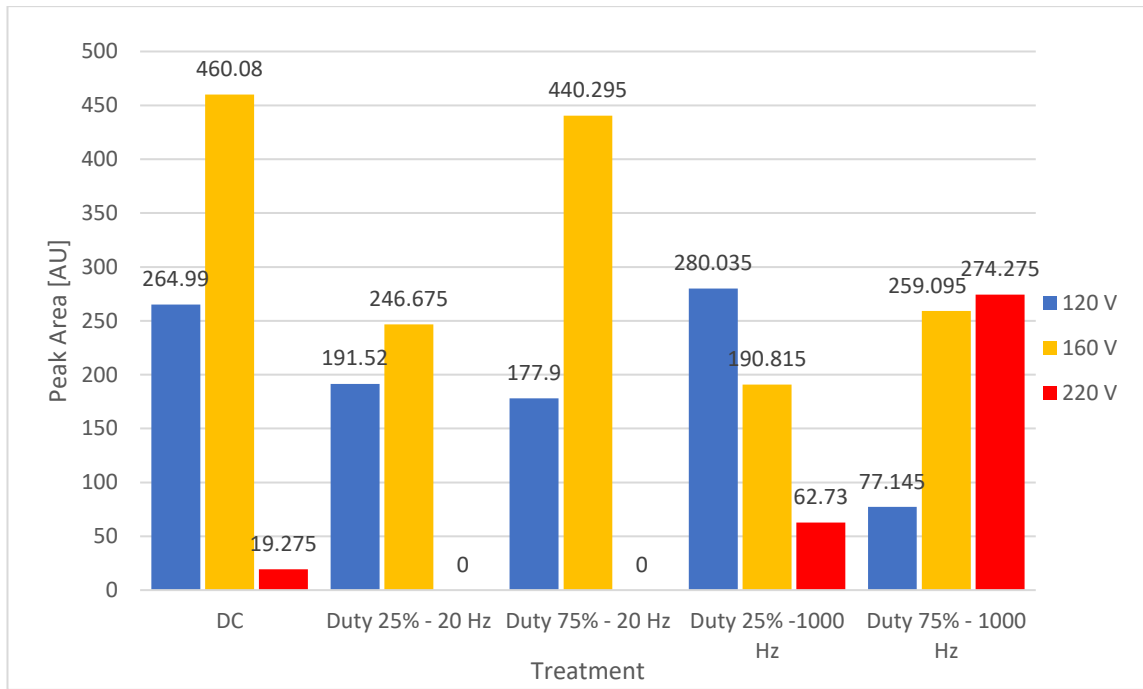


Figure 5.52 Anatase phase with different treatments

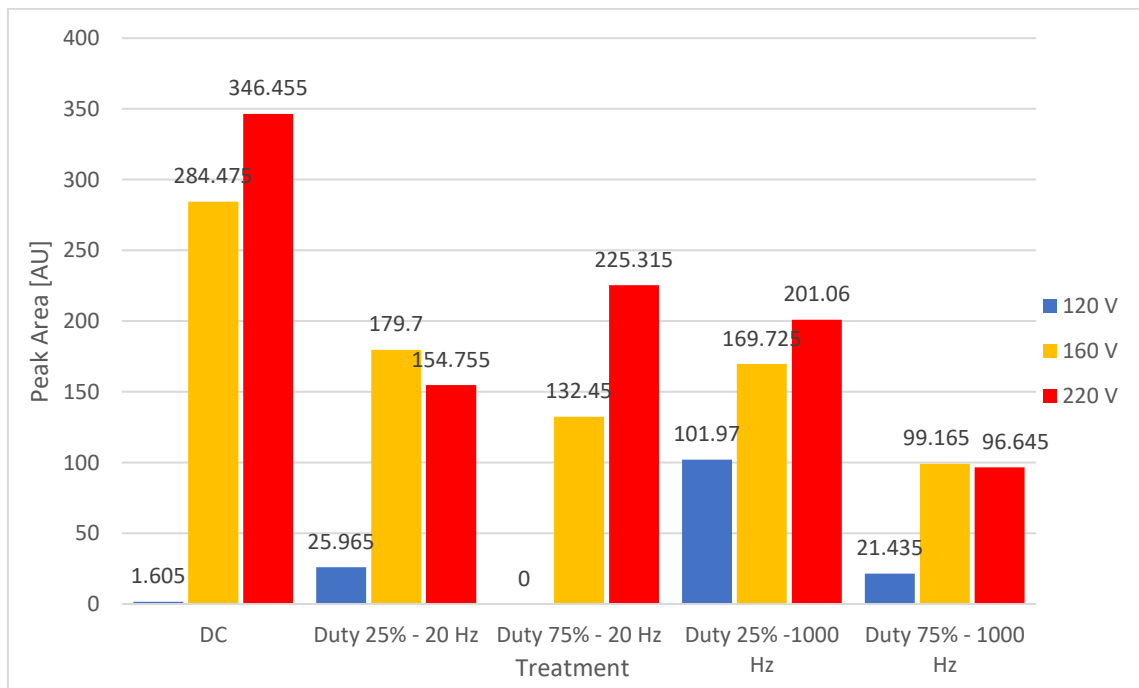


Figure 5.53 Rutile phase with different treatments

Since the corrosion resistance of the samples does not show a single well-defined treatment to improve Titanium corrosion resistance, also other factors of application have to be taken into account, as energy savings.

### 5.3.2 Energy Savings

One of the most interesting characteristic of the discontinuous anodization is the possibility of reaching the same performances as the DC anodization but saving energy. In facts, while for the DC anodization the current has to be supplied for the entire process, when a duty cycle is introduced the current is supplied only for a fraction of the time. It is possible to record the current at the end of the process for each treatment and to derive an approximation of the current supplied during the discontinuous treatment multiplying the current recorded with the percentage of the plateau ignoring the spike in cathodic and anodic direction. In table 5.58 all the data about the average of the current applied are reported.

Concerning energy savings, as depicted in Figure 2.7, during a duty cycle, the current assumes negative values when bringing the voltage to zero, but that value is proportional to the spike needed to bring it up at the beginning of a new cycle, and to the plateau, the ratio among the different samples remains the same. In addition, the duration of the spikes is negligible respect to the duration of a cycle. For these reasons, as a first approximation, it can be considered that the current is erogated constantly at the plateau value, also seeing the perfect reproducibility of the results (Table 4.5). In addition, the value of the plateau registered grows during the transient and the value reported in Table 4.5 is the final one, i.e. the maximum, however the transient is the same for all the curves. As a consequence, the value reported will be higher respect to the real consume of each duty cycle anodization, but the difference among the anodizing will be proportional to it.

Therefore, it is defined an average circulating current density, weighted on a period of 1 second and evaluated as follows:

$$i_{av} = i_{plateau} * Duty\% \quad 7)$$

Table 5.57 Calculated average current with different treatments

Waveform	Voltage[V]	Frequency[Hz]	I <sub>AV</sub>
<b>DC</b>	120	-	0.36
<b>DC</b>	160	-	0.8
<b>DC</b>	220	-	2.4
<b>DUTY 25%</b>	120	20	0.1
<b>DUTY 25%</b>	160	20	0.6
<b>DUTY 25%</b>	220	20	1.75

<b>DUTY 75%</b>	120	20	0.45
<b>DUTY 75%</b>	160	20	0.5
<b>DUTY 75%</b>	220	20	1.05
<b>DUTY 25%</b>	120	1000	0.4
<b>DUTY 25%</b>	160	1000	0.75
<b>DUTY 25%</b>	220	1000	1.5
<b>DUTY 75%</b>	120	1000	0.3
<b>DUTY 75%</b>	160	1000	0.97
<b>DUTY 75%</b>	220	1000	3.45

The treatment with 20 Hz of frequency and 25% of duty cycle reaching 120 V leads to the 70% of energy savings with respect to the DC treatment. For higher voltages the treatment with higher energy saving is the low frequency one. This could be explained with the energy needed to polarization and depolarization that are more numerous at high frequency. So, the higher the frequency, the higher the energy consumption. However, while the dependence to the frequency is constant and present for all the voltages, the dependence of the energy savings to duty cycle are less clear. At low voltages, close to the start of the anodic spark deposition regime, the 25% duty cycle is sufficient to grow the oxide layer, but when the thickness of the oxide layer increases and the temperature becomes higher, the 25% is no more sufficient to grow the oxide layer causing a decreasing in the energy savings. For this reason at higher voltages the increasing of the duty cycle leads to an increasing of the energy savings. Although less performant, even at 220 V pulsed anodizing results in more than 55% of energy saved respect to DC anodizing.

The current needed to the DC anodizing is generally lower respect to both duty cycles at 120 V, except for the duty 25% at 20 Hz, but increasing with the voltage it is evident that duty cycle anodizing results more convenient in terms of energy savings, except for the duty cycle 75% at 1000 Hz which is always above the consumption of the DC. Despite this, as said before, the lowest porosity is obtained with a duty cycle 75% at 1000 Hz, as a compromise, especially when considering industrial applications, it is recommended to anodize with a duty cycle 75% at 20 Hz. The duty cycle 25% at 20 Hz, despite being the best in terms of energy savings, can be recommended only for a voltage up to 160 V. Although, as mentioned before, the duty cycle 25% at 20 Hz shows a porosity higher than the duty 75%, however it is still lower respect to the DC case.

## ***Chapter 6 – Conclusions***

After a long excursus on the possible ways to improve titanium corrosion resistance such as thermal treatments, chemical treatments and anodizing, to improve to possible industrial application the last one has been optimized. Actually, in this study it has been found the possibility to not only obtain a corrosion resistance equal to the DC anodizing, but also to tune the superficial characteristics of titanium.

Titanium samples, after polishing with SiC papers and ultrasonic cleaning in ethanol, have been anodized in sulphuric acid 0.5 M following three different waveforms: duty cycle 25%, duty cycle 75% and DC. Each of them has been applied with three different final voltages: 120 V, 160 V and 220 V and with two values of frequency: 20 Hz and 1000 Hz. During the treatment, the current and the temperature of the solution have been kept under control in order to efficiently evaluate the energy consumption of each method for a possible industrial application.

SEM and XRD analysis have been carried out to characterize the surface of the samples treated. Those anodized with duty 75% presented the lowest values of porosity for each value of voltage and frequency respect to DC and duty 25%. Those anodized with duty 25% for low frequency values and a voltage up to 160 V showed a porosity smaller respect to DC, in the same conditions. Increasing the voltage and keeping the same frequency, the tendency is inverted. At higher frequencies, for each value of voltage, the area covered by pores is bigger respect to DC, in the same conditions. With all waveforms, the porosity increased with increasing the voltage.

Concerning crystallinity, with duty 25% for each value of frequency the rutile phase is already present at 120 V, differently from the DC case. With duty 75%, instead, at a frequency of 20 Hz, the trend is analogous to the one observed in the DC case, increasing the frequency and at high voltages (220 V) the anatase phase results predominant, differently from the other cases.

Then, various electrolytes have been tested on bare titanium and on samples anodized at 150 V, to find the right composition and parameters that would present the necessary

aggressiveness to attack anodized titanium, with sodium bromide 0.5 M at 50°C showing the desired behaviour. The corrosion resistance has been investigated by electrochemical potentiodynamic tests.

At a voltage of 120 V and frequency 20 Hz, both duty cycles presented a lower corrosion resistance respect to the DC case, but at the same voltage and increasing the frequency the duty cycles presented a superior behaviour. Increasing the voltage to 160 V the DC case resulted more corrosion resistant respect to both duties, regardless of the frequency, while reaching 220 V both duties, at each value of frequency, showed better resistance respect to the DC. However, in general, increasing the frequency, and also the voltage, it is observed an increase in the corrosion resistance, followed by an increase of the rutile phase and a decrease of the anatase, which is known for decreasing the corrosion resistance of titanium when present in higher amount respect to the rutile.

The results of pulsed anodizing in the form of duty cycle shows the possibility to obtain a more corrosion resistant oxide, at high voltages, respect to DC anodizing and, at the same time, to consume less energy, the lowest possible with duty 25% at 20 Hz. However, the energy saving and the corrosion resistance are not the only results that makes this study interesting. In facts, through the tuning of duty cycles, frequency and wave form, it was possible to modify as preferred the porosity, thickness and crystallinity of the final oxide layer. For example, the same results of corrosion resistance can be obtained with more than 70% of energy saving passing from DC anodizing to duty cycle 25% at 20 Hz in case of anodic oxidation carried out up to 120 V. It is also possible to reduce porosity by 60% using the same technique or decrease oxide crystallinity for applications in which amorphous oxide is desired. It is even possible to pass from oxides obtained at 220 V containing almost only rutile crystalline phase to oxides with the same corrosion resistance and porosity but composed principally by anatase crystalline phase. This tool could be an important matter of study for fine chemicals applications (catalysis) and superficial treatments that has to be deeper developed in future research in this field.

# Bibliography

1. Leyens C, Peters M r (2003) Titanium and titanium alloys: fundamentals and applications. Wiley-VCH ; John Wiley, Weinheim, Chichester
2. Greenwood NN, Earnshaw A (1997) Chemistry of Elements, 2nd edition. Butterworth-Heinemann, Oxford
3. Asharf Imam M, Froes FH, Dring KF (2010) Cost-affordable titanium III : selected, peer reviewed papers from the TMS 2010 spring Symposium on "Cost-affordable Titanium III." Trans Tech Publications Ltd, Stafa-Zurich
4. Virtanen S (2008) Corrosion of biomedical implant materials. Corros Rev 26:147–171
5. Eylon D (1981) Titanium for energy and industrial applications. Warrendale, Pa. : Metallurgical Society of AIME
6. titanium | Properties, Uses, & Facts | Britannica.com. <https://www.britannica.com/science/titanium>. Accessed 11 Nov 2018
7. Prando D, Brenna A, Diamanti MV, et al (2017) Corrosion of titanium: Part 1: aggressive environments and main forms of degradation. Journal of Applied Biomaterials & Functional Materials 15:0–0. <https://doi.org/10.5301/jabfm.5000387>
8. Zieliński A, Sobieszczyk S (2008) Corrosion of Titanium biomaterials, mechanisms, effects and modelisation. Corros Rev 26:1–22 . doi: <https://doi.org/10.1515/correv.2008.1>
9. Gurrappa I, Reddy DV (2005) Characterisation of titanium alloy, IMI-834 for corrosion resistance under different environmental conditions. J Alloys Compd 390:270–274 . doi: 10.1016/j.jallcom.2004.08.040
10. Schutz RW (2003) FN Speller Award Lecture: Platinum Group Metal Additions to Titanium: A Highly Effective Strategy for Enhancing Corrosion Resistance. Corrosion 59:1043–1057
11. Janisch R, Gopal P, Spaldin NA (2005) Transition metal-doped TiO<sub>2</sub> and ZnO - Present status of the field. Journal of Physics Condensed Matter 17:R657–R689. <https://doi.org/10.1088/0953-8984/17/27/R01>
12. Peacock DK, Grauman JS (1998) Crevice and under deposit corrosion resistance of titanium alloys in highly aggressive environments. Materials and Corrosion - Werkstoffe und Korrosion 49:61–68. [https://doi.org/10.1002/\(SICI\)1521-4176\(199802\)49:2<61::AID-MACO61>3.0.CO;2-I](https://doi.org/10.1002/(SICI)1521-4176(199802)49:2<61::AID-MACO61>3.0.CO;2-I)
13. Prando D, Brenna A, Bolzoni FM, et al (2017) Electrochemical anodizing treatment to enhance localized corrosion resistance of pure titanium. Journal of applied biomaterials & functional materials 15:e19–e24. <https://doi.org/10.5301/jabfm.5000344>
14. General Attack Corrosion. <https://www.nace.org/General-Attack-Corrosion/>. Accessed 1 Nov 2017

15. Peters M, Leyens C (2003) Non-Aerospace Applications of Titanium and Titanium Alloys. In: Leyens C, Peters M (eds) Titanium and Titanium Alloys. Wiley-VCH Verlag GmbH & Co. KGaA, pp 393–422
16. Gaul E (1993) Coloring titanium and related metals by electrochemical oxidation. *J Chem Educ* 70:176. <https://doi.org/10.1021/ed070p176>
17. Diamanti MV, Del Curto B, Pedferri M (2008) Interference colors of thin oxide layers on titanium. *Color Research & Application* 33:221–228. <https://doi.org/10.1002/col.20403>
18. Williams DF (1977) Titanium as a metal for implantation Part 1: physical properties. *J Med Eng Technol* 1:195–198
19. Brossia CS, Cragolino GA Effect of palladium on the corrosion behavior of titanium. *Corros Sci* 46:1693–1711 . doi: 10.1016/j.corsci.2003.10.003
20. Myers JR, Bomberger HB, Froes FH (1984) Corrosion behavior and use of titanium and its alloys. *JOM* 36:50–60
21. Mansfeld F, Liu G, Xiao H, et al (1994) The corrosion behavior of copper alloys, stainless steels and titanium in seawater. *Corros Sci* 36:2063–2095
22. Hodgkiss T, Asimakopoulos A (1981) Studies of the localised-corrosion behaviour of some stainless steels, incoloy 825 and titanium in seawater. *Desalination* 38:247–256 . doi: 10.1016/S0011-9164(00)86071-3
23. Corrosion resistance of Titanium (TIMET)
24. Shoesmith D, Noël JJ (2010) Corrosion of Titanium and its Alloys. *Shreirs Corros* 2042–2052 . doi: 10.1016/B978-044452787-5.00097-4
25. van Drunen J, Zhao B, Jerkiewicz G (2011) Corrosion behavior of surface-modified titanium in a simulated body fluid. *Journal of Materials Science* 46:5931–5939. <https://doi.org/10.1007/s10853-011-5548-y>
26. Protocol for Preparing Simulated Body Fluid (SBF). In: Dep. Mater. Chem. Grad. Sch. Eng. Kyoto Univ. <http://www.life.kyutech.ac.jp/~tmiya/SBF-e.html>. Accessed 3 Nov 2017
27. Ortiz AJ, Fernández E, Vicente A, et al (2011) Metallic ions released from stainless steel, nickel-free, and titanium orthodontic alloys: Toxicity and DNA damage. *American Journal of Orthodontics and Dentofacial Orthopedics* 140:e115–e122. <https://doi.org/10.1016/j.ajodo.2011.02.021>
28. Chiesa R, Giavaresi G, Fini M, et al (2007) In vitro and in vivo performance of a novel surface treatment to enhance osseointegration of endosseous implants. *Oral Surgery, Oral Medicine, Oral Pathology, Oral Radiology, and Endodontology* 103:745–756. <https://doi.org/10.1016/j.tripleo.2006.09.025>
29. Nakagawa M, Matsuya S, Shiraishi T, Ohta M (1999) Effect of fluoride concentration and pH on corrosion behavior of titanium for dental use. *J Dent Res* 78:1568–1572. <https://doi.org/10.1177/00220345990780091201>

30. Wang ZB, Hu HX, Liu CB, Zheng YG (2014) The effect of fluoride ions on the corrosion behavior of pure titanium in 0.05M sulfuric acid. *Electrochimica Acta* 135:526–535 . doi: 10.1016/j.electacta.2014.05.055
31. Andijani IN, Ahmad S, Malik AU CORROSION BEHAVIOR OF TITANIUM METAL IN PRESENCE OF INHIBITED SULFURIC ACID AT 50oC1
32. IMI IMINM (1960) Corrosion resistance of titanium. Birmingham: IMI
33. (2002) Titanium - Corrosion by Acids. In: AZoM.com. <https://www.azom.com/article.aspx?ArticleID=1240>.
34. Oxygen ion irradiation effect on corrosion behavior of titanium in nitric acid medium | Request PDF. In: ResearchGate. [https://www.researchgate.net/publication/241072519\\_Oxygen\\_ion\\_irradiation\\_effect\\_on\\_corrosion\\_behavior\\_of\\_titanium\\_in\\_nitric\\_acid\\_medium](https://www.researchgate.net/publication/241072519_Oxygen_ion_irradiation_effect_on_corrosion_behavior_of_titanium_in_nitric_acid_medium). Accessed 24 Oct 2018
35. Pound B (2014) Corrosion behavior of metallic materials in biomedical applications. I. Ti and its alloys. *CORROSION REVIEWS* 32:1. <https://doi.org/10.1515/corrrev-2014-0007>
36. Jiang Z, Dai X, Norby T, Middleton H (2011) Investigation of pitting resistance of titanium based on a modified point defect model. *Corrosion Science* 53:815–821. <https://doi.org/10.1016/j.corsci.2010.11.015>
37. Frankel GS (1998) Pitting Corrosion of Metals A Review of the Critical Factors. *J Electrochem Soc* 145:2186–2198. <https://doi.org/10.1149/1.1838615>
38. Leckie HP, Uhlig HH (1966) Environmental Factors Affecting the Critical Potential for Pitting in 18–8 Stainless Steel. *J Electrochem Soc* 113:1262–1267. <https://doi.org/10.1149/1.2423801>
39. Alvarez MG, Galvele JR (2010) 2.04 - Pitting Corrosion. In: Cottis B, Graham M, Lindsay R, et al (eds) *Shreir's Corrosion*. Elsevier, Oxford, pp 772–800
40. POURBAIX M (1970) SIGNIFICANCE OF PROTECTION POTENTIAL IN PITTING AND INTERGRANULAR CORROSION. *Corrosion* 26:431–438
41. Liu J, Alfantazi A, Asselin E (2015) Effects of Temperature and Sulfate on the Pitting Corrosion of Titanium in High-Temperature Chloride Solutions. *J Electrochem Soc* 162:C189–C196. <https://doi.org/10.1149/2.0541504jes>
42. Posey FA, Bohlmann EG (1967) Pitting of titanium alloys in saline waters. *Desalination* 3:269–279. [https://doi.org/10.1016/S0011-9164\(00\)80156-3](https://doi.org/10.1016/S0011-9164(00)80156-3)
43. Burstein GT, Liu C, Souto RM (2005) The effect of temperature on the nucleation of corrosion pits on titanium in Ringer's physiological solution. *Biomaterials* 26:245–256. <https://doi.org/10.1016/j.biomaterials.2004.02.023>
44. Casillas N (1994) Pitting Corrosion of Titanium. *Journal of The Electrochemical Society* 141:636. <https://doi.org/10.1149/1.2054783>
45. Huo S, Meng X (1990) The states of bromide on titanium surface prior to pit initiation. *Corrosion Science* 31:281–286. [https://doi.org/10.1016/0010-938X\(90\)90120-T](https://doi.org/10.1016/0010-938X(90)90120-T)

46. Crevice Corrosion. <https://www.nace.org/Corrosion-Central/Corrosion-101/Crevice-Corrosion/>. Accessed 6 Nov 2017
47. Antoniou RA, Radtke TC (1997) Mechanisms of fretting-fatigue of titanium alloys. *Materials Science and Engineering: A* 237:229–240. [https://doi.org/10.1016/S0921-5093\(97\)00419-X](https://doi.org/10.1016/S0921-5093(97)00419-X)
48. Jones RH (2017) *Stress-corrosion cracking, materials performance, and evaluation*, 2nd edition. ASM International, Materials Park, OH
49. Wood AC (1960) CORROSION RESISTANCE OF TITANIUM. *Anti-Corrosion Methods and Materials* 7:135–162. <https://doi.org/10.1108/eb019718>
50. Hollis AC, Scully JC (1993) The stress corrosion cracking and hydrogen embrittlement of titanium in methanol-hydrochloric acid solutions. *Corrosion Science* 34:821–835. [https://doi.org/10.1016/0010-938X\(93\)90102-M](https://doi.org/10.1016/0010-938X(93)90102-M)
51. Kolman DG, Scully JR (1997) Understanding the potential and pH dependency of high-strength  $\beta$ -titanium alloy environmental crack initiation. *Metall and Mat Trans A* 28:2645–2656. <https://doi.org/10.1007/s11661-997-0021-x>
52. Shoesmith D, J. Noel J, Hardie D, M. Ikeda B (2000) Hydrogen Absorption and the Lifetime Performance of Titanium Nuclear Waste Containers. *Corrosion Reviews* 18:331. <https://doi.org/10.1515/CORRREV.2000.18.4-5.331>
53. Clarke CF, Hardie D, Ikeda BM (1997) Hydrogen-induced cracking of commercial purity titanium. *Corrosion Science* 39:1545–1559. [https://doi.org/10.1016/S0010-938X\(97\)00055-3](https://doi.org/10.1016/S0010-938X(97)00055-3)
54. Wang ZB, Hu HX, Zheng YG, et al (2016) Comparison of the corrosion behavior of pure titanium and its alloys in fluoride-containing sulfuric acid. *Corrosion Science* 103:50–65. <https://doi.org/10.1016/j.corsci.2015.11.003>
55. Capela MV, Acciari HA, Capela JMV, et al (2008) Repeatability of corrosion parameters for titanium–molybdenum alloys in 0.9% NaCl solution. *Journal of Alloys and Compounds* 465:479–483. <https://doi.org/10.1016/j.jallcom.2007.10.115>
56. Schutz RW (2003) 2003 FN Speller Award Lecture: Platinum Group Metal Additions to Titanium: A Highly Effective Strategy for Enhancing Corrosion Resistance. *Corrosion* 59:1043–1057
57. Prando D, Pedefferri M, Brenna A, Ormellese M (2017) Surface treatment to improve corrosion resistance of pure titanium. *NACE - International Corrosion Conference Series* 3:1606–1619
58. Nakagawa M, Matono Y, Matsuya S, et al (2005) The effect of Pt and Pd alloying additions on the corrosion behavior of titanium in fluoride-containing environments. *Biomaterials* 26:2239–2246. <https://doi.org/10.1016/j.biomaterials.2004.07.022>
59. Michaelis A, Kudelka S, Schultze JW (2000) Corrosion of Ti and Ti0.2PD Under High-Level Waste Disposal Conditions With Microscopic Investigation of Passivity. *Corrosion Reviews* 18:. <https://doi.org/10.1515/CORRREV.2000.18.4-5.395>
60. Brossia CS, Cragolino GA (2004) Effect of palladium on the corrosion behavior of titanium. *Corrosion Science* 46:1693–1711. <https://doi.org/10.1016/j.corsci.2003.10.003>

61. Trenczek-Zajac A (2018) Influence of etching on structural, optical and photoelectrochemical properties of titanium oxides obtained via thermal oxidation. *Materials Science in Semiconductor Processing* 83:159–170. <https://doi.org/10.1016/j.mssp.2018.04.025>
62. Fazel M, Salimijazi HR, Golozar MA, Garsivaz jazi MR (2015) A comparison of corrosion, tribocorrosion and electrochemical impedance properties of pure Ti and Ti6Al4V alloy treated by micro-arc oxidation process. *Applied Surface Science* 324:751–756. <https://doi.org/10.1016/j.apsusc.2014.11.030>
63. Habazaki H (2018) Growth of Passive Films on Valve Metals and Their Alloys. In: Wandelt K (ed) *Encyclopedia of Interfacial Chemistry*. Elsevier, Oxford, pp 250–258
64. Diamanti MV, Garbagnoli P, Curto B, Pedferri MP (2015) On the Growth of Thin Anodic Oxides Showing Interference Colors on Valve Metals. *Current Nanoscience* 11:307–316. <https://doi.org/10.2174/1573413711666150212235619>
65. Casanova L. MA Photocatalytic reactor for dye degradation with TiO<sub>2</sub> nanotubes
66. Shibata T, Zhu Y-C (1995) The effect of temperature on the growth of anodic oxide film on titanium. *Corrosion Science* 37:133–144. [https://doi.org/10.1016/0010-938X\(94\)00125-P](https://doi.org/10.1016/0010-938X(94)00125-P)
67. Sibert ME (1963) Electrochemical Oxidation of Titanium Surfaces. *Journal of The Electrochemical Society* 110:65. <https://doi.org/10.1149/1.2425674>
68. Diamanti MV, Ormellese M, Pedferri M (2010) Alternating current anodizing of titanium in halogen acids combined with Anodic Spark Deposition: Morphological and structural variations. *Corrosion Science* 52:1824–1829. <https://doi.org/10.1016/j.corsci.2010.01.036>
69. Sul Y-T, Johansson CB, Jeong Y, Albrektsson T (2001) The electrochemical oxide growth behaviour on titanium in acid and alkaline electrolytes. *Medical Engineering & Physics* 23:329–346. [https://doi.org/10.1016/S1350-4533\(01\)00050-9](https://doi.org/10.1016/S1350-4533(01)00050-9)
70. Diamanti MV, Del Curto B, Pedferri M (2011) Anodic oxidation of titanium: from technical aspects to biomedical applications. *Journal of Applied Biomaterials & Biomechanics* 9:55–69. <https://doi.org/10.5301/JABB.2011.7429>
71. Diamanti MV, Pedferri MP (2007) Effect of anodic oxidation parameters on the titanium oxides formation. *Corrosion Science* 49:939–948. <https://doi.org/10.1016/j.corsci.2006.04.002>
72. Liu J, Yi J, Li S, et al (2010) Effect of electrolyte concentration on morphology, microstructure and electrochemical impedance of anodic oxide film on titanium alloy Ti-10V–2Fe–3Al. *Journal of Applied Electrochemistry* 40:1545–1553. <https://doi.org/10.1007/s10800-010-0132-8>
73. Williamson RS, Disegi J, Janorkar AV, et al (2015) Effect of duty cycle on the crystallinity, pore size, surface roughness and corrosion resistance of the anodized surface on titanium. *Surface and Coatings Technology* 277:278–288. <https://doi.org/10.1016/j.surfcoat.2015.07.020>
74. Diamanti MV, Pedferri M PRODUCTION AND CHARACTERIZATION OF THICK TITANIUM OXIDE FILMS BY ANODIC OXIDATION. 34

75. D. Prando Development and characterization of photocatalytic anodic TiO<sub>2</sub> films for wastewater treatment
76. Mazhar AA (1990) Effect of temperature on the formation and dissolution of anodic oxide films on titanium in acid solutions. *Journal of Applied Electrochemistry* 20:494–499. <https://doi.org/10.1007/BF01076062>
77. Corrosion Resistance of Anodized and Unanodized Titanium. <https://pubs.acs.org/doi/pdf/10.1021/ie50495a031>. Accessed 11 Oct 2018
78. Van Gils S, Mast P, Stijns E, Terryn H (2004) Colour properties of barrier anodic oxide films on aluminium and titanium studied with total reflectance and spectroscopic ellipsometry. *Surface and Coatings Technology* 185:303–310. <https://doi.org/10.1016/j.surfcoat.2004.01.021>
79. Diamanti MV, Del Curto B, Masconale V, et al (2012) Anodic coloring of titanium and its alloy for jewels production. *Color Research & Application* 37:384–390. <https://doi.org/10.1002/col.20683>
80. Diamanti MV, Pozzi P, Randone F, et al (2016) Robust anodic colouring of titanium: Effect of electrolyte and colour durability. *Materials & Design* 90:1085–1091. <https://doi.org/10.1016/j.matdes.2015.11.063>
81. da Fonseca C, Traverse A, Tadjeddine A, Belo M da C (1995) A characterization of titanium anodic oxides by X-ray absorption spectroscopy and grazing X-ray diffraction. *Journal of Electroanalytical Chemistry* 388:115–122. [https://doi.org/10.1016/0022-0728\(94\)03806-E](https://doi.org/10.1016/0022-0728(94)03806-E)
82. Diamanti MV, Bolzoni F, Ormellese M, et al (2010) Characterisation of titanium oxide films by potentiodynamic polarisation and electrochemical impedance spectroscopy. *Corrosion Engineering, Science and Technology* 45:428–434. <https://doi.org/10.1179/147842208X373191>
83. Prando D, Brenna A, Diamanti MV, et al (2018) Corrosion of titanium: Part 2: Effects of surface treatments. *Journal of Applied Biomaterials & Functional Materials* 16:3–13. <https://doi.org/10.5301/jabfm.5000396>
84. Banakh O, Journot T, Gay P-A, et al (2016) Synthesis by anodic-spark deposition of Ca- and P-containing films on pure titanium and their biological response. *Applied Surface Science* 378:207–215. <https://doi.org/10.1016/j.apsusc.2016.03.161>
85. Herbertz S, Aleksa P, Zielinski M, et al (2018) Bias voltage - Induced oxidation of titanium microelectrodes in planar Ti / TiO<sub>x</sub> heterojunctions. *Superlattices and Microstructures*. <https://doi.org/10.1016/j.spmi.2018.09.006>
86. Hu H, Liu X, Ding C (2010) Preparation and cytocompatibility of Si-incorporated nanostructured TiO<sub>2</sub> coating. *Surface and Coatings Technology* 204:3265–3271. <https://doi.org/10.1016/j.surfcoat.2010.03.028>
87. Babaei M, Dehghanian C, Vanaki M (2015) Effect of additive on electrochemical corrosion properties of plasma electrolytic oxidation coatings formed on CP Ti under different processing frequency. *Applied Surface Science* 357:712–720. <https://doi.org/10.1016/j.apsusc.2015.09.059>

88. Aliasghari S, Hashimoto T, Skeldon P, Thompson GE (2014) Effect of Chloride Ions in Plasma Electrolytic Oxidation of Titanium. *ECS Electrochemistry Letters* 3:C17–C20. <https://doi.org/10.1149/2.002405eel>
89. Sarbishei S, Faghihi Sani MA, Mohammadi MR (2016) Effects of alumina nanoparticles concentration on microstructure and corrosion behavior of coatings formed on titanium substrate via PEO process. *Ceramics International* 42:8789–8797. <https://doi.org/10.1016/j.ceramint.2016.02.120>
90. Sarbishei S, Faghihi Sani MA, Mohammadi MR (2014) Study plasma electrolytic oxidation process and characterization of coatings formed in an alumina nanoparticle suspension. *Vacuum* 108:12–19. <https://doi.org/10.1016/j.vacuum.2014.05.008>
91. Kaluđerović MR, Schreckenbach JP, Graf H-L (2016) Titanium dental implant surfaces obtained by anodic spark deposition – From the past to the future. *Materials Science and Engineering: C* 69:1429–1441. <https://doi.org/10.1016/j.msec.2016.07.068>
92. Lukiyanchuk IV, Rudnev VS, Tyrina LM, Chernykh IV (2014) Plasma electrolytic oxide coatings on valve metals and their activity in CO oxidation. *Applied Surface Science* 315:481–489. <https://doi.org/10.1016/j.apsusc.2014.03.040>
93. Curto BD, Diamanti MV, Pria PD, et al Anodic Spark Deposition treatments to increase reliability of Ti6Al4V modular prostheses. 7
94. Macak JM, Tsuchiya H, Ghicov A, et al (2007) TiO<sub>2</sub> nanotubes: Self-organized electrochemical formation, properties and applications. *Current Opinion in Solid State and Materials Science* 11:3–18. <https://doi.org/10.1016/j.cossms.2007.08.004>
95. Regonini D, Bowen CR, Jaroenworarluck A, Stevens R (2013) A review of growth mechanism, structure and crystallinity of anodized TiO<sub>2</sub> nanotubes. *Materials Science and Engineering: R: Reports* 74:377–406. <https://doi.org/10.1016/j.mser.2013.10.001>
96. Cai Q, Yang L, Yu Y (2006) Investigations on the self-organized growth of TiO<sub>2</sub> nanotube arrays by anodic oxidization. *Thin Solid Films* 515:1802–1806. <https://doi.org/10.1016/j.tsf.2006.06.040>
97. Li F, Zhang L, Metzger RM (1998) On the Growth of Highly Ordered Pores in Anodized Aluminum Oxide. *Chemistry of Materials* 10:2470–2480. <https://doi.org/10.1021/cm980163a>
98. Michal P, Vagaská A, Gombár M, et al (2014) Monitoring of influence of significant parameters during anodizing of aluminium. In: 2014 IEEE 12th International Symposium on Applied Machine Intelligence and Informatics (SAMI). pp 49–54
99. Vagaská A, Fečová E, Michal P, Gombár M (2016) The Influence of Input Factors of Aluminium Anodizing Process on Resulting Thickness and Quality of Aluminium Oxide Layer. *Procedia Engineering* 149:512–519. <https://doi.org/10.1016/j.proeng.2016.06.699>
100. Arrabal R, Matykina E, Hashimoto T, et al (2009) Characterization of AC PEO coatings on magnesium alloys. *Surface and Coatings Technology* 203:2207–2220. <https://doi.org/10.1016/j.surfcoat.2009.02.011>

101. Farina SB, Sanchez AG, Ceré S (2015) Effect of Surface Modification on the Corrosion Resistance of Zr-2.5Nb as Material for Permanent Implants. *Procedia Materials Science* 8:1166–1173. <https://doi.org/10.1016/j.mspro.2015.04.181>
102. Vázquez RM, Mozalev A, Calavia R, et al (2014) Gas sensing properties of the nanostructured anodic Zr–W oxide film. *Sensors and Actuators B: Chemical* 204:588–595. <https://doi.org/10.1016/j.snb.2014.08.014>
103. Trivinho-Strixino F, Guimarães FEG, Pereira EC (2008) Zirconium oxide anodic films: Optical and structural properties. *Chemical Physics Letters* 461:82–86. <https://doi.org/10.1016/j.cplett.2008.06.072>
104. Gomez Sanchez A, Ballarre J, Orellano JC, et al (2013) Surface modification of zirconium by anodisation as material for permanent implants: in vitro and in vivo study. *Journal of Materials Science: Materials in Medicine* 24:161–169. <https://doi.org/10.1007/s10856-012-4770-8>
105. Rosenfeld D, Schmid PE, Sz S Electrical transport properties of thin-film metal-oxide-metal Nb<sub>2</sub>O<sub>5</sub> oxygen sensors. 7
106. Mickova I (2010) Photoelectrochemical Study of Anodically Formed Oxide Films on Niobium Surfaces. *Croat Chem Acta* 8
107. Gomes MAB, Onofre S, Juanto S, Bulhões LO de S (1991) Anodization of niobium in sulphuric acid media. *Journal of Applied Electrochemistry* 21:1023–1026. <https://doi.org/10.1007/BF01077589>
108. Rešetić A, Jarić B (1990) Dielectric properties of anodic oxide layers on tantalum. *Journal of Applied Electrochemistry* 20:768–774. <https://doi.org/10.1007/BF01094304>
109. Chen W, Tu Q, Wu H, et al (2017) Study on morphology evolution of anodic tantalum oxide films in different using stages of H<sub>2</sub>SO<sub>4</sub>/HF electrolyte. *Electrochimica Acta* 236:140–153. <https://doi.org/10.1016/j.electacta.2017.03.024>
110. Sloppy JD, Lu Z, Dickey EC, Macdonald DD (2013) Growth mechanism of anodic tantalum pentoxide formed in phosphoric acid. *Electrochimica Acta* 87:82–91. <https://doi.org/10.1016/j.electacta.2012.08.014>
111. Zhang RF, Shan DY, Chen RS, Han EH (2008) Effects of electric parameters on properties of anodic coatings formed on magnesium alloys. *Materials Chemistry and Physics* 107:356–363. <https://doi.org/10.1016/j.matchemphys.2007.07.027>
112. Matykina E, Arrabal R, Mohedano M, et al (2017) Recent advances in energy efficient PEO processing of aluminium alloys. *Transactions of Nonferrous Metals Society of China* 27:1439–1454. [https://doi.org/10.1016/S1003-6326\(17\)60166-3](https://doi.org/10.1016/S1003-6326(17)60166-3)
113. Raj V, Rajaram MP, Balasubramanian G, et al (2003) Pulse Anodizing—An Overview. *Transactions of the IMF* 81:114–121. <https://doi.org/10.1080/00202967.2003.11871515>
114. Barati Darband G, Aliofkhaeizadeh M, Hamghalam P, Valizade N (2017) Plasma electrolytic oxidation of magnesium and its alloys: Mechanism, properties and applications. *Journal of Magnesium and Alloys* 5:74–132. <https://doi.org/10.1016/j.jma.2017.02.004>

115. Yokoyama K, Konno H, Takahashi H, Nagayama M (1982) ADVANTAGES OF PULSE ANODIZING. *Plating and Surface Finishing* 69:62–65
116. Hussein RO, Nie X, Northwood DO (2010) Influence of process parameters on electrolytic plasma discharging behaviour and aluminum oxide coating microstructure. *Surface and Coatings Technology* 205:1659–1667. <https://doi.org/10.1016/j.surfcoat.2010.08.059>
117. Yerokhin AL, Shatrov A, Samsonov V, et al (2005) Oxide ceramic coatings on aluminium alloys produced by a pulsed bipolar plasma electrolytic oxidation process. *Surface and Coatings Technology* 199:150–157. <https://doi.org/10.1016/j.surfcoat.2004.10.147>
118. Dehnavi V, Luan BL, Shoesmith DW, et al (2013) Effect of duty cycle and applied current frequency on plasma electrolytic oxidation (PEO) coating growth behavior. *Surface and Coatings Technology* 226:100–107. <https://doi.org/10.1016/j.surfcoat.2013.03.041>
119. Williamson RS, Disegi J, Janorkar AV, et al (2015) Effect of duty cycle on the crystallinity, pore size, surface roughness and corrosion resistance of the anodized surface on titanium. *Surface and Coatings Technology* 277:278–288. <https://doi.org/10.1016/j.surfcoat.2015.07.020>
120. Wu L, Liu JH, Wu GL, et al (2015) Growth behaviour of anodic oxide film on titanium alloy. *Surface Engineering* 31:904–911. <https://doi.org/10.1179/1743294414Y.0000000396>
121. Williamson RS, Disegi J, Griggs JA, Roach MD (2013) Nanopore formation on the surface oxide of commercially pure titanium grade 4 using a pulsed anodization method in sulfuric acid. *J Mater Sci: Mater Med* 24:2327–2335. <https://doi.org/10.1007/s10856-013-4985-3>
122. Torres-Cerón DA, Gordillo-Delgado F, Moya-Betancourt SN (2017) Effect of the voltage pulse frequency on the structure of TiO<sub>2</sub> coatings grown by plasma electrolytic oxidation. *Journal of Physics: Conference Series* 935:012067. <https://doi.org/10.1088/1742-6596/935/1/012067>
123. Babaei M, Dehghanian C, Vanaki M (2015) Effect of additive on electrochemical corrosion properties of plasma electrolytic oxidation coatings formed on CP Ti under different processing frequency. *Applied Surface Science* 357:712–720. <https://doi.org/10.1016/j.apsusc.2015.09.059>
124. Wang Y, Wang L, Zheng H, et al (2010) Effect of frequency on the structure and cell response of Ca- and P-containing MAO films. *Applied Surface Science* 256:2018–2024. <https://doi.org/10.1016/j.apsusc.2009.09.041>
125. S. G, T. A, N. R (2016) An investigation on pulsed DC plasma electrolytic oxidation of cp-Ti and its corrosion behaviour in simulated body fluid. *Surface and Coatings Technology* 301:63–73. <https://doi.org/10.1016/j.surfcoat.2016.02.043>
126. Wang J-H, Wang J, Lu Y, et al (2015) Effects of single pulse energy on the properties of ceramic coating prepared by micro-arc oxidation on Ti alloy. *Applied Surface Science* 324:405–413. <https://doi.org/10.1016/j.apsusc.2014.10.145>
127. Yao Z, Xu Y, Jiang Z, Wang F (2009) Effects of cathode pulse at low frequency on the structure and composition of plasma electrolytic oxidation ceramic coatings. *Journal of Alloys and Compounds* 488:273–278. <https://doi.org/10.1016/j.jallcom.2009.08.104>

128. Kim W-T, Choi W-Y (2017) Fabrication of TiO<sub>2</sub> photonic crystal by anodic oxidation and their optical sensing properties. *Sensors and Actuators, A: Physical* 260:178–184. <https://doi.org/10.1016/j.sna.2017.04.039>
129. Shoesmith DW, Noel JJ, Hardie D, Ikeda BM (2000) Hydrogen Absorption and the Lifetime Performance of Titanium Nuclear Waste Containers. *Corrosion Reviews* 18:. <https://doi.org/10.1515/CORRREV.2000.18.4-5.331>
130. Pitting corrosion on anodized titanium: Effect of halides - Prando - 2018 - *Materials and Corrosion* - Wiley Online Library. <https://onlinelibrary.wiley.com/doi/full/10.1002/maco.201810171>. Accessed 15 Nov 2018
131. Dugdale I, Cotton JB (1964) The anodic polarization of titanium in halide solutions. *Corrosion Science* 4:397–411. [https://doi.org/10.1016/0010-938X\(64\)90041-1](https://doi.org/10.1016/0010-938X(64)90041-1)
132. Trompette JL, Massot L, Arurault L, Fontorbes S (2011) Influence of the anion specificity on the anodic polarization of titanium. *Corrosion Science* 53:1262–1268. <https://doi.org/10.1016/j.corsci.2010.12.021>
133. Basame SB, White HS (2000) Pitting Corrosion of Titanium The Relationship Between Pitting Potential and Competitive Anion Adsorption at the Oxide Film/Electrolyte Interface. *Journal of The Electrochemical Society* 147:1376. <https://doi.org/10.1149/1.1393364>
134. Prando D, Brenna A, Diamanti MV, et al (2017) Corrosion of titanium: Part 1: aggressive environments and main forms of degradation. *Journal of Applied Biomaterials & Functional Materials* 15:0–0. <https://doi.org/10.5301/jabfm.5000387>
135. NICOLIS D (2017) Chemical and thermal treatments to improve corrosion resistance of titanium. <https://www.politesi.polimi.it/handle/10589/138133>. Accessed 15 Nov 2018
136. Prando D, Brenna A, Diamanti MV, et al (2018) Corrosion of titanium: Part 2: Effects of surface treatments. *Journal of Applied Biomaterials & Functional Materials* 16:3–13. <https://doi.org/10.5301/jabfm.5000396>
137. Lamolle SF, Monjo M, Rubert M, et al (2009) The effect of hydrofluoric acid treatment of titanium surface on nanostructural and chemical changes and the growth of MC3T3-E1 cells. *Biomaterials* 30:736–742. <https://doi.org/10.1016/j.biomaterials.2008.10.052>
138. Dance A *Metallography and Microstructures of Titanium and Its Alloys*
139. Prando D, Brenna A, Bolzoni FM, et al (2017) Electrochemical anodizing treatment to enhance localized corrosion resistance of pure titanium. *Journal of applied biomaterials & functional materials* 15:e19–e24. <https://doi.org/10.5301/jabfm.5000344>